GREENLY SYNTHESISED BIOCOMPATIBLE GRAPHENE/ZIRCONIA NANOCOMPOSITE: TOWARDS THE DEVELOPMENT OF A BIOSENSOR FOR THE DETECTION OF LUNG CANCER BIOMARKERS

LIN LIH POH

Thesis submitted to the University of Nottingham

For the degree of Doctor of Philosophy

28 June 2022

ABSTRACT

Early detection improves the survival rate of lung cancer. Routine check-up gives rise to early detection, however, conventional screening methods such as X-ray and computed tomography (CT) are incompetent for routine check-up of lung carcinoma due to health hazards associated with repeated exposure to ionizing radiation. These limitations call for a safer, faster, and cheaper solution - the biosensor. In this study, an electrochemical sensor was fabricated using graphene/zirconia (ZG)-modified screen-printed carbon electrode (SPCE). A green approach using solvent exfoliation alongside hydrothermal treatment was employed to prepare the ZG nanocomposites. Material characterisation suggested that pristine graphene and well-hybridised ZG nanocomposite were synthesised. Alongside material characterisation, a cytotoxicity test was performed on the ZG nanocomposite to address the issue of potential hazards during material synthesis and sensor fabrication. The result showed that the ZG nanocomposite had no adverse effects on human lung cells (MRC5) and skin cells (HaCaT), with a half-maximal inhibitory concentration (IC50) value of >500 µg/ml.

Before the development of an immunosensor and genosensor, the potential of the ZG-based platform as an electrochemical sensor for electroanalytical application was demonstrated via acetaminophen detection. The electrochemical sensor exhibited favourable performances for the detection of acetaminophen ranging from 10 µM to 100 µM. A limit of detection (LOD) of 75.5 nM, repeatability of < 3% relative standard deviation (RSD), reproducibility of 5 % RSD, stability of 95% after 5 days of storage alongside decent selectivity to acetaminophen in the presence of interfering species were observed. This finding subsequently motivated the exploration of the platform to serve as a genosensor enhanced with 1-pyrenebutyric-acid-N-hydroxysuccinimide-ester (PY) biolinker to differentiate wild-type and mutated exon-19 sequences in epidermal growth factor receptor (EGFR). The exon-19 mutation is common among lung cancers. The fabricated genosensor was able to quantify the concentration of wild-type exon-19 in the range of 5 nM to 1 µM, with a linearity coefficient of R^2= 0.99 and a LOD of 1.7 nM. The sensor was observed to produce reproducibility of 8.3% of RSD and stability of 90% after 8 days of storage. Most importantly, the sensor was capable of generating distinctive signals for wild-type and mutated exon-19, making it valuable for the detection of genetic mutation. An immunosensor for the detection of carcinoembryonic antigen (CEA) was proposed. CEA is a glycoprotein involved in cell adhesion and is known to be over-expressed in serum of lung cancer patients. Decent performances were exhibited by the immunosensor for CEA detection with a 4.25 pg/ml LOD and a correlation coefficient of R^2= 0.99 within a linear working range from 0.01 ng/ml to 10 ng/ml. The immunosensor exhibited high specificity for CEA against interfering species, decent stability

for up to 20 days, and reasonable reproducibility of 4.27% RSD. The immunosensor has also presented a good recovery of CEA in human serum, in which the detected CEA level was in close agreement (< 7% deviation) with the actual concentration.

The key characteristics of the sensors reported in this work offered appealing merits on their own: the stable PY biolinker immobilisation technique, the biocompatible ZG electrode material, the handiness of disposable design and the potential for miniaturisation; hence, hybridizing all these merits produced a promising electrochemical testing platform that subsequently opened up a new avenue for early detection of malignant conditions.

TABLE OF CONTENTS

ABSTRACT ..... **i**

TABLE OF CONTENTS ..... **iii**

ACKNOWLEDGEMENT ..... **vi**

LIST OF PUBLICATIONS ..... **vii**

LIST OF ABBREVIATIONS ..... **viii**

LIST OF FIGURES ..... **xii**

LIST OF TABLES ..... **xix**

1. RESEARCH MOTIVATIONS AND OBJECTIVES **1**

1.1. INTRODUCTION 1

1.2. RESEARCH MOTIVATIONS 4

1.3. RESEARCH AIM AND OBJECTIVES 6

1.4. REPORT OUTLINE 7

2. LITERATURE REVIEW **9**

2.1. INTRODUCTION 9

2.2. SYNTHESIS OF GRAPHENE 10

2.2.1. BOTTOM-UP APPROACH 10

2.2.2. TOP-DOWN APPROACH 15

2.3. SYNTHESIS OF GRAPHENE/METAL OXIDE NANOCOMPOSITE 20

2.3.1. SOL-GEL 20

2.3.2 HYDROTHERMAL/SOLVOTHERMAL 22

2.3.3 OTHER METHODS: MICROWAVE IRRADIATION AND ELECTROCHEMICAL DEPOSITION 26

2.4. APPLICATIONS OF GRAPHENE-BASED SENSING PLATFORMS 30

2.4.1. GRAPHENE-BASED PLATFORMS FOR THE DETECTION OF ELECTROACTIVE SPECIES 30

2.4.2. GRAPHENE-BASED PLATFORMS AS BIOSENSORS 33

2.5. BIOMARKERS FOR LUNG CANCER DETECTION 36

2.5.1 EPIDERMAL GROWTH FACTOR RECEPTOR (EGFR) 37

2.5.2 TP53 GENE 39

2.5.3 KRAS 41

2.5.4 NEURON SPECIFIC ENOLASE (NSE) 42

2.5.5 CYTOKERATIN 19 FRAGMENT 21-1 (CYFRA 21-1) 43

2.5.6 CARCINOEMBRYONIC ANTIGEN (CEA) 45

2.6. TRANSDUCERS FOR BIOSENSOR OF LUNG CANCER BIOMARKER 49

2.6.1. OPTICAL TRANSDUCER 49

2.6.2. MASS-BASED TRANSDUCER 53

2.6.3. ELECTROCHEMICAL TRANSDUCER 56

2.7. LUNG CANCER DETECTION WITH ELECTROCHEMICAL BIOSENSORS 64

2.7.1. GRAPHENE-BASED ELECTROCHEMICAL SENSORS FOR LUNG CANCER BIOMARKERS 65
2.7.2. GRAPHENE COMPOSITE-BASED ELECTROCHEMICAL SENSORS FOR LUNG CANCER BIOMARKERS 69
2.8. GRAPHENE/ZIRCONIA NANOCOMPOSITE 74
2.8.1. PROPERTIES OF ZIRCONIA 74
2.8.2. SYNTHESIS OF GRAPHENE/ZIRCONIA NANOCOMPOSITE 75
2.8.3. APPLICATION OF GRAPHENE/ZIRCONIA IN SENSORS 77
2.9. SUMMARY 81
3. SYNTHESIS AND CHARACTERISATION OF GRAPHENE/ ZIRCONIA NANOCOMPOSITE 82
3.1. INTRODUCTION 82
3.2. EXPERIMENTAL DETAILS 83
3.2.1 APPARATUS AND MATERIAL 83
3.2.2 SYNTHESIS OF GRAPHENE ZIRCONIA 84
3.2.3 PREPARATION OF SENSING PLATFORM FOR ELECTROCHEMICAL MEASUREMENTS 85
3.2.4 CELL CULTURE, CELL INCUBATION WITH ZG AND MICROSCOPIC EXAMINATION OF CELL 86
3.2.5 MTT ASSAY FOR CELLS VIABILITY STUDY 87
3.3 RESULTS AND DISCUSSION 87
3.3.1 CHARACTERISATION OF GRAPHENE AND GRAPHENE/ZIRCONIA 87
3.3.2 ELECTROCHEMICAL RESPONSE OF ZG/SPCE TOWARDS POTASSIUM FERRICYANIDE 94
3.3.3 MICROSCOPIC VISUALISATION OF CELL-MATERIAL INTERACTION 98
3.3.4 MTT CELL VIABILITY STUDY 102
3.4 SUMMARY 107
4 POTENTIAL OF THE GRAPHENE/ZIRCONIA-BASED PLATFORM AS AN ELECTROCHEMICAL SENSOR: ACETAMINOPHEN AS THE MODEL ANALYTE 109
4.1 INTRODUCTION 109
4.2 EXPERIMENTAL DETAILS 110
4.2.1 APPARATUS AND MATERIAL 110
4.2.2 FABRICATION OF THE ACETAMINOPHEN SENSOR AND ELECTROCHEMICAL MEASUREMENTS 110
4.2.3 DETECTION OF ACETAMINOPHEN IN COMMERCIAL TABLETS 111
4.3 RESULTS AND DISCUSSION 111
4.3.1 ANALYTICAL PERFORMANCE 111
4.3.2 REPEATABILITY, REPRODUCIBILITY, STABILITY AND SELECTIVITY 115
4.3.3 REAL SAMPLE ANALYSIS: DETECTION OF COMMERCIAL TABLETS 118
4.4 SUMMARY 119

5 AN IMPEDIMETRIC GENOSENSOR BASED ON CONTROLLABLE PI–PI FUNCTIONALISATION OF ZIRCONIA-DECORATED GRAPHENE TO DISTINGUISH BETWEEN WILD-TYPE AND MUTATED EXON-19 SEQUENCES IN EPIDERMAL GROWTH FACTOR RECEPTOR 120

5.1 INTRODUCTION 120

5.2 EXPERIMENTAL DETAILS 122

5.2.1 APPARATUS AND MATERIAL 122

5.2.2 PREPARATION OF PY-FUNCTIONALISED-ZG 122

5.2.3 DNA SEQUENCE DESIGN 123

5.2.4 FABRICATION OF THE GENOSENSOR AND ELECTROCHEMICAL MEASUREMENTS 124

5.2.5 DETECTION MECHANISM OF THE GENOSENSOR 127

5.2.6 ESTIMATION OF CAPTURE-DNA DENSITY 128

5.2.7 STABILITY AND SPECIFICITY STUDY 128

5.3 RESULTS AND DISCUSSION 129

5.3.1 CHARACTERISATION OF THE FABRICATION STEPS 129

5.3.2 OPTIMISATION OF THE FABRICATION AND SENSING PARAMETERS 133

5.3.3 ANALYTICAL PERFORMANCES, SPECIFICITY, REPRODUCIBILITY AND STABILITY 137

5.3.4 ESTIMATION OF CAPTURE-DNA DENSITY 140

5.3.5 ADVANTAGES OF THE GENOSENSOR 141

5.4 SUMMARY 142

6 AN IMMUNOSENSOR FOR THE RAPID DETECTION OF TUMOUR MARKER CARCINOEMBRYONIC ANTIGEN BASED ON GRAPHENE/ZIRCONIA-ENHANCED PLATFORM 143

6.1 INTRODUCTION 143

6.2 EXPERIMENTAL DETAILS 145

6.2.1 APPARATUS AND MATERIAL 145

6.2.2 FABRICATION OF THE IMMUNOSENSOR AND ELECTROCHEMICAL MEASUREMENTS 145

6.2.3 STABILITY, INTERFERENCE AND CEA RECOVERY TEST IN SERUM 146

6.3 RESULTS AND DISCUSSION 149

6.3.1 ELECTROCHEMICAL CHARACTERISATION OF THE SENSING PLATFORM 149

6.3.2 OPTIMISATION OF FABRICATION AND SENSING PARAMETERS 153

6.3.3 ANALYTICAL PERFORMANCE, SPECIFICITY, STABILITY AND REPRODUCIBILITY 157

6.3.4 DETECTION OF CEA IN HUMAN SERUM 160

6.3.5 ADVANTAGES OF THE IMMUNOSENSOR 160

6.4 SUMMARY 162

7 CONCLUSION, LIMITATIONS AND FUTURE WORKS 163

7.1 CONCLUSION 163

7.2 LIMITATIONS AND FUTURE WORKS 167

REFERENCES 169

ACKNOWLEDGEMENT

I wish to express my profound gratitude to my supervisors, Dr Michelle Tan Tien Tien, Dr Khiew Poi Sim and Dr Sandy Loh Hwei San, whose technical acumen, patience, motivation, suggestions and timely discussion have been extremely helpful. Thank you for all the support throughout these years. It was also my pleasure to have been guided by a group of brilliant people, Raphael, Qi Yan, and Dr Low Sze Shin. My sincerest appreciation goes to them for their generous knowledge sharing. I wish also to thank the wonderful technicians at our campus, Mr Fareez, Mr Asyraf and Ms Khairani for their help in material characterisation and laboratory equipment arrangement.

I wish also to thank my employer, Tunku Abdul Rahman University College for the monetary support and time granted to do this research. Part of this research is not possible without the help of my colleagues to take over my workload. I thank you all for your time, support and kind advice.

Unquestionably, I can never thank my family enough for their kindness, companionship and encouragement that enables me to be resilient in the face of challenges, especially after my hearing loss, for none of this would be possible without their constant love and patience.

Last but certainly not least, thank you, Kar Wai. The memory of how strong and calm you were in the face of the most unthinkable kept me going during my darkest days. You are missed beyond words. Till we meet again.

LIST OF PUBLICATIONS

Lin, L.P., Tham, S.Y, Loh, H.S., Tan, M.T.T., "Biocompatible Graphene-Zirconia Nanocomposite as a Cyto-safe Immunosensor for the Rapid Detection of Carcinoembryonic Antigen." *Scientific Reports*, vol 11, pp 22536, 2021.

https://doi.org/10.1038/s41598-021-99498-0

Lin, L.P., Loh, H.S., Tan, M.T.T., "Impedimetric Genosensor Based on Controllable Pi–Pi Functionalisation of Zirconia Decorated Graphene Nanoflakes for the Detection of Epidermal Growth Factor Receptor Exon-19 Mutation." *IEEE Sensors Journal*, vol 20, no 18, pp 10424-10432, 2020.

https://doi.org/10.1109/JSEN.2020.2994859

Lin, L.P., Loh, H.S., Tan, M.T.T., "Electrochemical DNA Sensor Based On Graphene/Zirconia Nanocomposite for Label-Free Detection of Exon-19 Mutations in Lung Cancer: A Preliminary Study." *ACM Proceedings of the Japan 9th International Conference on Biomedical Engineering and Technology,* pp 223-228, 2019.

https://doi.org/10.1145/3326172.3326176 *(Best Presentation Award)*

Lin, L.P., Khiew, P.S., Chiu, W.S., Tan, M.T.T., "A disposable electrochemical sensing platform for acetaminophen based on graphene/ZrO_2 nanocomposite produced via a facile, green synthesis method." *IEEE Sensors Journal*, vol 18, no 19, pp 7907–7916, 2018

https://doi.org/10.1109/JSEN.2018.286432

LIST OF ABBREVIATIONS

ΔEp	Peak-To-Peak Separation
2D	Two-Dimensional
3D	Three-Dimensional
AFM	Atomic Force Microscopy
AFP	Alpha-fetoprotein
AgNp	Silver Nanoparticle
AI	Artificial Intelligence
ATP	Adenosine Triphosphate
Au–PTBO	Gold/polytoluidine-blue O
AuNP	Gold Nanoparticles
BSA	Bovine Serum Albumin
CEA	Carcinoembryonic Antigen
CO_2	Carbon Dioxide
Co_3O_4	Cobalt Oxide
COVID-19	Coronavirus Disease 2019
CT	Computer Tomography
CTAB	Cetyltrimethyl Ammonium Bromide
CuO	Copper(ii) Oxide
CV	Cyclic Voltammetry
CVD	Chemical Vapour Deposition
CYFRA 21-1	Cytokeratin Fraction 21-1
DI	Deionised
DMEM	Dulbecco's Modified Eagle Medium
DMSO	Dimethyl Sulfoxide
DNA	Deoxyribonucleic Acid
DPBS	Dulbecco's Phosphate Buffered Saline
DPV	Differential Pulse Voltammetry
EDX	Energy-Dispersive X-Ray Spectroscopy
EGFR	Epidermal Growth Factor Receptor
EIS	Electrochemical Impedance Spectroscopy
ELISA	Enzyme-Linked Immunosorbent Assay

Epa	Anodic Peak Potential
Epc	Cathodic Peak Potential
FBS	Fetal Bovine Serum
Fe	Hemin@MIL-88B
$[Fe(CN)_6]^{3-/4-}$	Potassium Ferricyanide
Fe_3O_4	Iron (II, III) Oxide
FRET	Fluorescence Resonance Energy Transfer
GCE	Glassy Carbon Electrode
GDP	Guanosine Diphosphate
GTP	Guanosine Triphosphate
H_2	Hydrogen
H_2O_2	Hydrogen Peroxide
H_2SO_4	Sulphuric Acid
HaCaT	Human Immortalised Keratinocyte
$HAuCl_4$	Chloroauric Acid
HCl	Hydrochloric Acid
HOPG	Highly Oriented Pyrolytic Graphite
HRP	Horseradish Peroxidase
hTERT	Human Telomerase Reverse Transcriptase
IC50	Half-Maximal Inhibitory Concentration
IDA	Isothermal Solid-Phase DNA Amplification
IgG	Immunoglobulin G
Ket	Electron Transfer Rate
$KMnO_4$	Potassium Permanganate
LL/2	Murine Lewis Lung Carcinoma Cell Line
LOD	Limit of Detection
LSV	Linear Sweep Voltammetry
Lu	Luminol
m-ZrO_2	Monoclinic Zirconia
Mb	Magnetic Bead
MB	Methylene Blue
miRNA-21	MicroRNA21
MnO^-_4	Permanganate

MnO_2	Manganese Dioxide
MoS_2	Molybdenum Disulphide
MRC5	Human Lung Fibroblast
mRNA	Messenger RNA
MZI	Mach-Zehnder Interferometer
$NABH_4$	Sodium Borohydride
NADH	Nicotinamide Adenine Dinucleotide
NaOH	Sodium Hydroxide
NMP	1-methyl-2-pyrrolidinone
NRTG	Nanosheets Graphene/TiO_2 Nanorod
NSCLC	Non-Small Cell Lung Carcinoma
NSE	Neuron-Specific Enolase
PBS	Phosphate Buffer Saline
PCR	polymerase chain reaction
PdNPs	Palladium Nanoparticles
PET	Positron Emission Tomography
PY	1-Pyrene Butyric Acid N-Hydroxysuccinimide
PY-ZG	PY-Functionalised-Graphene/Zirconia
QCM	Quartz Crystal Microbalance
Rct	Charge Transfer Resistance
RGO	Reduced Graphene Oxide
RGO–Au–PTBO	Graphene/Gold/Polytoluidine-Blue
RSD	Relative Standard Deviation
$Ru(bpy)_3^{2+}$	Tris (2,2'-bipyridine) Ruthenium(II)
SCLC	Small Cell Lung Cancer
SEM	Scanning Electron Microscope
Si	Silicon
SiC	Silicon Carbides
SiO_2	Silicon Oxide
SnO_2	Tin(Iv) Oxide
SPCE	Screen-Printed Carbon Electrodes
SPR	Surface Plasmon Resonance
STG	Spherical Graphene/TiO_2 Nanosheets

t-ZrO_2	Tetragonal Zirconia
TBTN	Tetrabutyl Titanate
TCNQ	7,7,8,8,-Tetracyanoquinodimethane
TEM	Transmission Electron Microscope
TiO_2	Titanium Dioxide
UCNP	Up Conversion Nanoparticles
USTG	Ultra-Small Graphene/TiO_2
V_2O_5	Vanadium Pentoxide
XRD	X-Ray Diffraction
ZG	Graphene/Zirconia
ZnO	Zinc Oxide
ZrO_2	Zirconia
$ZrOCl_2$	Zirconyl Chloride

LIST OF FIGURES

Figure 2.1. LEED patterns from of SiC samples (a) at 1050 °C, (b) at 1100 °C, (c) at 1250 °C and (d) at 1400 °C. First-order SiC and graphite spots were observed starting at 1250 °C..... 11

Figure 2.2. AFM images of graphene grown in (a) argon atmosphere and (b) ultra-high vacuum. The surface morphology of graphene produced in an argon-flow atmosphere was mostly smoother, and the graphene size was larger compared to those produced via vacuum graphitisation 12

Figure 2.3. SEM images of (a) graphene grown on copper foil through CVD and (b) graphene transferred to glass. The as-grown graphene can be easily transferred to other substrates for various assessments and applications 14

Figure 2.4. Schematic of one-step CVD growth of graphene on Si-coated copper foil. 14

Figure 2.5. Chemical reduction of graphene oxide. Graphene oxide is usually obtained by oxidation of natural graphite powder with various oxidants in acidic media 16

Figure 2.6. Schematic representation of thermal exfoliation technique. The use of a high-vacuum environment allowed the achievement of graphene exfoliation at temperature much lower than that used in the normal-pressure thermal exfoliation technique 18

Figure 2.7. Schematic illustration of sol-gel synthesis procedure for the preparation of graphene/TiO_2 nanocomposite. Graphene/TiO_2 nanocomposite was synthesised with TBTN and graphite oxide as the starting materials to form sol that was subsequently annealed at high temperature 21

Figure 2.8. Schematic illustration of solvothermal synthesis. Graphene/TiO_2 nanocomposite of different nanostructures is achievable through the manipulation of synthesis parameters 23

Figure 2.9. XRD result of the graphene/SnO_2 nanocomposite synthesised via the solvothermal method. Solvothermal methods have been widely used to synthesise high-crystalline nanocomposites 24

Figure 2.10. Schematic illustration for the synthesis of graphene–MnO_2 composite via microwave radiation. The reaction is characterised by electron transfer from the carbon to the oxidant upon activation by heat from microwave radiation 27

Figure 2.11. Amperometric i–t curves of Au–PTBO (blue), RGO (black), and RGO–Au–PTBO (red) modified electrode in response to H_2O_2 reduction. The affinity of Au-PTBO toward the reduction of H_2O_2 was amplified by the integration of graphene 32

Figure 2.12. DPV peaks recorded at graphene/TiO_2/Nafion-modified electrode for the voltammetric detection of acetaminophen in the presence of dopamine and ascorbic acid. A clear separation of at least 0.2 V was observed between the redox peaks 33

Figure 2.13. Schematic presentation of an immunosensor fabrication. The graphene sheets served as an excellent antibody immobilisation platform 35

Figure 2.14. Mutation in exon 18,19,20 and 21 within the tyrosine kinase domain of EGFR. Abnormal activity of the EGFR can promote tumour cell proliferation, differentiation and migration 38

Figure 2.15. (a) Mutation effect and pattern of TP53 gene. (b) percentage of single-base substitution at different codons. Mutant gene resulted in a codon that coded for different proteins 40

Figure 2.16. Cytokeratins of cells. Cytokeratins are intermediate filaments to support the cells from mechanical stress 44

Figure 2.17. Probability of survival for patients with an elevated level of serum CYFRA-21. Lung cancer patients with a serum CYFRA 21-1 level over 3.6 ng/ml was shown to have a shorter survival 44

Figure 2.18. The survival rate of early-stage lung cancer patients with elevated CEA levels. The 5-year survival rate of early-stage lung cancer was relatively lower for patients with CEA of more than 2.5 ng/ml 45

Figure 2.19 (a) A light source is projected through a prism to the plasmon surface where surface plasmons are generated. (b) the shift of critical angle of light from angle a to angle b upon the formation of the receptor-analyte complex. Change in the RI gives rise to the quantitative measurement of the analyte 50

Figure 2.20. An SPR-based biosensor for CYFRA 21-1. The sensor is functionalised with graphene oxide for the detection of CYFRA 21-1 in spiked human serum 51

Figure 2.21. A mass-based sensor for TP53 mutation detection. The sensor which is based on strand displacement reaction unfolds the capture probe upon binding with the target sequence (TP53 gene fragment). The unfold probe hybridised with the reporter probe to induce the mass change that is proportional to the concentration of TP53 gene fragments 54

Figure 2.22. A mass-based immunosensor. The resonant frequency of the sensor changed due to the additional mass resulting from the binding between antigen on the LL/2 cell surface with its specific antibody [232]. 55

Figure 2.23. An electrochemical sensor for CEA detection. The hybridisation of CEA antibody with CEA resulted in an insulative immunocomplex that reduced the electron transfer 57

Figure 2.24. A sandwiched assay. A labelled reporting probe is introduced to the sensor after the interaction of the bio-receptor and the target. The catalytic response is initiated by the addition of an enzymatic substrate and the generated signal is associated with the quantity of the target..... 59

Figure 2.25. Modification scheme of a P53 sensor. The analytical signal was given by the reduction of thionine 62

Figure 2.26. Detection of H_2O_2 on various electrodes. The highest oxidation peak current was observed for electrodes with the sandwich structure of G/Mb-CAb/CEA/DAb-HRP-AuNP, endorsing its effectiveness 65

Figure 2.27. Modification scheme of a 3D graphene-based sensor for NSE detection. The porous structural design, decent electrochemical stability and high electron transfer rate have accumulatively led to better sensor sensitivity 66

Figure 2.28. Modification scheme of CVD-grown graphene on copper substrate. The single-step electrode fabrication proposed in the study is an advantage over other reported techniques..... 68

Figure 2.29 TEM image of AuNp-decorated graphene sheet. Thin graphene was synthesised as advocated by its transparent appearance and AuNPs were well-anchored onto the graphene sheets 70

Figure 2.30. A portable point-of-care system with wireless transmission of data to an Android application. The miniature system was an integration of a microfluidic paper-based electrode, an electrochemical transducer and a smartphone to perform DPV measurements..... 71

Figure 2.31. The DPV detection of acetaminophen, phenylephrine hydrochloride and cytosine. Distinct peaks were exhibited by the sensing platform modified with graphene/ZrO_2 nanocomposite..... 77

Figure 2.32. The layer-by-layer structure of a vapour-phase ammonia sensor. The sensor was constructed on a ZrO_2 substrate so that the sensor could cool down within seconds after each measurement to give a high cycle of duty 78

Figure 2.33. TEM shows the decoration of RGO with ZrO2 nanoparticles. Spherical ZrO2 nanoparticles are homogeneously distributed on the graphene oxide sheet [26]..... 79

Figure 3.1. Raman spectra of (a) exfoliated graphene, and SEM images of (b) exfoliated graphene (c) G1Zr2, (d) G1Zr4, (e) G1Zr8 and (f) G1Zr16. Exfoliated graphene was found to be thin and with well-dispersed ZrO_2 nanoparticles..... 90

Figure 3.2: TEM images of (a) exfoliated graphene (b) G1Zr8, and (c) EDX of ZG nanocomposite. The TEM results complement the SEM observation that the synthesised graphene is thin and ZrO_2 are well-anchored on the graphene sheets. 91

Figure 3.3. XRD peak of graphene, ZrO_2 and ZG nanocomposite at different precursor ratios. ZG nanocomposite displays diffraction peaks of both ZrO_2 and graphene, indicating successful hybridisation..... 93

Figure 3.4 CV of (a) bare SPCE, graphene-modified SPCE, ZrO_2-modified SPCE, and ZG-modified SPCE (G1Zr2, G1Zr4, G1Zr8, G1Zr16), (b) effect on peak current for different ZG dispersion concentrations, (c) effect on peak current for the different drop-casted volume of ZG dispersion. 96

Figure 3.5. CV of G1Zr8/SPCE at various scan rate (from inner to outer curve); 25, 50, 75, 100, 125, 150. 175 and 200 mV /s. The electrochemical reaction at G1Zr8/SPCE is found to be a diffusion-controlled process in 0.01 M PBS of pH 7.4. 97

Figure 3.6. Nyquist plots for bare SPCE, graphene-modified SPCE, ZrO_2-modified SPCE, and G1Zr8-modified SPCE, obtained in 0.01 M PBS(pH 7.4) containing 10 mM of redox probes.. 98

Figure 3.7: Microscopic characterisation of untreated MRC5 cells at (a) 24 hours, (b) 48 hours, (c) 72 hours, and MRC5 cells treated with 50 µg/ml of ZG nanocomposite at (d) 24 hours, (e) 48 hours, (f) 72 hours. The presence of ZG nanocomposite did not present a threat to the viability of MRC5 cells. Cells appeared healthy and retained their fibroblastic morphology throughout 72 hours of the incubation period..... 100

Figure 3.8. Microscopic characterisation of untreated HaCaT cells at (a) 24 hours, (b) 48 hours, (c) 72 hours; and HaCaT cells treated with 50 µg/ml of ZG nanocomposite at (d) 24 hours, (e) 48 hours, (f) 72 hours. The presence of ZG nanocomposite did not considerably inhibit the viability of HaCaT cells. Treated cells retained comparable morphology as the control throughout 72 hours of the incubation period. 101

Figure 3.9. Cell viability of HaCaT and MRC5 cells lines treated with ZG nanocomposite for (a) 24 hours, (b) 48 hours, (c) 72 hours. HaCaT cell line and MRC5 cell line retained high cell viability after incubation with the nanocomposite. ZG nanocomposite was considered to be biocompatible for both cell lines. 105

Figure 4.1. (a) DPVs of acetaminophen on bare SPCE and G1Zr8/SPCE in 0.01 M PBS (pH 7.4). (b) effect of pulse width on peak current. (c) effect of pulse amplitude on peak current. 100 mV pulse amplitude and 60 ms pulse width were selected to maximise the peak current without shape distortion. 113

Figure 4.2. DPV response of the sensor towards various concentrations of acetaminophen ranging from 10 µM to 100 µM. Inset: Calibration equation of the proposed sensor. The detection limit of the sensor was found to be 75.5 nM. 114

Figure 4.3. DPV for the (a) repeatability study. (b) reproducibility study (c) stability study and (d) selective determination of acetaminophen in the presence of ascorbic acid and dopamine. The sensor demonstrated repeatability of < 3% RSD, reproducibility of 5 % RSD, stability of 95% after 5 days of storage and good selectivity to acetaminophen in the presence of interfering species117

Figure 5.1: Diffusion of redox probe at an electrode/electrolyte interface. The diffusion of the redox ions is greatly affected by the presence of substrate on the electrode surface..... 127

Figure 5.2. (a) Impedance spectrum and (b) CVs of the ZG/SPCE, PY-ZG/SPCE, cDna/PY-ZG/SPCE, and tDna/cDna/PY-ZG/SPCE in PBS with 10 mM of $[Fe(CN)_6]^{3-/4-}$. The results from CV and EIS confirmed the success of each fabrication step. 132

Figure 5.3. Effects of (a) PY ratio, (b) capture-DNA concentration, (c) capture-DNA immobilisation time, (d) hybridisation time, and (e) hybridisation temperature on the sensor response ΔR/R. The most optimum ratio of PY: ZG was found to be 4:1, whereas SPCE immobilised with 0.1 µM of the capture-DNA for 60 minutes was observed to present the highest hybridisation efficiency when incubated with the target-DNA for 60 minutes at 26 ºC. Hence, these parameters were adopted as the sensing protocol. 136

Figure 5.4. (a) The relationship between the ΔR/R and the logarithm of target-DNA concentration, (b) specificity test, and (c) stability test. The sensor exhibited a correlation of $R^2 = 0.99$ for the detection of exon-19 wild-type DNA. 139

Figure 5.5. DPV curves of the cDna/PY-ZG/SPCE (single-stranded DNA) and the tDna/cDna/PY-ZG/SPCE (double-stranded DNA). Hybridised SPCE exhibited higher current due to the greater intercalative affinity of MB towards double-stranded hybridised DNAs..... 140

Figure 6.1. (a) CVs and (b) EIS of ZG/SPCE, PY-ZG/SPCE, Ab/PY-ZG/SPCE, SM/Ab/PY-ZG/SPCE and CEA/SM/Ab/PY-ZG/SPCE. Each functionalisation step introduced a higher physical barrier at the electrode surface and increased the charge transfer resistance..... 152

Figure 6.2. Influence of (a) ZG: PY ratio, (b) Ab concentration, (c) Ab immobilisation time, (d) active-site blocking time and (e) Ab-CEA binding time on signal response rRct. The adopted value for ZG: PY ratio, Ab concentration, Ab immobilisation time, active-site blocking time and Ab-CEA binding time was 1:4, 10 μg/ml, 50 minutes, 20 minutes and 75 minutes respectively, for enhanced sensor performance. 156

Figure 6.3. (a) Linear correlation between rRct and logarithmic value of CEA concentration, (b) specificity study of the immunosensor and (c) stability study of the immunosensor. The fabricated immunosensor was highly selective to CEA and was able to quantity CEA ranging from 0.01 ng/ml to 10 ng/ml. 159

LIST OF TABLES

Table 2.1: Merits and Demerits of Different Graphene/Metal Oxide Synthesis Methods 29

Table 2.2: Common Lung Cancer Biomarkers 46

Table 2.3 Various Transducers for the Detection of Lung Cancer Biomarkers 63

Table 2.4 Electrochemical Biosensors Based on Graphene and Graphene Nanocomposite for the Detection of Lung Cancer Biomarkers 73

Table 3.1: Weight Ratio Of Graphene: ZrO_2 Precursor 85

Table 3.2: Comparison of IC_{50} for Nanomaterials Commonly Used in Biosensors Fabrication 106

Table 4.1: Performance of the Fabricated Acetaminophen Sensor Against Other Reported Acetaminophen Sensors. 114

Table 4.2: Determination Of Acetaminophen In Commercial Tablets 118

Table 5.1. Exon-19 DNA Sequences 123

Table 5.2. Comparison of The Analytical Performance of the ZG Genosensor Against Other Platforms 137

Table 6.1: Analytical Performance of the Fabricated CEA Immunosensor Against Other Reported CEA Sensors 158

Table 6.2: Recovery Test of Spiked Human Sample 160

1. RESEARCH MOTIVATIONS AND OBJECTIVES

1.1. INTRODUCTION

Lung cancer is the most common cancer worldwide, responsible for more deaths per year than any other cancer [1]. An estimation of 132,000 deaths due to lung cancer was projected for the year 2021 in the USA, more than twice the mortality caused by oral-related cancers, breast cancer and skin cancers combined [2]. Lung cancer has much lower survival rates despite the advancement in radiological tests, predominantly computer tomography (CT) and positron emission tomography (PET), surgical procedures, post-surgery care as well as chemotherapy and radiotherapy techniques. At only 15%, the 5-year survival rate of lung cancer patients has been persistently low and constant over the last 20 years, mainly limited by the high relapse rate, the rapid development of metastases and delayed detection [3]. Routine check-up gives rise to early detection, however, conventional screening methods such as X-ray and CT which use radiation to produce images of the lungs are incompetent for routine screening of lung carcinoma due to health hazards particularly elevated cancer risk associated with repeated radiation exposure [4]. The ionizing nature of radiography renders early detection via routine check-up infeasible; often, the investigation is initiated only after patients have developed symptoms such as weight loss and haemoptysis that may not present at the early stage of the malignancy [5], resulting in delayed treatment. Therefore, the anticipation to revolutionise the detection of lung cancer for early detection and timely treatment lies in the innovation of sensing technologies, particularly biosensors that could provide rapid detection of lung cancer biomarkers. Biosensors that detect and quantify biomarkers in easily accessible biological samples such as the serum, sputum and exhaled breath have demonstrated promising outcomes in the early diagnosis of lung malignancies [6].

Recent trend shows that various nanocomposites, particularly graphene-based nanomaterials have been incorporated into biosensors to amplify signal response and consequently enhance the

sensitivity of the sensors for biomarker detection, leading to lung cancer diagnosis [7]–[10] Graphene, a two-dimensional (2D) material consisting of a single atomic layer of carbon arranged in a honeycomb lattice was discovered in 2004 by Novoselov et al. [11]. Owing to the extraordinary properties of graphene which include fast electron transportation, high surface area, excellent thermal conductivity and superior mechanical strength [12], graphene has drawn tremendous attention in the field of nanoelectronics, nanoelectromechanical, energy storage, optical biosensor and electrochemical sensor [13]–[16]. Often, there are strong synergistic interactions between graphene and its composite components, which can significantly improve the electrochemical performance of the material. Graphene layers decorated with evenly distributed nanoparticles on the surface could lead to less aggregation which was caused by Van der Waals interaction. Some of these nanoparticles include metal oxide, magnetic-nanoparticle and nanowires [17]–[19]. Among these, metal oxide nanoparticles are probably one of the most explored due to their superior biological compatibility, high surface-to-volume ratio and great conductivity [20]. The hybridisation between graphene and metal oxides sees the graphene providing a conductive platform for easy charge transfer while the metal oxide acts as spacers to avoid the restacking of graphene sheets to offer more active surface areas.

Keeping in view the exploitation of the synergetic effect between graphene and metal oxide, zirconia (ZrO_2) is the material of interest as it is chemically inert and biocompatible. It was applied broadly in orthopaedic devices, contaminant removal and recently, in biosensing [21]–[25]. Given the excellent properties of graphene and ZrO_2, there is an anticipation of developing a hybrid composite graphene/zirconia (ZG) that will outperform the individual component, to deliver a novel material that has enhanced properties including effective surface area, biocompatibility and electrical conductivity [15]. Nanocomposite ZG has been recognised to be an enhancement with regards to bio-sensing performance, as proposed by the findings of previously reported works [26], [27]. However, its application for the detection of lung cancer markers is yet to be extensively

explored as compared to other nanomaterials [28], [29]; therefore the potential of a ZG-based biosensor for lung cancer detection is worth exploring.

The ease of material processing and low synthesis cost has encouraged the employment of nanomaterial in electrochemical biosensors out of the several types of biosensors [30]. Electrochemical sensors measure signals generated by electrochemical oxidation and reduction. The signal recorded during the redox process is contributed by the recognition of a target analyte, and its intensity is always proportional to the concentration of the target analyte. Intrinsic advantages of electrochemical sensors are their robustness, feasible miniaturisation, high sensitivity, good detection limits and the potential to be used with low analyte volumes [31]. The unfortunate fact of having the glucose sensor as the sole commercially successful electrochemical sensor has driven the need to develop more inexpensive and reliable electrochemical sensors, which may be achieved by exploiting the synergies between nanomaterial and electrochemistry. Nanoscale dimensions of nanomaterials are comparable to those of the biological and chemical species being sensed; contributing to excellent primary transduction of signals that are ultimately interfaced with macroscopic instruments and give rise to reliable sensing [32]. As such, the application of a ZG-based electrochemical platform for cancer detection is much anticipated.

In a nutshell, graphene-nanocomposite combines the physiochemical attributes of graphene and its hybridised components nanomaterials, such as ZrO_2 to provide extraordinary properties. Therefore, the nanocomposite offers the possibility of a specific, sensitive and reliable graphene-based biosensors that not only measure the concentration of electroactive redox species but also serve as a feasible point-of-care assay for diseases such as lung cancer.

1.2. RESEARCH MOTIVATIONS

The extraordinary property of graphene depends strongly on the dispersion quality of graphene sheets. However, π-π stacking interactions among individual graphene sheets result in their tendency to restack and intervention is necessary to reduce the stacking. Metal oxide ZrO_2 is chemically inert and biocompatible, and ZrO_2 nanoparticles have been shown to act as spacers against the aggregation of individual graphene sheets caused by Van der Waals interactions [27], leading to improved electrochemical properties of the graphene. Many researchers have attempted to synthesise ZG nanocomposite in which a handful of methods such as sol-gel method, electrodeposition, reflux method and microwave-assisted method have been employed [33]–[37]. However, most of the attempts involved tedious multi-step synthesis, reduction of graphene oxide with chemical, and high-energy processes [35], [38]–[40]. In cases where the precursor graphite or graphene oxide was not completely reduced, the presence of oxygenated functional groups on the graphene surface was common. Furthermore, excessive reducing agents such as sodium borohydride ($NABH_4$) and hydrazine used in producing reduced graphene oxide (RGO) may introduce contaminants to the graphene nanocomposite, consequently reducing the performance of the graphene-based sensor [41]. Thus said, there is a need to explore the possibility of using alternative synthesis processes that are cleaner and safer, yet able to produce ZG of reproducible yields and quality. Cytotoxicity of synthesised nanocomposite is often not evaluated for biosensing applications. Although biosensing were *in vitro* applications, material cytotoxicity should still be a concern. During the process of nanocomposite synthesis and sensor fabrication, researchers are unavoidably exposed to the nanomaterial, through inhalation and physical contact with the skin. Toxic nanomaterial once inhaled can deposit in the respiratory tract, either directly damage the lung epithelium or diffuse into the bloodstream at the tissue-vessel interface [42]. Meanwhile, dermal contact with toxic material can cause effects ranging from mild redness or eczema to severe conditions including tissue destruction and absorption into the bloodstream [43]. Thus it is

important to assess the cytotoxicity of the synthesised ZG nanocomposite to create a safe working environment and safeguard the well-being of researchers.

Detection of lung cancer is crucial for the effective and accurate admission of the treatment regime. Unfortunately, clinical features of lung disease, especially during the early stage are often non-specific and mimic many other illnesses that may lead to misdiagnosis [44]. Imaging techniques such as CT and X-Ray are unfavourable for routine screening due to the ionizing radiation. To complement these standard screening methods, biosensors arose as an innovation to provide detection of lung carcinoma via the detection of deoxyribonucleic acid (DNA) mutation or protein biomarkers present during cancer development. It is anticipated that the development of biosensors could introduce a non-ionizing detection scheme to be fitted into the routine checks of individuals.

The development of biosensors for the detection of cancer biomarkers is also motivated by the issue of laboratory shortage, especially amid a pandemic. The impact of the coronavirus disease 2019 (COVID-19) pandemic has had a dreadful consequence on the delivery of cancer diagnostic and treatment. An alarming finding showing a decrease in cancer diagnostic was reported by the Netherlands Comprehensive Cancer Organisation, in which relative diagnosis of cancer was found to be as low as 40% of the usual capacity during the outbreak of COVID-19 in early 2020 [45]. Diagnostic evaluations were either postponed or had prolonged waiting times because hospital resources and laboratory facilities were relocated to alleviate the burden on health care caused by COVID-19. As early diagnosis and rapid treatment regimes have been the indispensable factor behind improved cancer survival, the impending mortalities induced by delayed diagnosis is worrying [46]. It is anticipated that the issue of laboratory shortage can be addressed with the development of serum-based biosensors that allow the detection of lung cancer biomarkers without exploiting laboratory resources. Various nanomaterial-modified biosensors have emerged; nonetheless, the incorporation of ZG nanocomposite into the detection of lung cancer markers is yet to be extensively explored as compared to other nanomaterials [28], [29]; With the excellent

properties of ZG nanocomposite, it is research-worthy to explore the possibility of a ZG-modified biosensor to provide specific, sensitive and reliable early detection of lung carcinoma.

1.3. RESEARCH AIM AND OBJECTIVES

This research aims to develop an electrochemical biosensing platform based on the greenly-synthesised ZG nanocomposite for the detection of DNA mutation and protein biomarkers associated with lung cancer.

The research objectives are:

1. To develop a green and scalable method based on solvent-exfoliation and hydrothermal to synthesise residual-free ZG nanocomposite, and to evaluate the material properties and cytotoxicity of the as-synthesised ZG nanocomposite.
2. To construct an electrochemical sensor based on the ZG nanocomposite, and to evaluate the electrochemical sensing potential of the sensor using acetaminophen as the model electroactive analyte.
3. To fabricate a genosensor based on the ZG nanocomposite, and to investigate the electroanalytical performances of the fabricated genosensor under optimised sensing conditions for the differentiation between wild-type and mutated DNA sequences of exon-19 in epidermal growth factor receptor.
4. To fabricate an immunosensor based on the ZG nanocomposite, and to investigate the electroanalytical performances of the fabricated immunosensor under optimised sensing conditions for the detection of carcinoembryonic antigen.

1.4. REPORT OUTLINE

The organisation for the rest of the report are as follows:

Chapter 2: Literature Review

This chapter introduces various synthesis methods of graphene and graphene/metal oxide nanocomposites, followed by a review of related works in the area of electrochemical sensing and biosensing with sensors enhanced with graphene-based nanocomposites. The chapter continues with the review of various biomarkers for lung cancer, including genomics and proteomics biomarkers; as well as the review of transducers employed for lung cancer detection. Lastly, the review of previous works on the application of graphene-based nanocomposite in lung cancer detection is also presented in this chapter.

Chapter 3: Synthesis And Characterisation Of Graphene/Zirconia Nanocomposite

This chapter reports the solvent exfoliation and the hydrothermal method employed to synthesise the pristine and residual-free ZG nanocomposite. Characterisation of the nanomaterial in terms of morphology, crystallinity and chemical composition alongside the electrochemical response of the as-synthesised nanocomposite are presented in this chapter. In conjunction with the broader application of graphene-based nanocomposites, raise the concern of material-induced cytotoxicity. This chapter also presents a cytotoxicity study in terms of a microscopic evaluation and an *in vitro* cell proliferation study on human lung fibroblast (MRC5) and human immortalised keratinocyte (HaCaT).

Chapter 4: Potential Of The Graphene/Zirconia-Based Platform As An Electrochemical Sensor: Acetaminophen As The Model Analyte

This chapter reports the development of an electrochemical sensor based on screen-printed carbon electrodes (SPCE) modified with the as-synthesised ZG nanocomposite for the detection of acetaminophen. The analytical performances of the sensor for both reagent-grade and pharmaceutical-grade acetaminophen are presented in this chapter.

Chapter 5: An Impedimetric Genosensor Based On Controllable Pi–Pi Functionalisation Of Zirconia-Decorated Graphene To Distinguish Between Wild-Type and Mutated Exon-19 Sequences in Epidermal Growth Factor Receptor

Owing to its good electrochemical performance in acetaminophen detection as demonstrated in chapter 4, the potential of the ZG nanocomposite to serve as a genosensor is further explored. This chapter reports an impedance-based genosensor enhanced with 1-pyrenebutyric acid N-hydroxysuccinimide (PY)-functionalised-ZG nanocomposite to distinguish between wild-type and mutated exon-19 sequences of the epidermal growth factor receptor that is common among lung cancer patients. Fabrication steps, sensing conditions optimisation, analytical performances, specificity, stability and reproducibility of the genosensor are presented in this chapter.

Chapter 6: An Immunosensor For The Rapid Detection Of Tumour Marker Carcinoembryonic Antigen Based on Graphene/Zirconia-Enhanced Platform

The good performance of the genosensor reported in chapter 5 encourages the further exploration of the ZG nanocomposite platform to detect protein biomarkers. This chapter presents a disposable and label-free electrochemical immunosensor for the rapid detection of carcinoembryonic antigen (CEA) that is often overly expressed in lung cancer. Fabrication steps, sensing conditions optimisation, analytical performances, specificity, stability and reproducibility of the CEA sensor, together with the detection of CEA in human serum samples are presented in this chapter.

Chapter 7: Conclusion, Limitations and Future Works

This chapter summarises the work done and findings thus far. This report ends with the limitations and the future works that the as-developed sensing platform can be driven towards.

2. LITERATURE REVIEW

2.1. INTRODUCTION

Graphene is a one-atom-thick planar sheet of Sp^2 bonded carbon atoms in a honeycomb crystal lattice. Its broad application, thanks to its extraordinary electronic, mechanical, thermal, and optical properties [47], results in high demand for scalable and effective synthesis routes. The extraordinary property of graphene depends strongly on the dispersion quality of graphene sheets [16]. However, aggregation of graphene sheets tends to occur due to Van der Waals and π-π stacking interactions among sheets [20]. Restacking and serious agglomeration of graphene sheets cause great loss of active surface area resulting in poorer electrochemical performance. Research has demonstrated that exploiting the collective merits of both graphene and metal oxides can improve the electrochemical of the nanocomposite [48]–[50]. Graphene decorated with evenly distributed nanoparticles on the surface could lead to well-dispersed graphene with an exceptional surface area. The synergistic effects between graphene and metal oxides resulted in a composite that is a new material with different properties and functionalities and not a mere sum of the individual components. Some common methods to synthesise graphene include micromechanical cleavage of graphite [11], chemical vapour deposition (CVD) [51] and reduction of graphite oxide [52]. Meanwhile, the sol-gel method [53], hydrothermal treatment [27], and electrodeposition [54] are frequently employed in the synthesis of graphene-based nanocomposites. On this account, the review of various synthesis methods for graphene and graphene-based nanocomposites will be presented in sections 2.2 and 2.3 of this chapter. Alongside, the applications of the synthesised nanocomposite as electrochemical sensors and biosensors will be presented in section 2.4.

Research shows that lung cancer varies from one patient to another, and this triggers a different tactic for cancer treatment, termed personalised medicine, which is made feasible by the discovery of unique lung cancer biomarkers [55]. Biomarkers are molecular characteristics of a tumour that can, in some cases, useful to determine a suitable treatment regime. Biomarkers for lung cancer

can be in the form of circulating tumour nucleic acid and tumour cells, serum antigen or antibody, messenger RNA (mRNA) and some others [56]. Events between the biorecognition element with the biomarker are meaningless if they are not converted to quantitative measurements; therefore, a transducer is necessary to, as the name implies, transduce bio-recognition events into measurable signals in the form of optical, electrical, piezoelectrical, etc. Accordingly, this chapter provides an overview of various biomarkers for lung cancer detection and a review of transducers commonly employed in the detection of lung cancer biomarkers.

Lastly, this chapter presents a review of graphene-based and graphene nanocomposite-based sensors that have been fabricated and applied to the detection of lung cancer biomarkers. As mentioned earlier, graphene was added into a biosensor as an electrochemically active material with a massive conductive network ensuring good electron transfer; while graphene nanocomposite was integrated into a biosensor for synergetic effects. The knowledge from the reported literature provides valuable insight into the underlying detection mechanism and performance enhancement strategy of the ZG-based biosensor to be proposed in this work.

2.2. SYNTHESIS OF GRAPHENE

The first piece of graphene sheets was obtained via manual mechanical cleavage of graphite with Scotch tape [11]. Pristine single-layer graphene was yielded from this method, and the graphene sheets demonstrated superior mechanical and electrical properties. Though limited by low yield, this pioneering work has inspired continuous efforts to develop more scalable and effective synthesis methods of graphene. These methods can be generally classified as the bottom-up and top-down approaches.

2.2.1. BOTTOM-UP APPROACH

The bottom-up approaches involve the direct synthesis of graphene from carbon sources, and it is commonly subdivided into two categories, namely epitaxial growth of graphene and the chemical vapour deposition of graphene.

2.2.1.1 EPITAXIAL GROWTH

The fundamental epitaxial growth of graphene lies in the graphitisation that occurs when silicon carbides (SiC) are annealed at high temperatures. Graphene growth takes place slowly leading to the formation of thin layers. The general steps of epitaxial growth of graphene on SiC are: (i) surface treatment through hydrogen (H_2) etching (ii) treatment in high-vacuum to induce graphitisation, (iii) transfer of the sample to metal contacts, (iv) electron-beam patterning and (v) oxygen plasma etch to define graphite structures [57]. Ultrathin epitaxial graphite films which show remarkable electron gas behaviour was synthesised by thermal decomposition on the (0001) surface of SiC by a team of researchers in 2004 [58]. After surface-treatment by H_2 etching, SiC samples were heated by electron bombardment in an ultrahigh vacuum to about 1000 °C in order to remove the oxide. Samples were heated to temperatures ranging from 1250 °C to 1450 °C up to 20 minutes following the removal of the oxide layer which was confirmed by Auger electron spectroscopy. Thin graphite layers were formed via this high-temperature evaporation of Silicon (Si) in an ultrahigh vacuum. Figures 2.1 (a)-(d) show low energy electron diffraction (LEED) patterns at different temperatures. LEED verified that the graphene sheets grew epitaxially with the underlying SiC starting at about 1250 °C.

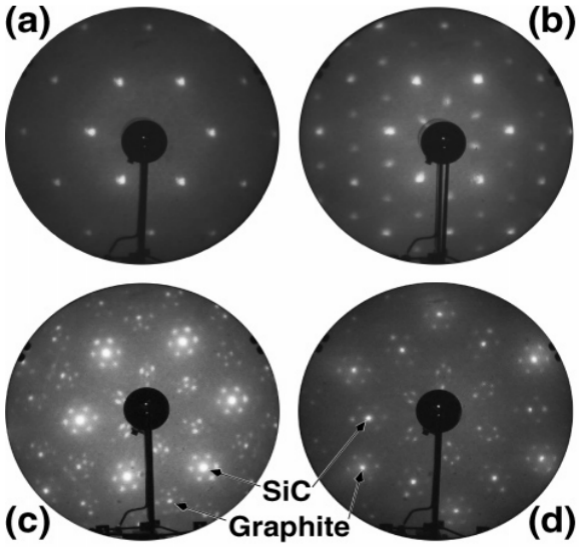


Figure 2.1. LEED patterns from of SiC samples (a) at 1050 °C, (b) at 1100 °C, (c) at 1250 °C and (d) at 1400 °C. First-order SiC and graphite spots were observed starting at 1250 °C [58].

Epitaxial development of graphene on SiC surfaces by high vacuum presented a breakthrough for high-yield graphene synthesis. Nevertheless, this method yielded graphene with small structural domain sizes, and it was not a reproducible technique for producing graphite films with controllable thickness for intended applications [59], [60]. Therefore, an alternative method was proposed, in which single-layer graphene of much larger domain sizes than previously achievable was produced via graphitisation of SiC in an argon atmosphere of about 1 bar [61]. SiC wafer was etched in H_2 (grade 5) at a temperature of 1550 °C for 15 minutes at atmospheric pressure of 1 bar to eliminate polishing destruction. The growth of graphene was induced in a chilled-wall vertical reactor that housed a quartz tube that was cooled by water and a graphite susceptor positioned within a low-speed argon air flow. Figure 2.2 (a) and (b) shows the atomic force microscope (AFM) images of samples grown in the Argon atmosphere in comparison to the sample grown in an ultra-high vacuum furnace. It shows that the surface of graphene produced in a high vacuum (Figure 2.2 (b)) was covered with nano-scale pits that led to considerable roughening and inhomogeneous thickness. In contrast to the rough-surfaced graphene produced by vacuum graphitisation, films grown in slow argon flow exhibited a greatly improved surface morphology with long continuous terraces parallel to the step edges.

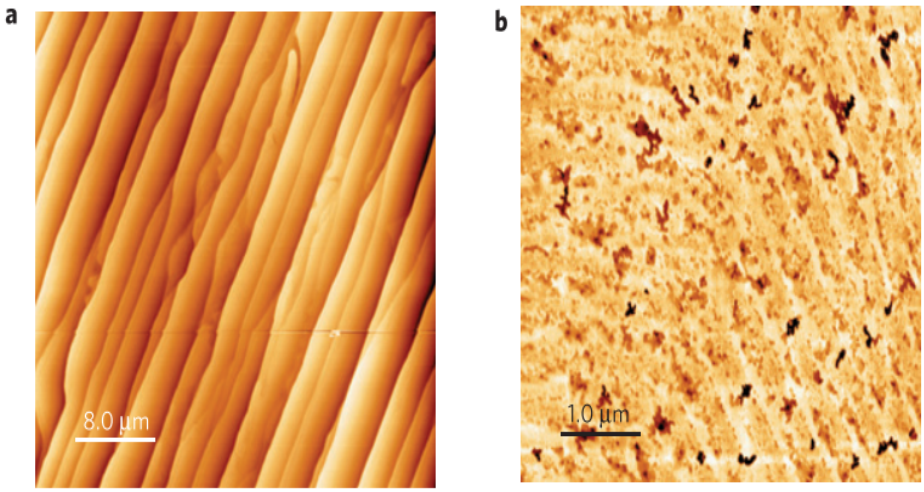


Figure 2.2. AFM images of graphene grown in (a) argon atmosphere and (b) ultra-high vacuum. The surface morphology of graphene produced in an argon-flow atmosphere was mostly smoother, and the graphene size was larger compared to those produced via vacuum graphitisation [61].

Although there were improvements to the techniques since it was first proposed, the difficulty in controlling the quality of graphene synthesised via epitaxial growth persisted. Therefore, it has prompted the development of more effective alternatives. One of them is the chemical vapour deposition technique that is to be discussed in the following section.

2.2.1.2 CHEMICAL VAPOUR DEPOSITION

It has been known for decades that thin graphitic layers can be produced from the chemical vapour deposition of hydrocarbons on reactive nickel or transition-metal surfaces. However, thick graphite crystals are usually formed instead of graphene films due to the massive amount of carbon sources absorbed on nickel foils during the synthesis process. A solution proposed was to use an electron-beam evaporator to deposit a thin layer of nickel in nanoscale thickness onto silicon oxide (SiO_2) /Si substrates [51]. The samples were then heated to 1000 °C and followed by a flowing reaction gas mixture (Methane: H_2: Argon) before it was rapidly cooled down to room temperature using flowing argon. The proposed method allowed the control of averaged graphene layers and surface size through manipulation of the nickel thickness and growth time, consequently presenting a promising technique to customise the growth of graphene for various applications.

Other than nickel, graphene has also been grown on different metal surfaces, such as copper foil [62]. Graphene was grown on 25 μm copper foils at temperatures up to 1000 °C by deposition of carbon under a reaction mixture gas of methane and H_2. The graphene films grow directly on the copper foil by a surface-catalysed process and can be transferred easily to other substrates. Figure 2.3 (a) and (b) show the scanning electron microscopy (SEM) images of graphene on copper foil and glass respectively. One of the key advantages of this proposed technique is its capability to lead to very large graphene sheets in which graphene can be grown on 300-mm copper films on the Si substrate and the graphene sheets formed were predominantly (~95%) thin graphene.

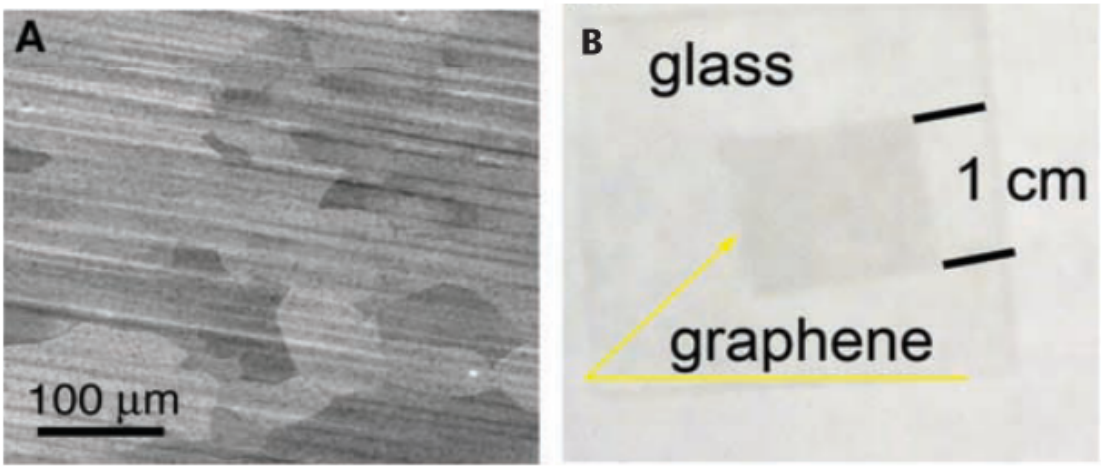


Figure 2.3. SEM images of (a) graphene grown on copper foil through CVD and (b) graphene transferred to glass. The as-grown graphene can be easily transferred to other substrates for various assessments and applications [62].

A more recent effort to synthesise graphene from the copper surface was reported in which graphene film was grown via CVD uniformly on the copper foil decorated with silicon nanoparticles [63]. Nanoscale silicon nanoparticles were dispersed in ethanol and subsequently spin-coated on the surface of copper foil. Placed in a furnace with a continuous flow of H_2/Argon (20:80), the sample was heated at a temperature that gradually increased to 900 °C to reduce the surface oxide. Subsequently, ethanol vapour was purged into the sample to induce the growth of graphene. Figure 2.4 illustrates the one-step growth of graphene by CVD on silicon nanoparticles coated copper film. Silicon nanoparticles were exploded to condense copper vapour from the copper film at a high temperature to form copper nanoparticles that subsequently catalysed the growth of carbon elements.

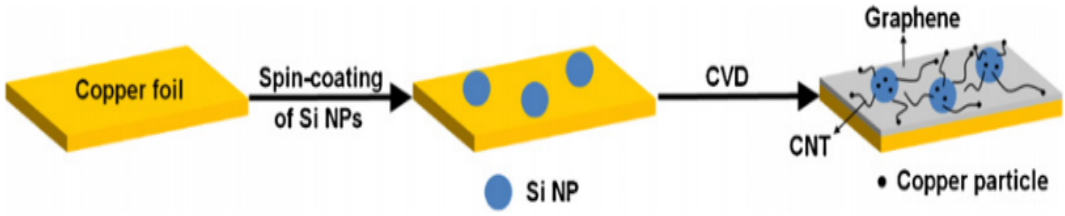


Figure 2.4. Schematic of one-step CVD growth of graphene on Si-coated copper foil. It is a one-step synthesis that can produce a highly conductive graphene hybrid without the employment of surfactant [63].

2.2.2. TOP-DOWN APPROACH

Bottom-down approaches produce graphene sheets of good quality samples interacting strongly with their substrates, but successful electrically-isolated single-layer graphene for device applications is still limited. Also, the widespread of bottom-up methods is hampered by their complexity and the high cost of the metal substrates. Advanced from the bottom-up approaches, the top-down approaches are beneficial in terms of high yield, simple implementation and feasibility to be solvent-based [64]. It is much easier to achieve the mass production of graphene through a top-down approach by using graphite or graphene oxide as the source material.

2.2.2.1 CHEMICAL REDUCTION

The most extensively employed top-down approach is the chemical reduction of graphene oxide. Chemical reduction of graphene oxide is usually obtained by oxidation of natural graphite powder with various oxidants in acidic media with the most representative method being Hummer's method developed by Hummers and co-workers [65], as illustrated in Figure 2.5. In this proposed method, the oxidation of powdered flake graphite to graphene-oxide was achieved by treating graphite with essentially a mixture of concentrated sulphuric acid (H_2SO_4) sodium nitrate and potassium permanganate ($KMnO_4$), followed by washing with water and hydrogen peroxide (H_2O_2) to reduce the residual permanganate (MnO^-_4) and manganese dioxide (MnO_2). Graphite oxide obtained through Hummer's method could be exfoliated into graphene oxide sheets via aqueous-ultrasonication. Graphene from RGO is known to have an abundance of functional groups, such as hydroxyls and epoxides [66]. Processes employed to remove these functional groups such as the annealing and reduction process can result in a significant amount of defects that disrupt the electronic properties of graphene oxide. The consistently defective RGO was observed to be electrical less conductivity as compared to pristine graphene [67].

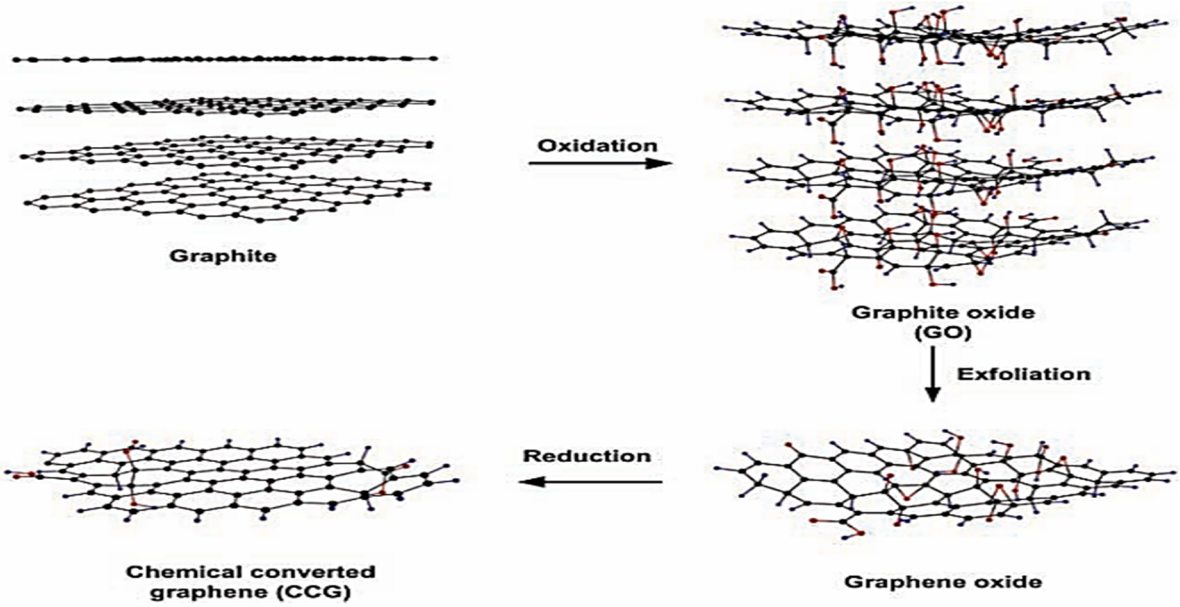


Figure 2.5. Chemical reduction of graphene oxide. Graphene oxide is usually obtained by oxidation of natural graphite powder with various oxidants in acidic media [68].

A more recent improvement of the chemical reduction method was proposed in which $KMnO_4$ served as the sole oxidant and an acidic mixture comprised of phosphoric acid and H_2SO_4 in the ratio of 1:9 served as the acidic medium [69]. On top of improved oxidation efficiency, this method also introduced toxic-gas-free synthesis in which the production of toxic gases, such as nitrogen dioxide and nitrogen tetroxide was not observed. The graphene oxide synthesised by this method possesses a more regular dimension than that produced by Hummers' method.

Graphene oxide can be chemically reduced to graphene via various reducing agents, with hydrazine monohydrate being the most widely used, thanks to its strong reductive nature and high aqueous stability [70]. A great amount of oxygen-containing functional groups of graphene oxide were removed upon reduction with hydrazine. Due to its highly flammable and corrosive nature, hydrazine possesses a potential health hazard to personnel and a safety threat for amenities that produce hydrazine-RGO. Therefore, a team of researchers has developed a hydrazine-free reduction method in which graphene oxide was solvothermally treated at 200 °C in an aqueous-based solvent of 1-methyl-2-pyrrolidinone (NMP) [71]. It was observed that the surface tension of NMP matches that of graphene; consequently, NMP presented strong interaction with graphite and

was capable of producing a mixture of monolayer and few-layered graphene dispersions without the use of hydrazine.

2.2.2.2 THERMAL EXFOLIATION

Thermal exfoliation of graphite was realised through the explosive pressure from the internal to external space of graphite at high temperatures, as demonstrated in previous works [72], [73]. High heat decomposed heat-sensitive functional groups and generated gases that diffused along the lateral direction and produced enormous interlayer pressure between adjacent layers. Once the interlayer pressure exceeded the Van der Waals force between the layers, the pressure pushed layers apart from each other and produced exfoliated graphene. Both studies concluded that thermal exfoliation is a promising technique for the mass production of graphene. Thermal exfoliation is advantageous procedure thanks to its simple procedure that required only a few minutes as well as its feasibility to achieve exfoliation without the need for a liquid environment, which in turn, eliminated the possible aggregation in the solvent removal process.

A high temperature (above 1000 °C) is usually applied to the sample to achieve rapid exfoliation, resulting in high energy consumption. In addition, the generated gases may react with the carbon atoms at high temperatures and subsequently introduce more defects on the produced graphene. To overcome this issue, Lv et al. developed a low-temperature (200 °C) exfoliation technique carried out in high-vacuum to produce graphene that has exhibited excellent energy storage performance [74]. The high-vacuum environment accelerated the exfoliation by introducing an external pulling force in addition to the interlayer pressure that was produced by the thermal decomposition of functional groups. Figure 2.6 illustrates the mechanism of high-vacuum and low-temperature exfoliation. The high vacuum, together with the oxygen flow imposed an outward pulling on the expanding graphene layers and enhanced the exfoliation efficiency.

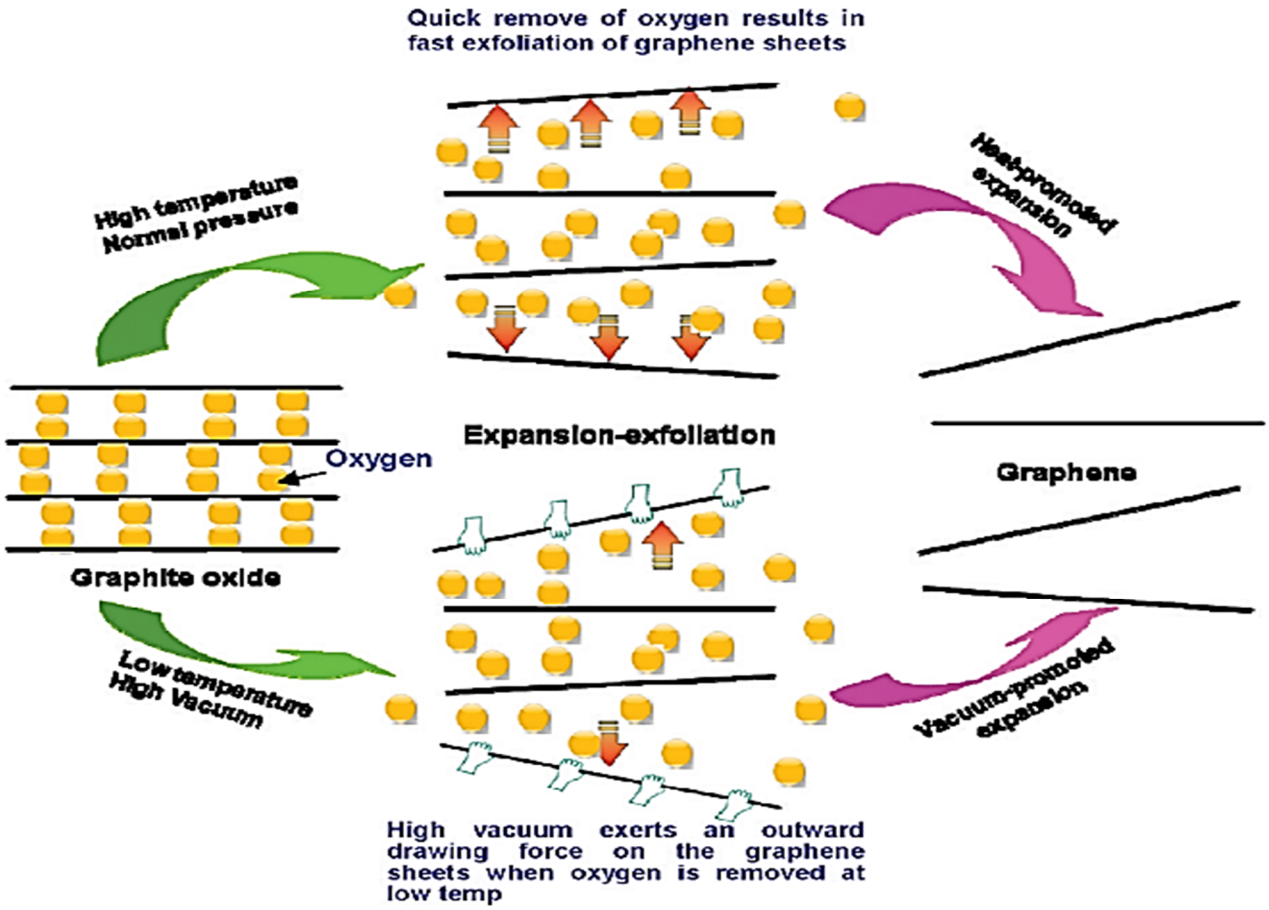


Figure 2.6. Schematic representation of thermal exfoliation technique. The use of a high-vacuum environment allowed the achievement of graphene exfoliation at temperature much lower than that used in the normal-pressure thermal exfoliation technique [74].

Exfoliation of graphene is achieved through the synergetic effect of inner and outer puller forces. Therefore, other than introducing external pulling force through high-vacuum, another approach to achieve low-temperature thermal exfoliation is by enhancing the inner pushing forces which were caused by the decomposition of interlayer functional groups. Kaniyoor et al. developed an H_2-induced low-temperature method to exfoliate graphite into graphene of a few layers [75]. Exfoliation was realised within a minute at a low temperature of 200 °C due to the aggressive reaction between H_2 with hydroxyl groups that accelerated graphene exfoliation. The authors postulated that the H_2 reacted with the hydroxyl groups on graphene oxide to form water. The aggressive reaction of oxygen and H_2 was hypothesised as an exothermic reaction that furnished energy to disrupt the basal planes of graphene oxide and exfoliate it into graphene. CO_2 was also

produced due to the partial reduction of the carbonyl group and carboxyl groups, as suggested by the result from Fourier transform infrared spectroscopy. This novel gas-assisted exfoliation approach successfully generated high-quality graphene sheets.

2.2.2.3 OTHER METHODS

Some other methods to synthesise graphenes such as microwave-assisted exfoliation and solvent-based exfoliation have also been reported in the literature. A derivative approach from the conventional thermal exfoliation synthesis, the microwave-assisted exfoliation, synthesise graphene by using high temperature from microwave irradiation to expand graphitic from within. Rapid microwave irradiation has the ability to expand graphite through the expulsion of co-intercalated compounds, due to sudden vaporisation or decomposition, as reported by previous works [76], [77].

The conventional oxidation methods employ highly reactive acids or oxidising agents, resulting in the presence of defects in the synthesised graphene [77]. This shortcoming induced the beginning of the exfoliation of natural graphite in suitable organic solvents. Water and organic solvent such as NMP and 7,7,8,8,-Tetracyanoquinodimethane (TCNQ) was employed to exfoliate powdered graphite and produce graphene in the liquid phase without oxidation or defect formation [78], [79]. The yield of graphene obtained in this method ranged from 1 mg/ml in NMP, 5 mg/ml in TCNQ to 7 mg/ml in water. Solvent exfoliation is a simple synthesis method that introduces graphene synthesis without the need for oxidation. The major concern of this method is the choice of solvent; a study showed that the solvent exfoliation method produced graphene dispersion whose stability was very much dependent on the type of solvent used [80]. Therefore, the choice of solvent should be carefully evaluated to achieve optimum solvent exfoliation.

2.3. SYNTHESIS OF GRAPHENE/METAL OXIDE NANOCOMPOSITE

Graphene is often hybridised with metal oxides to produce nanocomposites that would outperform the individual components. The role of graphene in graphene-based nanocomposite is to provide large-surface-area support for the anchoring of metal oxide particles. Meanwhile, nanoparticles of metal oxide serve as spacers to prevent the restacking of graphene. Synergetic effects between graphene and metal oxides often enhance the charge transfer as well as the mechanical strengths of resulting composites, thus boosting the efficiency of various graphene-based applications. Therefore, there is a need to explore a cost-effective and scalable synthesis method to produce graphene/metal oxide of reproducible quality and yields. Various synthesis methods have been proposed, among those, hydrothermal methods, sol-gel processes, microwave-assisted growth and electrodeposition have drawn the most attention [81].

2.3.1. SOL-GEL

Sol-gel is a wet-chemical procedure that involves the formation of an inorganic colloidal suspension (sol) and gelation of the sol in a continuous liquid phase (gel) to form a three-dimensional (3D) network structure under heat treatment [82]. Sol-gels can be in the form of nanoscale films or particles, with metal precursors that undergo a series of hydrolysis reactions and eventually crystallise. In other words, the synthesis route starts with hydrolysis and condensation of a precursor leading to the formation of sol that, after subsequent chemical or heat treatment turns into a gel, which is calcined to obtain the final composite.

Taking titanium dioxide (TiO_2) synthesis as an example [53], the typical precursors of tetrabutyl titanate (TBTN) was first added drop-by-drop into graphene suspension followed by mixing of the suspension with acetic acid glacial to induce hydrolysis of the precursor. The mixture was stirred for two days to form a sol that was subsequently annealed in air or nitrogen atmospheres at 450 ºC for 2 hours to form graphene/TiO_2 nanocomposite. The process for preparing graphene/TiO_2 nanocomposite is illustrated in Figure 2.7. Metal oxide precursors in the form of sol coated the

surface of graphene sheets via self-assembly, and annealing of the sample led to the crystallisation of metal oxide precursors producing graphene sheets decorated by titanium oxide nanoparticles.

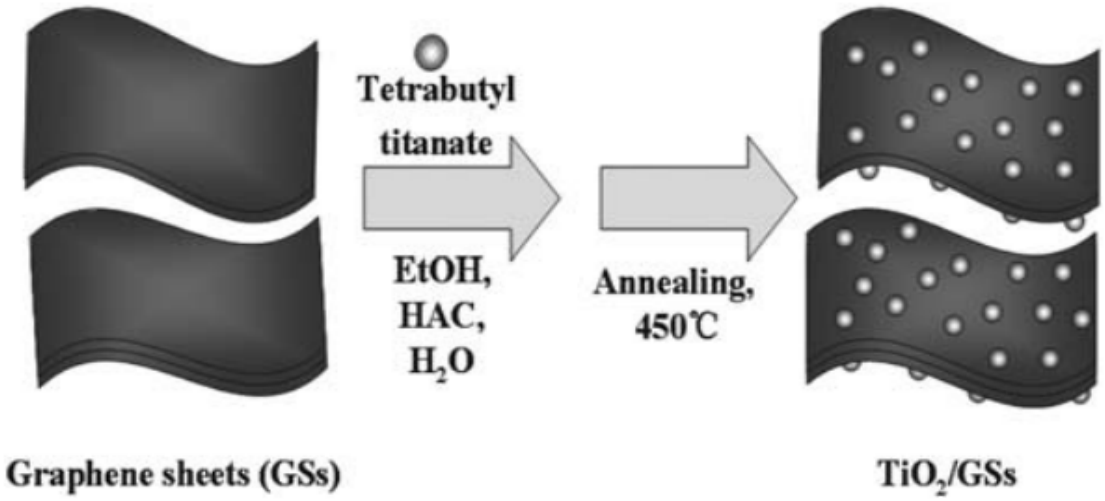


Figure 2.7. Schematic illustration of sol-gel synthesis procedure for the preparation of graphene/TiO_2 nanocomposite. Graphene/TiO_2 nanocomposite was synthesised with TBTN and graphite oxide as the starting materials to form sol that was subsequently annealed at high temperature [53].

On top of its simple procedure, nanocomposite synthesised via the sol-gel method has been proven to show excellent electrochemical, electrical and mechanical properties, as demonstrated by Liu et al. [83], Hu et al. [84] and Du et al. [85]. Liu et al. have proposed a sol-gel based technique to synthesise vanadium pentoxide (V_2O_5)/graphene nanocomposite. The nanocomposite was prepared by mixing the graphene oxide suspension with the vanadium precursor and subsequently aged for about 21 days to acquire the hydrogel of graphene oxide/V_2O_5. After freeze-drying and annealing at 400 °C, where the reduction of graphene oxide into graphene occurred, the graphene/V_2O_5 nanocomposite was synthesised. The nanocomposite exhibited near-ideal specific capacity, durable cyclability and significantly improved rate capability for lithium-ion batteries. Such performance was the result of the synergetic effects of graphene and vanadium, which respectively have provided excellent structural stability and active redox reaction. Similarly, RGO/Tin(IV) oxide (SnO_2) synthesised by Hu et al. using the sol-gel method has also exhibited good electrochemical performance and stability for supercapacitor applications. The experimental

results indicated that the sol-gel method was a facile and practical approach for nanocomposite synthesis. Besides, nanocomposites synthesised by sol-gel methods were also applied in waste-water treatment for instance the macro-mesoporous graphene/TiO_2 composite synthesised by Du et al.. The nanocomposite have demonstrated improved rapidness in adsorbing and photodegrading of organic dyes, which are essential for waste-water treatment and other industrial applications.

The advantages of the sol-gel method include scalable production of the nanocomposite, homogeneous and strong interactions between nanoparticles and the underlying graphene material as well as the production of nanocomposite with a stable surface alongside a high surface area [64], [86]. Nonetheless, the sol-gel method is limited by the difficulty in controlling the main properties of the resulting product; since the properties of a gel and its behaviour on heat treatment could be very sensitive to the structure previously formed during the sol stage, slight variations of the chemical conditions under which the nanomaterial is polymerised may lead to drastic changes to the structure and the morphology of the final product [87].

2.3.2 HYDROTHERMAL/SOLVOTHERMAL

Hydrothermal/solvothermal synthesis is a common technique for the synthesis of inorganic nanocrystals, which operates in a confined space at an elevated temperature to generate high pressure, in another word, the hydrothermal/solvothermal process utilises high temperature and high vapour pressure to crystallise substances from solvent. The method is termed hydrothermal if water is used as the solvent. Various metal oxides such as Copper(II) oxide (CuO), TiO_2 and zinc oxide (ZnO) have been incorporated into graphene via the hydrothermal/solvothermal method [27], [88]–[90]. In general, an autoclave reactor made of stainless steel with a Teflon container of a certain volume is used. Metal oxide precursor solution with concentrations suited to different applications is loaded into the Teflon container, placed in a sealed autoclave reactor, and subsequently heated up at a certain temperature for certain durations to yield the desired nanocomposite. Graphene/metal oxide synthesised through the hydrothermal/solvothermal

process has been employed in various applications including biosensing [90], supercapacitors [91], lithium-ion batteries [92], solar cells [93] and cytotoxicity studies [94].

One of the greatest advantages of the hydrothermal/solvothermal process is its capability to customise the properties of the synthesised materials. He et al. demonstrated that by manipulating experimental parameters such as concentrations of precursor solutions, reaction temperature and time, graphene/TiO_2 nanocomposites with controlled nanostructure were easily obtained using the solvothermal method [93]. Figure 2.8 shows the solvothermal approach adopted to produce different graphene/TiO_2 nanocomposites. Titanium precursor was added dropwise into different organic dispersion of graphene oxide. Subsequently, a one-step solvothermal reaction induced the reduction of graphene oxide and crystallisation of TiO_2 simultaneously. Different nanostructures namely ultra-small 2 nm graphene/TiO_2 nanosheets (USTG), 12 nm spherical graphene/TiO_2 nanosheets (STG) and graphene/TiO_2 nanorod (NRTG) were obtained under different solvothermal parameters.

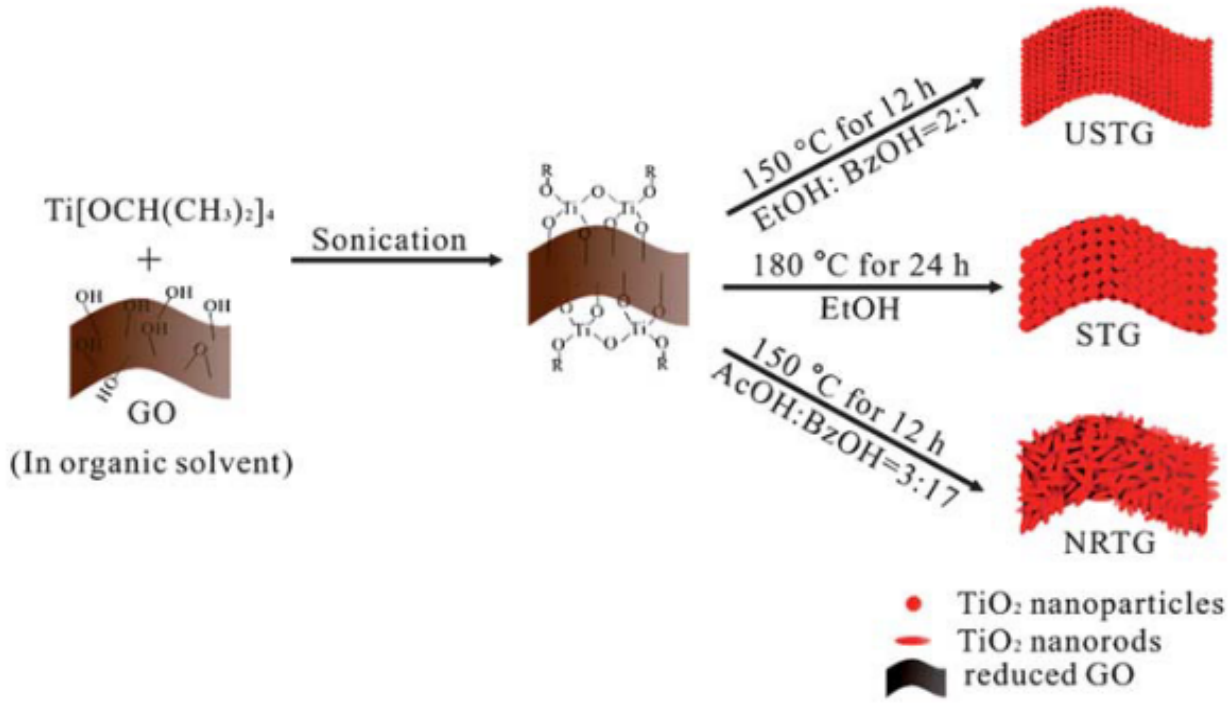


Figure 2.8. Schematic illustration of solvothermal synthesis. Graphene/TiO_2 nanocomposite of different nanostructures is achievable through the manipulation of synthesis parameters [93].

The one-pot hydrothermal/solvothermal process can give rise to nanostructures with high crystallinity without post-annealing or calcination. This benefit was demonstrated by Huang et al. who has employed a facile one-step solvothermal synthesis route to hybridise graphene/SnO_2 nanocomposite for the first time [95]. Rod-like SnO_2 nanocrystals were uniformly distributed on the graphene sheets along with well-preserved crystallinity. Figure 2.9 shows the crystalline structure of SnO_2. The relatively sharp X-Ray diffraction (XRD) peaks suggested the nanocrystalline nature of the SnO_2. . This work has also demonstrated the other benefits of the hydrothermal/solvothermal method where nanocomposites are formed directly from the solution and is instantly retrievable.

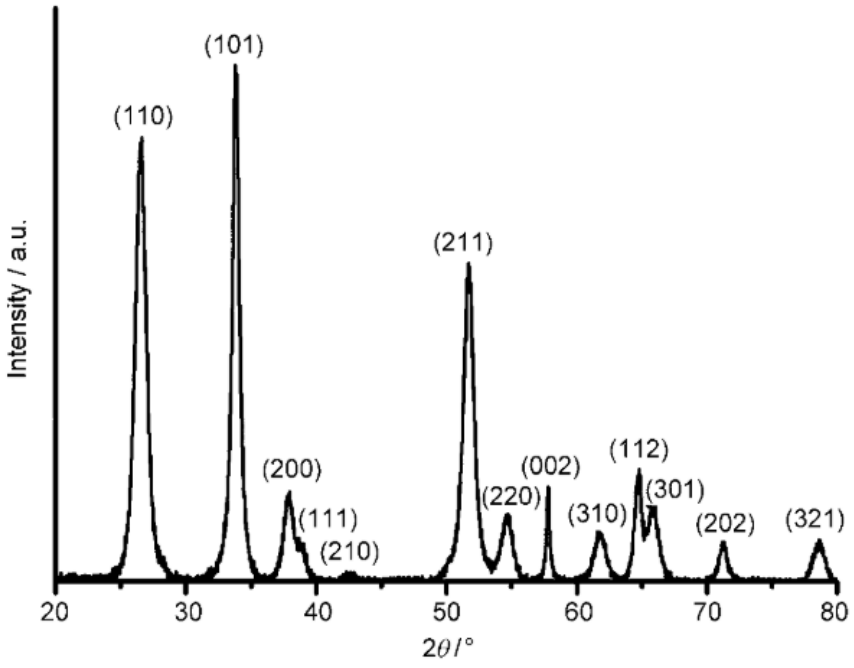


Figure 2.9. XRD result of the graphene/SnO_2 nanocomposite synthesised via the solvothermal method. Solvothermal methods have been widely used to synthesise high-crystalline nanocomposites [95].

Graphene-based nanocomposite with excellent charge transfer property has been employed in sensors that operate based on the field-effect transistor, such as that reported by Munusami et al. [96]. The hydrothermal method was used to produce the graphene/molybdenum disulphide (MoS_2) nanocomposite that has been shown to have enhanced charge transfer across the heterojunction interface. Graphene and MoS_2 were placed in a sealed container which was subsequently heated

to 200 °C under high pressure. MoS_2 and graphene possess an N-type and P-type nature respectively; thus under hydrothermal treatment, the excited electrons of MoS_2 jumped and filled the hole of graphene. Material characterisation such as SEM, XRD and Raman spectroscopy showed that graphene and MoS_2 were well-hybridised. The graphene/MoS_2 nanocomposite was used to modify a gas sensor to detect elements such as hydrogen and carbon monoxide. The sensor has exhibited excellent sensing capability, attributed to the presence of MoS_2 nanoparticles which presented enhanced interaction with the gas molecules thanks to their high surface area.

Biosensors functionalised with graphene-based nanocomposites that were synthesised using the hydrothermal method has been reported, such as that from Siew et al. [97]. In this work, TiO_2 was hybridised with graphene via 12 hours of hydrothermal treatment in an autoclave at 130 °C. Hydrolysis and condensation took place to produce a graphene nanocomposite with well-anchored TiO_2 nanoparticles. An immunosensor for the detection of dengue virus IgG antibodies was developed based on the as-synthesised graphene/TiO_2. The author credited the good sensitivity and specificity of the sensor to the large specific area and excellent catalytic properties of G/TiO_2 nanocomposites.

In short, the hydrothermal/solvothermal synthesis method is favourable thanks to its simple procedure and feasibility to produce high crystallinity composite without post-annealing or calcination. Materials produced by the hydrothermal/solvothermal method have good crystallinity, dispersity, and minimal macroscopic agglomeration [98].

2.3.3 OTHER METHODS: MICROWAVE IRRADIATION AND ELECTROCHEMICAL DEPOSITION

Other methods used to synthesise graphene/metal oxide nanocomposite, for instance, microwave irradiation and electrochemical deposition, have also been reported in the literature. Microwave irradiation deploys the principle of microwave dielectric heating in which liquids or solids uses the electromagnetic radiation provided by the microwave oven to generate heat to drive chemical reactions. This method is a swift and simple method for metal oxide precursors to crystallise on graphene. Microwave irradiation has been used to prepare various graphene/metal oxide nanocomposites such as graphene/MnO_2 and graphene/cobalt oxide (Co_3O_4). Aided by microwave irradiation, Yan et al. synthesised graphene/MnO_2 nanocomposite by exploiting the redox reaction between $KMnO_4$ and graphene, as illustrated in Figure 2.10 [99]. The mixture of $KMnO_4$ and graphene was heated via microwave radiation for 5 minutes at 700 Watt, leading to the conversion of aqueous MnO^-_4 into the insoluble MnO_2, which in turn deposited on the surfaces of graphene. Similarly, graphene/Co_3O_4 nanocomposite was also synthesised by Yan et al. using the microwave-assisted method [100]. The mixture of cobalt nitrate hexahydrate, urea and graphene oxide was heated using a household microwave oven at 700 Watt for 10 minutes to yield the graphene/Co_3O_4 nanocomposite that has a Co_3O_4 mass percentage of about 25%.

In brief, the microwave irradiation method provides fast kinetics of crystallisation and immensely reduces synthesis duration from days and hours to minutes and seconds; Nonetheless, the application of the microwave-assisted synthesis route is limited by the inability to control the morphology and phase of the final product [101].

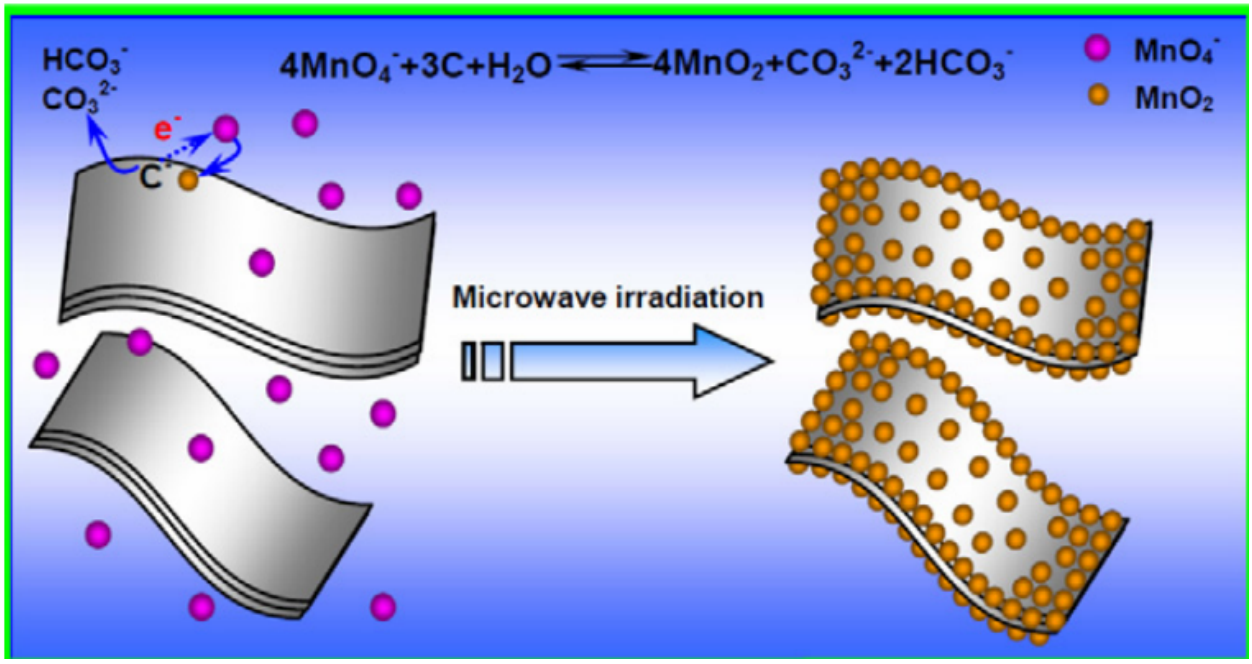


Figure 2.10. Schematic illustration for the synthesis of graphene–MnO_2 composite via microwave radiation. The reaction is characterised by electron transfer from the carbon to the oxidant upon activation by heat from microwave radiation [99].

Electrochemical deposition of metal oxide on graphene or graphene oxide is another method to synthesise graphene/metal oxide nanocomposite The core of electrodeposition is given by electrochemical redox reactions in which metal is deposited at the cathode when an electric current passes through the metal salt solution. Electrochemical deposition of ZnO nanorods on graphene for photovoltaic applications has been reported [54], [102], in which a three-electrode cell using a silver/silver chloride reference electrode, a platinum counter electrode and a graphene working electrode was used as the setting to deposit ZnO on graphene films. By applying a constant current to the electrodes placed in an oxygen-saturated aqueous solution containing precursor zinc chloride, monocrystalline ZnO nanorods with high donor capability were electrochemically deposited on the graphene sheet, according to equations 2.1 and 2.2.

$$O_2 + 2H_2O + 4e^- \rightarrow 4OH^- \qquad \text{(Eq 2.1)}$$

$$Zn^{2+} + 2OH^- \rightarrow ZnO + H_2O \qquad \text{(Eq 2.2)}$$

A similar technique was also employed by the same research group to deposit copper oxide (Cu_2O) films on graphene oxide films that were spin-coated on polyethene terephthalate substrates [102]. The doping control (p-type or n-type) for Cu_2O can be achieved by adjusting the pH value of the deposition electrolyte. Deposited Cu_2O showed high density and good crystallinity, with a promising potential for solar cell fabrication.

It is worth pointing out that the electrochemical deposition process is strongly affected by the conductivity of graphene films, in which graphene films that have better conductivity will lead to a higher concentration of hydroxide ion from oxygen reduction, which in turn result in more densely packed metal oxide on the graphene sheets; and vice versa. Therefore, the decision to use electrochemical deposition for graphene/metal oxide synthesis should be evaluated based on the condition and quality of the graphene sheets. In short, electrochemical deposition is a low-temperature, cost-efficient, and simple technique to synthesise nanocomposite with uniform morphology; nevertheless, its low-scale production is still the main hindrance to practical applications [101].

Each of the synthesis techniques has its advantages and disadvantages. Table 2.1 summaries briefly the merits and demerits of the mentioned synthesis methods employed in preparing graphene/metal oxide nanocomposites.

Table 2.1: Merits and Demerits of Different Graphene/Metal Oxide Synthesis Methods

Synthesis Method	Advantages	Disadvantages	Example of Synthesised Nanocomposite
Sol-Gel	• Scalable production • Nanoparticles anchored homogeneously to the underlying graphene material • Yield nanocomposite with a stable surface alongside a high surface area	• Slight variations of the conditions under which the material is polymerised may lead to drastic changes to the structure and the morphology of the final product	Graphene /TiO_2 [53] Graphene /V_2O_5 [83] RGO/SnO_2 [84]
Hydrothermal /Solvothermal	• Easy control in properties of the final product • Require no post-annealing or calcination • Produce nanostructures with high crystallinity • A one-pot method in which nanocomposites are formed directly from the solution	• Long hour of treatment • Require tightly-sealed autoclave reactor to ensure the high temperature and high-pressure environment	RGO/ZrO_2[27] RGO/TiO_2 [88] Graphene /CuO [89] Graphene/ZnO [90] Graphene /SnO_2 [95]
Microwave Irradiation	• Curtail synthesis time • Fast kinetics of crystallisation	• Difficult to control the morphology and phase of the synthesised product	Graphene/MnO_2 [99] Graphene/Co_3O_4 [100] Graphene/ZrO_2[36]

Electrodeposition	• Produce nanocomposite with uniform morphology • Low-temperature operation	• Small scale production	Graphene/ZnO [54] Graphene/Cu_2O [102] RGO/ZrO_2 [33]

2.4. APPLICATIONS OF GRAPHENE-BASED SENSING PLATFORMS

Before delving deeper into graphene-based sensors for lung cancer detection, it is essential to first review some common applications of graphene-based platforms. Apart from its great potential in solar cells [102], wastewater treatment [103] and supercapacitor applications [66], graphene/metal oxide nanocomposite with its excellent electrical conductivity and high surface-to-volume ratio, serves also as a promising platform for electrochemical sensing and biomolecules detection, which will be briefly reviewed in section 2.4.1 and 2.4.2.

2.4.1. GRAPHENE-BASED PLATFORMS FOR THE DETECTION OF ELECTROACTIVE SPECIES

One of the most established electrochemical sensings is the detection of glucose levels in blood or serum. The metabolic disorder of diabetes mellitus results in abnormal blood glucose concentration higher or lower than the normal range. Glucose oxidase (GOx) is the most widely employed enzyme to achieve specific glucose sensing. GOx oxidises glucose to gluconic acid and donates electrons to oxygen to yield H_2O_2, which is usually the target analyte to be detected electrochemically [74]. The key to the efficient fabrication of glucose sensors is the availability of a platform for the immobilisation of GOx on the electrode surface. Graphene and graphene/metal oxide nanocomposite have been employed in many schemes for glucose detection [104]–[109]. The high conductivity of graphene promoted heterogeneous electron transfer at its edges or defects in the basal plane; therefore, the high surface area of graphene facilitates large amounts of defects and subsequently promoted the electron transfer of GOx. In a nutshell, glucose sensing has

progressed through the integration of graphene and graphene/metal oxide nanocomposite to provide higher sensitivity, lower detection limit and better specificity.

H_2O_2 is not only a by-product of the oxidation of glucose; in fact, it is a common enzymatic product of oxidases. The high level of H_2O_2 is highly associated with excessive oxidative stress and neurodegenerative diseases, such as Alzheimer and Parkinson's disease [110]. Chang et al. have proposed an amperometric approach to evaluate the oxidative stress imposed by H_2O_2 on cells, in which an electrochemical sensing platform based on RGO was fabricated to evaluate the concentration of H_2O_2 selectively [111]. Figure 2.11 illustrates the amperometric responses measured at the RGO electrode, the gold/polytoluidine-blue-O film (Au–PTBO) electrode and the graphene/gold/polytoluidine-blue-O films (RGO–Au–PTBO) electrode in a PBS buffer spiked with H_2O_2 stock solution. The result showed that the amperometric response towards H_2O_2 at the RGO–Au–PTBO electrode was five times higher than that of Au–PTBO modified electrode, manifesting enhancement of H_2O_2 reduction by the hybridised graphene-based nanocomposite.

While most of the H_2O_2, sensors reported in the literature are proof-of-concept, Bai et al. reported a real-sample detection of H_2O_2, based on copper sulfide-decorated RGO [112]. The as-fabricated sensor was able to quantify H_2O_2 released from human cervical cancer cells with a recovered ratio of between 96% to 99%, establishing the capability of the graphene-based sensor to operate in a physiological *in vivo* environment.

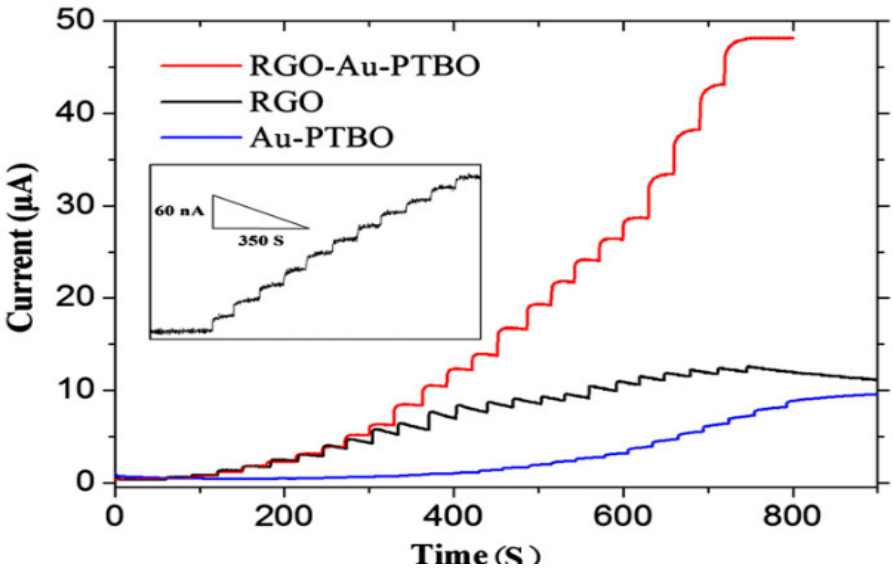


Figure 2.11. Amperometric i–t curves of Au–PTBO (blue), RGO (black), and RGO–Au–PTBO (red) modified electrode in response to H_2O_2 reduction. The affinity of Au-PTBO toward the reduction of H_2O_2 was amplified by the integration of graphene [111].

The simultaneous determination of acetaminophen, ascorbic acid, uric acid and dopamine has been widely reported. While there have been reports stating that the simultaneous determination of uric acid, ascorbic acid, acetaminophen and dopamine is challenging due to their overlapping oxidation peak [113], many research groups have successfully developed graphene and graphene/metal oxide-based sensor to realise simultaneous detection of these compounds. Chang et al. fabricated an electrode enhanced with nanoplatelets of graphene oxide for simultaneous detection of ascorbic acid and uric acid [114]. Linear sweep voltammetry (LSV) was recorded at different electrodes; compared to the overlapped redox peaks of uric acid and ascorbic acid at the bare-electrode, there was a clear separation of about 0.3 V between the peaks at the modified electrode. Fan et al. have also proposed a sensor based on graphene/TiO_2/Nafion-modified electrode for voltammetric detection of acetaminophen in the presence of dopamine and ascorbic acid [115]. As shown in Figure 2.12, acetaminophen exhibited well-defined differential pulse voltammetry (DPV) peak with good separations from ascorbic acid and dopamine, attributed to the presence of TiO_2 nanoparticles that have effectively modified the surface chemistry of graphene and provided an active interface for the simultaneous detection of these compounds.

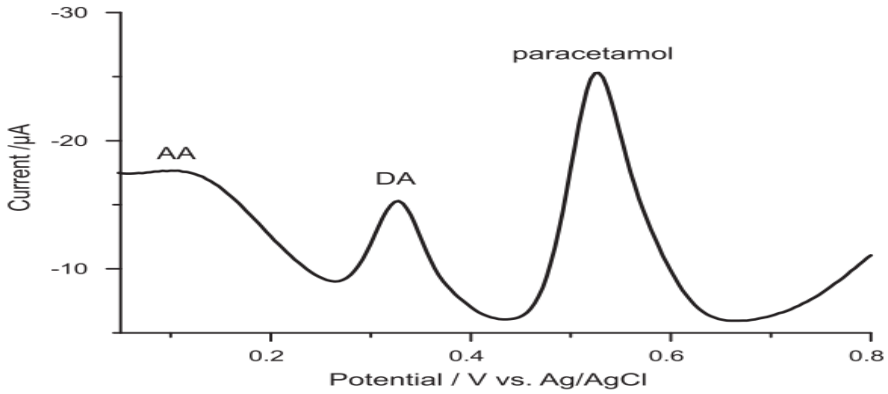


Figure 2.12. DPV peaks recorded at graphene/TiO_2/Nafion-modified electrode for the voltammetric detection of acetaminophen in the presence of dopamine and ascorbic acid. A clear separation of at least 0.2 V was observed between the redox peaks [115].

2.4.2. GRAPHENE-BASED PLATFORMS AS BIOSENSORS

Works reported in the literature showed that graphene-based sensors were highly sensitive to electroactive molecules and were able to provide excellent quantification; nonetheless, the potential of these graphene-based platforms was not limited to the detection of simple redox species. Disease detection was also made feasible with the advancement of graphene-based platforms into biosensors, which is a self-contained integrated device that is capable of providing specific quantitative or identification of biomolecules using a biological recognition element or sometimes known as a bioreceptor. The recognition elements refer to biomolecules capable of recognising and interacting with specific analytes, such as nucleic acid, antibody, antigen and enzyme. The interaction between the bioreceptor with the analyte is transduced into measurable signals for further processing. The main two groups of biosensors are genosensor and immunosensor.

Genosensors, or more commonly known as DNA biosensors exploit the specific binding between complementary single-stranded nucleic acid sequences and have been increasingly employed in various analytical strategies for the detection of genetic and infectious diseases [86]-[88]. DNA sensing enhanced with graphene or graphene/metal oxide composite started with the detection of four nucleotides (guanine, adenine, thymine, cytosine), as demonstrated by Lim et al. and Wang

et al. [119], [120]. It was shown that graphene could significantly enhance the specific surface area and electrical conductivity of the nucleotides sensing platform and lead to amplified oxidation peaks as compared to the bare electrode. Advancing from the proof-of-concept nucleotide detection, single-stranded DNA was immobilised on the surface of graphene materials to detect pathogenic or genetic diseases, in which the hybridisation (double-helix formation) between the single-stranded probe-DNA and its complementary single-stranded target-DNA was detected by voltammetry [121], [122] or impedimentary techniques [123], [124]. These studies collectively emphasised that graphene and graphene composited-based sensors were able to discriminate between single-stranded and double-stranded DNA as well as identify matching and non-matching DNA, enabling the detection of DNA mutation. One of the fundamental concerns of genosensor is the immobilisation of probe-DNA for hybridisation/recognition wherein linker-functionalised graphene and graphene/metal oxide composite have emerged as an excellent solution to achieve specific probe-DNA immobilisation. By means of π-π stacking, Singal et al. non-covalently attached PY biolinker to graphene and immobilised DNA strands to the sensor for the quantitative detection of human cardiac troponin [125]. Similar functionalisation was also demonstrated by Luo et al. that has prepared graphene/1-aminopyrene hybrids for the detection of colitoxin DNA sequence. The π-stacking interaction between graphene and 1-aminopyrene was shown to have effectively immobilised the recognition layer while preserving graphene's inherent properties of high surface area, good electrical conductivity, large surface area and low toxicity [124].

Immunosensors are sensing platforms that depend on the interactions between an antibody and antigen at the electrode interface to form a stable complex. The formation of the immunocomplex would be translated into measurable signals. Thanks to the strong affinity between antibody and antigen, immunosensing presents itself as a specific and sensitive detection scheme. The sensitivity and stability of immunosensors are often enhanced by the association of graphene-based nanostructure [126]. Liu et al. fabricated a sandwich-type electrochemical immunosensor to detect alpha-fetoprotein (AFP) for cancer diagnosis [127], as illustrated in Figure 2.13. The sensor

exploited the high-surface-area graphene sheets as an excellent anchor material that allowed the immobilisation of a large volume of primary antibodies due to host-guest interaction. Under optimised experimental parameters, the sensor exhibited a decent detection limit of 0.16 pg/ml, coupled with a wide working range from 0.5 pg/ml to 10 ng/ml for AFP detection. Incorporation of graphene-based composite into immunosensing was also demonstrated for the detection of carcinoembryonic antigen (CEA), neuron-specific enolase (NSE) and Cytokeratin 19 fragment 21-1 (CYFRA 21-1) [128]–[130].

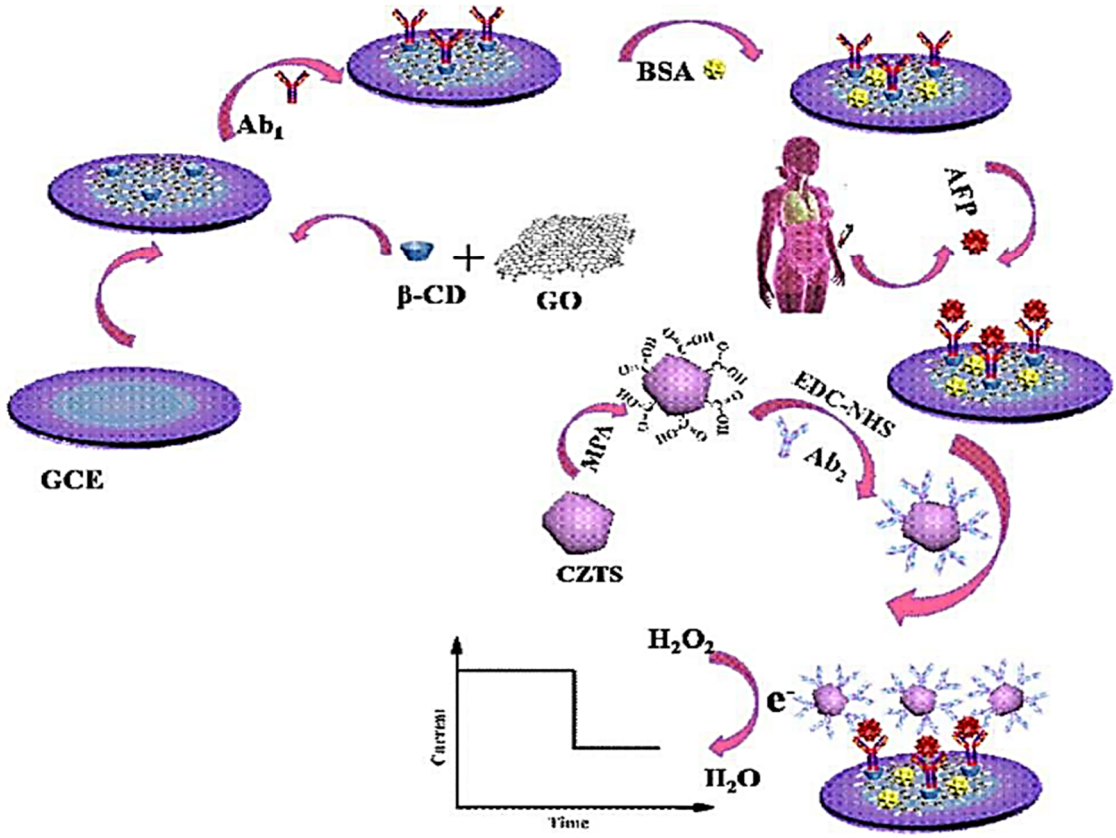


Figure 2.13. Schematic presentation of an immunosensor fabrication. The graphene sheets served as an excellent antibody immobilisation platform [127].

In short, these studies have attributed the enhancement of sensing to the presence of graphene and its composite that presented high surface area, good conductivity, and the ease to be functionalised for bioreceptor immobilisation. A more detailed review of graphene-based biosensors for lung cancer detection will be presented in the following sections.

2.5. BIOMARKERS FOR LUNG CANCER DETECTION

Lung cancer is a prevalent illness accompanied by a high mortality rate of estimated 135,720 deaths, close to 25 % of all cancer deaths in the USA for the year 2020 [1]. Rapid screening offers the opportunity for early detection, which is known to increase the survival rate for cancers of the lung [131]; correspondingly, lung cancer biomarkers serve the need for rapid screening. Biomarkers are biomolecules circulating in the body due to the presence of cancerous tumours, in which levels higher than that of healthy persons led to their diagnostic role as tumour markers. Biomarkers that become more concentrated following the advancement of lung cancer stages serve the purpose of early diagnosis, evaluation of treatment efficiency and prediction of relapse [132], [133]. Biomarkers for lung cancer can be in the form of circulating tumour nucleic acid and tumour cells, immune antigens, antibodies, mRNA and some others [56]. These biomarkers could be derived from the non-invasive source of saliva and exhaled breath, as well as minimally invasive sources such as blood components and bronchial epithelium. Generally, the biomarkers of lung cancer are divided into two categories: genomic biomarkers and proteomic biomarkers [134].

Genomic biomarkers are biomarkers produced due to alterations in the chromosome structures and gene expression that induce lung cancer. These include mutations in the RAS gene, TP53 gene, epidermal growth factor receptor (EGFR) and some other genetic materials that are characterised by altered protein expression, loss of cell cycle control, hyper-proliferation, abnormal gene promoter methylation, and augmented vascular development [135]–[137]. Detecting genomic biomarkers at an early stage is crucial since early-stage cancer started with methylation of promoter sequences in lung tumour suppressor genes; in which these tumour suppressor genes were deactivated or silenced eliciting the progression of the malignant lung condition [136].

Meanwhile, proteomics biomarkers are protein-based biomarkers that are emerging as a more profound tool for diagnostic and therapeutic monitoring of lung cancer. During the abnormal growth and proliferation, tumour cells produce substance/protein as an interaction with the surrounding for invasion and metastasis. These secreted proteins can reach the blood and other

body fluids thus giving them value as a diagnostic biomarker [138]. Protein biomarkers can be a precise representation of the degree of malignancy since expressed proteins are close depictions of cancer stages [139]. Chronic inflammation is a core characteristic of cancers which may induce cytoskeletal reorganisation, a process that moderates cell movement and metastasis; consequently the expression of several cytoskeletal proteins, such as CYFRA 21-1 is altered and such change is proposed as a prospective cancer biomarker marker [139]. Besides, proteins such as NSE and CEA which are usually of low concentration in serum, experience elevation in patients with lung carcinoma; therefore serum CEA and NSE levels higher than that of healthy persons led to their diagnostic role as cancer indicators [140], [141].

In the following, several common genomic and proteomic biomarkers for lung cancer are briefly reviewed to provide an insight into lung cancer detection via biomarkers.

2.5.1 EPIDERMAL GROWTH FACTOR RECEPTOR (EGFR)

The EGFR is a 170 kDa transmembrane protein that binds to specific ligands and phosphorylates several types of tyrosine residues [142], triggering the signalling cascade leading to cell migration, proliferation, adhesion, metastasis, apoptosis, or angiogenesis, all of which are associated with cancer development should EGFR are mutated. A study showed that EGFR mutation was found in 31.6% of all patients with non-small cell lung carcinoma (NSCLC) [143].

Mutation of the EGFR occurs within the tyrosine kinase domain as shown in Figure 2.14. Three major categories of mutant DNA have been discovered: exon-19 mutation within the tyrosine kinase domain of EGFR accounts for about 60% of all mutations; single point replacement (L858R) in exon-21 make-up 25% of all cases; whereas duplications/insertions in exon-20 together with the nucleotide alterations in exons-21, 20 and 18 accounts for the remaining 15% [144], [145]. There are several types of hotspot mutations in exon-19, which are mostly located in the sequence encoding the 746th to the 753rd amino acids, and are primarily deletions and substitutions affecting DNA sequences [146]; such as Δ E746-A750 that involves deletion at nucleotide 2235 -

2249, D761Y that involves the substitution of nucleotide 2281 from guanine (G) to thymine (T), and Δ L747 -E749 that involves deletion at nucleotide 2239-2247 [147]. Meanwhile, about 90% of all exon-20 mutation is a post-C helix insertion of one to four amino acids; infrequently, T790M mutation occurs involving the substitution of threonine (T) with a methionine (M) at position 790 of exon-20.

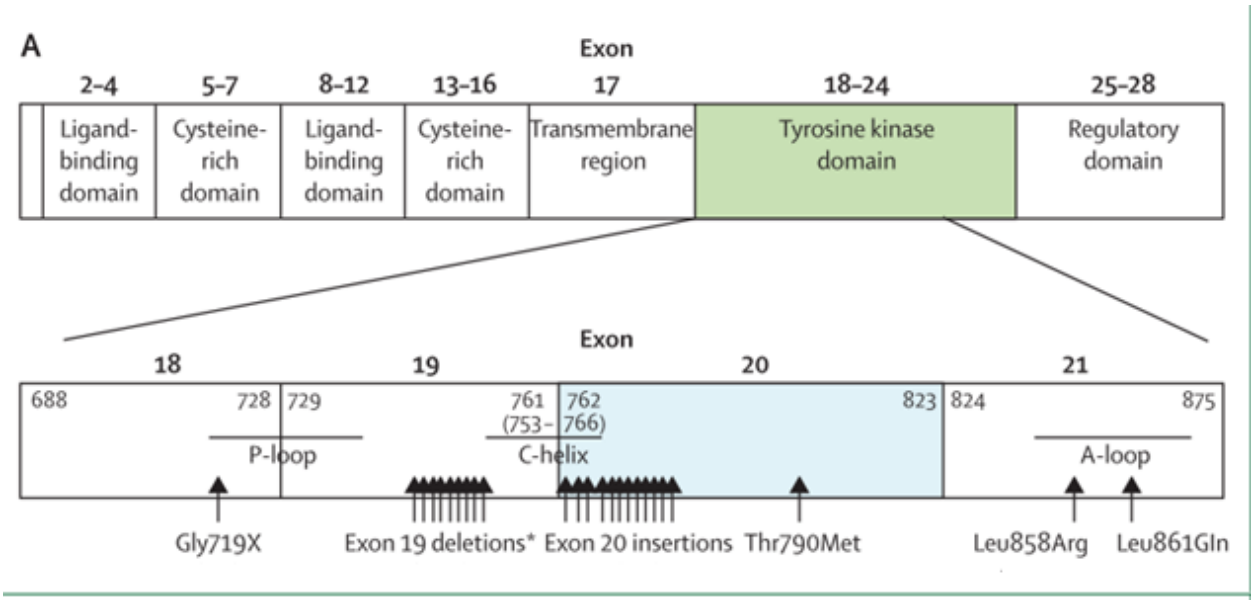


Figure 2.14. Mutation in exon 18,19,20 and 21 within the tyrosine kinase domain of EGFR. Abnormal activity of the EGFR can promote tumour cell proliferation, differentiation and migration [148].

The treatment strategy involving the inhabitation of the tyrosine kinase activity of the EGFR can suppress the development of mutation-induced growth. Nonetheless, Yasuda et al. suggested that tyrosine kinase inhibitors (TKIs) would only be clinically effective for the common L858R and exon-19 mutations, and it is not effective for patients with exon-20 insertions or T790M mutation [144], [148]. Exon-19 deletions, being the most common mutation, is associated with *in vivo* or *in vitro* sensitivity to gefitinib or erlotinib, in which the clinical outcomes of patients treated with these TKIs have been improved as compared to those treated with standard cytotoxic chemotherapy [149]. Given the sensitivity of exon-19 and L858R mutation to TKIs, several bio-sensing works to detect these mutations have been reported. Weng et al. proposed a sandwich-type electrochemical biosensor based on DNA probes to identify six common exon-19 mutations [146]. The results of the work concluded that the optimised biosensors could perform as consistent as

direct sequencing. Liu et al. developed a novel EGFR mutation testing system, which was based on a Mach-Zehnder Interferometer (MZI) sensor and isothermal solid-phase DNA amplification (IDA) to detect the L858R mutation [150]. The results indicated that the MZI-IDA sensor system was versatile where it could detect even a single-base difference in the DNA sequences and identify L858R mutation successfully. Besides, detection of the least common T790M was also reported by Wang et al. who used a detection scheme based on luminescent resonance energy transfer between upconversion nanoparticles (UCNP) and the intercalating dye, SYBR Green I to detect the presence of the target DNA [151]. A detection limit of 0.01 pmole was achieved in this study.

2.5.2 TP53 GENE

The first tumour suppressor gene to be identified, the TP53 gene was discovered in the year 1979. The TP53 tumour suppressor gene is found on chromosome 17 (17p13) and has a critical role in regulating the DNA repair process and cell growth [152]. There are 11 exons spanning in the TP53 gene [153]. TP53 gene encodes the production of p53, a tumour suppressor protein that moderates cell division to be under normal rate. Nonetheless, numerous forms of cellular trauma, for example, DNA impairment triggered by UV exposure, can lead to the mutation of the TP53 genome. The TP53 pathway is altered so that the normal cell-cycle routine is not preserved, leading to the mutation of functioning cells into cancerous cells [153]. Mutated TP53 contributes a major part to the development of malignant epithelial cells in the lung. TP53 gene mutations occur in about half of the NSCLC patients population, in which the suppressor gene function is deactivated by mutations [154]. More than 70% of TP53 gene mutations are of missense effects, as shown in Figure 2.15 (a), in which a single nucleotide was substituted and resulted in a codon that codes for a different protein [155]. As shown in Figure 2.15 (b), the majority of mutations occur between codons 125 and 300. Amongst one-base substitutions, nearly ¼ are C: G > T: A substitutions that occur mainly at three common spots, namely codon-273, codon-248 and codon-175 [155].

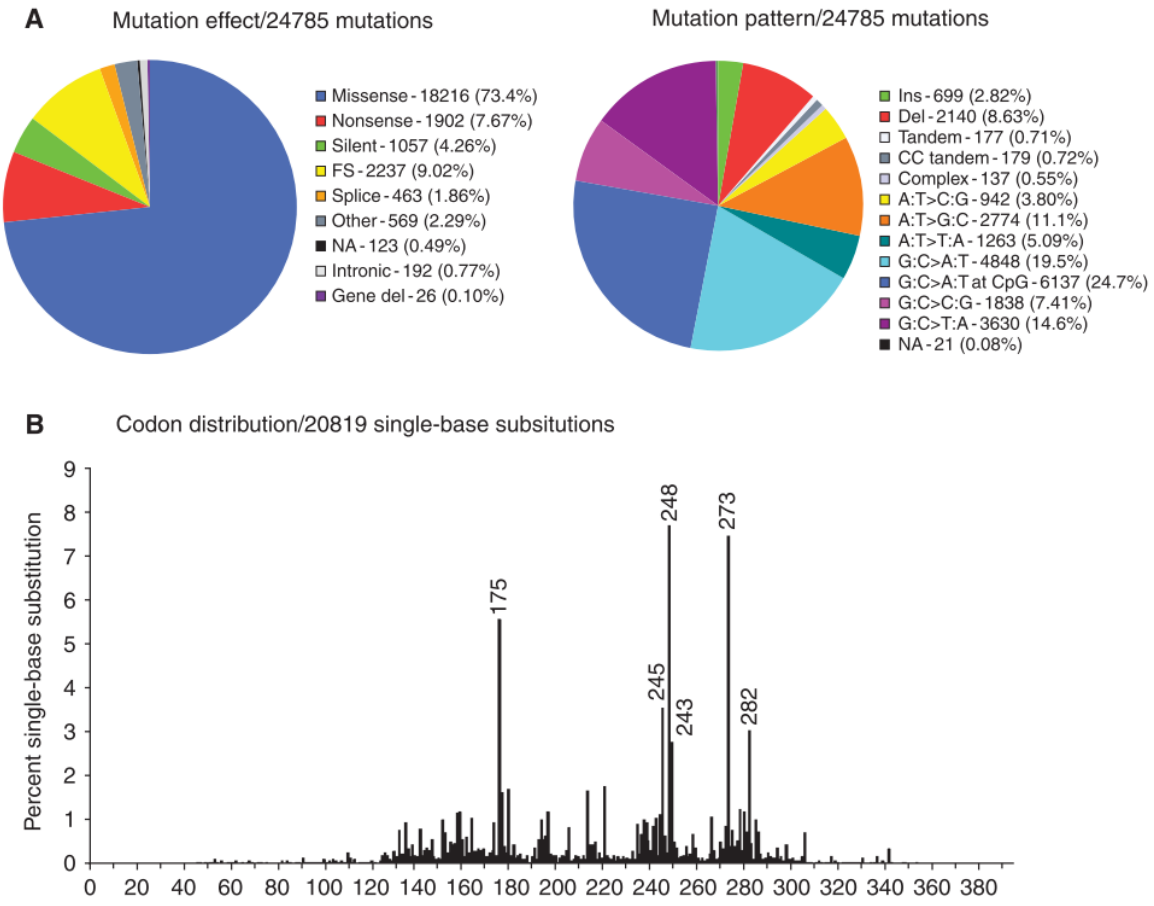


Figure 2.15. (a) Mutation effect and pattern of TP53 gene. (b) percentage of single-base substitution at different codons. Mutant gene resulted in a codon that coded for different proteins [155].

Mutant P53 proteins are often overly-expressed in many lung cancer cases and allegedly stimulate cancer metastasis [156], [157]. The P53 protein level is usually elevated in blood components or urine of lung cancer patients. Therefore, it was observed that sensing works to detect the mutation of the TP53 gene were geared towards the detection of protein P53 instead. The detection of TP53 mutation presents not only diagnostic but also therapeutic values, where numerous approaches have been established to restore regular TP53 roles such as the introduction of p53-reactivating small molecules named PRIMA-1, which offers great potential for the advancement in anticancer drugs [158], [159]. Several detection schemes particularly electrochemical sensing platforms modified with nanomaterials have been proposed for TP53 detection [152], [160]–[162]. Overall, the developed sensors have promising perspectives as a simple, reliable and analytically robust diagnostic tool.

2.5.3 KRAS

RAS is a group of genes that produces signalling proteins that play a key role in signal transduction and regulation of cell proliferation and death. RAS genes carry the information to synthesise proteins such as HRAS, KRAS, and NRAS that can interchangeably bind to small molecules guanosine triphosphate (GTP) and guanosine diphosphate (GDP); active when bound to GDP and inactive when bound to GTP. RAS can bind to various effector proteins, and these RAS-effector connections result in a cascade of downstream signalling events [163], [164]. In healthy cells, RAS signalling is vital for cell growth, differentiation, adhesion and survival. Meanwhile, irregular RAS signalling results in interrupted cellular metabolism, augmented proliferation, diminished apoptosis and greater angiogenesis, all distinctive characteristics of cancer [165]. Though the expression of HRAS and NRAS proteins is extensive, KRAS expression is found in nearly all cell kinds. A study involving the investigation of normal cell function in rats has shown that neither HRAS nor NRAS were compulsory for normal cell control, but KRAS was essential [166]. Activating mutations in the KRAS gene have been the contributing factor to lung cancer. It is described that KRAS gene mutation occurs in approximately 35% of lung cancers [166]. The development of lung cancer caused by constitutive abnormal signalling may happen due to a mutation in the RAS-GTPase domain, which renders it constitutively inactive [167]. In a report, KRAS was shown to be a strong prognostic indicator, in which only 37% of lung cancer patients with KRAS mutation survived the follow-up period of 36 months (median) as compared with 68% of patients with no KRAS mutation that survived through the same observation period [168]. Some inhibitors against RAS effectors such as Raf, MEK1/2, PI3K, and AKT have already entered into clinical trials [163]. Due to the significance of KRAS identification in lung cancer diagnosis and treatment, numerous sensors based on different strategies have been explored for the detection of KRAS mutation, including electrochemiluminescence [169], plasmonic method [170], chronocoulometric [171], electrochemical [172] and some others. In general, the proposed sensors

have demonstrated promising results for the assay of KRAS in whole blood samples and presented a good alternative for the expensive and tedious biopsy of tumour tissue.

2.5.4 NEURON SPECIFIC ENOLASE (NSE)

NSE is a core enzyme of the glycolytic pathway, a series of enzymatic reactions for glycolysis (break down glucose) to generate energy source adenosine triphosphate (ATP) and nicotinamide adenine dinucleotide (NADH). NSE is highly localised in the neurons, due to this organ-specificity, its elevated level in biological fluids such as blood and serum provides clinically valuable data for the diagnosis of NSE-secreting malignancy [141]. Studies have shown that enhanced glycolysis or the Warburg effect is a distinguishing hallmark of cancer progression. Cancer cells utilise glycolysis instead of mitochondrial oxidative phosphorylation for glucose metabolism [173], [174]. Therefore high NSE serum level is meaningfully associated with advanced lung cancer stages [141], [175]. In general, small cell lung cancer (SCLC) becomes suspicious when the level of total NSE in serum is elevated to 5 -15 ng/mL [176]. Serum NSE level has enabled the establishment of a prognostic index based on a simple algorithm, and it is also useful for monitoring of treatment regime, such as the intervention using p19ras that inhibited the enzymatic activity of NSE and thus reduced lung cancer cell proliferation in H1299 cells [177], [178]. Taken together, these results suggest that NSE detection has its predictive and prognostic value; various sensing schemes have been developed for this purpose, including fluoroimmunoassay [179], electrochemical sensor [180], photoelectrochemical assay [181], chemiluminescence method [138] and some others. In general, the sensing platforms proposed were able to detect overexpression of NSE as a serum tumour marker in the diagnosis of lung cancer.

2.5.5 CYTOKERATIN 19 FRAGMENT 21-1 (CYFRA 21-1)

Cytokeratins are structural proteins, in the form of 10 nm - 12 nm long keratin intermediate filaments, as illustrated in Figure 2.16, that form the subunits of epithelial intermediary with the role of supporting the plasma membrane, resisting mechanical stress and regulating metabolic processes [182]. Lung cancer causes degradation of the keratin filaments including phosphorylation and reorganisation of the keratin intermediate filaments thus affecting the bioactivity and solubility of the filaments [183], [184]. Cytokeratins serve as valuable biomarkers for epithelial malignancies should they be released from proliferating or apoptotic cells as soluble fragments and circulate in the blood of lung cancer patients [184], [185]. CYFRA 21-1 is a fragment of cytokeratin 19, which exists mainly in tumour cells of epithelial origin. Cytokeratin 19 fragments are released in the blood because of cell lysis and tumour necrosis [185]. Expression of CYFRA 21-1 is higher in lung cancer patients as compared to non-cancerous epithelial diseases [138]. The serum levels of CYFRA 21-1 are considered to be elevated when they exceeded 2.0 ng/ml [186]. Several studies have attained good sensitivity and specificity when using a CYFRA 21-1 threshold of about 3.5 - 3.6 ng/mL to distinguish lung cancer cases [187], [188]. As shown in Figure 2.17, a study demonstrated that patients with CYFRA 21-1 level higher than 3.6 ng/mL have shorter survival than patients with this marker equal to, or less than the threshold [189]. CYFRA 21-1 have been extensively used as serum tumour markers for monitoring lung cancer progression [190]–[192]. To date, a variety of techniques have been developed to detect and diagnose CYFRA 21-1, from lab-based methods like flow cytometric array [193] and enzyme-linked immunosorbent assay (ELISA) [194] to various biosensing platforms [195]–[197] that offer more rapid detections. Cytokeratin tumour markers can accurately predict disease status and biosensors of such markers offer a simple, non-invasive, cheap, and reliable tool for more efficient cancer management.

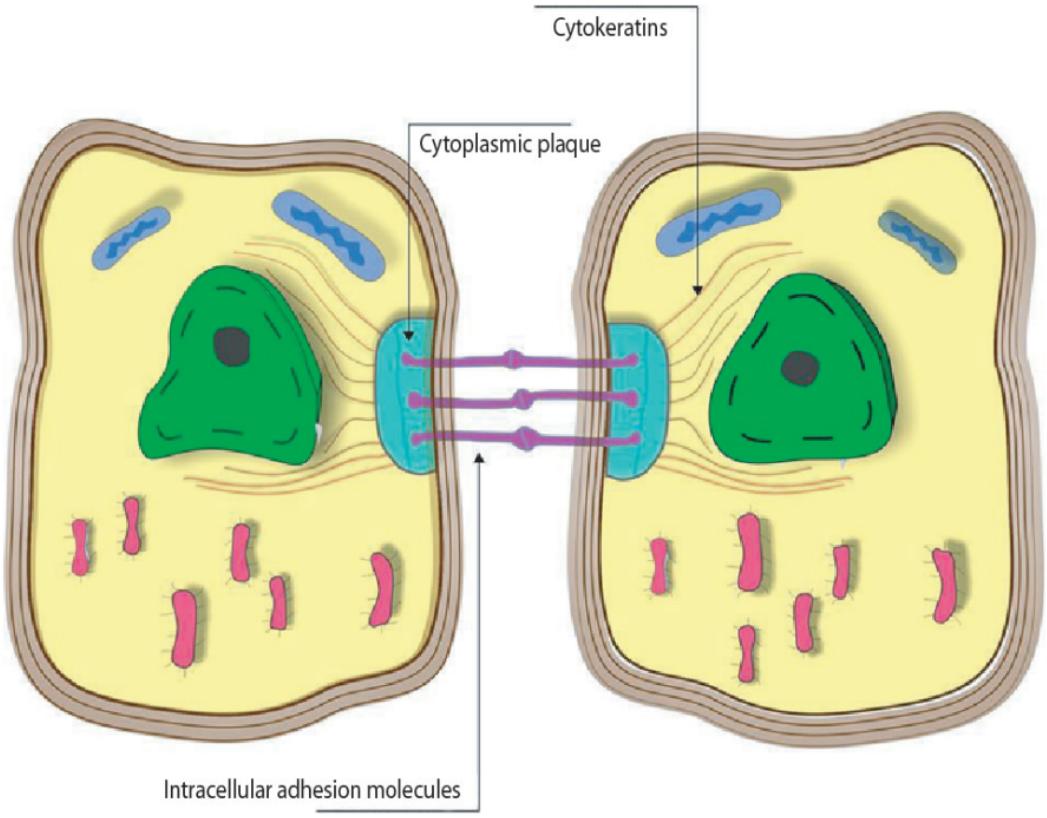


Figure 2.16. Cytokeratins of cells. Cytokeratins are intermediate filaments to support the cells from mechanical stress [198].

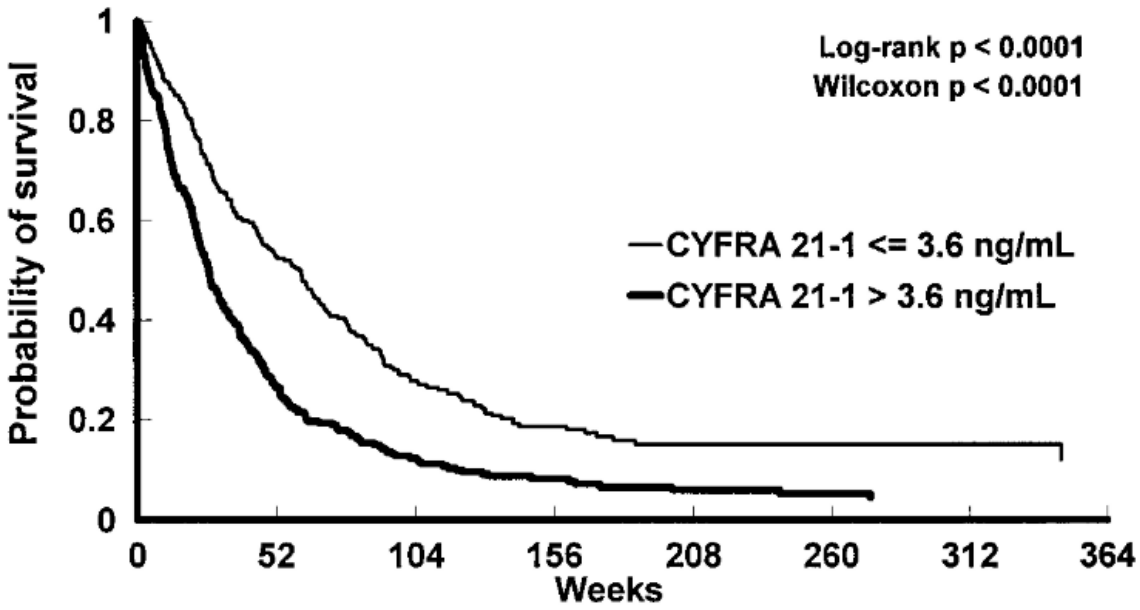


Figure 2.17. Probability of survival for patients with an elevated level of serum CYFRA-21. Lung cancer patients with a serum CYFRA 21-1 level over 3.6 ng/ml was shown to have a shorter survival [189].

2.5.6 CARCINOEMBRYONIC ANTIGEN (CEA)

CEA was first identified in 1965 by Phil Gold and Samuel O. Freedman [199]. Belonging to the immunoglobulin superfamily and as an essential cell adhesion protein, this transmembrane glycoprotein is a complex, highly glycosylated macromolecule with a molecular weight of about 200 kDa [200]. CEA on the surfaces of the normal epithelial cells is expressed in a structured pattern, in which it is organised in a polar manner. In cancer patients, tumour cells have lost their polarity and CEA is distributed around the entire cell surface and eventually gets into the blood. Or in another word, the polar expression of normal cell-surface glycoproteins is not maintained and polarity is lacking in cancerous cells [201]. As well, randomly distributed CEA connect healthy cells and tumour cells, which stimulates metastasis [202]. Elevated levels of serum CEA in lung cancer patients or tumour relapse have been reported in numerous studies [203]–[206]. Studies have also shown that serum CEA level has its prognostic value, in which patient with elevated CEA level has shorter overall survival [186], [207], [208]. An example is shown in Figure 2.18, in which the 5-year survival rate of early-stage patients (tumour of less than 3 cm and confined within the lung) in the normal CEA and elevated CEA groups was 91.6% and 80.1%, respectively [186].

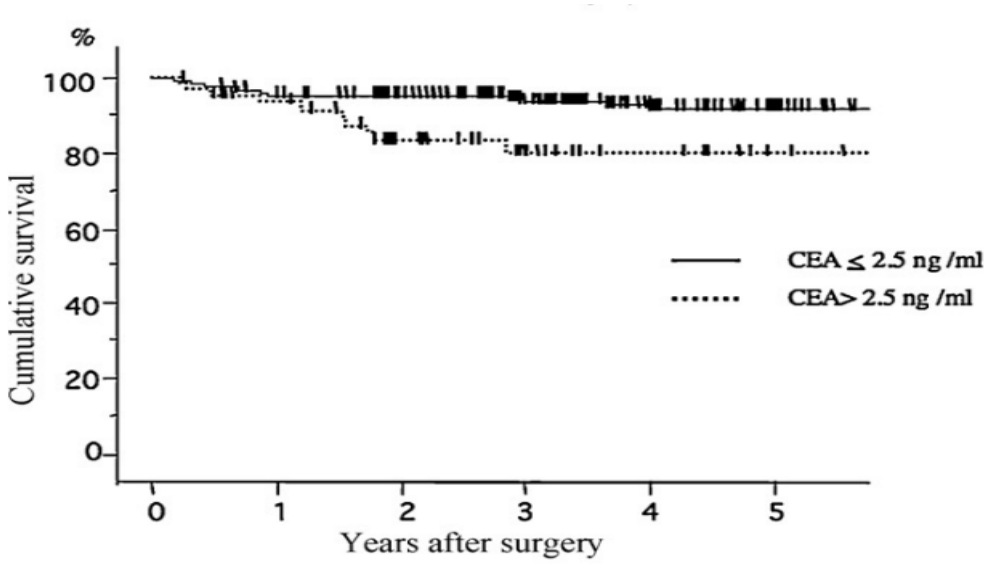


Figure 2.18. The survival rate of early-stage lung cancer patients with elevated CEA levels. The 5-year survival rate of early-stage lung cancer was relatively lower for patients with CEA of more than 2.5 ng/ml [186].

The CEA level of a healthy individual is ideally below 5.0 ng/ml [140], therefore serum CEA levels higher than that of healthy persons led to its diagnostic role as a cancer indicator. A sensitive, accurate and rapid CEA detection method is well desirable for routine lung cancer screening. Although conventional methods such as the ELISA and polymerase chain reaction (PCR) are well developed in CEA diagnosis [209]–[211], they still suffer from some drawbacks such as the need for trained personnel to perform the test [212], lengthy assay duration [213], background noise [214] and potential false readings associated with the complex coloured sample [215]. These drawbacks have encouraged the development of CEA biosensors based on fluorescence [216], chemiluminescence [217], surface plasmon resonance (SPR) [218] and some others. The electrochemical method is one of the most employed due to its short diagnostic time, lower cost and the possibility of miniaturisation [219], [220]. Various electrochemical strategy including potentiometric [221], voltammetric [10], amperometric [222] and impedimetric [223] have been reported. In general, the developed sensors presented a great potential application in promoting CEA protein as a cancer marker in microarray research and clinical diagnoses.

Each lung cancer biomarker is unique; nonetheless elevated level always points to the possibility of lung carcinoma. Table 2.2 summarises the various genomic and proteomics lung cancer biomarkers discussed.

Table 2.2: Common Lung Cancer Biomarkers

Type of Biomarker	Biomarker	Brief description	Reported Works
	EGFR	EGFR is a transmembrane protein that controls the cascade of the signalling process. Mutation of the EGFR occurs within the tyrosine kinase domain from exon-18 to exon-21. Abnormal activity of the EGFR can promote tumour cell proliferation, differentiation and migration. Exon-19 mutations are associated with significant clinical responses to TKIs treatment, hence its detection helps with better treatment planning.	[146] [150] [151]

Genomic	TP53	TP53 gene is a critical player in cell growth control and DNA repair regulation. The TP53 gene encoded the synthesis of p53, a tumour suppressor protein. Mutant p53 proteins are over-expressed in lung cancers, allegedly stimulating cancer metastasis. Detection of TP53 mutation has not only diagnostic value but is also bundled with therapeutically benefits as numerous approaches have been established to restore regular TP53 roles such as the introduction of p53-reactivating small molecules named PRIMA-1, which offers great potential for the advancement in anticancer drugs	[152] [160] [161] [162]
	KRAS	RAS is a group of genes that produces signalling proteins that is essential for signal transduction and cell proliferation/death. RAS genes carry the information to synthesise proteins such as HRAS, KRAS, and NRAS. RAS can bind to various effector proteins to result in a cascade of downstream signalling events. In healthy cells, RAS signalling is vital for cell growth, differentiation, adhesion and survival. Meanwhile, irregular RAS signalling results in interrupted cellular metabolism, augmented proliferation, diminished apoptosis and greater angiogenesis, giving rise to distinctive characteristics of cancer	[169] [170] [171] [172]
	NSE	NSE is a key enzyme of the glycolytic pathway, a series of enzymatic reactions for glycolysis (break down glucose) to generate energy sources. Studies have shown that enhanced glycolysis is a distinguishing hallmark of cancer progression where cancer cells utilise glycolysis instead of mitochondrial oxidative phosphorylation for glucose metabolism. Therefore, a high NSE serum level is associated with advanced lung cancer stages. In general, lung cancer becomes suspicious when the level of total NSE in serum is elevated to 5 -15 ng/mL.	[138] [179] [180] [181]

Proteomics	CYFRA 21-1	CYFRA 21-1 is a fragment of cytokeratin 19, which exists mainly in tumour cells of epithelial origin. Lung cancer causes degradation of the keratin filaments including phosphorylation and reorganisation of the keratin intermediate filaments thus affecting the bioactivity and solubility of the filament. Cytokeratins serve as valuable biomarkers for epithelial malignancies should they be released from proliferating or apoptotic cells as soluble fragments and circulate in the blood of lung cancer patients. Cytokeratin 19 fragments are released in the blood because of cell lysis and tumour necrosis. The serum level of CYFRA 21-1 was considered to be elevated when it exceeded 2.0 ng/ml.	[193] [194] [195] [196]
	CEA	CEA is a transmembrane glycoprotein of about 200 kDa and it is an essential cell adhesion protein. CEA on the surfaces of the normal epithelial cells is expressed in a polar manner. In cancer patients, tumour cells have lost their polarity and CEA is distributed around the entire cell surface and eventually gets into the blood. Elevated levels of serum CEA in lung cancer patients or tumour relapse have been reported in numerous studies. The CEA level of a healthy individual is ideally below 5.0 ng/m, therefore serum CEA levels higher than that of healthy persons led to its diagnostic role as a cancer indicator.	[10] [216] [217] [218] [219] [220] [221] [222] [223]

2.6. TRANSDUCERS FOR BIOSENSOR OF LUNG CANCER BIOMARKER

Over the past few decades, a tremendous amount of development in the area of biosensors has been presented. Biosensors are small devices utilising biochemical molecular recognition mechanisms as the foundation for specific detection. The major processes involved in any biosensor system are target recognition, signal transduction, and instrument output. Upon the interaction of the bio-recognition elements with the target molecules, lung cancer biomarkers discussed in section 2.5 in our context, there is a need for transducers to convert the biological events into a measurable analytical signal. Numerous transducers are utilised in the fabrication of cancer biosensors, namely electrochemical, optical and mass-based transducers. In electrochemical transducers, an electrochemical signal in the form of voltage, current, conductance or impedance is produced from the interaction of the recognition elements and the biomarkers [10], [221]–[223]. Meanwhile, in optical transducers, light properties such as light absorption, fluorescence, luminescence, SPR and other optical phenomena between the recognition element and target molecules are utilised to quantify detection [216]–[218]. On the other hand, a mass-based transducer, as the name implies measures mass-change caused by the interaction between the bio-recognition molecule and the biomarker. These transducers utilise a piezoelectric crystal that oscillates at a particular frequency due to an applied electric field and the oscillation changes according to mass at the crystal [224]. The following section reviews some common transducers employed in the detection of lung cancer biomarkers.

2.6.1. OPTICAL TRANSDUCER

An optical transducer converts physical light into electronic signals that are measurable via techniques such as SPR, fluorescence, chemiluminescence and others. One of the most common optical sensors is based on SPR. In general, SPR biosensors are made up of metal or metal-dielectric surface, gold film for example, that supports surface plasmon. As illustrated in Figure 2.19 (a), polarised light from a laser source is directed through a prism to the surface where surface plasmons (resonating electrons) are generated at a critical angle of the incident light. The light is

absorbed leading to a reduction in the intensity of the reflected light. The critical angle of reflection changes when target molecules bind to the immobilised bio-recognition elements [225]. Figure 2.19 (b) shows the alteration of the critical angle of light from angle a to angle b upon binding of the target molecule. Change in the reflective index (RI) such as resonant wavelength, intensity, or phase gives rise to the quantitative measurement of analyte bindings [226]. An example of SPR-based biosensors was reported by Chiu et al. [227] in which an ultrasensitive SPR immunosensor for detecting CYFRA 21-1 based on cystamine as a linker on graphene oxide sheet was developed, as shown in Figure 2.20. The biosensor demonstrated good stability and sensitivity for CYFRA 21-1 detection in plasma samples.

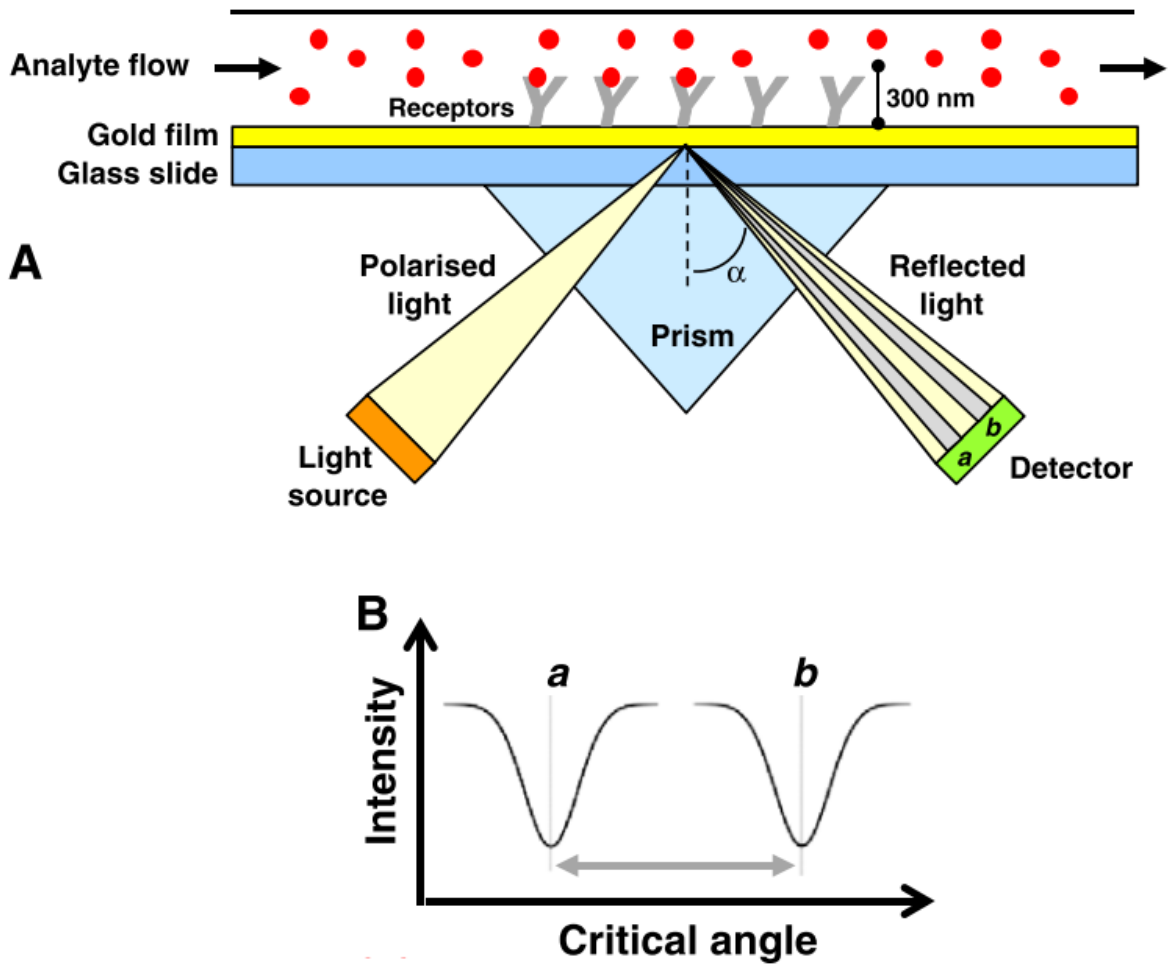


Figure 2.19 (a) A light source is projected through a prism to the plasmon surface where surface plasmons are generated. (b) the shift of critical angle of light from angle a to angle b upon the formation of the receptor-analyte complex. Change in the RI gives rise to the quantitative measurement of the analyte [225].

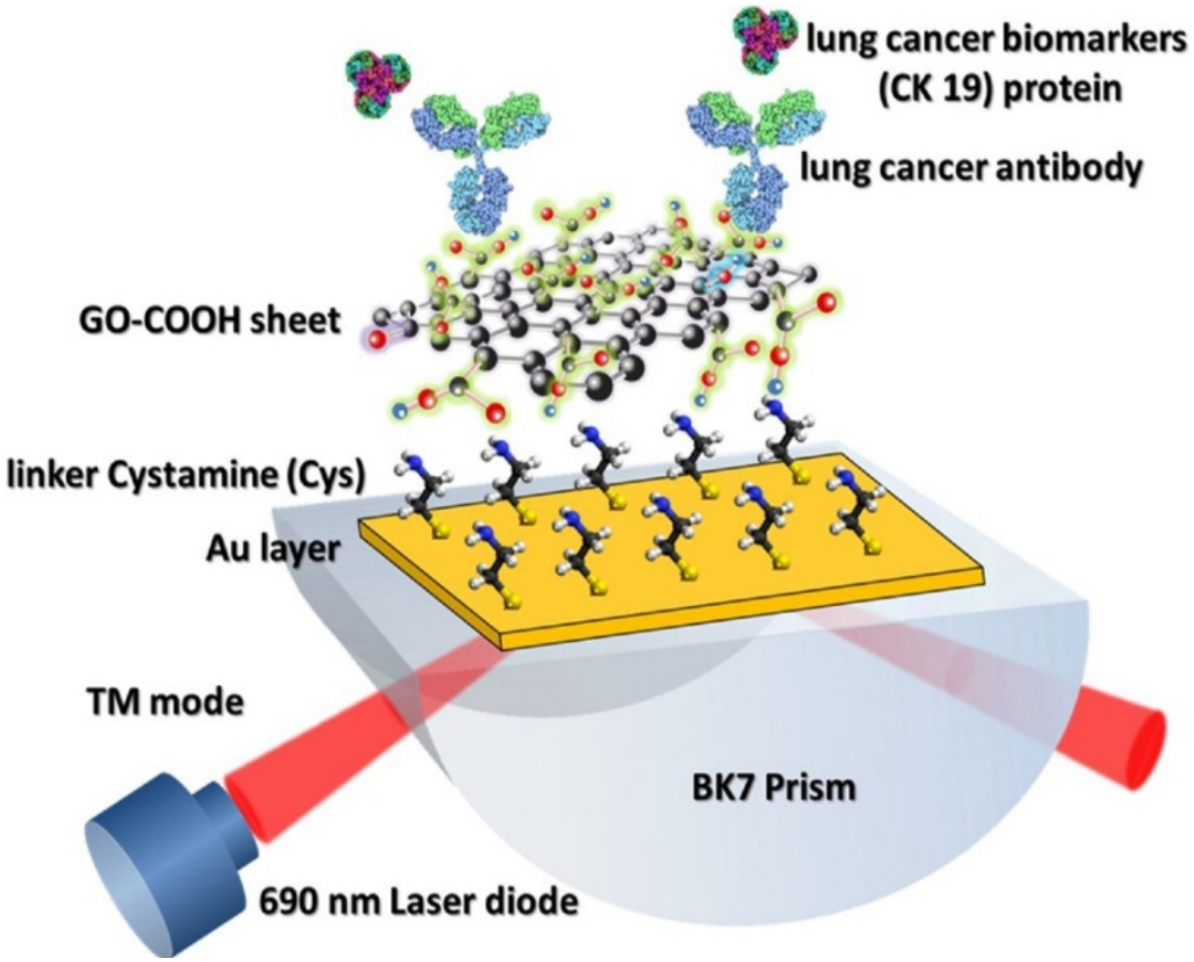


Figure 2.20. An SPR-based biosensor for CYFRA 21-1. The sensor is functionalised with graphene oxide for the detection of CYFRA 21-1 in spiked human serum [227].

Other than the SPR technique, a CEA biosensor was constructed based on fluorescence resonance energy transfer (FRET) between UCNPs and palladium nanoparticles (PdNPs) by Li et al. [216]. FRET is a distance-dependent process by which energy is transferred from an excited donor to an acceptor, the fluorophore. CEA aptamer was conjugated to the UCNPs, and the presence of the aptamer attracted PdNPs to UCNPs. Hence FRET between energy donor (UCNPs) and acceptor (PdNPs) occurred accompanied by fluorescence quenching of UCNPs. When the CEA aptamer was bound with the targeted CEA, the conformational change occurred and the interaction between the CEA aptamer and PdNPs was weakened. Consequently, the gap between UCNPs and PdNPs increased and the FRET process was halted. The fluorescence recovery of UCNPs was observed and the degree of fluorescence recovery was linearly related to the concentration of target CEA. With the detection limit of 0.8 pg/mL, the sensor has performed well in CEA detection,

demonstrating a linear range of 2 pg/mL to 100 pg/mL and 4 pg/mL to 100 pg/mL in aqueous buffer and human sample respectively.

Another common optical transducer technique, chemiluminescence, is the emission of light as the result of binding between bio-recognition elements with target biomarkers labelled with chemiluminescence reagent such as luminol (Lu). A chemiluminescence aptasensor for sensitive detection of CEA based on dual aptamer-conjugates was developed by Han et al. [217]. In this study, aptamers functionalised with luminol, in the presence of CEA, undergo conformational changes to form CEA-aptamer sandwiched structure. H_2O_2 was administrated to trigger chemiluminescence and the intensity of chemiluminescence was obtained using a chemiluminescence analyser. The intensity of chemiluminescence has a strong linear relationship with the concentration of CEA in the solution and a linear range can be obtained from 0.01 ng/mL to 100 ng/ml. In addition, the sensor was challenged to the detection of CEA in a complex matrix. Good recovery ranging from 98.5% to 102.6 % endorsed the practicality of the optical CEA sensor.

Many other optical sensors have been reported in the literature for the detection of lung cancer biomarkers, to name a few, fluorescence technique for NSE [179], photochemical assay for CYFRA 21-1 [228], luminescent resonance energy transfer method for EGFR T790M mutation [151], electrochemiluminescence for KRAS [169] and electrochemiluminescence for TP53 [229]. The performances of these sensors are summarised in table 2.3.

2.6.2. MASS-BASED TRANSDUCER

A mass-based transducer, as the name implies quantifies the mass change resulting from the interaction between the bio-recognition elements and the bonded biomarkers. Generally, a piezo-electric crystal that oscillates at a particular frequency due to an applied electric field is used. The oscillation is dependent on the mass of the crystal [224]. Piezoelectric transducers are typically the classic quartz crystal microbalance (QCM), which is a fine layer of circular quartz plate with metallic electrodes placed on the opposite sides. QCM quantifies mass difference per unit area by examining the frequency variation of the quartz crystal resonator. In biosensors, the bio-recognition element is immobilised on the crystal, upon the interaction of the bio-receptor with targeted biomarkers, the mass of the crystal changes and the oscillation frequency varies accordingly.

A mass-based sensor was developed by Wang et al. for the detection of the TP53 gene mutation [230]. As shown in Figure 2.21, a toehold-functionalised hairpin-structured capture probe was immobilised on the gold electrode surface of QCM. Upon introduction of the target strand which hybridised with the toehold strands, a strand displacement reaction occurred, leading to the unfolding of the hair-pin capture probe. Eventually, the opened capture probe hybridised with the streptavidin-labelled reporter probe and this conformational change resulted in a mass amplification and consequently the QCM signal change. The proposed QCM biosensor exhibited noteworthy specificity between TP53 gene fragments against single-base mutant sequences. The sensor was versatile as the application of the toehold-functionalised QCM technique can be extended to other DNA-based detection. TP53 mutation was also measured by Altintas and Tothill using a mass-based sensor [231]. In this study, the DNA capture strategy was direct. A single-stranded detection probe was immobilised on the crystal. The detector probe was designed to be fully complementary to the mutant single-stranded target DNA; hence, a greater mass response was anticipated from the hybridisation of the detection probe with the mutant-type target than the

wild-type sequence. Complementary detection yielded a correlation coefficient of 0.978. This output represented a very encouraging simple technique for the detection of TP53 mutation.

Chen et al. developed a QCM immunosensor based on murine lewis lung carcinoma cell line (LL/2) [232]. As shown in Figure 2.22, LL/2 cells were initially cultured onto the surface of gold electrode-based quartz crystals. Resonant frequency changed as the result of binding between cell surface antigen with its specific antibody that induced additional mass. A frequency counter was used to measure the frequency difference correlated to the concentration of the LL/2 antibody. The result concluded that the threshold for LL/2 antibodies detection in serum is to have the antibodies present at the nanogram level. The sensor demonstrated a positive detection rate of more than 80% and is a promising platform for early lung cancer detection.

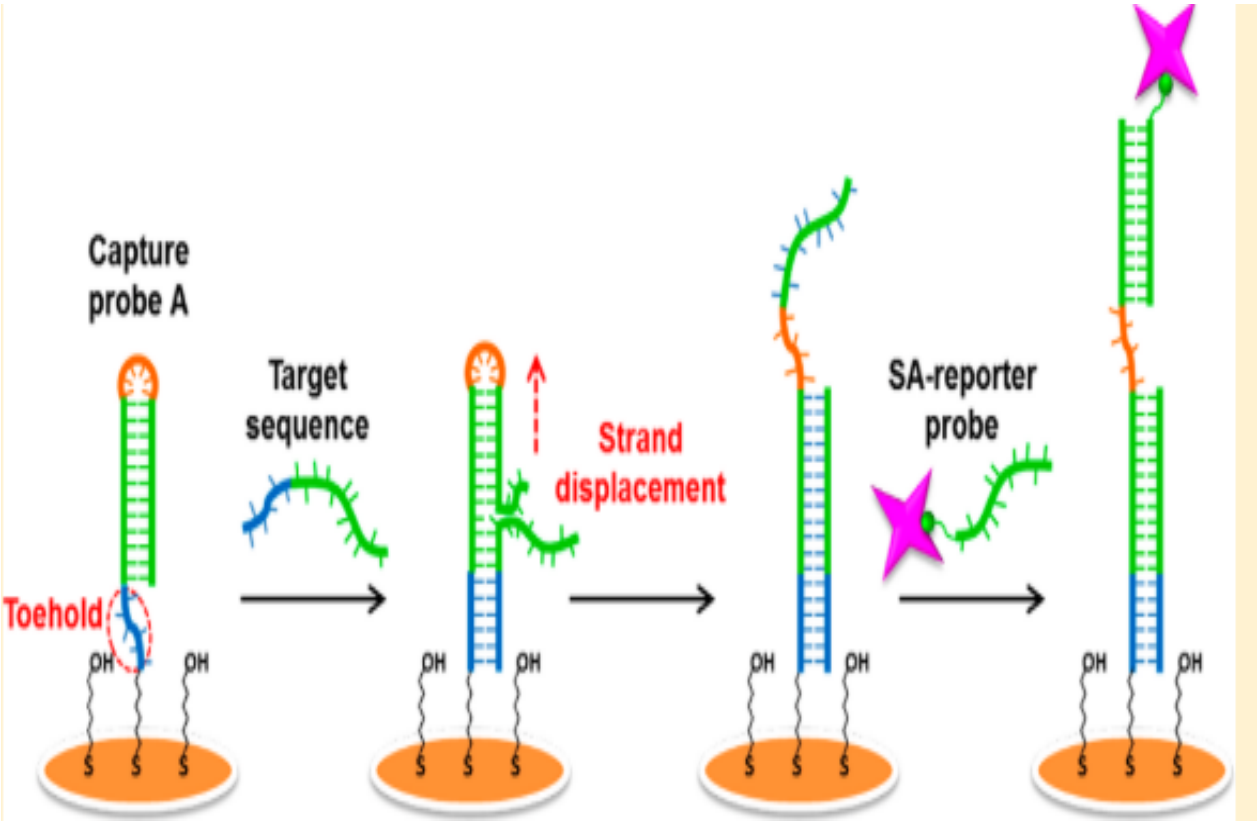


Figure 2.21. A mass-based sensor for TP53 mutation detection. The sensor which is based on strand displacement reaction unfolds the capture probe upon binding with the target sequence (TP53 gene fragment). The unfold probe hybridised with the reporter probe to induce the mass change that is proportional to the concentration of TP53 gene fragments [230].

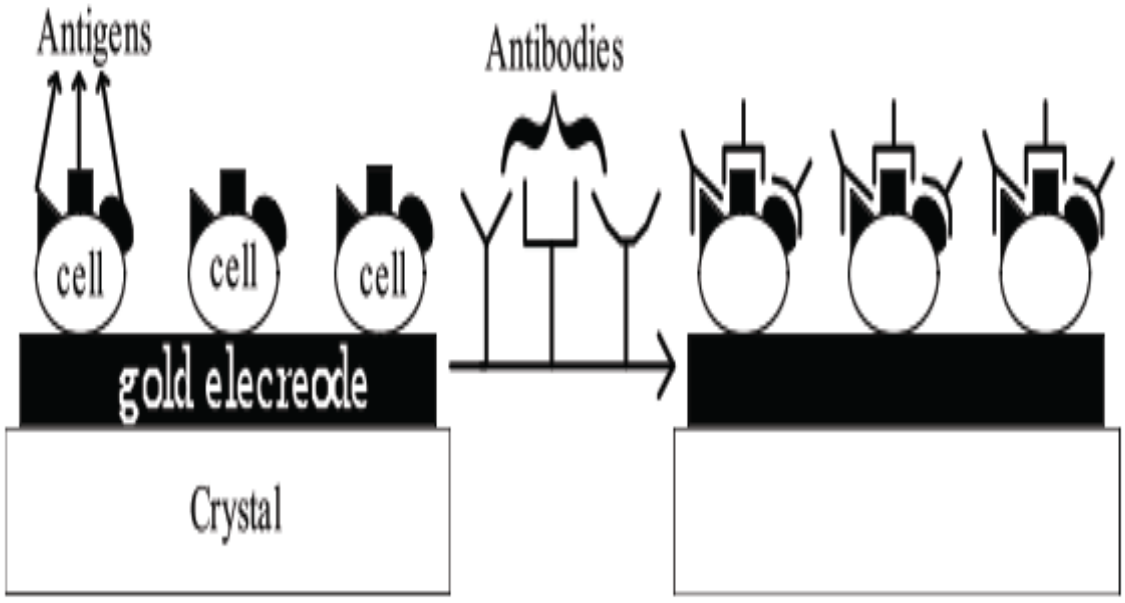


Figure 2.22. A mass-based immunosensor. The resonant frequency of the sensor changed due to the additional mass resulting from the binding between antigen on the LL/2 cell surface with its specific antibody [232].

A microfluidic detection system based on QCM was developed to detect lung cancer cells A549 [233]. The mass-based sensor was modified by suspended superparamagnetic micro-beads which were functionalised with binding protein, the wheat germ agglutinin. Human lung carcinoma cell line, A549 cells were later introduced to the sensor and trapped by the binding protein resulting in an increased mass which was correlated to the alteration in the resonant frequency. The author inferred that the simplicity, low production cost and high efficiency of the sensor would be useful for future point-of-care applications.

Some other mass-based sensors such as the one developed for the detection of EGFR mutation [234] and CEA expression [235] have also been reported. Performances of these sensing platforms are summarised in table 2.3.

2.6.3. ELECTROCHEMICAL TRANSDUCER

In an electrochemical sensor, the interactions between the bio-recognition element and the biomarker induce changes in terms of electron transfer rate, surface conductivity, impedance, the potential of redox reaction and some others [236]. For instance, the alteration in the electron transfer rate influences the produced current output; while the change in the surface conductivity leads to shifting of impedance; regardless of which parameter is employed by the sensor, the extent of the generated electrochemical signal is proportional to the biomarker concentration.

In a study to detect lung cancer via CYFRA 21-1 biomarker, a glassy carbon electrode (GCE) was modified by 3D graphene decorated with gold to improve the conductivity of the platform [195]. The anti-CYFRA 21-1 was immobilised on the modified GCE through the cross-linking of anti-CYFRA 21-1 with chitosan and glutaraldehyde. The DPV peak current was used to quantify the specific binding between anti-CYFRA 21-1 and CYFRA 21-1. Under optimised conditions, the fabricated sensor demonstrated a wide linear range of 0.25 ng/ml to 800 ng/mL and a superior detection limit of 100 pg/ml (S/N = 3) for CYFRA 21-1 detection. The detection employed in the study is a label-free technique where the analytical signal was given directly by the current change caused by the binding of the bio-recognition element and the biomarker. The formation of the anti-CYFRA 21-1 and CYFRA 21-1 altered the electrical properties of the biosensor surface where the electron transfer rate at the interface of the biosensor was reduced according to the concentration of the CYFRA 21-1 biomarker.

Using a similar label-free technique, Butmee et al. developed a CEA electrochemical sensor based on SPCE enhanced with MnO_2-functionalised graphene [10]. CEA antibodies were attached to gold nanoparticles and core-shell iron (II, III) oxide (Fe_3O_4), and subsequently immobilised on the magnet-coupled electrode. The modification scheme of the sensor is shown in Figure 2.23.

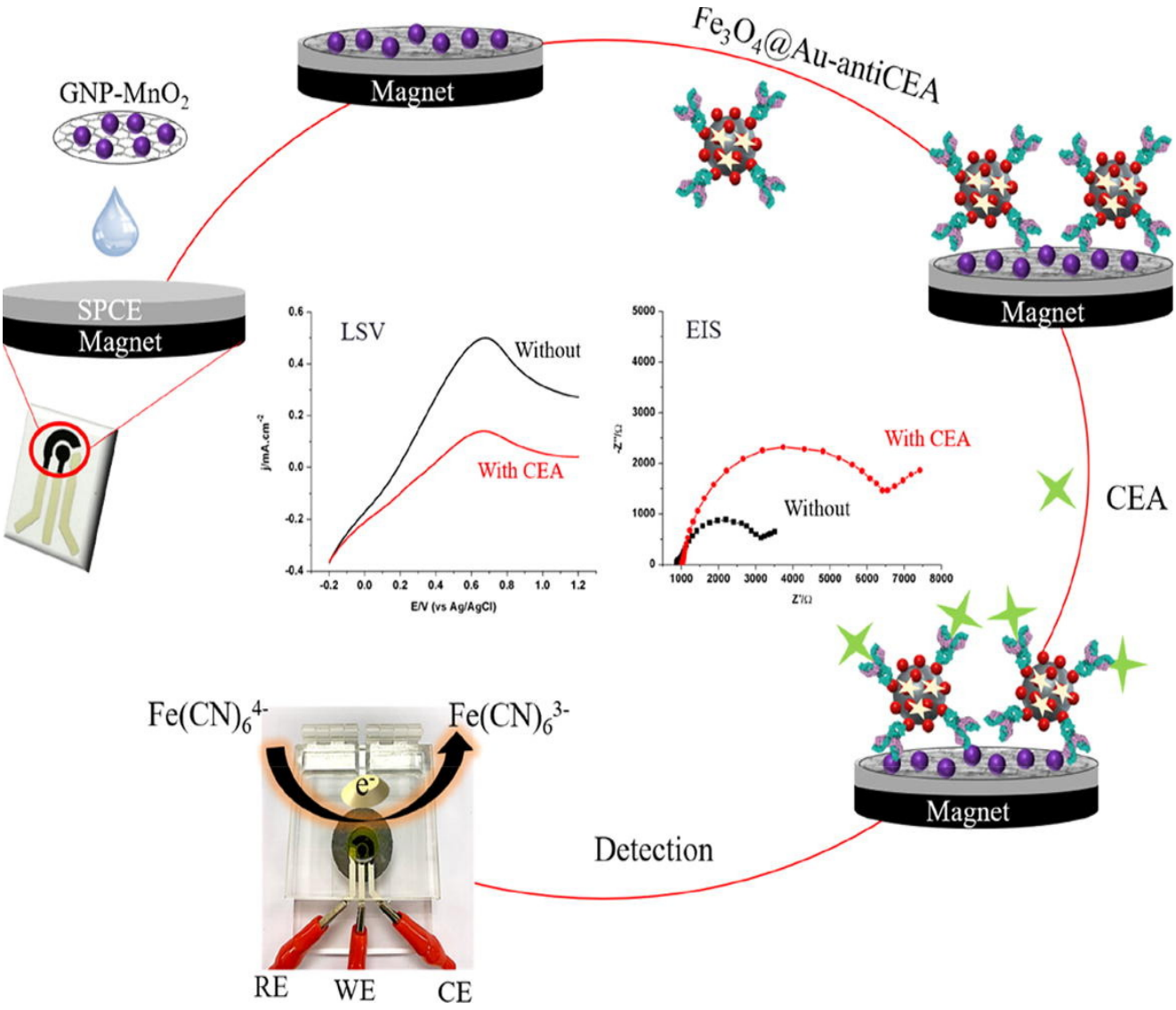


Figure 2.23. An electrochemical sensor for CEA detection. The hybridisation of CEA antibody with CEA resulted in an insulative immunocomplex that reduced the electron transfer [10].

The analytical performance of the sensor was evaluated by LSV and electrochemical impedance spectroscopy (EIS). Insulation of the antibody-antigen complex hindered the electron transfer of the redox species at the electrode surface. Therefore, hybridisation of CEA and CEA antibodies increased the surface impedance, resulting in lower signal response for LSV; and higher signal response for EIS. Under optimised conditions, the sensor could detect CEA within the range of 0.001 ng/ml to 100 ng/mL, and the detection limits were 0.10 pg/mL (LSV) and 0.30 pg/mL (EIS). Other label-free electrochemical sensors such as an amperometric electrochemical sensor for

Exon-21 mutation [237], a voltammetric sensor for KRAS mutation [172] and NSE detection [129] have also been reported.

Label-free electrochemical detections of dual biomarkers have been gaining more attention. Thus, innovation was demonstrated by Taheri et al. who have developed a label-free electrochemical sensor using molecularly imprinted polymer electrodes for the detection of CEA and AFP [238]. Charge transfer resistance (Rct) from EIS was employed as the analytical signal. To measure AFP concentration, CEA-specific sites on the electrode were saturated with CEA until there was no longer a change in the Rct. The CEA-saturated electrode was subsequently exposed to AFP where the concentration of AFP caused a linear increment of the Rct. Similarly, for the detection of CEA, the AFP-specific sites on the electrode were pre-saturated with AFP before the electrode was incubated with CEA which also demonstrated a linear relationship with Rct change. The sensor has demonstrated a satisfactory working range for both AFP (10 pg/ml – 10 ng/ml) and CEA (5 pg/ml – 10 ng/ml).

Other than label-free electrochemical sensors, another common detection scheme is the sandwiched-type detection which usually uses a layered structure: (a) bio-recognition element (b) target and (c) labelled reporting probe. Figure 2.24 illustrates the basic mechanism of a sandwiched assay. Upon interaction of the bio-recognition element and the biomarker, an additional labelled reporting probe is added and attached to the biomarker. The catalytic response is initiated by the addition of an enzymatic substrate and the generated signal is associated with the quantity of the biomarker.

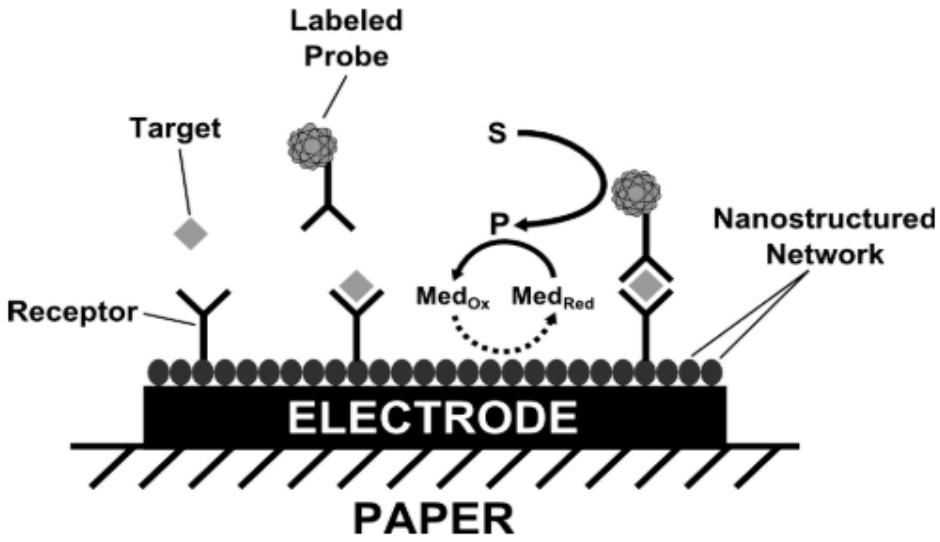


Figure 2.24. A sandwiched assay. A labelled reporting probe is introduced to the sensor after the interaction of the bio-receptor and the target. The catalytic response is initiated by the addition of an enzymatic substrate and the generated signal is associated with the quantity of the target [239].

A sandwich-type electrochemical immunosensor for the detection of p53 protein based on streptavidin-biotin bioconjugate was proposed by Afsharan et al. [162]. The electrode was first functionalised with thiol-modified graphene oxide and streptavidin-modified gold nanoparticles. Biotinylated p53-antibodies were subsequently introduced and immobilised onto the electrode surface through streptavidin-biotin interaction. Upon the hybridisation of p53-antibodies and p53 proteins, secondary p53-antibodies labelled with horseradish peroxidase (HRP) were introduced and these secondary antibodies with bind to the p53 immunocomplex, forming a sandwich structure as shown in Figure 2.25. The reaction was performed in PBS buffer containing thionine and H_2O_2, therefore, the conjugated HRP was able to reduce thionine in the presence of catalyse H_2O_2. The high concentration of p53 protein led to compact loading of the HRP-labelled secondary antibody which consequently amplified the reduction of thionine and resulted in a higher electrochemical peak current. The reduction of thionine in the presence of HRP labelled biosensor and H_2O_2 is shown in equations 2.3 to 2.5. The output current of the immunosensor was proportional to the p53 concentration from 0.2 pM to 2 pM and 2 pM to 200 pM. The limit of detection (LOD) was 30 fM.

$$HRP\ (red) + H_2O_2 \rightarrow HRP\ (ox) + H_2O \quad \text{(Eq 2.3)}$$

$$thionine\ (red) + HRP\ (ox) \rightarrow HRP\ (red) + thionine\ (ox) \quad \text{(Eq 2.4)}$$

$$thionine\ (ox) + 2e^- \rightarrow thionine\ (red) \quad \text{(Eq 2.5)}$$

More recently, Lu et al. have developed a sandwich-type electrochemical sensor for the detection of CYFRA 21-1 using ring-opening polymerization as the amplification strategy [240]. The anti-CYFRA 21-1 probe was immobilised on the electrode by amide bonding; the probe captured CYFRA-21 specifically. The sandwich structure was formed when the detection antibody attached to the CYFRA-21 that has been captured. The detection continued with the trigger of the ring-opening polymerization process by the amino group on the detection antibody. Through the ring-opening polymerization reaction where N-carboxyanhydride/Ferrocene acted as the monomer, a large number of electroactive polymer chains can be attached to each detected CYFRA 21-1, thus amplifying the oxidation signal of the sensor. The sensor exhibited an excellent detection limit of 0.009 pg/ml.

The sandwiched assay was also employed to detect CEA [241], CYFRA 21-1 [130] and NSE [242]. In general, satisfactory results are obtained for the determination of biomarkers in both the buffer and real clinical serum samples, indicating the potential of the electrochemical sensors to be applied in clinical analysis.

A novel electrochemical sensing method based on the change in the ratio of two different redox probes was also recently proposed. Yang et al. have synthesised a sensor for the detection of CEA based on 2D material MXene that has been functionalised with redox probes $[Ru(NH3)6]^{3+}$ [243]. MXene is a type of material that consists of few-atoms-thick layers of transition metal carbides, nitrides, or carbonitrides. Double-stranded DNA with one of its strands tagged with ferrocene was immobilised on the sensor. In the presence of CEA, CEA attached to the ferrocene-tagged sequence and left the electrode surface, or in other words, the detection of CEA reduced the amount of ferrocene on the electrode. The electrochemical signal of ferrocene decreased proportionally to

the amount of detected CEA; meanwhile, the electrochemical signal from $[Ru(NH3)6]^{3+}$ remained unchanged as this redox probe was functionalised on the material and experienced no change after the CEA detection. The ratio of the electrochemical signal from ferrocene and $[Ru(NH3)6]^{3+}$ was associated with the concentration of detected CEA. The sensor was able to quantify CEA within 1 pg/ml to 1 µg/ml, a working range that is suitable for the physiological concentration of CEA in serum.

In short, this section has discussed numerous transducers that have been implemented for the detection of lung cancer biomarkers. Each transducer is unique and is selected to suit its intended applications. Table 2.3 summarises the performance of various transducers mentioned.

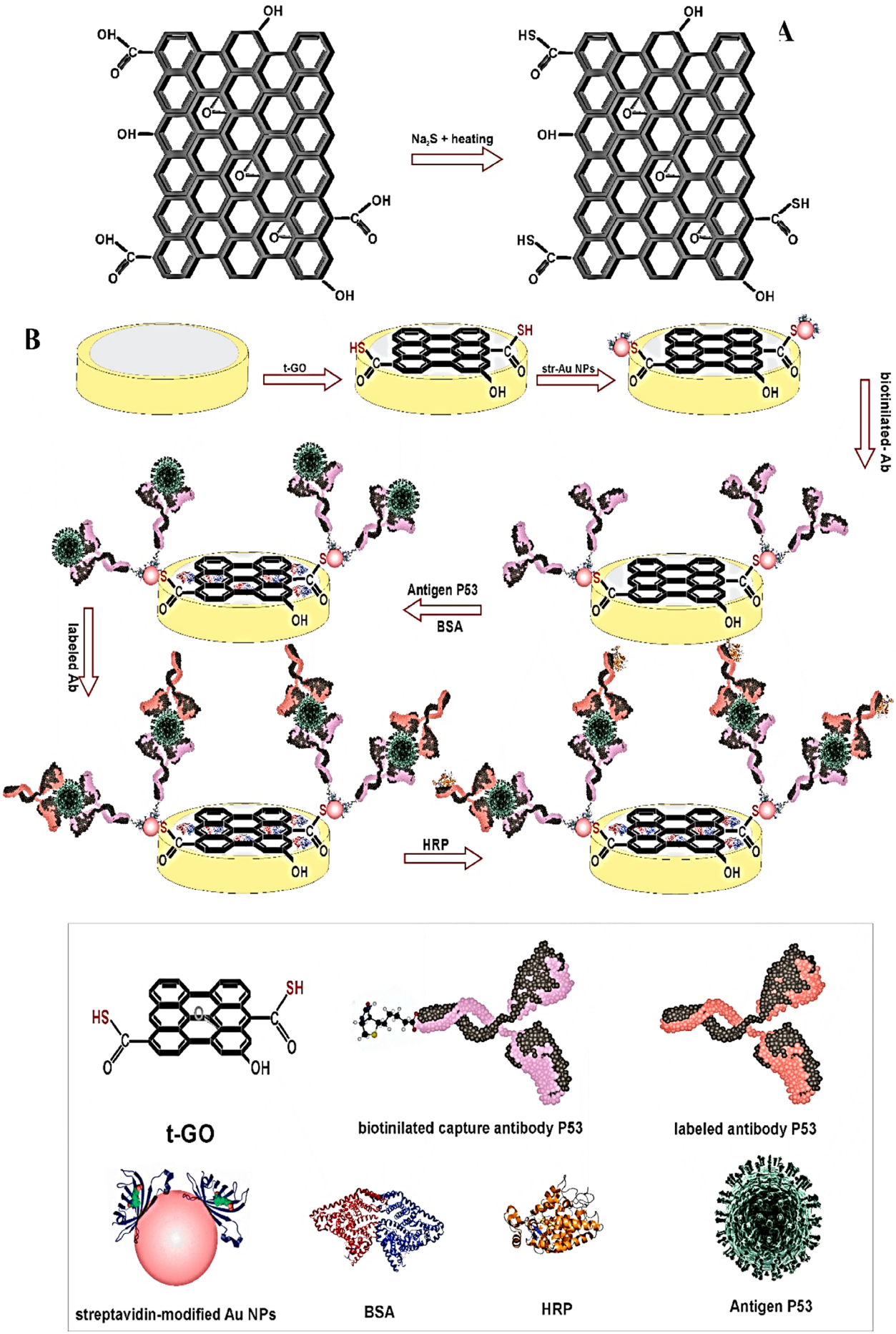


Figure 2.25. Modification scheme of a P53 sensor. The analytical signal was given by the reduction of thionine [162].

Table 2.3 Various Transducers for the Detection of Lung Cancer Biomarkers

Transducer	Biomarker	Linear Range	LOD	Ref
Optical	CYFRA 21-1	0.001 pg/ml – 100 pg/ml	0.001 pg/ml	[227]
	CYFRA 21-1	10 pg/ml – 100 ng/ml	2.5 pg/ml	[228]
	CEA	2 pg/mL to 100 pg/mL	0.8 pg/mL	[216]
	CEA	0.01 ng/ml –100 ng/mL	0.0015 ng/mL	[217]
	KRAS	0.001 pM–2500 pM	0.13 fM	[169]
	NSE	3.9 ng/ml -62.5 ng/ml	370 pg/mL	[179]
	EGFR	0.01 pM – 2 pM	0.01 pM	[151]
	TP53	1 pg/ml – 1 ng/ml	0.5 pg/ml	[229]
Mass-based	TP53	0.5 nM−20 nM	0.3 nM	[230]
	TP53	0.03 µM –2 µM	NA	[231]
	A549 lung cancer cells	NA (indicative sensor)	NA	[233]
		Remark: Cancer detection was given by 90.6 ng of accumulated cancer cell		
	EGFR	0.01 µg/mL –10 µg/mL	10 ng/ml	[234]
	CEA	66.7 ng/ml –466.7 ng/mL	66.7 ng/ml	[235]
Electrochemical	CYFRA 21-1	0.25–800 ng mL	100 pg/ml	[195]
	CYFRA 21-1	0.1 ng/ml - 150 ng/ml	43 pg/ml	[130]
	CYFRA 21-1	1 pg/ml – 1 µg/ml	0.009 pg/ml	[240]
	CEA	0.001 ng/ml-100 ng/mL	0.1 pg/ml (LSV) 0.3 pg/ml (EIS)	[10]
	CEA	0.001 ng/ml–80 ng/mL	0.3 pg/ml	[241]
	CEA	1 pg/ml - 1 µg/mL	0.62 pg/ml	[243]
	CEA	5 pg/ml – 10 ng/ml	1.6 pg/ml	[238]
	NSE	0.5 pg/mL-10.0 ng/ml	0.1 pg/ml	[129]
	NSE	0.02 pg/mL to 35 ng/mL	0.008 pg/mL	[242]
	EGFR	0.1 µM to 3 µM	120 nM	[237]
	KRAS	0.5 fM to 50 nM	0.5 fM	[172]
	P53	0.2 pM -2 pM 2pM- 200 pM	30 fM	[162]

2.7. LUNG CANCER DETECTION WITH ELECTROCHEMICAL BIOSENSORS

Out of the several transducers discussed in section 2.6, electrochemical platforms have conventionally received a greater share of attention in biosensor innovation [244]. Electrochemical platforms are advantageous as they are based on a well-established redox mechanism to turn biological recognition events into useful electrical signals. For instance, amperometric biosensors function by applying a fixed potential, observing the current from the reduction or oxidation of electroactive analytes and associating the signal to the recognition events. Such working principles are simple and well-established, rendering the electrochemical method a favourable transducer.

In addition, electrochemical platforms allow the easy incorporation of nanomaterial into the sensing protocol [31]. Since electron transfers are usually detected only close to the electrode surface, the electrode material and dimension, as well as surface modification, could be manipulated to acquire desired sensor performances. Therefore, the ease to modify the electrodes, especially with nanomaterials has further boosted the attractiveness of electrochemical sensors.

The inherent feasibility for miniaturisation and portability of electrochemical platforms permit them to rival the other transducers. Indeed, the easy-to-use glucose sensor, based on screen-printed electrodes attached to a portable amperometric tester has dominated the current point-of-care market for decades [245]. While cancer-related detection is more complicated than the quantification of glucose, portable and smart-phone based electrochemical biosensors have recently demonstrated encouraging potential for detecting cancer biomarkers and DNA mutations [246], [247]. The favourable potential and the great room for improvement contribute to the widespread research interest in electrochemical sensors.

As discussed earlier, graphene is employed not only in its pristine form but also as a nanocomposite with one or two other materials for synergistic effects. Graphene-based electrochemical sensor, thanks to its excellent electrocatalytic ability, high electron transfer, and large surface area [248] has joined the evolutionary shift of lung cancer diagnosis that sees the emergence of biomarkers detection as a part of health routine screening.

Broadly categorised into graphene-enhanced sensors and graphene composite-enhanced sensors, the following section presents the development of electrochemical biosensors based on these nanomaterials for the detection of lung cancer biomarkers.

2.7.1. GRAPHENE-BASED ELECTROCHEMICAL SENSORS FOR LUNG CANCER BIOMARKERS

The most straightforward enhancement of the sensing platform is that modified with graphene or graphene oxide, such a modification was reported by Jin et al. who have fabricated a sensitive electrochemical sensor for rapid CEA detection using a graphene electrode [249]. Graphene sheets were synthesised via the CVD method and magnetic beads (Mb) conjugated with the capture antibody (CAb) were linked to the graphene sheets through the magnetic field to yield graphene/Mb-CAb electrode. The sensing electrode was able to form an immuno-complex with CEA upon detection, which was subsequently amplified using the conjugation of the detection antibody (DAb), HRP and gold nanoparticles (AuNP) that resulted in the sandwich structure of graphene/Mb-CAb/CEA/DAb-HRP-AuNP. As depicted in Figure 2.26, the role of the nanomaterial was to accelerate the electron transport between the electrode and H_2O_2 to give the highest response among all tested electrodes.

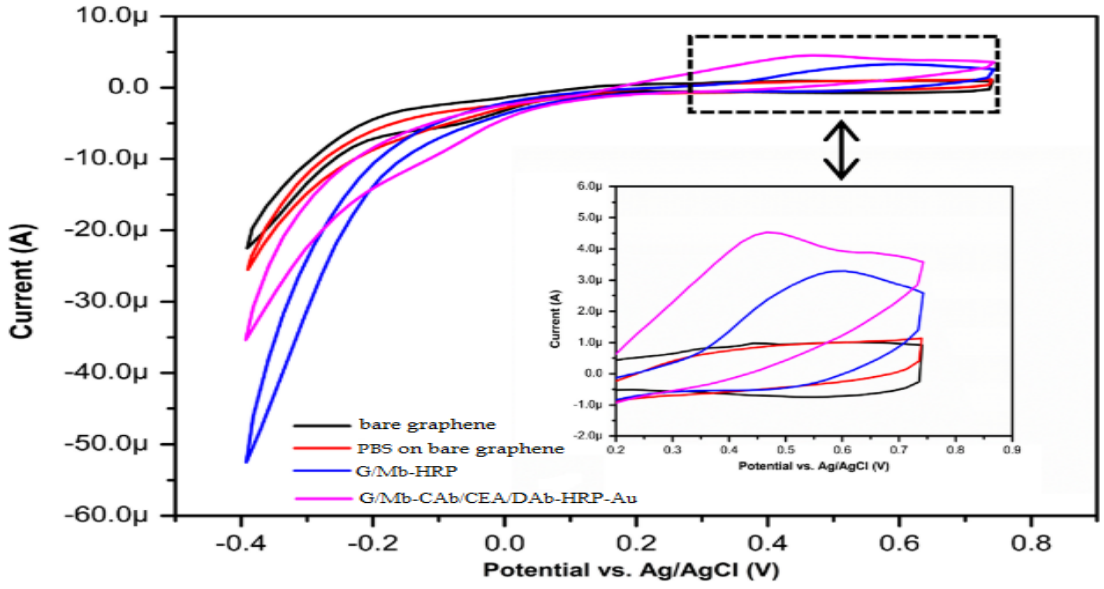


Figure 2.26. Detection of H_2O_2 on various electrodes. The highest oxidation peak current was observed for electrodes with the sandwich structure of G/Mb-CAb/CEA/DAb-HRP-AuNP, endorsing its effectiveness [249].

Innovation with the use of graphene was demonstrated by Fang et al. for NSE detection in which graphene oxide was treated with starch at high temperature and pressure to produce a porous 3D graphene structure for antibody immobilisation [242]. The 3D graphene electrode has not only accelerated the electron transfer rate but also increased the number of capture proteins. NSE detection was achieved via a sandwiched-type assay, as shown in Figure 2.27. Amplified signals were generated by electrodes modified with the 3D graphene-starch as compared to that from electrodes without the functionalisation. The enhancement was contributed by the porous structural design, the electrochemical stability and the high electron transfer of the 3D graphene-starch. The sensor demonstrated a linear range of 0.02 pg/mL to 35 ng/mL with a LOD of 0.008 pg/mL for NSE detection; a comparison made to the ELISA method yielded satisfactory agreement which endorsed the feasibility of the biosensor for clinical routines.

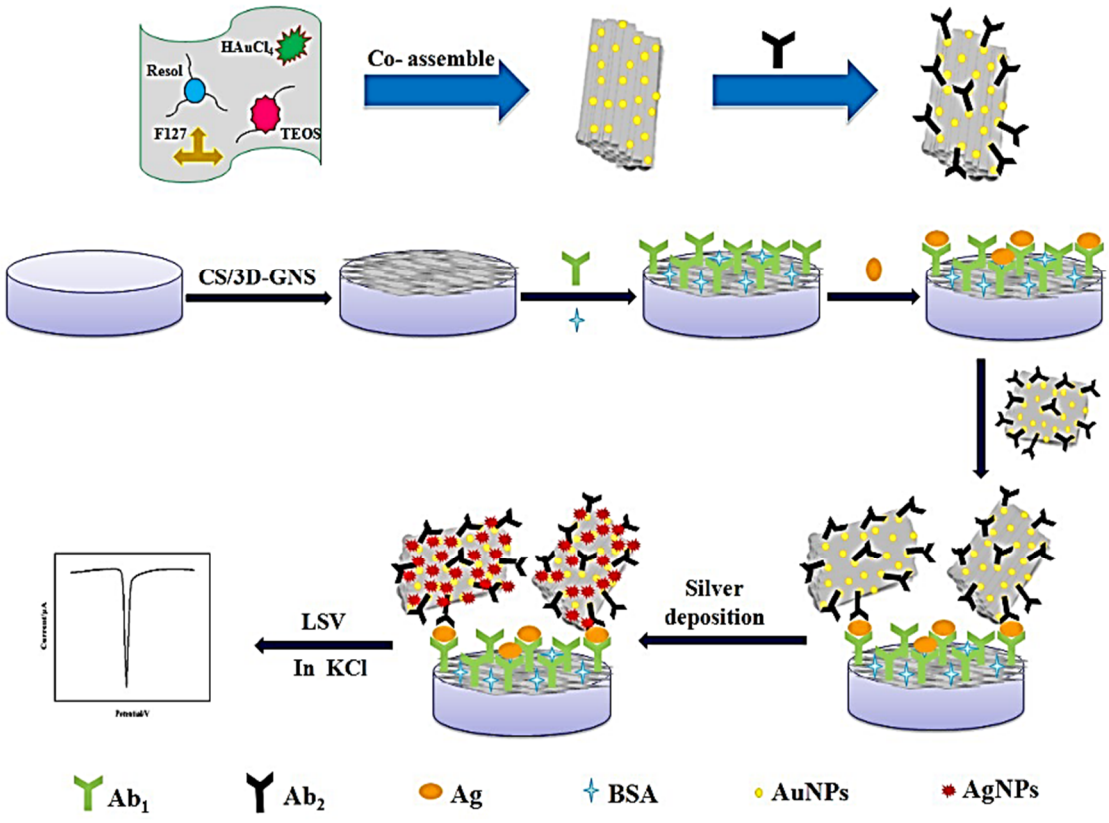


Figure 2.27. Modification scheme of a 3D graphene-based sensor for NSE detection. The porous structural design, decent electrochemical stability and high electron transfer rate have accumulatively led to better sensor sensitivity [242].

Detections of less common biomarkers using graphene-based platforms were likewise presented in the literature; an immunosensor developed by Choudhary et al. to detect human telomerase reverse transcriptase (hTERT) was one of the many [250]. hTERT is the catalytic subunit of telomerase on chromosome 5p 15.33. It is related to cell immortalisation and the development of malignancy in which free circulating genes of hTERT discovered in the blood plasma of lung cancer patients was almost eight-fold the value detected in non-cancer patients [251]. The immunosensor was fabricated via covalent immobilisation of anti-hTERT antibody onto graphene oxide sheets on indium tin oxide (ITO) electrode. DPV measurements from the immunosensor demonstrated good specificity and low LOD of 10 ag/ml towards the targeted antigen, attributed to the improved electron transfer and greater loading of hTERT antibody on the substantial surface area granted by the exfoliated graphene. Another less common biomarker, CD59 was detected using a graphene-based sensor, as reported by Deepa et al. [252]. The abnormal level of CD59 led to uncontrolled signalling and resistance to cell apoptosis. CD 59 is often overexpressed in NSCLC patients. The CD59 immunosensor was achieved using a graphite electrode functionalised by graphene oxide. The immunosensor with immobilised monoclonal CD59 antibody was able to quantify CD59 within the concentration of 1 fg/mL to 10 ng/mL. The author attributed the presence of graphene oxide as the reason for the improved conductivity of the immunosensor.

Other than serving as electrode material, graphene sheet was also applied as nanotag in sensors to amplify the detection signal, like the one demonstrated by Li and Tian for NSE detection using guanine-decorated graphene as nanotags [253]. Anti-NSE was immobilised on GCE and reacted with NSE to form an immuno-complex on the electrode surface. Meanwhile, Guanine and anti-NSE reporting probes were immobilised on graphene sheets to serve as the nanotag for the quantification of NSE concentration. Employing the sandwich-assay, the detection was performed in an electrolyte containing $Ru(bpy)_3^{2+}$, where the catalytic oxidation of $Ru(bpy)_3^{2+}$ toward the guanine (electron transfer) gave rise to the analytical current signal. Linear detection ranges from 0.005 ng/ml to 80 ng/ml and LOD of 1 pg/ml was demonstrated by the sensor for NSE detection,

attributed to the great amount of immobilised Guanine on the graphene nanotag that amplified the detection signal.

Other than modifying the common GCE and SPCE, graphene has also been used directly on a metallic substrate such as copper for the detection of lung cancer biomarkers, as demonstrated by Vijay Singh et al. [254]. In this study, a label-free CEA sensor was developed based on homogenous graphene sheets that were grown on a copper surface using a liquid precursor CVD route. The graphene films, anchored to the copper substrate, served directly as the sensing electrode and eliminated the need to transfer the graphene onto other surfaces that may compromise the quality of the graphene. Graphene sheets of high surface area gave rise to excellent electrochemical properties; with anti-CEA immobilised as the biorecognition layer, the sensor demonstrated a LOD of 0.23 ng/ml that fulfilled the requirements of clinical detection of lung cancer. Figure 2.28 shows the modification scheme of the graphene-copper bioelectrode.

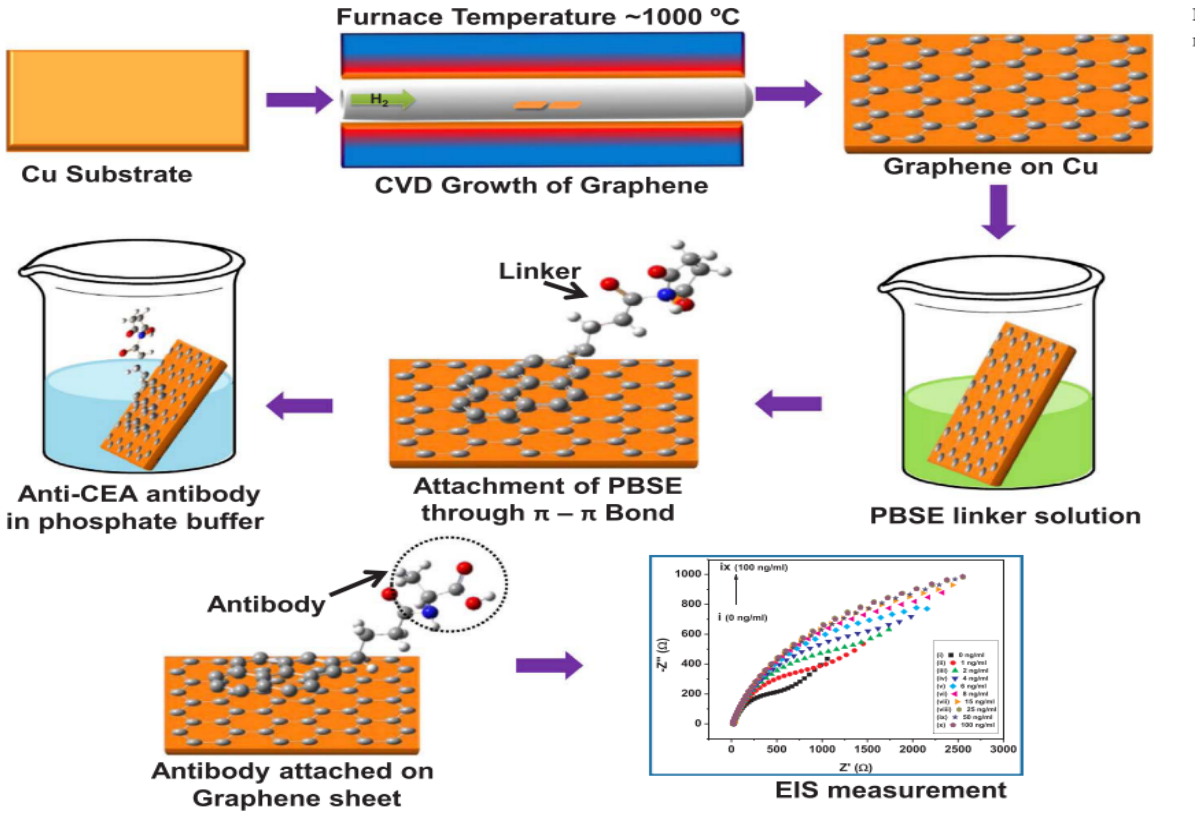


Figure 2.28. Modification scheme of CVD-grown graphene on copper substrate. The single-step electrode fabrication proposed in the study is an advantage over other reported techniques [254].

2.7.2. GRAPHENE COMPOSITE-BASED ELECTROCHEMICAL SENSORS FOR LUNG CANCER BIOMARKERS

Although graphene can be functionalised to form covalent bindings with the protein and amino-modified oligonucleotides, in most cases, graphene is further treated with other nano-particles to form a nanocomposite in conjunction with the prominent growth of nanotechnology. As discussed earlier, the hybrid nanomaterials are usually used to modify electrodes to reduce restacking and to increase electrode surface-to-volume ratio, which in turn allows better immobilisation of biorecognition elements.

One of the most common nanoparticle-graphene interactions is the AuNP-graphene composite. In view that disulfides, which are abundant in protein, bind firmly to AuNP surfaces via Au-S bond to generate a self-assembled monolayer [255], graphene decorated with AuNP was widely exploited to conjugate with biorecognition protein or DNA. The surface chemical properties of AuNP associated with its negative surface charge and its connections with functional amino acids have been assessed by Zhong et al. [256], who suggested that AuNP can be arranged into comprehensive architectures and functional materials over a broad spectrum of pH.

A common method to synthesise AuNP-graphene composite is via the reduction of chloroauric acid, $HAuCl_4$ in the presence of graphene. As demonstrated by Zhu et al., an AuNP–decorated graphene composite was effectively synthesised by heating $HAuCl_4$ with graphene dispersed in water to boiling, followed by the addition of trisodium citrate, a reducing agent and a non-aggregation agent [8]. The synthesised AuNP-graphene, as depicted in the TEM image shown in Figure 2.29, consisted of a pristine thin graphene sheet anchored with homogenously distributed AuNP with a small radius of 25 nm to 50 nm which greatly improved the surface area for electrochemical responses. The AuNP-graphene composite was drop-casted on a GCE, followed by the immobilisation of an anti-CEA on the electrode surface. Under optimised conditions, the peak current measured from DPV was linearly proportional to CEA concentration from 0.10 ng/ml to 0.08 pg/ml with a LOD of 0.04 ng/ml. This sensing platform demonstrated good reproducibility,

stability and specificity. The real sample application of the sensor, viz the determination of CEA in human serum samples was performed and the results agreed strongly with that generated by ELISA.

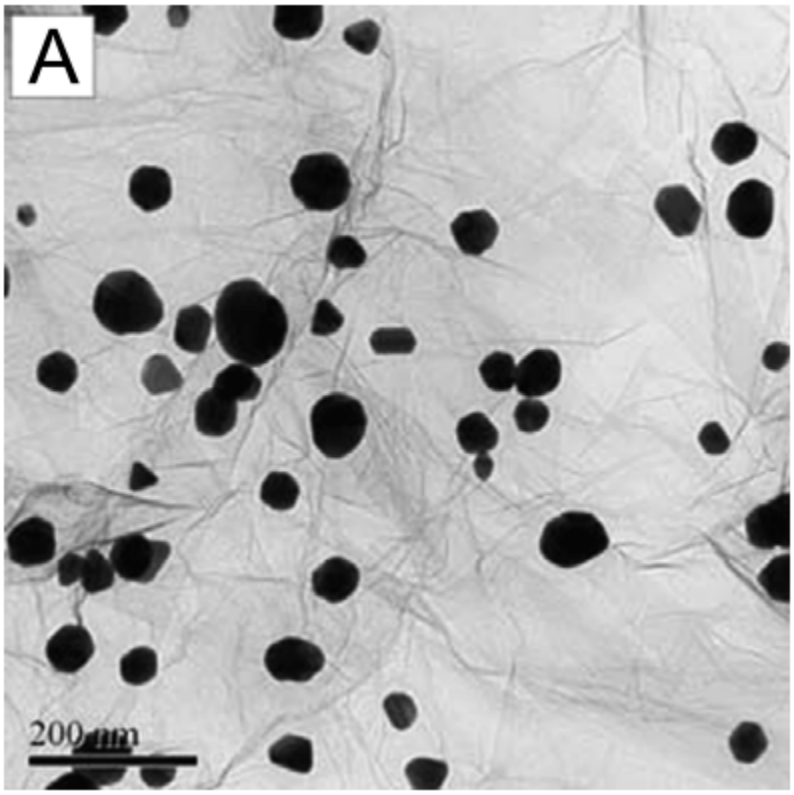


Figure 2.29 TEM image of AuNp-decorated graphene sheet. Thin graphene was synthesised as advocated by its transparent appearance and AuNPs were well-anchored onto the graphene sheets [8].

Employing a comparable AuNP-graphene synthesis route, Zeng et al. fabricated a label-free electrochemical immunosensor based on signal amplification using AuNP-graphene composite for the quantification of biomarker CYFRA 21-1 [195]. The AuNP-3D graphene composite was dissolved in chitosan solution to give AuNP-graphene-chitosan composite. Glutaraldehyde was included in the fabrication to immobilise proteins to the nanocomposite. The signal of the immunosensor was amplified and its sensitivity was improved, attributed to the excellent dispersion, large surface area and good conductivity granted by the AuNP-graphene-chitosan nanocomposite. Together with the outstanding immobilisation of antibodies through the glutaraldehyde cross-linker, a broad working range of 0.25 ng/ml to 800 ng/ml, LOD of 0.1 ng/ml, and serum samples recovery rate from 95 % to 109% were attained.

The upsurge for on-site testing of lung cancer biomarkers aiming to diagnose, stage and predict the prognosis of the illness has encouraged the participation of graphene nanocomposite-based electrochemical sensors in the emerging wave of wireless point-of-care systems. Fan et al. fabricated a point-of-care platform for the detection of NSE based on a microfluidic paper-based electrochemical sensor enhanced by AuNP-thionine-graphene nanocomposite [246]. The detection of NSE was quantified by the measurements from DPV and the instantaneous detection result could be displayed on an Android device via Bluetooth module, as shown in Figure 2.30. The DPV results presented a linear association of the sensor response with the logarithm of NSE concentration ranging from 1 ng/ml to 500 ng/ml and a LOD of 10 pg/ml. The superior sensor performance was credited to the good signal amplification given by AuNP-graphene nanocomposite and the functional immobilisation of the anti-NSE on the electrode surface via electrostatic and hydrophobic interactions. On top of comparable performance with commercial potentiostats, the portable point-of-care system had likewise established a satisfactory agreement with results from ELISA for the NSE recovery test in human serum, rendering it a promising platform for on-site detection of other tumour markers.

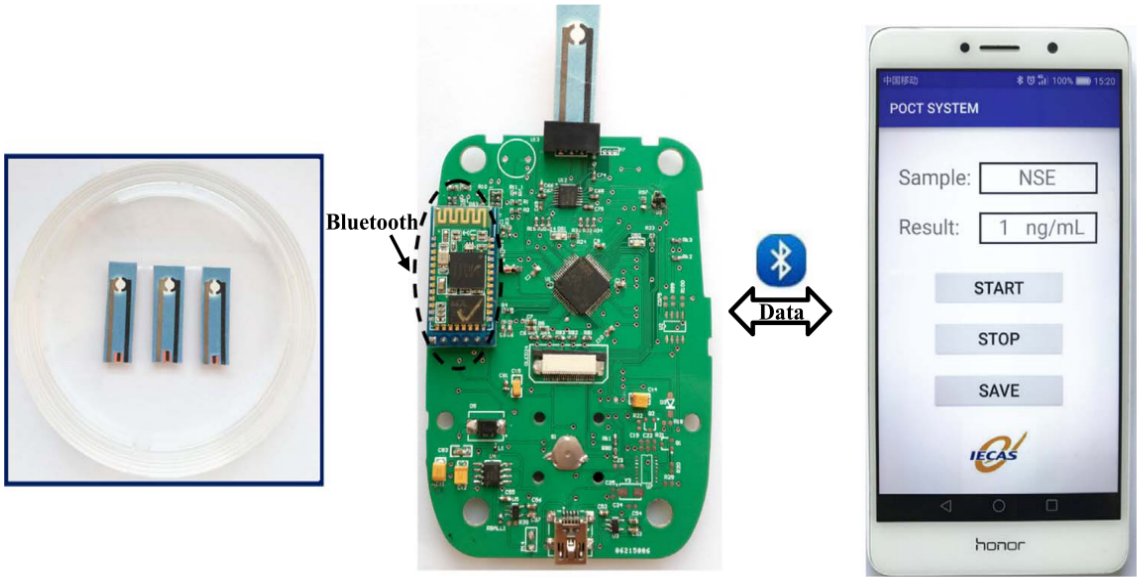


Figure 2.30. A portable point-of-care system with wireless transmission of data to an Android application. The miniature system was an integration of a microfluidic paper-based electrode, an electrochemical transducer and a smartphone to perform DPV measurements [246].

Numerous other nanoparticles have attracted significant interest for developing electrochemical biosensors, including novel work reported by Chen et al. [257] which used a noble metal, the silver nanoparticle (AgNP) to develop a sensitive electrochemical genosensor for the detection of CYFRA 21-1 in lung cancer patients. AgNp is broadly applied in biosensing attributed of its outstanding properties in electron transfer and biocompatibility. The study synthesised a 3D graphene/AgNPs nanocomposite that offered secure binding to the single-stranded DNA probe through the strong Ag-S bond. The interface provided a favourable environment to preserve the bioactivity of the immobilised single-stranded DNA probes and to allow the genosensor to detect the complementary CYFRA 21-1 in real lung cancer samples with satisfactory outcomes.

Some other reported works that have employed graphene-based material as electrode materials include a sandwich-type CEA sensor based on GCE functionalised with nano platinum-thionine-graphene nanomaterial [258], a genosensor for the detection of EGFR exon-21 point mutation on pencil graphite electrode that was modified by RGO [237], an impedimetric sensor based on protein G for EGFR detection [259], a CEA sensor based on AuNP anchored on amino functionalised graphene [222] as well as a sandwich-type immunosensor for NSE detection based on RGO/AuNP nanocomposite that has high catalytic activity resulting in signal intensification [180]. The list goes on, nonetheless, all reported works endorsed the advantages of graphene and graphene-nanocomposite in terms of enhanced sensing area for more abundant protein immobilisation, improved electron transfers for the amplification of quantification signal, and the offer of a constructive environment that preserved the integrity of the bio-recognition elements. Table 2.4 summarises the performance of the sensors discussed.

Table 2.4 Electrochemical Biosensors Based on Graphene and Graphene Nanocomposite for the Detection of Lung Cancer Biomarkers

Platform	Biomarker	Detection Technique	Linear Range	LOD	Ref
Graphene/magnetic beads-CEA antibody	CEA	CV	5 ng/ml – 60 ng/ml	5 ng/ml	[249]
GCE/3D graphene starch/anti-NSE	NSE	LSV	0.02 pg/mL - 35 ng/mL	8 fg/ml	[242]
ITO /graphene oxide/anti-hTERT	hTERT	DPV	10 ag/ml – 50 ng/ml	10 ag/ml	[250]
Graphite/graphene oxide/anti-CD59	CD59	CV	1 fg/ml – 10 ng/ml	1 fg/ml	[252]
Graphene-guanine nanotag	NSE	DPV	5 pg/ml - 80 ng/ml	1 pg/ml	[253]
Copper/graphene/anti-CEA	CEA	EIS	1 ng/ml -25 ng/ml	0.23 ng/ml	[254]
GCE/AuNP-graphene/HRP-anti CEA	CEA	DPV	0.1 ng/ml – 80 ng/ml	0.04 ng/ml	[8]
GCE/AuNP-graphene-chitosan/anti-CYFRA 21-1	CYFRA 21-1	DPV	0.25 ng/ml - 800 ng/ml	0.1 ng/ml	[195]
SPCE/AuNP-thionine-graphene	NSE	DPV	1 ng/ml - 500 ng/ml	10 pg/ml	[246]
GCE/ nano platinum-thionine-graphene/anti-CEA	CEA	CV	2 pg/ml – 80 ng/ml	1 pg/ml	[258]
Graphite electrode /RGO/ordered mesoporous carbon/single stranded DNA	EGFR Exon-21	DPV	0.1 µM - 3 µM	120 nM	[237]
Au electrode/AuNP/ cysteamine/ 1,4- phenylene diisothiocyanate/protein-G/anti-EGFR	EGFR	CV	1 pg/mL- 1 µg/mL	0.93 pg/ mL	[259]
GCE/AuNP-NH_2 graphene/anti-CEA	CEA	SWV	500 fg/mL -5.0 ng/mL	167 fg/mL	[222]
GCE/AuNP-RGO/chitosan	NSE	DPV	0.1 ng/ml- 2 µg/mL	0.05 ng/ml	[180]
3D graphene-AgNP/single-stranded DNA	CYFRA 21-1	DPV	0.01 pM – 100 nM.	0.01 pM	[257]

2.8. GRAPHENE/ZIRCONIA NANOCOMPOSITE

2.8.1. PROPERTIES OF ZIRCONIA

The π -π stacking interactions among individual graphene sheets result in their tendency to restack and intervention is necessary to reduce the stacking. Metal oxide nanoparticles offer a versatile solution to the problem of restacking due to their small sizes. In recent years, ZrO_2 has drawn interest due to its favourable properties such as high thermal stability and chemical inertness [260].

Physically, ZrO_2 does not decompose easily under the influence of heat. As well, change in the crystallographic phase would not occur unless the material is treated with extremely high heat. ZrO_2 is thermally stable even though it has three crystallographic phases, namely monoclinic, tetragonal and cubic. For instance, tetragonal ZrO_2 remains in the same phase up to 1200 °C before it eventually transformed into a monoclinic phase with < 5 % volume expansion [261]. This thermal stability property of ZrO_2 can be exploited by sensors that operate in high-temperature environments, for example, gas sensors that monitor the gas concentration in the engine and gas boiler.

While other materials may experience chemical alteration upon interacting with the medium/environment they are exposed to and compromise their integrity, ZrO_2 is chemically stable under a reducing and oxidizing environment [262]. An experiment showed that, when reacted with alkoxysilane, ZrO_2 presented no sub-layer of mixed oxide, in comparison, the reaction of TiO_2 with alkoxysilane led to the development of a surface sub-layer of mixed oxide [263]. The stability of ZrO_2 is favourable for sensing works that operate in complex mediums such as the detection of heavy metal/ions in river water.

Besides, ZrO_2 has been shown to have low cytotoxicity [264]. It was postulated that the biocompatibility of ZrO_2 is given by its inertness that does not trigger the production of reactive oxygen species, the main culprit of toxicity [265]. The biocompatibility of ZrO_2 is beneficial for *in vivo* sensors and wearable sensors. Meanwhile, for *in vitro* sensors, the low cytotoxicity of the

ZrO_2 presents a safer working environment for the researcher/manufacturer that synthesises the material.

In terms of sensing, ZrO_2 has been reported to have a strong affinity to phosphoric groups and was initially reported in the sensing of phosphopeptide and organophosphorus compounds [266]–[269]. ZrO_2 affinity for the phosphoric group has also been explored to allow immobilization of DNA where oligonucleotide probes with phosphate group were bonded to ZrO_2 to form sensors [270], [271]. Most importantly, ZrO_2 has been shown to reduce the aggregation of graphene leading to improved electrochemical properties of the graphene [27], [34]. It was postulated that the well-dispersed ZrO_2 on the graphene served as spacers and thus prevent graphene from restacking, leading to better graphene stability [27].

In summary, ZrO_2 possesses favourable properties including chemical inertness, lack of toxicity, affinity for groups containing oxygen and thermal stability that are worth exploring for possible applications in sensing.

2.8.2. SYNTHESIS OF GRAPHENE/ZIRCONIA NANOCOMPOSITE

Graphene decorated with evenly distributed ZrO_2 nanoparticles on the surface could lead to well-dispersed graphene with an exceptional surface area. The synergistic effects between graphene and ZrO_2 resulted in a composite that has improved electrochemical properties. Hydrothermal treatment, microwave irradiation and electrodeposition are some of the frequently employed techniques in the synthesis of graphene/ZrO_2 nanocomposites.

Kumar et al. deposited ZrO_2 nanoparticles on graphene oxide using the hydrothermal method [26]. Graphene oxide was produced via Hummer's method which involved the use of hydrochloric acid (HCl). A 0.2 M zirconium ethoxide precursor solution, a 0.8 M sodium hydroxide (NaOH) solution that has promoting effects on the nucleation of ZrO_2, and a 0.1 M solution of cetyltrimethylammonium bromide (CTAB) that enhanced the growth of ZrO_2 crystallites were separately prepared in deionised (DI) water. The solution of NaOH was added to the ZrO_2

precursor solution followed by the dropwise addition of CTAB solution and the mixture was kept stirring for about 4 hours. Subsequently, the stirred mixture was added to the graphene oxide dispersion. The mixture was transferred to an autoclave and subjected to hydrothermal treatment at 170 ˚C for 17 hours to yield ZrO_2-decorated graphene oxide. The synthesis route was successful in which spherical ZrO_2-nanoparticles were found to be homogeneously distributed on the graphene oxide sheet.

Microwave irradiation has also been applied in graphene/ZrO_2 synthesis, such as the one demonstrated by Zou et al. for the production of graphene-reinforced ZrO_2 [36]. Dried-pressed and sintered ZrO_2 was placed into an impregnating device and vacuum extracted (-0.09 MPa to -0.1 MPa), followed by the inclusion of graphene dispersion into the device. Argon gas at 20MPa was flown into the device for 20 hours to produce the graphene-inforced ZrO_2 ceramic preform, which was subsequently sintered by microwave for 3 hours at 1250° C, 1350° C, 1450° C with a heating power of 2.0 KW in a vacuum environment. The study showed that the microwave sintering technique offered fast heating and graphene was well distributed in the composite.

Vilian et al. fabricated an electrode functionalised by ZrO_2-decorated RGO via electrodeposition [33]. Graphene oxide was synthesised via modified Hummer's method and its suspension was drop-casted on a GCE. Subsequently, the electrode coated with graphene oxide was subjected to 10 cycles of cyclic voltammetry (CV) in 5.0 mM of zirconyl chloride ($ZrOCl_2$) solution to induce electrochemical reduction and electrodeposition of ZrO_2 particles. This technique allowed the synthesis of graphene/ ZrO_2 electrodes with a large surface-to-volume ratio, resulting in reduced cost while enhancing the catalytic properties of the electrode.

In brief, the review of the synthesis technique for graphene/ZrO_2 nanocomposite suggests that each of the synthesis techniques has its advantages and disadvantages, and there is much room for exploration.

2.8.3. APPLICATION OF GRAPHENE/ZIRCONIA IN SENSORS

Apart from its great potential in orthopaedic, dental and drug delivery applications, ZrO_2 and graphene/ZrO_2 have also found a place in sensing applications. The applications of graphene/ZrO_2 nanocomposite in the detection of electroactive analytes have been reported in the literature. Murugun and Poongan hybridised graphene with ZrO_2 and subsequently modified GCE with the synthesised nanocomposite for the detection of acetaminophen, phenylephrine hydrochloride and cytosine [272]. The graphene/ZrO_2 nanocomposite was produced using the hydrothermal method where the mixture of graphene and ZrO_2 was treated at high heat (180 °C) for 12 hours in an autoclave. The graphene/ZrO_2 was drop-casted on GCE and dried at the ambient condition. By using DPV, the sensor was able to detect acetaminophen, phenylephrine hydrochloride and cytosine, with distinct redox peaks for each analyte, as shown in Figure 2.31. Material characterisations showed that the anchored ZrO_2 was about 30 nm – 60 nm, therefore, the great performance of the sensor can be attributed to the large surface area of graphene/ZrO_2 nanocomposite.

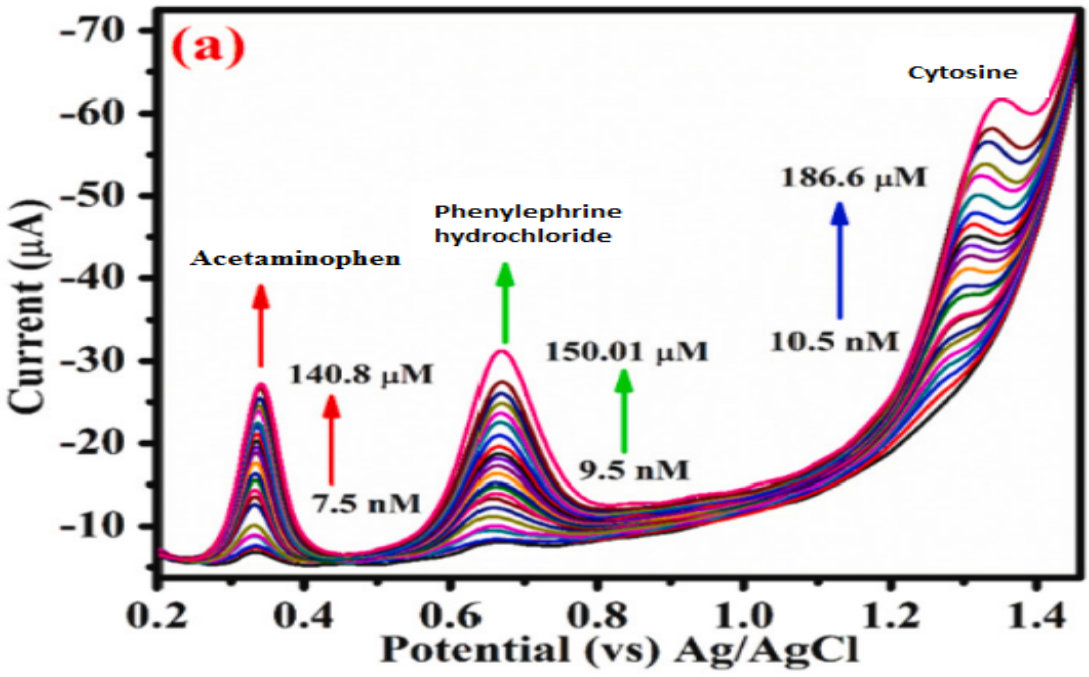


Figure 2.31. The DPV detection of acetaminophen, phenylephrine hydrochloride and cytosine. Distinct peaks were exhibited by the sensing platform modified with graphene/ZrO_2 nanocomposite [272].

The thermally stable ZrO_2 was also exploited by Ricci and Gregory for the detection of vapour-phase ammonia [273]. The vapour-phase ammonia sensor employed a microheater that was deposited onto ultrathin ZrO_2 substrate. The microheater was connected to the digital control system via four thin-film leads. The sensor constructed by the team is shown in Figure 2.32 in which parts labelled with 1,2,3,4 were the zirconia substrate, adhesion layer, microheater and the metal oxide catalyst (SnO^{1+}) layer, respectively. The heat generated by the catalytic decomposition of ammonia in the presence of SnO^{1+} caused the alteration in electrical power necessary to keep the microheater baseline. The alteration was measured and quantified by the digital control system. To encourage catalytic decomposition of ammonia, the sensor operated at about 100 °C. The ZrO_2-based sensor allowed the sensor to not experience a drastic temperature increment and was able to resume to room temperature within seconds after each measurement; therefore, permitting high usability. The sensor was capable of providing trace-level detection of ammonia in real-time, attributed to the thermal stability of the ZrO_2 substrate.

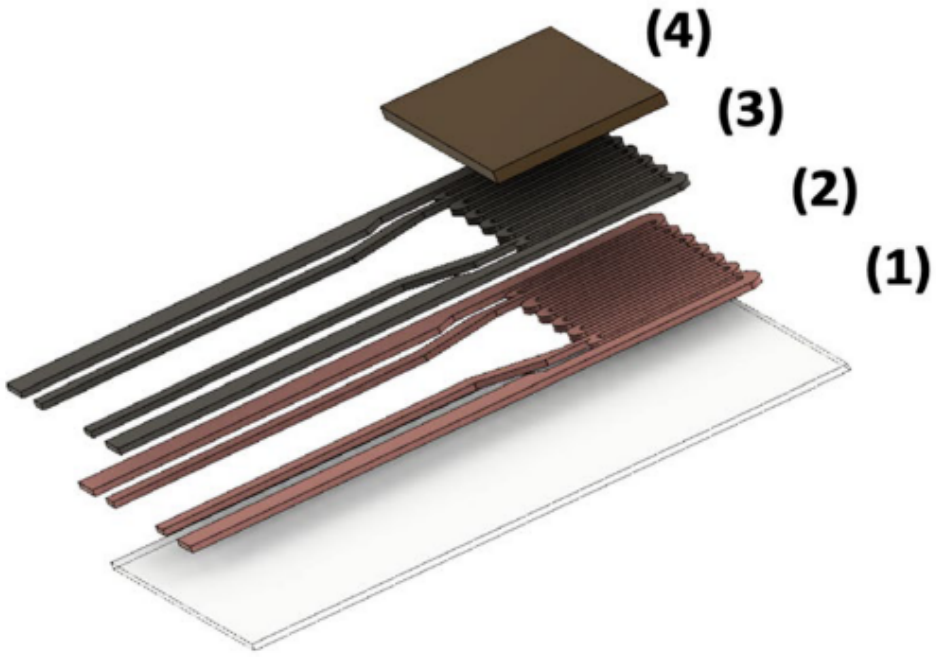


Figure 2.32. The layer-by-layer structure of a vapour-phase ammonia sensor. The sensor was constructed on a ZrO_2 substrate so that the sensor could cool down within seconds after each measurement to give a high cycle of duty [273].

The integration of ZrO_2 into graphene-based composites for cancer biomarker sensing was demonstrated for the first time by Kumar et al. [26]. In this study, ZrO_2 nanoparticles were deposited to RGO, as shown in Figure 2.33, to give a composite ZrO_2-RGO with enhanced physicochemical properties. The nanocomposite which was subsequently electrophoretically coated on the ITO glass substrate exhibited enhanced charge transfer (twice) to that from electrodes without the ZrO_2-RGO layer. The developed platform was immobilised with an anti-CYFRA 21-1 capture layer and demonstrated a wide linear detection range within 2 ng/ml to 22 ng/ml alongside a noteworthy LOD at 0.122 ng/ml for CYFRA 21-1 detection.

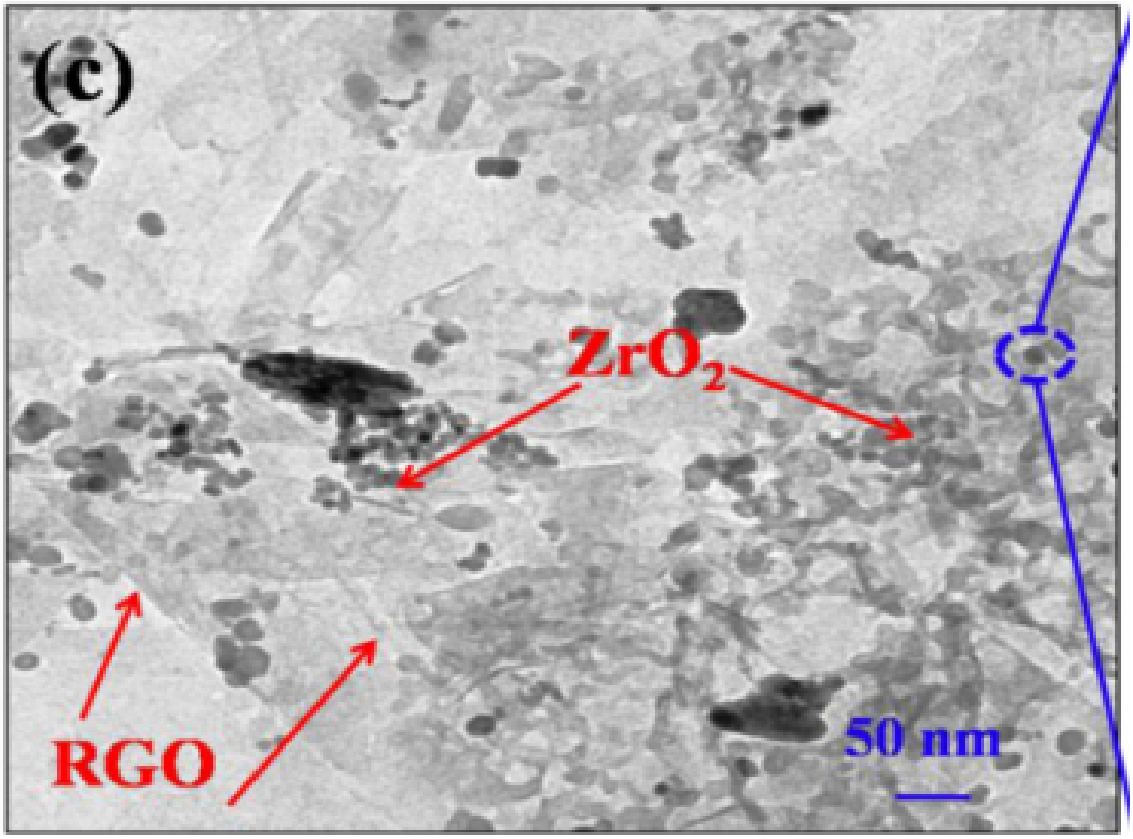


Figure 2.33. TEM shows the decoration of RGO with ZrO2 nanoparticles. Spherical ZrO2 nanoparticles are homogeneously distributed on the graphene oxide sheet [26].

While Kumar et al. have developed an immunosensor, Zhang et al. have fabricated a genosensor for the detection of microRNA21 (miRNA-21) based on ZrO_2-RGO modified electrode [274]. MicroRNAs are small endogenous non-coding RNAs with sizes between 17 to 22 nucleotides that are essential in the regulation of gene expression for tumorigenesis. Biomarker miRNA-21 is

deregulated in lung carcinoma, giving rise to its diagnostic and prognostic role in lung cancer [275]. The study established that the presence of the ZrO_2 has delivered a favourable environment for the immobilisation of DNA probes and the detection of miRNA-21.

In summary, nanocomposite ZG has been recognised to be an enhancement with regards to sensing performance, as proposed by the findings of previously reported works. However, its application for the detection of lung cancer markers is yet to be extensively implemented as compared to other nanomaterials; and therefore is worth exploring.

2.9. SUMMARY

This chapter presented the principles as well as past research governing the main approaches in the synthesis of graphene and graphene/metal oxide composite. The review of various synthesis methods led to the conclusion that each method has its own merits and demerits. The absence of a simple and reproducible synthesis method, calls for the necessity to refine the synthesis routes to realise more scalable and efficient production of graphene and graphene-based nanocomposite. Regardless of the synthesis route, the high surface area and good conductivity of graphene-nanocomposite have been greatly exploited to produce reliable and specific detections; and have opened up a new avenue for more creative use of graphene-based material in the biosensing field. Lung cancer is the most common cancer worldwide, therefore, the anticipation to revolutionise the detection of lung cancer for early detection and timely treatment lies in the innovation with sensing technologies, particularly biosensors that could provide rapid detection of lung cancer biomarkers. Review shows that various biomarkers such as CEA, NSE, EGFR and many more have been discovered and employed in the detection of lung cancer. Each biomarker is unique, nonetheless, the elevated value of these biomarkers would always point to possible malignancies. Having identified feasible biomarkers for lung cancer detection, various transducers that convert the interactions of bioreceptor with biomarkers into measurable signals were also reviewed; in which optical, mass-based and electrochemical are some of the most commonly employed transducing techniques for lung cancer detection. Likewise, each technique is unique and has plenty of room for further exploration. Lastly, graphene-based sensors have exhibited outstanding performance in lung cancer detection as evidenced by the positive results from a great number of reported works. Most of the reported biosensors have provided valuable proof-of-concept demonstrations of lung cancer detection with much space available for further improvements.

3. SYNTHESIS AND CHARACTERISATION OF GRAPHENE/ ZIRCONIA NANOCOMPOSITE

3.1. INTRODUCTION

Many researchers have attempted to synthesise ZG nanocomposite; however, most of the attempts involved tedious multi-step synthesis, reduction of graphene oxide with harsh reducing agents, the addition of hazardous acid, and the need for a high-temperature annealing process [20]–[23], [53]. In cases where the precursor graphite or graphene oxide was not completely reduced, the presence of oxygenated functional groups on the graphene surface was common. Furthermore, excessive reducing agents such as $NABH_4$ and hydrazine used in producing graphene oxide may introduce contaminants to the nanocomposite, thus reducing the performance of the graphene-nanocomposite-based sensor [41]. The lack of a safe and clean synthesis route motivated us to propose a simple strategy that combines solvent-exfoliation and hydrothermal treatment to synthesise ZG nanocomposite. This method is green and scalable wherein it is based solely on the manipulation of surface energy balance between water and ethanol to effectively exfoliate graphite with mild sonication [248] and subsequently utilises high temperature and high vapour pressure to crystallise ZrO_2 nanoparticles on the graphene sheets. The proposed method omits harsh chemical usage which results not only in a safer procedure but also produces ZG nanocomposites that are free from residual functional groups such as epoxide, hydroxyls, carboxyls and carbonyls that could reduce the electrical properties of the nanocomposite and decrease the overall electrochemical performance of the modified sensors [276]. The developed method is also economically efficient as the raw materials (ethanol and water) are inexpensive, while sonication and hydrothermal treatment are easily scalable.

In conjunction with the broader application of graphene-based nanocomposites, raise the concern of material-induced cytotoxicity. Cytotoxicity is the extent to which a material can reduce the viability of cells or in other words, it is the measurement of how harmful a substance is to living

organisms. Many nanocomposites are known to be toxic to human cells, yet they are applied in biosensors for enhanced performances [277]–[279]. Although biosensings were *in vitro* applications, material cytotoxicity should still be a concern. During the nanocomposite synthesis process and the sensor fabrication steps, researchers are unavoidably exposed to the nanomaterial, through inhalation and physical contact with the skin. Toxic nanomaterial once inhaled can deposit in the respiratory tract, either directly damage the lung epithelium or diffuse into the bloodstream at the tissue-vessel interface [42]. Meanwhile, dermal contact with toxic material can cause effects ranging from mild redness or eczema to severe conditions including tissue destruction and absorption into the bloodstream [43]. In other words, the absence of cytotoxicity evaluation reflects the negligence of potential hazards from material toxicity, especially during the sensor fabrication process. As lungs, together with skins, suffer the utmost exposure to nanomaterial through inhalation and physical contact, it is imperative to investigate the effects of nanocomposite-cell interaction for these two types of cells [280].

Our work performed a cytotoxicity study of the ZG nanocomposite in which ZG nanocomposite was subjected to microscopic assessment of morphology and an *in vitro* cell proliferation study (MTT assay) to evaluate its biocompatibility on human lung fibroblast (MRC5) and human immortalised keratinocyte (HaCaT).

3.2. EXPERIMENTAL DETAILS

3.2.1 APPARATUS AND MATERIAL

Raw graphite flakes (99% carbon purity) were purchased from Bay Carbon (Michigan, USA). Zirconyl chloride octahydrate (98%, reagent grade), phosphate buffer saline (PBS), fetal bovine serum (FBS), dimethyl sulfoxide (DMSO) and Dulbecco's phosphate-buffered saline (DPBS) were purchased from Sigma-Aldrich (USA). Ethanol and potassium ferricyanide (III), $K_3Fe(CN)_6$ (99%) were obtained from R&M Chemicals (Malaysia). Growth media RPMI-1640, Dulbecco's Modified Eagle Medium (DMEM), 1% penicillin-streptomycin solution, 0.25% trypsin and 3-

(4,5-dimethylthiazol-2-yl)-(2,5-diphenyltetrazolium bromide) (MTT) that were purchased from Nacalai (Japan). All the chemicals were used as received without further purification. SPCEs were acquired from Metrohm (Netherland). Ultrapure MQ water (Millipore Milli-Q system) was used in cell culture. The Raman spectra of the powdered samples were recorded in the range of 500 cm^{-1} to 3000 cm^{-1} using a Renishaw inVia Raman microscope at room temperature. The morphology of the sample was observed through a scanning electron microscope (SEM) (FEI Quanta-400 FESEM, 20 kV) and transmission electron microscope (TEM) (JEOL JEM-2100 F). Energy-dispersive X-ray spectroscopy (EDX) (Oxford Instruments X-Max, 20 mm^2 detector) was performed in conjunction with SEM to identify the elements present in the samples. The XRD (Philip-X'pert X-ray diffractometer) pattern was used to characterise the structural features of ZrO_2 and ZG composites, at scanning rate of 0.02/ s^{-1} in a 2θ range of 10° to 80° θ with Cu Kα radiation at λ=1.5406 Å. The absorbance of the coloured solution for the MTT assay was measured at 570 nm via VersaMax Elisa Microplate Reader (Molecular Device, USA). Cells morphologies were observed using an inverted optical microscope (Nikon Eclipse TS100, USA)

3.2.2 SYNTHESIS OF GRAPHENE/ZIRCONIA

Graphene was synthesised from highly oriented pyrolytic graphite (HOPG) by the mild exfoliation method [248]. In brief, 50 mg of HOPG was dispersed in a 100 ml solution of ethanol/DI water (2:3). The resultant mixture was placed in a conventional ultrasonic bath working (37 kHz, 100% amplitude, 180 W) at room temperature for 3 hours to form a darkish black suspension. The solution was then centrifuged (3000 rpm, 30 min) and the sediment was dried overnight in the oven to yield exfoliated graphene. Subsequently, zirconyl chloride octahydrate was dissolved in DI water and stirred for even mixing. Graphene was re-dispersed in ethanol/DI water solution (2:3) and sonicated for homogenous re-dispersion. The mixture of both solutions was further sonicated for 2 hours to produce a uniform dispersion. The mixture was transferred to a 50 ml Teflon stainless steel autoclave and put in an oven for 18 hours at 180 °C. The solid precipitation was isolated from the solution by centrifugation, repeatedly washed with ethanol/DI water and dried

overnight at 70°C in an oven to yield the ZG nanocomposite. Pure ZrO_2 nanoparticles were prepared following the same reaction conditions with the absence of graphene. When zirconyl chloride octahydrate was dissolved into DI water, it hydrolysed into $Zr(OH)_4$ and HCl in the solution as stated in equation 3.1 [281]. During the hydrothermal process, high heat will cause the produced HCl to volatilise. As a result, the equilibrium shifted toward the right and the concentration of $Zr(OH)_4$ increased with the hydrothermal time. ZrO_2 nuclei are formed during the long-hour hydrothermal process. The process can be expressed in equation 3.2.

$$ZrOCl_2 + 3H_20 \rightarrow Zr(OH)_4 + 2HCl \qquad (Eq\ 3.1)$$

$$Zr(OH)_4 \rightarrow ZrO_2 + 2H_2O \qquad (Eq\ 3.2)$$

Table 3.1 shows the information on the different ratios of graphene to zirconyl chloride octahydrate (ZrO_2 precursor) which was used to prepare the ZG nanocomposites. The as-prepared samples with different weight ratios of graphene: ZrO_2 precursor (1:2, 1:4, 1:8, 1:16) were marked as G1Zr2, G1Zr4, G1Zr8 and G1Zr16, respectively.

Table 3.1: Weight Ratio Of Graphene: ZrO_2 Precursor

Name of Sample	Mass of Graphene (mg)	Mass of Precursor (mg)	Weight Ratio of Graphene: Precursor
G1Zr2	25	50	1:2
G1Zr4	25	100	1:4
G1Zr8	25	200	1:8
G1Zr16	25	400	1:16

3.2.3 PREPARATION OF SENSING PLATFORM FOR ELECTROCHEMICAL MEASUREMENTS

SPCE was first rinsed with DI water and soaked in PBS for 15 minutes for conditioning purposes. The as-prepared ZG nanocomposite was re-dispersed into an ethanol/DI water mixture via ultrasonication for about 30 minutes. 10 µL of the sonicated ZG nanocomposite dispersion (1 mg/ml) was drop-casted onto the working electrode of the SPCE and dried at the ambient condition to give ZG/SPCE. Likewise, ZrO_2/SPCE and graphene/SPCE were fabricated by drop-casting 10 µL of ZrO_2 dispersion (1 mg/ml) and graphene dispersion (1 mg/ml) respectively onto the working

electrode of SPCE. The electrochemical performances of the modified electrodes in connection with CV and EIS were analysed with AUTOLAB PGSTAT302N. CV analysis was carried out on SPCEs using PBS buffer (0.01 M, pH 7.4) containing 0.1 mM potassium ferricyanide $[Fe(CN)_6]^{3-/4-}$ as the redox probe. The CV was swept between -0.4 V to 0.8 V at a scan rate of 100 mV/s. Each CV was run for 10 cycles. EIS analysis was carried out on the SPCE in PBS buffer (0.01 M, pH 7.4) with 10 mM $[Fe(CN)_6]^{3-/4-}$ as the active redox probe, in a frequency range of 0.10 Hz to 100 kHz with a voltage amplitude of 100 mV at an open circuit potential.

3.2.4 CELL CULTURE, CELL INCUBATION WITH ZG AND MICROSCOPIC EXAMINATION OF CELL

For the study of material cytotoxicity, two mammalian cell lines namely the skin cell HaCaT, and lung cell MRC5 were cultured in a sterile condition. The cell culture procedure was performed in 10 ml of DMEM and RPMI-1640 for HaCaT and MRC5, respectively. The medium was replenished twice a week. In order to facilitate cell growth and survival, FBS (10%) and penicillin-streptomycin solution (1%) were included in the T-75 cell culture flasks. Incubation of the cells was performed in a humidified atmosphere in the presence of 5% CO_2 at 37 °C. Typically, cells were passaged by trypsinisation at 70–80% confluence. The growth medium was aspirated and 3 ml of 0.25% trypsin was added to promote cells dissociation. Subsequently, the collected cells were re-suspended in 4 ml of growth media, added to 10 ml of complete media and maintained accordingly. The cultured cells were introduced to ZG nanocomposite by incubating the cells with ZG of various concentrations. The synthesised ZG nanocomposite was redispersed in ethanol/DI water (2% ethanol) and sonicated for 15 minutes for homogenous dispersion. ZG dispersion of various concentration (0.5, 2.5, 5, 25, 50, 250, 500 µg/ml) was prepared. The material-treated cells were seeded into 96-wells plates (circa 5,000 cells/well) and incubated at 37 °C. At points 24-hour, 48-hour and 72-hour, the 96-well plates were retrieved from the incubator and placed under an inverted microscope for examination of cell morphologies. The images of the cells were captured with the attached camera.

3.2.5 MTT ASSAY FOR CELLS VIABILITY STUDY

An MTT assay was performed to investigate the cell viability of treated HaCaT and MRC5 cells. MTT solution was prepared by dissolving MTT in DPBS to reach a final concentration of 5 mg/ml. The as-prepared MTT solution was filter-sterilised using a 0.2 μm syringe filter. At point 24-hour, 48-hour and 72-hour, the material-treated cells were added with MTT solution (10 μl/well). The MTT-treated cells were incubated for 4 more hours at 37 °C to induce the reduction of tetrazole to formazan by the living cells. Subsequently, the media and MTT solution were substituted with DMSO solution to dissolve the reduced formazan into a coloured solution. The degree of light absorbance of the coloured solution is relative to the concentration of formazan accumulated on and inside the cell. The higher the formazan concentration, the darker the purple colour and hence the greater the absorbance. Since formazan was reduced by living cells, the magnitude of absorbance represented the measurement of cell viability. Cells grown in media without any ZG incubation (untreated cells) were used as the negative control. The cell viability was calculated via equation Eq.3.3, as determined at several time points (24-hour, 48-hour and 72-hour). IBM SPSS Statistic was used to perform statistical analysis on the MTT data collected. The experiments were carried out in triplicates in three independent experiments.

$$Cell\ viability, \% = \frac{Absorbance_{treated\ sample} - Absorbance_{background}}{Absorbance_{untreated\ sample}} \times 100 \qquad \text{(Eq. 3.3)}$$

3.3 RESULTS AND DISCUSSION

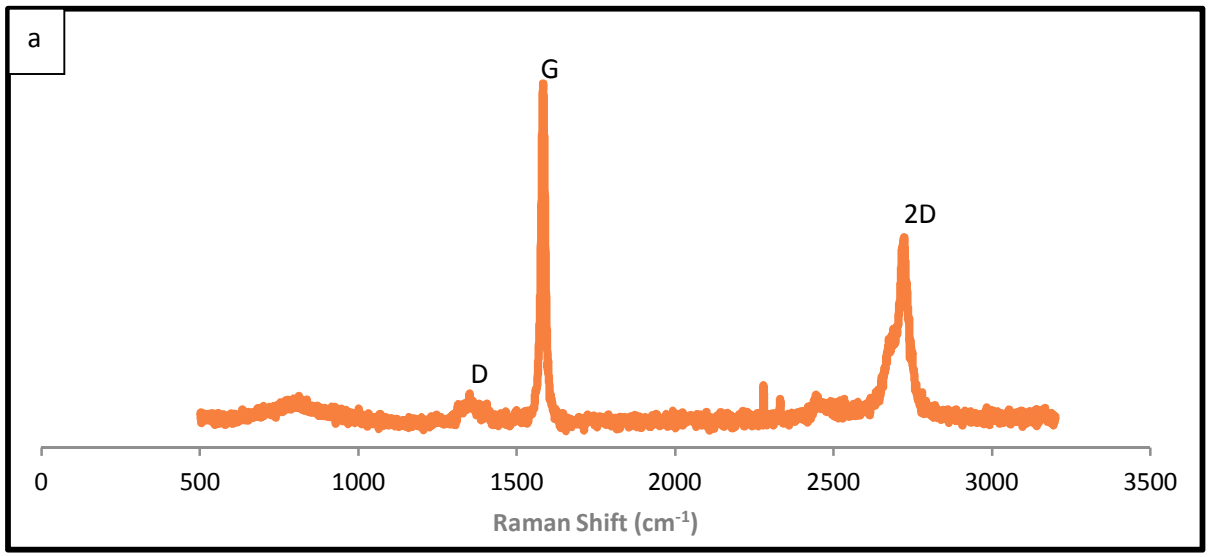
3.3.1 CHARACTERISATION OF GRAPHENE AND GRAPHENE/ZIRCONIA

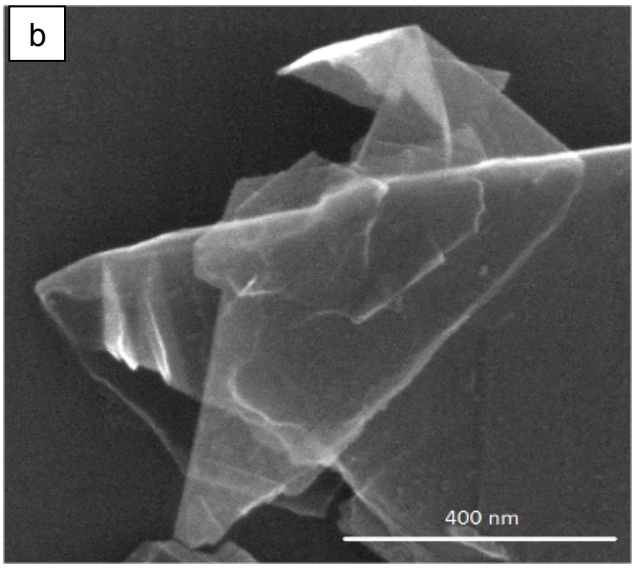
Raman spectroscopy is a well-recognised technique to evaluate the quality of the as-synthesised graphene. The Raman spectra of graphene, as shown in Figure. 3.1 (a) exhibited three distinctive peaks that are associated with the vibration bands of graphene. These vibrational bands furnished imperative information about graphene quality via the peak position, intensity and sharpness. The band observable at about 1580 cm^{-1} was the G-band (C-C bond stretching) which was attributed to the in-plane vibration of the sp^2 carbon atoms. Meanwhile, the two peaks at about 1346 cm^{-1}

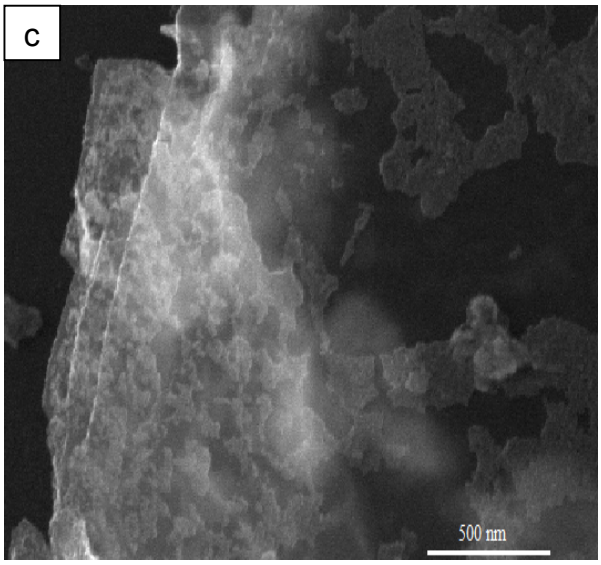
and 2720 cm^{-1} were identified as the D band ('disorder band') and the 2D band ('multipeak feature') respectively [282]. To evaluate the quality of the as-synthesised graphene, D and 2D peaks were the peak-of-interest as they furnish an insight into graphene quality in terms of exfoliation efficiency or other words, the thickness of the produced graphene. The D peak was usually contributed by the presence of edge defects in graphene, produced during the exfoliation of graphite into graphene. A pronounced D peak reflected the detection of edges and endorsed the efficiency of the exfoliation method. On the other hand, the 2D peak characterised the number of layers of the synthesised graphene. In multi-layer graphene, the 2D peak was usually split into 4 sub-peaks, namely 2D1a, 2D1b, 2D2a and 2D2b [283]. The 2D peak exhibited by Raman spectroscopy of the graphene synthesised in this work has only a single peak; nonetheless, the peak is slightly broad with a shoulder, suggesting that few-layer graphene was produced. The intensity ratio of D to G (I_D/I_G) for the exfoliated graphene was found to be 0.20 which was an increase compared to graphite which usually has an I_D/I_G ratio of 0.06 - 0.07 [284]. The I_D/I_G ratio for graphene increased due to the introduction of edge defects and the increased formation of sp^2 domain after the exfoliation [285],[286]. In short, the Raman spectroscopy shows that the ethanol-water exfoliation method employed in this study has efficiently produced thin graphene sheets.

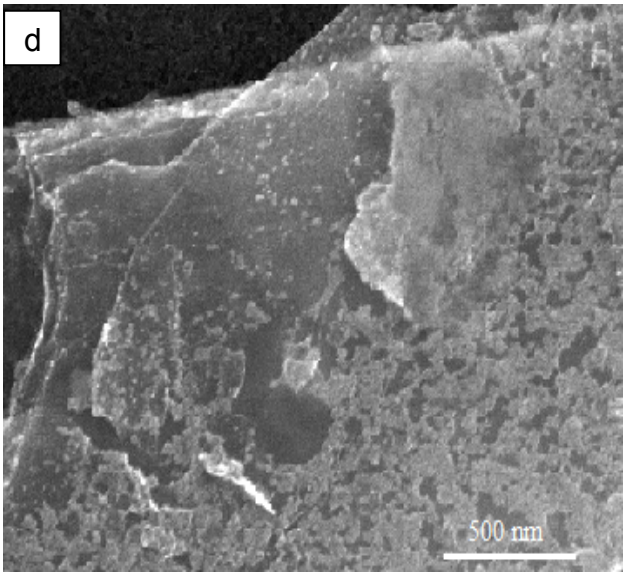
The morphology of the as-synthesised graphene and ZG were analysed with SEM. As shown, the effective exfoliation of graphite into single or few layers sheets was evidenced from their transparent appearances in Figure 3.1 (b); meanwhile, ZG nanocomposites synthesised from different precursor mass ratios have a varying degree of ZrO_2 nanoparticles deposition on the edges and surface of the graphene sheets. The lower mass ratio of precursor (G1Zr2 and G1Zr4) led to relatively uneven growth of the nanoparticles on the surface and edges of the graphene sheets as shown in Figure 3.1 (c)-(d), with certain graphene areas free from the coating of ZrO_2. Following the further increase of precursor ratio, the graphene flakes were observed to be homogeneously decorated by ZrO_2 for G1Zr8 as shown in Figure 3.1 (e), while slight agglomeration was seen for the highest precursor ratio of G1Zr16 as shown in Figure 3.1 (f), suggesting saturation of precursor

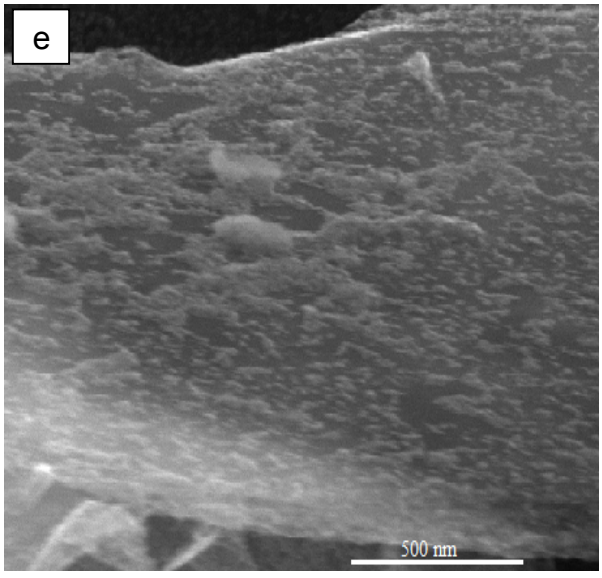
mass. The good distribution of ZrO_2 on graphene given by the graphene: precursor ratio of 1:8 suggests that it is the most optimum precursor loading ratio out of the four ratios investigated.











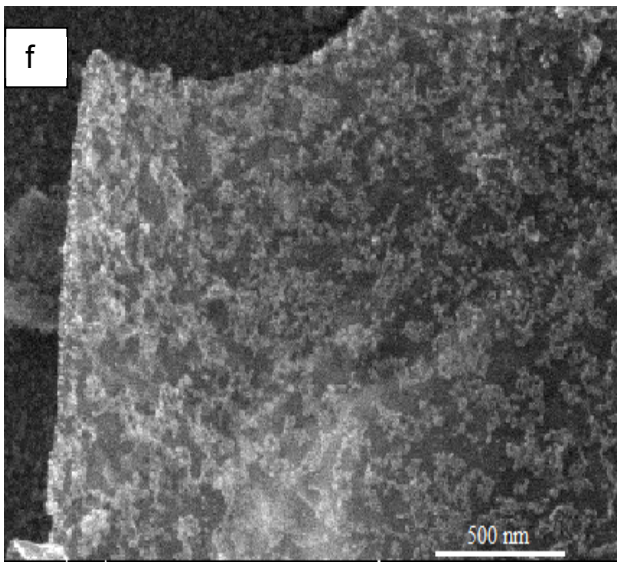


Figure 3.1. Raman spectra of (a) exfoliated graphene, and SEM images of (b) exfoliated graphene (c) G1Zr2, (d) G1Zr4, (e) G1Zr8 and (f) G1Zr16. Exfoliated graphene was found to be thin and with well-dispersed ZrO_2 *nanoparticles.*

The evidence of the formation of ZrO_2 nanoparticles on the surface of graphene was also supplemented by TEM analysis shown in Figure 3.2 (a)-(b). In agreement with the SEM result, TEM showed that the exfoliated graphene was transparent, indicating its thinness (Figure 3.2 (a)) and the nanocomposite G1Zr8 has a well-dispersed layer of ZrO_2 nanoparticles coated on the thin graphene (Figure 3.2 (b)). The chemical composition of the nanocomposites was analysed by EDX. The peaks of C, O and Zr in the EDX spectrum (Figure 3.2(c)) showed the presence of carbon (graphene) and ZrO_2 compounds. The peak corresponding to Si in the EDX spectrum was due to the silicon substrate used for the characterisation. No other peak was detected endorsing the purity of the ZG composites.

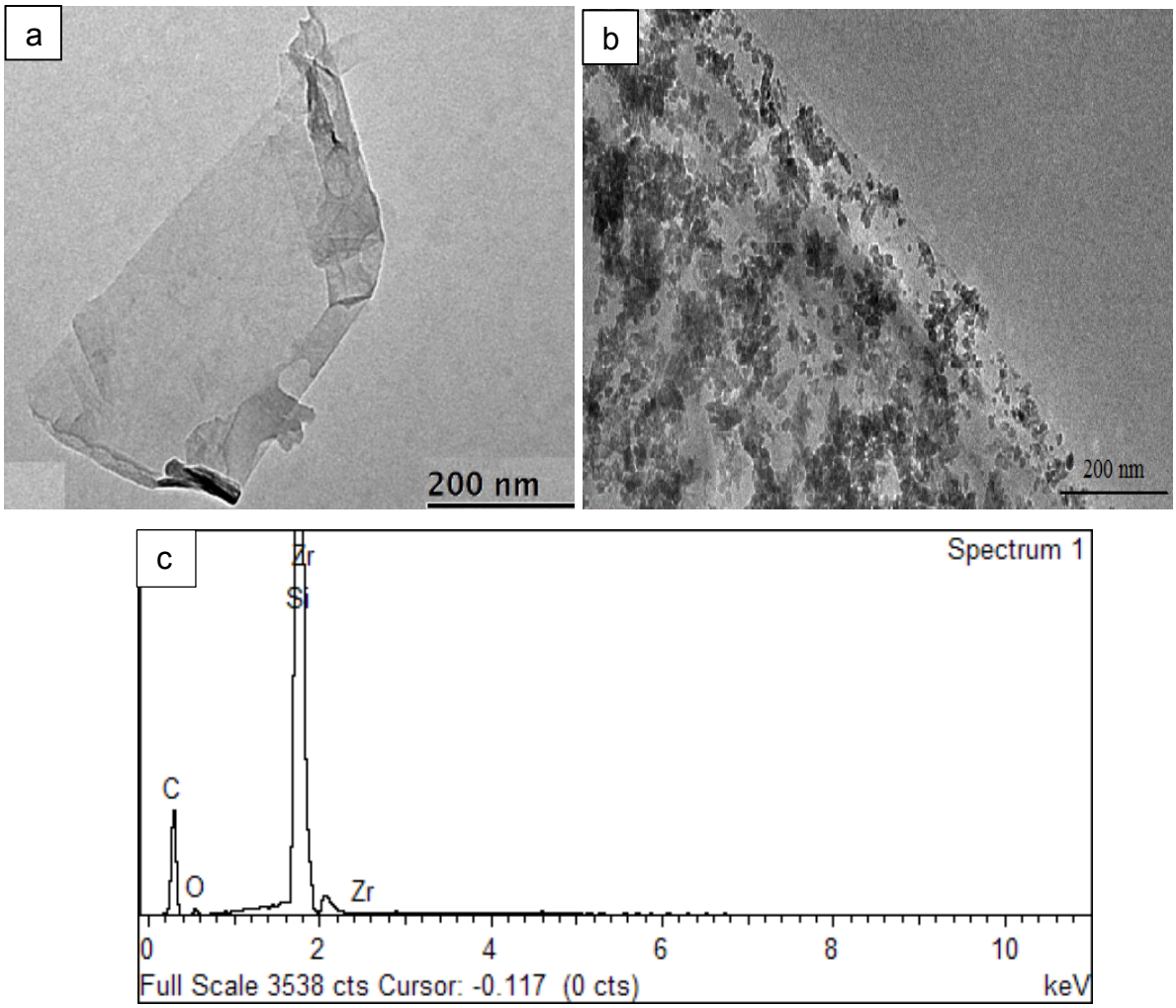


Figure 3.2: TEM images *of (a) exfoliated graphene (b) G1Zr8, and (c) EDX of ZG nanocomposite. The TEM results complement the SEM observation that the synthesised graphene is thin and* ZrO_2 *are well-anchored on the graphene sheets.*

The XRD of ZrO_2 and the ZG composites are shown in Figure 3.3. The pristine nature of graphene was well-preserved after the hydrothermal process as indicated by the two intense diffraction peaks observed in both graphene and the composite samples at around 2θ values of 26° and 55°, attributed to (002) and (004) reflections of graphite respectively (ICSD No. 98-005-2916). The synthesised ZrO_2 nanoparticles were composed of a mixture of monoclinic zirconia (m-ZrO_2) and tetragonal zirconia (t-ZrO_2) with peaks at 2θ of 28.06°, 30.6°, 31.6°, 34.6°, 50.3°, 55°, 60.3°, which can be identified as m (-111), t (101), m (111), m (200), t (220), m (122) and t (311) crystal planes, respectively [26], [27]. As can be seen, the ZG nanocomposite displayed obvious diffraction peaks of both ZrO_2 and graphene. The increase in intensities of the corresponding diffraction peaks of the nanocomposites was a direct reflection of the mass loading increase of ZrO_2, with G1Zr8 and

G1Zr16 having relatively higher intensity and sharper peaks, suggesting a more successful hybridisation of the nanocomposite. The XRD result was consistent with SEM analysis that showed a relatively better dispersion of ZrO_2 on graphene sheets for G1Zr8 and G1Zr16.

Molar fractions of monoclinic (X_m) and tetragonal phases (X_t) of ZrO_2 were estimated using the equations proposed by Toraya shown in equation 3.4 [287]:

$$Xm = \frac{I\,m(\bar{1}11)+I\,m(111)}{I\,m(\bar{1}11)+I\,m(111)+I\,t(101)} \qquad \text{(Eq 3.4)}$$

Where $I\,m(\bar{1}11)\ and\ I\,m(111)$ are the intensities of (-111) and (111) diffraction peak of m-ZrO_2, $I\,t(101)$ is the intensity of (101) diffraction peak of t-ZrO_2 and X_m is the intensity ratio of m-ZrO_2. The calculated intensity ratio X_m was about 65%, which suggests that m-ZrO_2 and t-ZrO_2 coexist in the ZG nanocomposites. According to the monoclinic-tetragonal phase transformation of ZrO_2, the tetragonal phase is usually formed above 1170 ˚C, but it could also be formed as a metastable tetragonal phase at low temperature as seen in this work [288].

The average grain size (D) of the nanocomposite was calculated using the Scherrer formula shown in equation 3.5 [26]:

$$D = \frac{k\lambda}{\beta \cos\theta} \qquad \text{(Eq 3.5)}$$

Where λ (=1.54060 Å) is the Cu-Ka radiation wavelength, β is the full width at half maximum of the diffraction peak, k is the diffraction constant (0.9), and θ is the Bragg angle. Based on the XRD, the calculated average size was about 10.46 nm, which favoured the formation of composite with a high surface-to-volume ratio.

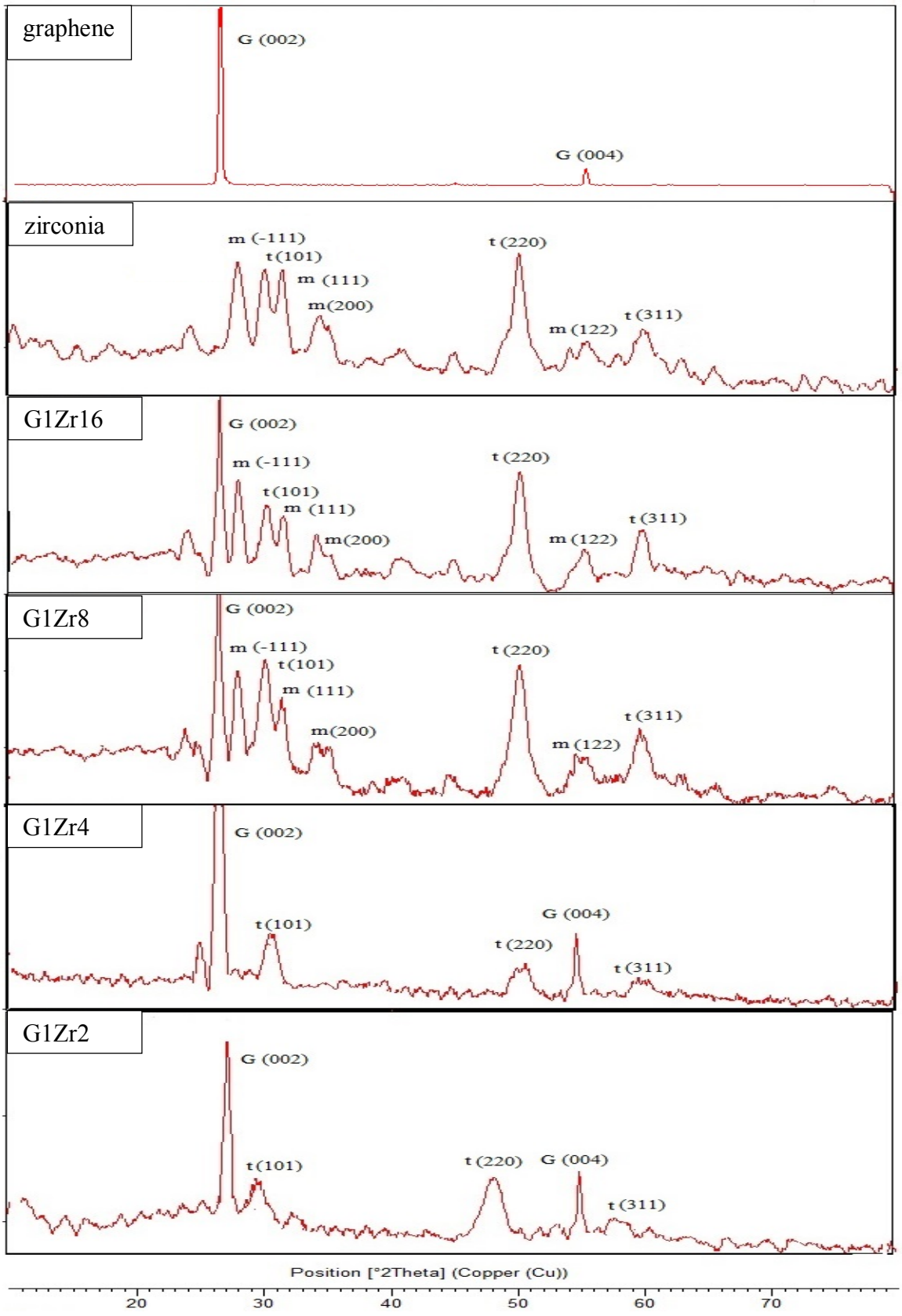


Figure 3.3. XRD peak of graphene, ZrO_2 and ZG nanocomposite at different precursor ratios. ZG nanocomposite displays diffraction peaks of both ZrO_2 and graphene, indicating successful hybridisation.

3.3.2 ELECTROCHEMICAL RESPONSE OF ZG/SPCE TOWARDS POTASSIUM FERRICYANIDE

In order to investigate the potential of the as-synthesised nanocomposite for electrochemical applications, CV analysis was carried out on the SPCEs. As shown in Figure 3.4 (a), the bare electrode showed a pair of redox peaks at anodic peak potential, Epa = 0.2 V and cathodic peak potential Epc = 0 V. A decrease in peak-to-peak separation (ΔEp) was observed for ZG/SPCE (G1Zr8 and G1Zr16), with Epa = 0. 17 V and Epc = 0.03 V. The smaller peak separation indicated the fact that the overpotential of the redox process of $[Fe(CN)_6]^{3-/4-}$ at ZG/SPCE was smaller and the electron transfer rate is faster compared with the bare SPCE [289]. Both G1Zr8/SPCE and G1Zr16/SPCE showed an increase in peak current as compared to bare electrodes with G1Zr8 modified electrodes exhibiting the best electrochemical response, attaining almost a 30% increase of peak current as compared to bare SPCE. A low current response was observed for G1Zr2/SPCE and G1Zr4/SPCE, which was likely due to the inhomogeneous adhesion of nanoparticles on the graphene sheet as suggested by SEM and TEM. The particle aggregation of ZrO_2 formed non-conducting layers that can increase its intrinsic resistivity and deteriorate the charge transfer capacity. Also, these non-conducting layers on the SPCE working electrode surface reduced the amount of surface area accessible to the electrolyte ions thereby limiting its electrochemical performance [30]. The existence of graphene seemed to be an essential contribution to the observed electrochemical activity of the composite, as it was observed that the ZrO_2-modified electrode did not improve the conductivity of the electrode. The role of ZrO_2 on the graphene surface was to act as spacers and prevent restacking of the graphene sheet [27]. Graphene served as high-performance support to allow ZrO_2 to disperse on its plane uniformly, and the charge transfer at the interface of the composite could demonstrate a synergistic effect that was different from graphene and ZrO_2 individually as shown by the G1Zr8/SPCE. Accordingly, G1Zr8/SPCE which demonstrated the highest redox current was used in all subsequent analyses.

To investigate whether the amount of ZG nanocomposite deposited on the electrode would affect the sensing capability of G1Zr8/SPCE, the effect of dispersion concentration and dispersion volume used to modify the working electrode was assessed. ZG dispersion of different concentrations (0.5 mg/ml – 2.5 mg/ml) was deposited on the working electrode, and CV measurements were taken for each deposition. The result (Figure 3.4 (b)) showed that as the dispersion concentration was increased from 0.5 mg/ml to 2 mg/ml, the peak current increased accordingly, likely due to improved surface-area-to-volume ratio and better electron transfer kinetics following the incorporation of more nanocomposite on the modified electrode. Further increment of concentration to 2.5 mg/ml resulted in the decrease of peak current. This could be attributed to the agglomeration of deposited nanocomposite which hindered the surface electron transfer kinetics [248]. Similarly, ZG dispersion of different volumes (2 uL – 10 uL) was deposited on the working electrode, and the volume of dispersion that gave the highest response was observed to be 8 uL (Figure 3.4 (c)). The plateau of peak current was observed for a volume of more than 8 uL, probably due to the poor electron transfer caused by the overly dense nanocomposite as mentioned earlier. In short, the investigation supported the fact that an optimum amount of nanocomposite deposited on an electrode surface could contribute to improved sensing capability.

In any diffusion-controlled and chemically reversible electrochemical process (Nernstian system), the peak current is always linearly proportional to the square root of the scan rate [290]. Figure 3.5 shows the effect of varying the CV scan rate from 25 mV to 200 mV. With the maximum peak currents always occurring at the same voltage, a higher peak current was observed when a faster scan rate was used. The magnitudes of both anodic and cathodic peak currents in this work exhibited a linear relationship with the square root of scan rate, with a correlation factor R^2 of 0.99. This indicates that the electrochemical reaction at G1Zr8/SPCE is a diffusion-controlled process [6].

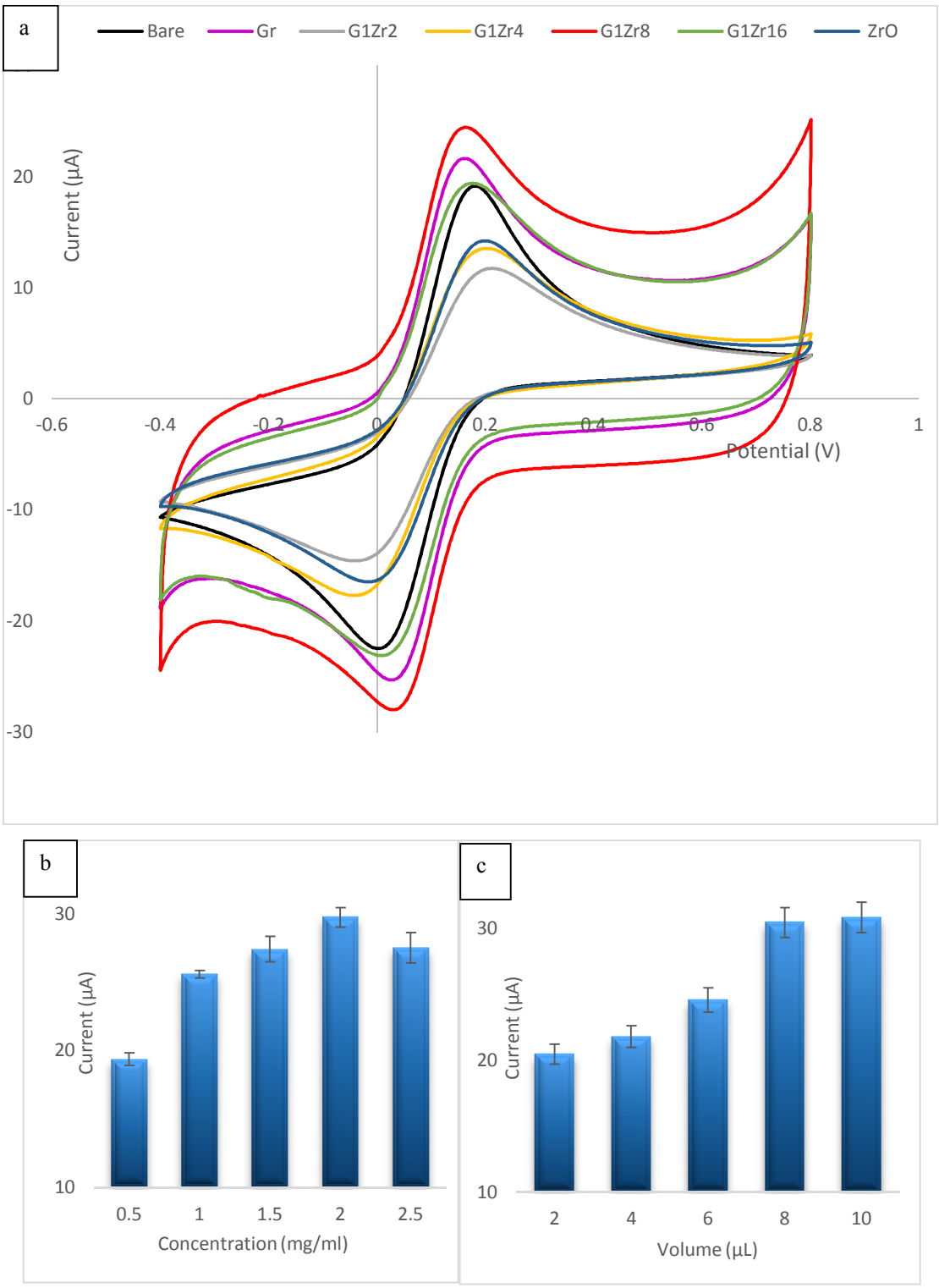


Figure 3.4 CV of (a) bare SPCE, graphene-modified SPCE, ZrO_2-modified SPCE, and ZG-modified SPCE (G1Zr2, G1Zr4, G1Zr8, G1Zr16), (b) effect on peak current for different ZG dispersion concentrations, (c) effect on peak current for the different drop-casted volume of ZG dispersion. It was observed that G1Zr8/SPCE produced the highest peak current due to the increase of the surface area to react with the redox probes.

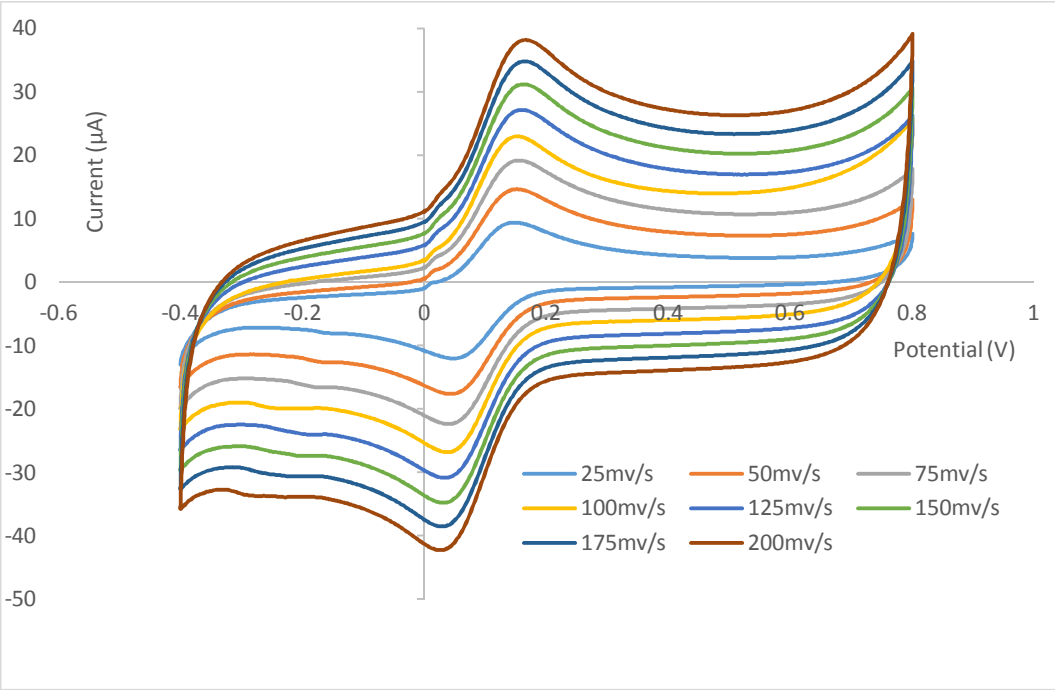


Figure 3.5. CV of G1Zr8/SPCE at various scan rate (from inner to outer curve); 25, 50, 75, 100, 125, 150. 175 and 200 mV /s. The electrochemical reaction at G1Zr8/SPCE is found to be a diffusion-controlled process in 0.01 M PBS of pH 7.4.

The electrochemical properties of the modified SPCE were further investigated by EIS measurements. Nyquist plots were used to analyse the response of the modified electrode in the frequency domain. Ideally, the Nyquist plot consists of two regions: a low-frequency region that represents mass transport phenomena which are characterised by a vertical line with a 45° slope; a high-frequency region that represents electron charge transfer at the electrode/electrolyte interface which is represented by a semicircle. Figure 3.6 shows the Nyquist plot of modified electrodes in which the intercept of the real components at the start of the semicircle indicates the resistor-like behaviour of the electrolyte, and the diameter of the semicircle arc on the real axis represents the Rct between the electrode/electrolyte interfaces. For comparison, the Rct was arranged in the order of ZrO_2/SPCE > bare SPCE> graphene/SPCE > G1Zr8/SPCE, with G1Zr8/SPCE having the lowest Rct of all electrodes. Since Rct is inversely related to current, this finding was in agreement with the CV measurement that had demonstrated G1Zr8/SPCE having the highest peak current, or in other words, the fastest electron transfer among the four modified electrodes. Similar to the finding reported in the literature [34], the ZrO_2-modified electrode

showed relatively larger semicircles suggesting that modification of the electrode with only ZrO_2 particles introduced greater resistance to the redox process. The presence of ZrO_2 nanoparticles alone may not be beneficial and it was obvious that the synergetic effect of graphene and ZrO_2 was the key to the improved electrochemical performance. The introduction of ZrO_2 prevented the restacking of the graphene sheets and increased the active surface area for the redox reaction.

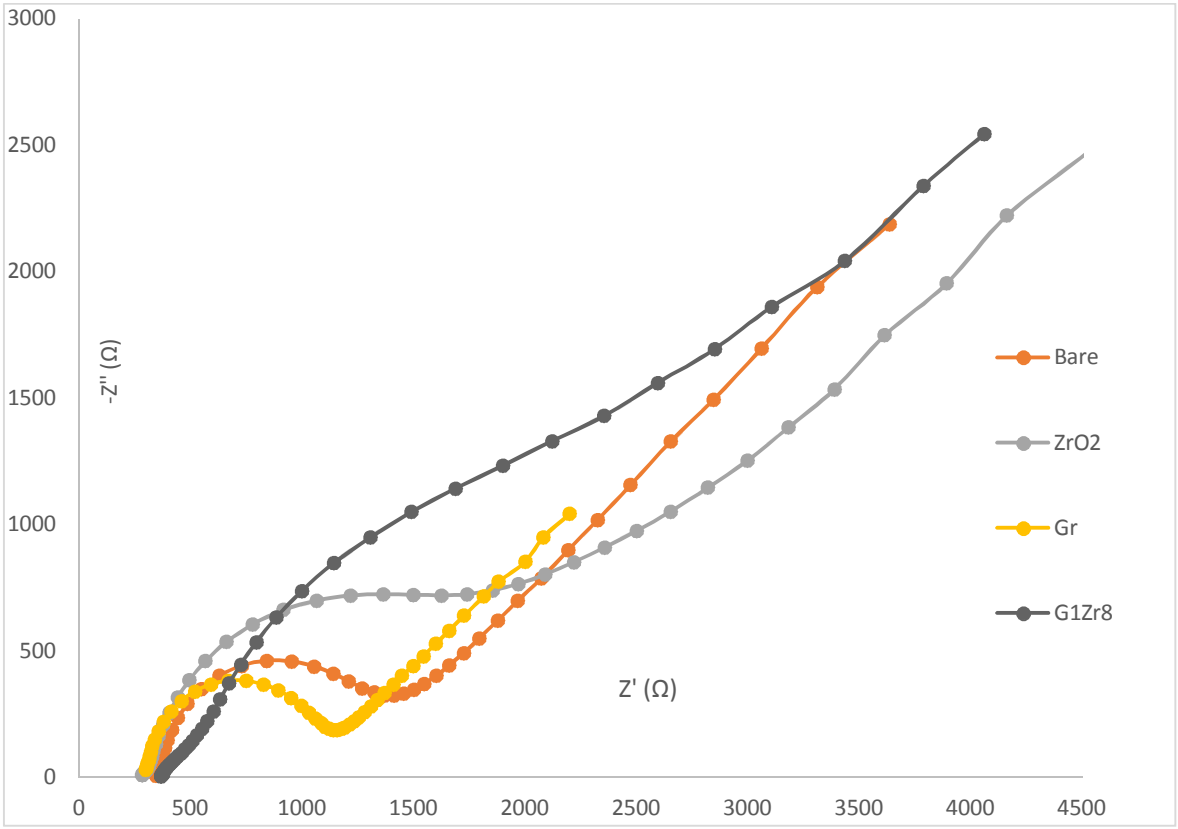


Figure 3.6. Nyquist plots for bare SPCE, graphene-modified SPCE, ZrO_2-modified SPCE, and G1Zr8-modified SPCE, obtained in 0.01 M PBS(pH 7.4) containing 10 mM of redox probes.

3.3.3 MICROSCOPIC VISUALISATION OF CELL-MATERIAL INTERACTION

MRC5 and HaCaT are both mammalian cells that grow on substrates. At near 80% confluence, the cells would associate with each other in colonies. MRC5 is a diploid human cell culture line composed of fibroblasts derived from human lung tissue. A healthy MRC5 cell has an elongated appearance; it is fibroblastic and can be bipolar or multipolar. Meanwhile, HaCaT is the immortalised keratinocyte cell line from adult human skin. Healthy HaCaT cells have a cobblestone appearance, in which cells are rounded and display a high mitotic index. The two

characteristics evaluated via the microscope were the apparent cell density (corresponding to proliferation) and the morphology of the cells. Some of the ZG nanocomposites may have agglomerated after the long hours of incubation giving rise to the appearance of black dots seen in treated cells. Nonetheless, it is postulated that the low degree of agglomeration was not affecting the cytotoxicity study as most of the ZG nanocomposites were still in the nanometer range.

Untreated MRC5 cells (Figure 3.7 (a)-(c)) and HaCaT cells (Figure 3.8 (a)-(c)) showed ongoing proliferation and increase in density throughout the 72 hours of observation. A similar apparent density of cells was also observed for MRC5 cells (Figure 3.7 (d)-(f)), and HaCaT cells (Figure 3.8 (d)-(f)) treated with 50 μg/ml of ZG nanocomposite. This observation suggested that ZG nanocomposite did not seemingly inhibit the proliferation of both cell lines. Other than that, typical signs of cell death including granularity around the nucleus, cytoplasmic shrinkage and detachment of the cells from the substrate were not observed for both treated cell lines up to 72 hours of incubation with ZG, endorsing the low cytotoxicity of the nanocomposite.

The morphology of treated MRC5 cells and HaCaT cells was similar to that of the untreated cells. Throughout the 72 hours of incubation, treated MRC5 cells appeared healthy and retained their elongated fibroblastic morphology; likewise, treated HaCaT cells had similar cobblestone morphology to the untreated cells. In a nutshell, both treated and untreated cell lines exhibited no significant change in terms of proliferation rate and morphology, accompanied by no significant sign of necrosis induced by the ZG nanocomposite.

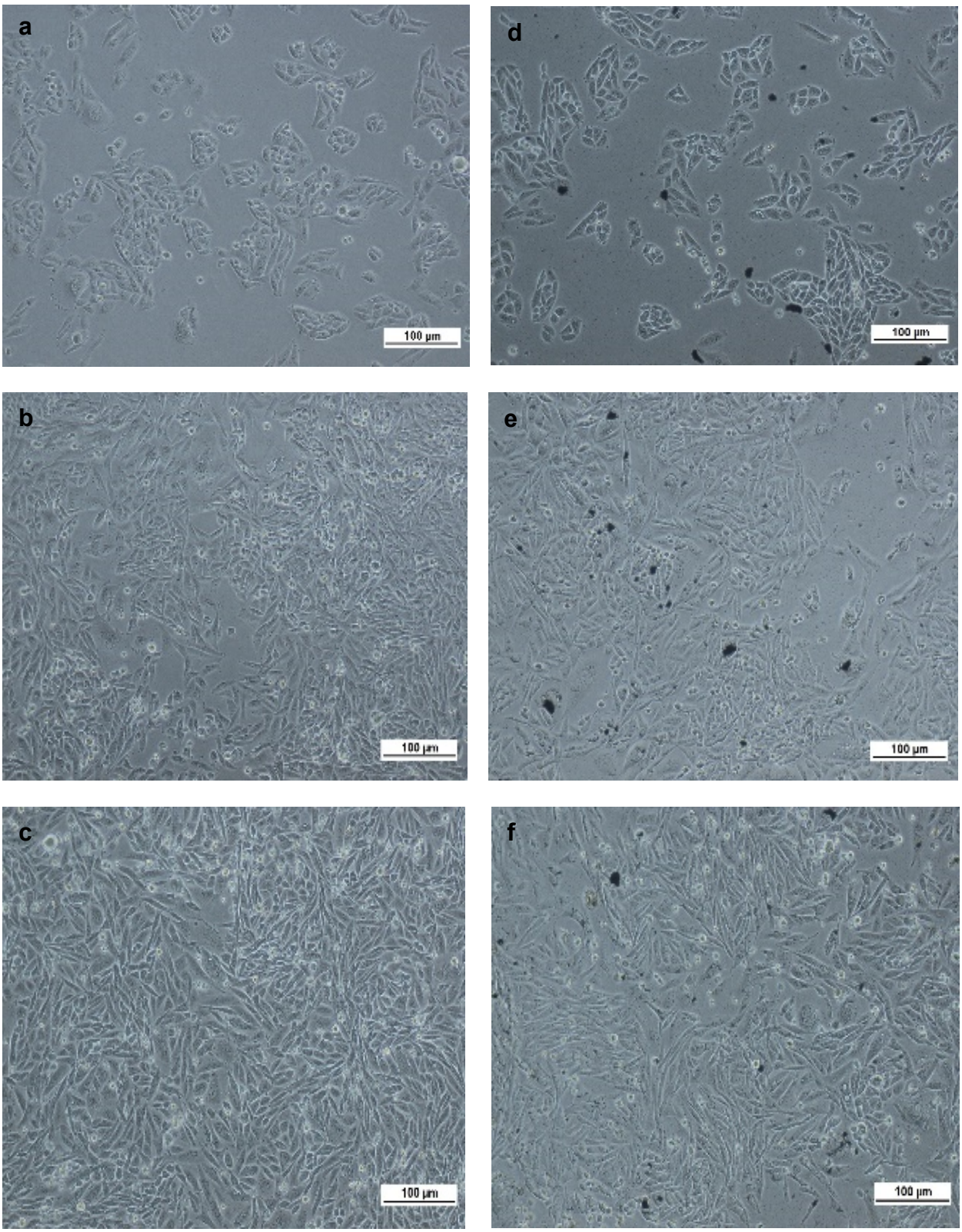


Figure 3.7: Microscopic characterisation of untreated MRC5 cells at (a) 24 hours, (b) 48 hours, (c) 72 hours, and MRC5 cells treated with 50 µg/ml of ZG nanocomposite at (d) 24 hours, (e) 48 hours, (f) 72 hours. The presence of ZG nanocomposite did not present a threat to the viability of MRC5 cells. Cells appeared healthy and retained their fibroblastic morphology throughout 72 hours of the incubation period.

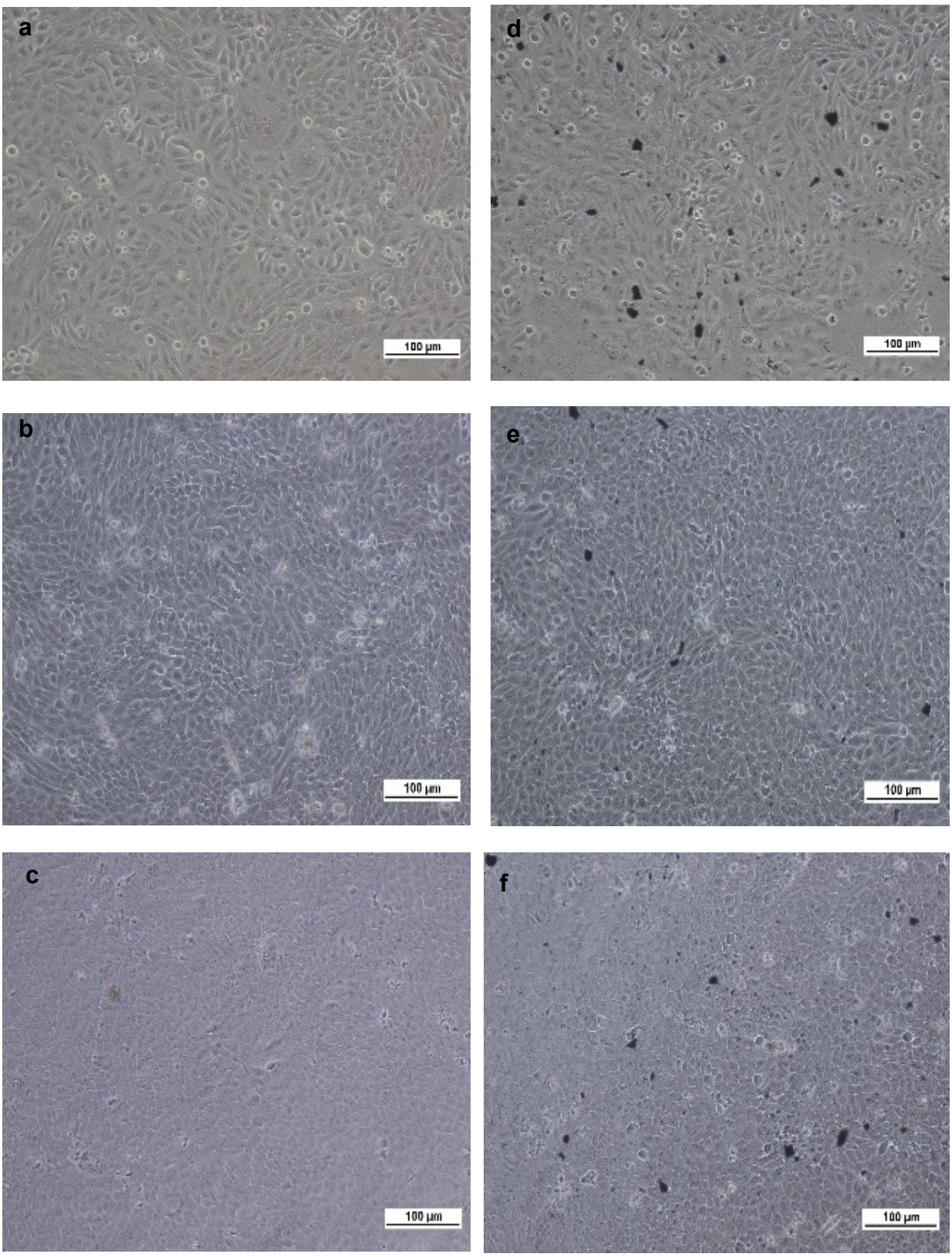


Figure 3.8. Microscopic characterisation of untreated HaCaT cells at (a) 24 hours, (b) 48 hours, (c) 72 hours; and HaCaT cells treated with 50 µg/ml of ZG nanocomposite at (d) 24 hours, (e) 48 hours, (f) 72 hours. The presence of ZG nanocomposite did not considerably inhibit the viability of HaCaT cells. Treated cells retained comparable morphology as the control throughout 72 hours of the incubation period.

3.3.4 MTT CELL VIABILITY STUDY

In parallel to microscopic analysis of material-cell interaction, cell viability was evaluated via the conventional MTT reduction assay. The MTT assay quantified the mitochondrial metabolic activity of the viable cells, henceforth serving as an indication of the intracellular redox state [291]. Only cells retaining normal metabolic function were able to reduce tetrazolium salt to formazan purple solution via the action of mitochondrial dehydrogenase enzyme [292]. Hence the absorbance of the solution corresponded to the rate of cell survival; a higher rate of cell viability would result in a greater degree of absorbance and vice versa.

MTT assessment of the ZG nanocomposite exhibited duration-dependent and dose-dependent toxic effects on cell viability, as shown in Figure 3.9. It was observed that a higher concentration of nanocomposite induced greater loss of viability given constant incubation time; meanwhile, at a constant ZG concentration, cell viability declined greater with longer exposure to the material. Based on ISO 10993-5, the percentages of cell viability indicate that >80% as non-cytotoxic at all; within 60%–80% as weakly cytotoxic; within 40%–60% as moderate cytotoxic and <40% as strong cytotoxic to cells [293].

Notably, the cell viability was observed to be generally high for cells incubated with ZG nanocomposite for only 24 hours. As manifested in Figure 3.9 (a), cell viability after 24 hours of incubation with 0.5 µg/ml (lowest concentration) and 500 µg/ml (highest concentration) of ZG nanocomposite was observed to be > 99% and >90% respectively for HaCaT cell line, and >99% and >94% respectively for MRC5 cell line, endorsing its non-cytotoxicity according to ISO 10993-5 standard. ANOVA analysis showed that the reduction in cell viability caused by the increase of ZG nanocomposite concentration was statistically insignificant ($p > 0.05$) for MRC5 cells but had met statistical significance ($p < 0.05$) for HaCaT cells. Nonetheless, Dunnett's comparison test further indicated that the reduction of cell viability of HaCaT cells was significant as compared to the control ($p < 0.05$) only at ZG concentration ≥ 50 µg/ml. In short, it is established that exposure

to a low concentration of ZG nanocomposite (< 50 μg/ml) for a short duration of time (24 hours) was practically harmless for both cell lines.

Likewise, as shown in Fig. 3.9 (b), cell viability after 48 hours of incubation with 0.5 μg/ml to 500 μg/ml of ZG nanocomposite was observed to decrease from 99% to 89% for HaCaT cells and 98% to 74% for MRC5 cells. ANOVA analysis supported the suggestion that the difference in cell viability was statistically insignificant ($p > 0.05$) for HaCaT cells at 48-hour time point; Meanwhile, ANOVA and Dunnett's comparison analysis showed that reduction of cell viability for MRC5 cells was statistically significant ($p < 0.05$) following incubation with ZG concentration of ≥ 50 μg/ml. In summary, at the 48-hour time point, it was recognised that HaCaT cells demonstrated resistance to the presence of ZG nanocomposite while MRC5 cells were insignificantly affected by exposure to ZG nanocomposite of less than 50 μg/ml.

As the incubation time was extended to 72 hours, as shown in Fig. 3.9 (c), the HaCaT cell line was observed to be rather resilient, retaining approximately 82% of cell viability after incubation with 500 μg/ml of ZG nanocomposite, indicating no cytotoxicity. On the other hand, the MRC5 cell line was observed to experience slightly more loss following the same incubation condition, with approximately 67% of cell viability retained, suggesting reasonable biocompatibility (only weak cytotoxicity) on lung cells according to the ISO 10993-5 standard. ANOVA and Dunnett's analysis validated that the reduction of cell viability for both cell lines was statistically significant, in which the statistical difference as compared to the control started at a ZG concentration of ≥ 50 μg/ml for both HaCat cells and MRC5 cells ($p < 0.05$).

In short, the MTT result revealed that the treated HACaT and MRC5 cells were not affected by ZG of < 50 μg/ml up to 72 hours of incubation. Supported by high cell viability measured at the 24-hour time point, it was also advocated that short-term exposure to ZG was practically harmless to the cells even at high concentrations. As well, according to ISO 10993-5 standard, ZG is non-toxic at all to HaCat cells which retained > 80% of viability after 72 hours of incubation with the highest 500 μg/ml of ZG nanocomposite, it is also non-toxic to MRC5 cells for incubation with

ZG material of less than 250 µg/ml. A vast majority of the cell populations survived up to 72 hours of incubation, and ZG nanocomposite was deemed safe for biomedical and bio-sensing applications.

The half-maximal inhibitory concentration, IC50, is established to be the inhibitor concentration (in this case, the concentration of the ZG nanocomposite) that decreases the cell viability by 50% [294]. It is a comparative index to quantify the toxicity of different materials. A low IC50 indicates that a material induces cell death at a low concentration of material exposure and the material concerned is deemed highly toxic to cells; meanwhile, a high IC50 suggests that material is highly biocompatible wherein most cells remain healthy even after exposure to a high concentration of the material. IC50 of the ZG nanocomposite was found to be > 500 µg/ml for both HaCaT and MRC5 cells, or in other words, 500 µg/ml of ZG nanocomposite was well below the toxic level of diminishing half of the cell population. The IC50 of ZG was excellent as compared to other nanocomposites. Table 3.2 summarises the comparison of IC50 for nanomaterials commonly used in biosensors fabrication.

The high cell viability and thus the superior IC50 given by the ZG nanocomposite indicated that the nanocomposite was safe on human lung (MRC5) and skin (HaCaT), the two organs most susceptible to nanocomposite toxicity through inhalation and physical contact. This finding strongly endorsed the application of the as-synthesised ZG for medical and industrial purposes, including the functionalisation of the immunosensor demonstrated in this work. While being equally proficient in DNA and antigen detection, the genosensor and immunosensor fabricated in this work were a more superior option considering health and safety requirements. Some other sensors that were fabricated using highly toxic nanomaterials may be hazardous for researchers exposed to the materials through inhalation or physical contact. These materials may also induce severe environmental concerns during mass production. In a nutshell, nanocomposite ZG is a safe and promising electrode material; therefore, our proposed sensors that employed a cyto-safe material have established an upper hand over other reported sensing platforms.

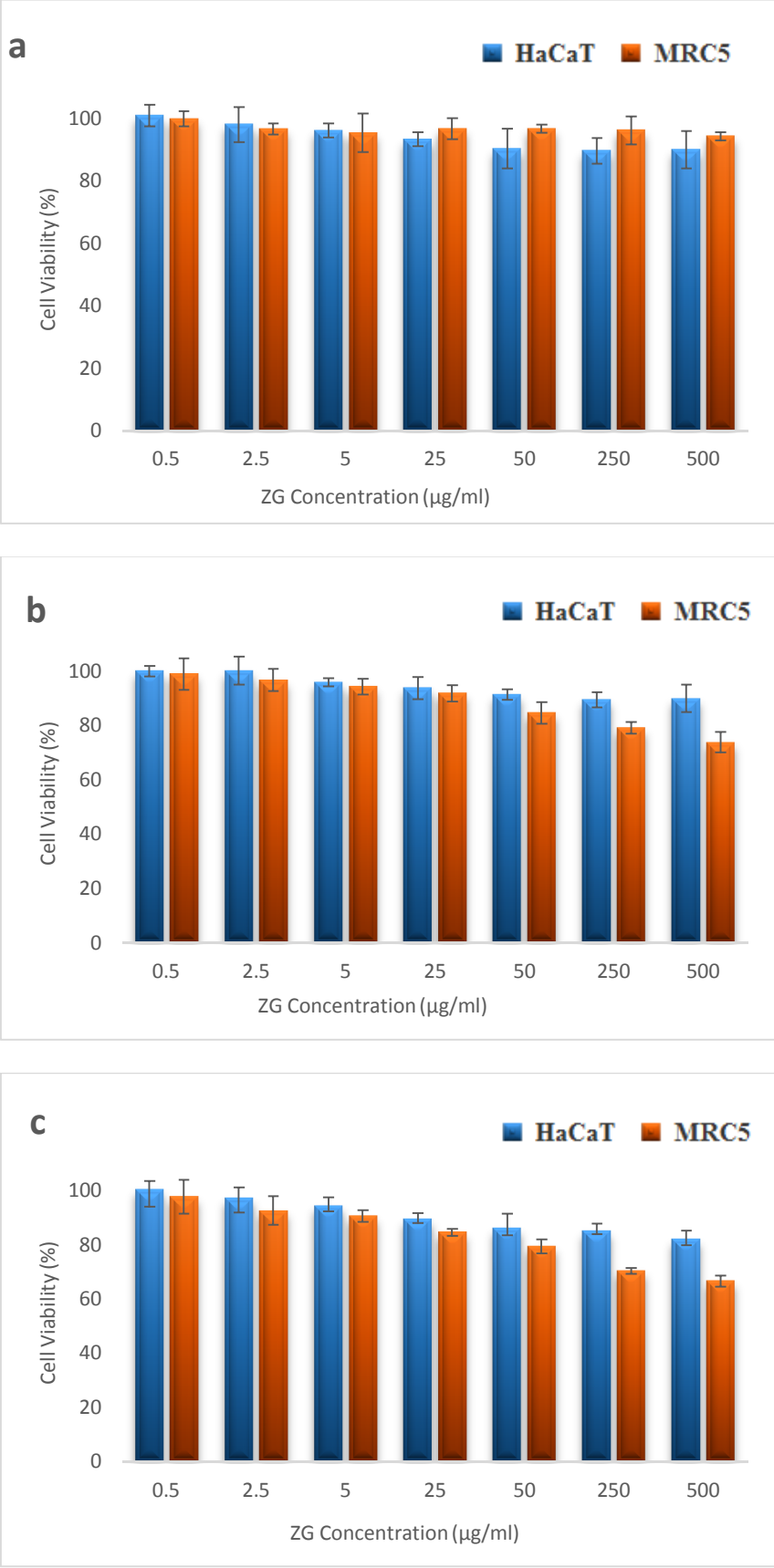


Figure 3.9. Cell viability of HaCaT and MRC5 cells lines treated with ZG nanocomposite for (a) 24 hours, (b) 48 hours, (c) 72 hours. HaCaT cell line and MRC5 cell line retained high cell viability after incubation with the nanocomposite. ZG nanocomposite was considered to be biocompatible for both cell lines.

Table 3.2: Comparison of IC_{50} for Nanomaterials Commonly Used in Biosensors Fabrication

Nanomaterials	Cell line	Endpoint	Toxicity Value	Ref
Graphene/ZrO_2	Lung fibroblast, MRC5	MTT assay (24 h) MTT assay (48 h) MTT assay (72 h)	IC_{50} > 500 µg/ml IC_{50} > 500 µg/ml IC_{50} > 500 µg/ml	This work
	Human keratinocyte, HaCaT	MTT assay (24 h) MTT assay (48 h) MTT assay (72 h)	IC_{50} > 500 µg/ml IC_{50} > 500 µg/ml IC_{50} > 500 µg/ml	
ZrO_2	Human monocytic, THP-1	MTT assay (24 h)	IC_{50} ~ 171.9 µg/ml	[295]
	Rat pheochromocytoma, PC 12	MTT assay (12 h) MTT assay (24 h) MTT assay (48 h)	IC_{50} ~ 66.68 µg/ml IC_{50} ~ 53.32 µg/ml IC_{50} ~ 40.82 µg/ml	[296]
	Rat neuroblastoma, N2a	MTT assay (12 h) MTT assay (24 h) MTT assay (48 h)	IC_{50} ~ 45.49 µg/ml IC_{50} ~ 33.06 µg/ml IC_{50} ~ 26.27 µg/ml	
Co_3O_4	Human bronchial epithelial, BEAS-2B	MTT assay (24 h)	IC_{50} ~ 50 µg/ml	[297]
		Lactate dehydrogenase assay (24H)	IC_{50} ~ 100 µg/ml	
ZnO	Human lung adenocarcinoma cells, A549	Neutral red uptake assay (24 H)	IC_{50} ~ 25 µg/ml	[298]
	Human epithelial colorectal adenocarcinoma cells, Caco2		IC_{50} ~ 30 µg/ml	
Graphene oxide nanosheet	Human adenocarcinomic alveolar basal epithelial cell line, A549	MTT assay (24 h)	IC_{50} ~ 100 µg/ml	[299]
Graphene/TiO_2	Human keratinocyte, HaCaT	MTT assay (24 h) MTT assay (48 h) MTT assay (72 h)	IC_{50} = 25 µg/ml IC_{50} = 25 µg/ml IC_{50} = 5 µg/ml	[300]

3.4 SUMMARY

In summary, a facile, green approach for the synthesis of graphene and ZG nanocomposite without any harsh chemicals has been reported. Solvent-exfoliation and hydrothermal methods were used to produce graphene and the ZG nanocomposite. Material characterisation suggested that pristine graphene and well-hybridised nanocomposite was synthesised: the Raman spectra of graphene showed that exfoliation was successful and thin layers of graphene has been produced, XRD results indicated that both graphene and ZrO_2 retained their crystalline structures without any visible lattice disruption caused by the synthesis process, EDX result showed only the presence of carbon and ZrO_2 endorsing the absence of harsh chemical residual, and TEM/SEM analyses showed that graphene was thin and ZrO_2 nanoparticles were homogeneously distributed on the surface of graphene sheets. Apart from material characterisation, the electrochemical performance of the ZG nanocomposite was as well investigated in which the ZG-modified electrodes exhibited excellent activity towards potassium ferricyanide, an active redox probe, as compared to the bare electrode. This improvement was a result of the great properties given by ZG that sees graphene improving the conductivity of the sensor while ZrO_2 nanoparticles serve as spacers to reduce the re-stacking of graphene sheets and increase surface area for redox reaction. Overall, the finding in this study suggests that ZG nanocomposite could serve as a potential platform for fast, low cost and accurate electrochemical sensing.

Our work addressed the safety concern of nanocomposites exposure with a cytotoxicity study of the ZG nanocomposite. Thanks to the scalable and green synthesis method, the ZG nanocomposite was free from residual chemicals resulting in cytotoxicity analysis that showed no adverse effects on human lung and skin cells. The microscopic study revealed that material-treated cells retained comparable morphology and proliferation rate as the control. Meanwhile, the MTT assay showed that exposure to a low concentration of ZG nanocomposite (<50 µg/ml), even up to 72 hours, was practically harmless for both cell lines. Similarly, short term exposure of 24 hours to the ZG nanocomposite (up to 500 µg/ml) was also found to be non-cytotoxic. According to ISO 10993-5

standard, ZG nanocomposite is non-toxic at all to HaCat cells which retained > 80% of viability after 72 hours of incubation with the highest 500 μg/ml of ZG nanocomposite, it is also non-toxic to MRC5 cells for incubation with ZG material of less than 250 μg/ml. A vast majority of the cell populations survived up to 72 hours of incubation; therefore, the IC50 value, which was the concentration of the ZG nanocomposite that reduced the cell viability by 50%, was found to be >500 μg/ml for both MRC5 cells and HaCaT cells. Excellent biocompatibility of the ZG nanocomposite strongly endorsed the application of the material for medical and industrial purposes, including the functionalisation of sensors demonstrated in this research.

4 POTENTIAL OF THE GRAPHENE/ZIRCONIA-BASED PLATFORM AS AN ELECTROCHEMICAL SENSOR: ACETAMINOPHEN AS THE MODEL ANALYTE

4.1 INTRODUCTION

The immunosensor and the genosensor that aimed to detect lung cancer markers would be presented in chapters 5 and 6. These cancer biosensors are essentially electrochemical-based sensors that translate the bio-recognition events (the hybridization of DNA and the antigen-antibody binding) into quantifiable impedance change. The detection of cancer biomarkers is more complicated than the detection of simple electroactive analytes, thus being able to detect electroactive analytes serves as the fundamental requirement of an electrochemical sensor. Therefore, prior to the development of the electrochemical immunosensor and genosenor, it is essential to assess the potential of the ZG platform to serve as a simple electrochemical sensor, taking acetaminophen as the model analyte. The as-synthesised ZG nanocomposite as described and characterised in chapter 3, was applied to modify SPCE and its feasibility for chemical species sensing was demonstrated via acetaminophen detection using DPV. Acetaminophen was chosen as the model analyte as it was widely available as an over-the-shelf medication and prone to overdosing. The improper usage of acetaminophen will lead to overdosing, resulting in the accumulation of toxic metabolites that will cause kidney and liver failures [301]. According to the modified Rumack-Matthew nomogram, acetaminophen concentration in blood serum should drop below 100 μM (ideally 50 μM) 24 hours after ingestion [302]. Given the need to detect overdosing, research is geared towards the development of a simple and effective sensor for the detection of acetaminophen [303]–[306]. The results of this work showed that the proposed ZG-sensor exhibited excellent performance for acetaminophen detection. The sensor response was linearly associated with the concentration of acetaminophen from 10 μM to 100 μM, which fit the clinical concentration of acetaminophen in blood. The sensor was able to selectively detect acetaminophen

against interferences of dopamine and ascorbic acid. Lastly, the sensor performed well in the quantification of acetaminophen in pharmaceutical samples, rendering it a favourable platform for clinical applications.

4.2 EXPERIMENTAL DETAILS

4.2.1 APPARATUS AND MATERIAL

Material additional to those reported in chapter 3 includes acetaminophen, $CH_3CONHC_6H_4OH$ (99%), dopamine, $(HO)_2C_6H_3CH_2CH_2NH_2 \cdot HCl$ (99% Reagent Grade), L-Ascorbic acid, $C_6H_8O_6$ (99%), hydrogen peroxide (H_2O_2, 30%) and glucose that were purchased from Sigma-Aldrich (USA). All the chemicals were used as received without further purification. DI water was used throughout the experiment. DPV measurements of all electrodes were performed using Autolab PGSTAT302N potentiostat (Metrohm, Netherlands) interfaced with analysis software NOVA 1.11.

4.2.2 FABRICATION OF THE ACETAMINOPHEN SENSOR AND ELECTROCHEMICAL MEASUREMENTS

SPCE was first rinsed with DI water and soaked in PBS for 15 minutes for conditioning purposes. The as-prepared ZG nanocomposite was re-dispersed into an ethanol/DI water mixture via ultrasonication for about 30 minutes to form a homogenous dispersion. The sonicated ZG nanocomposite dispersion was drop-casted onto the working electrode of the SPCE and dried at ambient conditions. The modified electrode was ready for acetaminophen detection in PBS buffer. The electrochemical performances of the acetaminophen sensor in connection with DPV were carried out on SPCEs using PBS buffer (0.01 M, pH 7.4) at 100 mV pulse and 60 ms pulse width. Error bars for electrochemical measurements represent the standard deviation of the mean, for triplicates in three independent experiments (n=9).

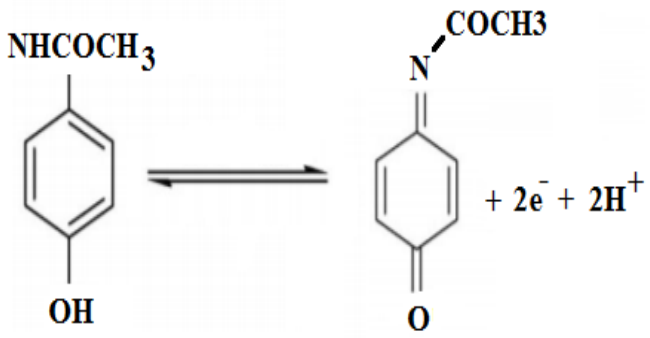
4.2.3 DETECTION OF ACETAMINOPHEN IN COMMERCIAL TABLETS

Pharmaceutical samples of acetaminophen were used to assess the real-sample detection of the proposed sensor. Three different brands of over-the-shelf acetaminophen were obtained from a pharmacy. Acetaminophen tablet was weighted and grounded to fine powder and dissolved in ethanol. To increase the solubility of the tablets, the solvent was mildly warmed and placed under continuous stirring conditions. The stock was then diluted to a working concentration range for the DPV electrochemical determination on the G1Zr8/SPCE.

4.3 RESULTS AND DISCUSSION

4.3.1 ANALYTICAL PERFORMANCE

DPV has the advantages of better sensitivity and resolution for electrochemical quantitative analysis [307]; therefore, DPV was used to investigate the electrochemical behaviour of acetaminophen on G1Zr8/SPCE. DPV analysis was carried out on SPCEs using a PBS buffer of pH 7.4. While there have been reports on the influence of pH on the redox reactions of acetaminophen, pH 7.4, the physiological pH close to human serum, is preferred in terms of practical applications, such as the analysis of acetaminophen levels in physiological fluids. Initially, DPV measurements were taken for G1Zr8/SPCE and bare SPCE in 0.01 M PBS containing 30 μM acetaminophen to investigate the effect of modifying the SPCE with nanocomposite. As shown in Figure 4.1 (a), acetaminophen showed a relatively low redox peak for the bare SPCE, which indicates less efficient electrocatalytic activity towards the oxidation of acetaminophen. Meanwhile, it exhibited a distinctly higher peak current at the G1Zr8/SPCE which can be soundly credited to improved conductivity and surface area of G1Zr8/SPCE [308]. Scheme 4.1 shows the redox mechanism of acetaminophen, which belongs to a two-electron and two-proton process [309]. The reactant was easier to be oxidised at G1Zr8/SPCE, where the over-potential of acetaminophen at G1Zr8/SPCE became lower than that on the bare SPCE with a shifting of 70 mV, probably due to the catalytic effects of graphene sheets [310].



Scheme 4.1: Redox mechanism of acetaminophen. The redox reaction is a two-electron and two-proton process.

Before the sensor is tested against acetaminophen of different concentrations, the effect of pulse width and pulse amplitude of the DPV measurement was evaluated. The pulse width was altered from 20 ms to 100 ms and its effect on the detection of 30 µM of acetaminophen was recorded as shown in Figure 4.1 (b). A rise in the peak current following the increment of pulse width was observed; however, with an increment higher than 60 ms, the peak current starts to decrease probably because of the decay of faradaic current (diffusion-controlled current) due to prolonged diffusion. Since the current was highest at 60 ms, it is adopted for subsequent DPV measurements; Likewise, the optimum pulse amplitude was investigated by varying the pulse amplitude from 25 mV to 250 mV as shown in Figure 4.1 (c). The peak current increased linearly with the increase of pulse amplitude until 100 mV before it started to exhibit a plateau and a slight broadening of the peak. Therefore, 100 mV pulse amplitude was selected as it was sufficiently large to result in a faradaic reaction in response to the redox potential of the redox species, yet without shape distortion of the output peak current.

Subsequently, the fabricated G1Zr8/SPCE was calibrated as an acetaminophen sensor using DPV as shown in Figure 4.2. The inset of the figure shows the corresponding calibration curves obtained at various concentrations of acetaminophen. The sensor response increased following the higher concentration of acetaminophen and gave rise to a linear relationship between the peak current with the concentration of acetaminophen. A linear range from 10 µM to 100 µM, with a linear regression equation of $Ip = 0.1171 \times C\ (\mu M) + 0.4$ ($R^2 = 0.98$) was obtained for acetaminophen detection using the sensor. The detection limit was 75.5 nM (S/N=3).

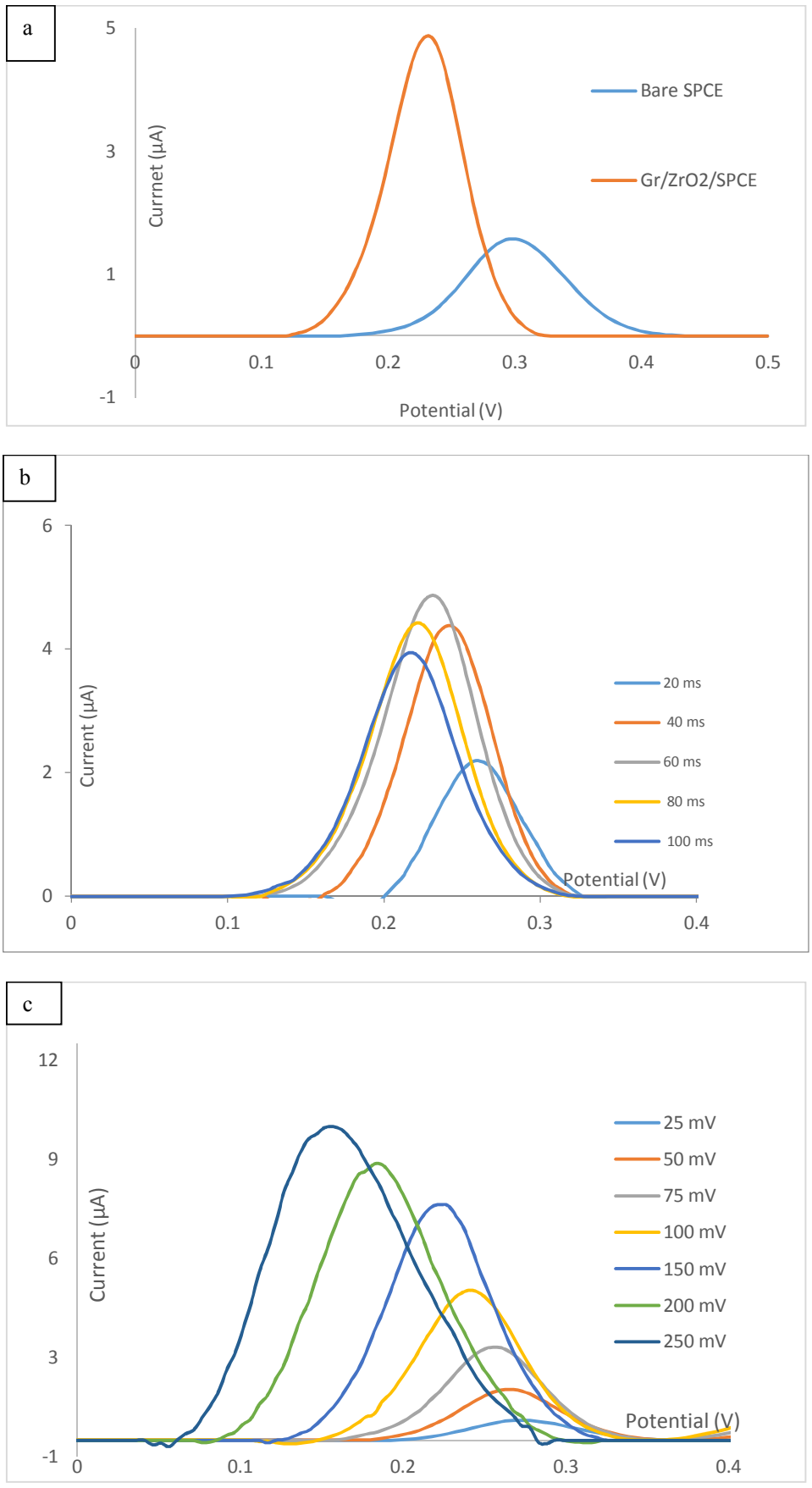


Figure 4.1. (a) DPVs of acetaminophen on bare SPCE and G1Zr8/SPCE in 0.01 M PBS (pH 7.4). (b) effect of pulse width on peak current. (c) effect of pulse amplitude on peak current. 100 mV pulse amplitude and 60 ms pulse width were selected to maximise the peak current without shape distortion.

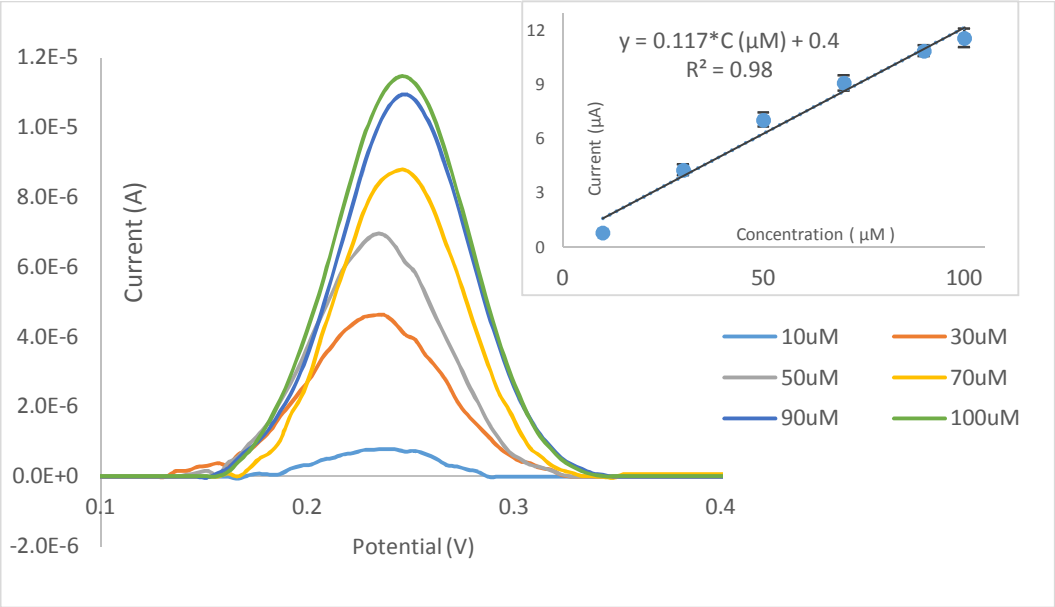


Figure 4.2. DPV response of the sensor towards various concentrations of acetaminophen ranging from 10 µM to 100 µM. Inset: Calibration equation of the proposed sensor. The detection limit of the sensor was found to be 75.5 nM.

A comparison of the as-fabricated sensor to other acetaminophen sensors was made. As shown in Table 4.1, the performance of the ZG-modified sensor is comparable to other similar works reported. On top of the comparative analytical performance, our proposed technique of graphene synthesis is scalable and omitted the use of harsh chemical processing. It is a great improvement as compared to other sensing platforms that used graphene oxide synthesised with harsh acid treatments and results in residual functional groups on the produced RGO [311].

Table 4.1: Performance of the Fabricated Acetaminophen Sensor Against Other Reported Acetaminophen Sensors.

Electrode modification	LOD	Linear Range	Reference
ZG/SPCE	75.5 nM	10 - 100 µM	This work
Carbon nanotube/carbon-ceramic electrode	120 nM	0.2 -100 µM	[312]
RGO-carbon black-chitosan/GCE	53 nM	2.8 -19 µM	[311]
Carbonnanotube-poly(amidoamine) dendrimers/GCE	100 nM	30-200 µM	[309]
poly(p-aminobenzene sulfonic acid)/GCE	43 nM	0.05-100 µM	[304]

4.3.2 REPEATABILITY, REPRODUCIBILITY, STABILITY AND SELECTIVITY

A reliable sensor should be able to produce repeatable and reproducible detections. Therefore, the repeatability of the fabricated acetaminophen sensor was investigated through repeated DPV determination of acetaminophen. After each detection, adsorbents on the SPCE were removed through 10 successive CV swept between 0.0 V and 0.5 V at the rate of 100 mVs^{-1} in blank PBS. The detection-regeneration cycle was repeated 10 times, and 10 measurements show good repeatability with a relative standard deviation (RSD) of less than 3% as depicted in Figure 4.3 (a). Meanwhile, to study the reproducibility of the fabricated sensor, three electrodes were prepared in parallel and used to detect acetaminophen. An acceptable RSD of 5% was observed as shown in Figure 4.3 (b), denoting the good reproducibility of the proposed sensor.

Other than that, a sensor is anticipated to be stable under proper storage. Hence, the stability of the acetaminophen sensor was studied by preserving the sensor at ambient conditions for 5 days before DPV of acetaminophen detection was performed and compared with the response from freshly prepared electrodes. The preserved electrode demonstrated reasonable stability in which it retained about 95% of response output as compared to freshly fabricated electrodes as shown in Figure 4.3 (c). Selectivity is a crucial factor in evaluating the performance of any sensor. DPV responses of the sensor toward acetaminophen in the presence of some possible interfering species namely dopamine, ascorbic acid, glucose and H_2O_2 were studied. Dopamine and ascorbic acid were selected as interfering species because they are often found oxidised at close potential with acetaminophen, resulting in overlapped sensor response [113], [312]. Glucose was selected due to its coexistent with acetaminophen in serum [313]. Acute kidney injury is common among individuals with acetaminophen-induced hepatotoxicity [314], and patients with acute kidney injury have been shown to display a high concentration of H_2O_2 [315], thus it was also worth investigating the interfering effect of H_2O_2. The selective experiments were carried out by testing the sensor against samples containing both the acetaminophen and the different interfering species. It was found that the sensor was not distinctly affected by the presence of glucose and H_2O_2, in

which no additional peak was observed. Meanwhile, well-defined and separated peaks were obtained for acetaminophen detection in the presence of dopamine and ascorbic acid as shown in Figure 4.3 (d), with peak separation of 0.2 V (acetaminophen-dopamine) and 0.23 V (acetaminophen-ascorbic acid). While there have been reports that electrochemical determination of acetaminophen is challenging due to the overlapping oxidation peak with dopamine and ascorbic acid [113], this result indicates that the proposed ZG-based sensor is highly selective with distinct redox potential for the detection of acetaminophen.

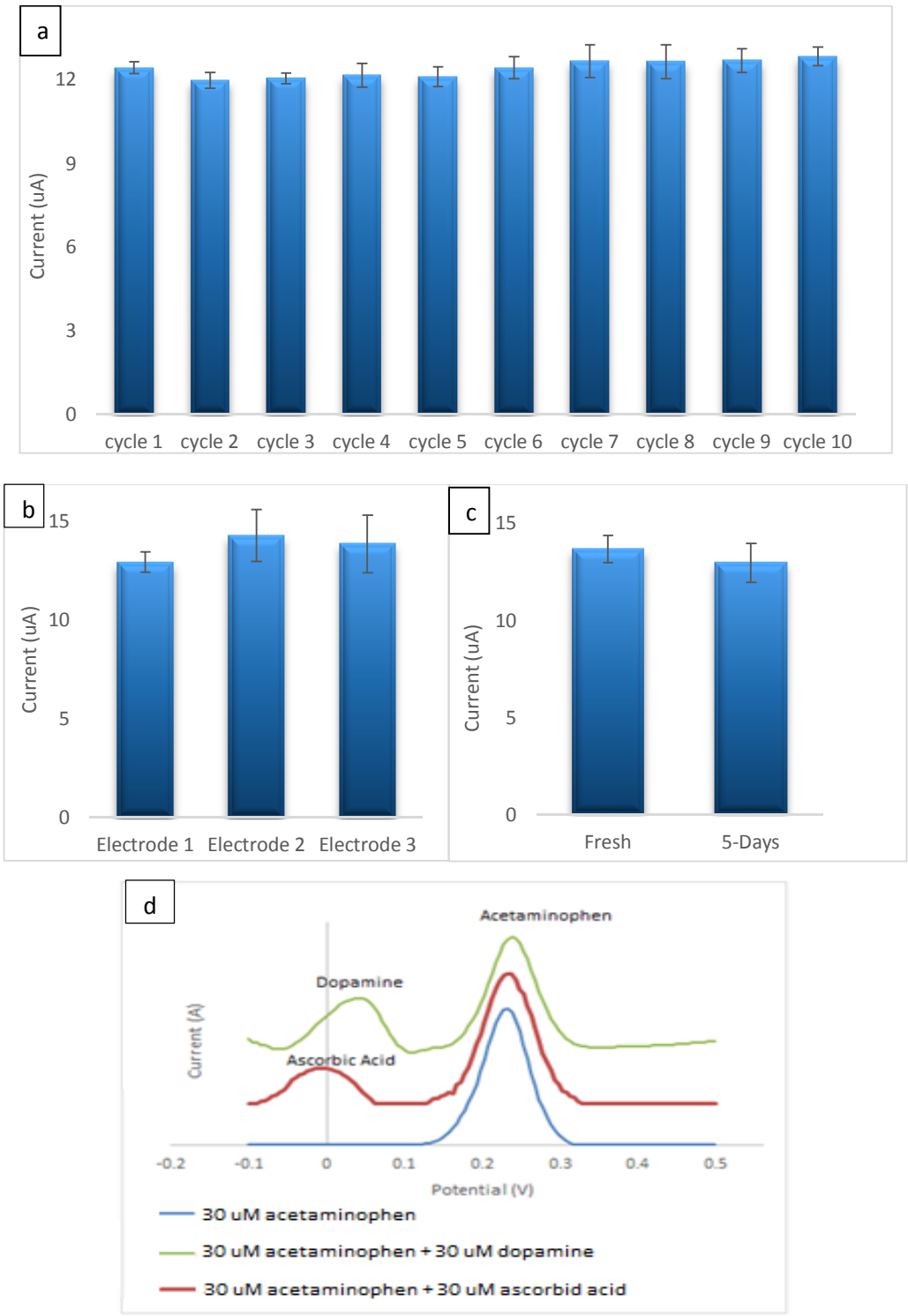


Figure 4.3. DPV for the (a) repeatability study. (b) reproducibility study (c) stability study and (d) selective determination of acetaminophen in the presence of ascorbic acid and dopamine. The sensor demonstrated repeatability of < 3% RSD, reproducibility of 5 % RSD, stability of 95% after 5 days of storage and good selectivity to acetaminophen in the presence of interfering species.

4.3.3 REAL SAMPLE ANALYSIS: DETECTION OF COMMERCIAL TABLETS

Over-the-shelf acetaminophen is easily available to the public and the abuse of the substance is highly likely. Therefore, it is worth investigating the ability of the fabricated sensor to detect acetaminophen from commercial tablets. The sensor was tested against three different brands of acetaminophen that contained 500 mg to 650 mg of acetaminophen. As shown in Table 4.2, acceptable recoveries were obtained in the range of 80% to 85% for three different types of pharmaceutical samples, indicating reasonable, practical applicability of the proposed sensor. In the formulation of tablets, excipients such as pre-gelatinised maize starch and hypromellose were added to provide an extensive range of functionalities, such as better tablet binding ability and more active pharmaceutical bioavailability [316]. The addition of excipients may have affected the release profile of the commercial tablets and resulted in a small amount of undissolved acetaminophen in the stock solution which might, in turn, have contributed to the percentage of error for the electrochemical detection.

Table 4.2: Determination Of Acetaminophen In Commercial Tablets

Pharmaceutical Samples/ Content	Detected	Recovery
Panadol (500mg acetaminophen)	426 mg	85.2%
Uphamol (650mg acetaminophen)	524 mg	80.6%
PORO (500mg acetaminophen)	416 mg	83.2%

4.4 SUMMARY

Acetaminophen is an over-the-shelf medicine that could be easily abused, therefore, an electrochemical sensing platform based on the proposed ZG/SPCE was employed for the detection of acetaminophen using the DPV technique that is capable of sensitive detection. Before the sensor was tested against acetaminophen of various concentrations, pulse width and pulse amplitude of the DPV test were optimised to amplify sensor response. The electrochemical sensor exhibited favourable electrocatalytic performances for the detection of acetaminophen ranging from 10 μM to 100 μM; a LOD of 75.5 nM, repeatability of < 3% RSD, reproducibility of 5 % RSD, stability of 95% after 5 days of storage alongside decent selectivity to acetaminophen in the presence of interfering species were observed. Other than that, the sensor was also challenged with the detection of acetaminophen in commercial tablets. Quantification of acetaminophen gave acceptable recovery in the range of 80% to 85% for three different brands of pharmaceutical samples, supporting the practical applicability of the electrochemical sensor. In a nutshell, the proposed sensor has demonstrated reliable detection for acetaminophen, but its application is far beyond this. The sensor could be employed in the detection of other chemical compounds with the advantages of being low cost and disposable.

5 AN IMPEDIMETRIC GENOSENSOR BASED ON CONTROLLABLE PI–PI FUNCTIONALISATION OF ZIRCONIA-DECORATED GRAPHENE TO DISTINGUISH BETWEEN WILD-TYPE AND MUTATED EXON-19 SEQUENCES IN EPIDERMAL GROWTH FACTOR RECEPTOR

5.1 INTRODUCTION

Lung cancer is a prevalent illness accompanied by a high mortality rate of estimated 132,000 deaths for the year 2021 in the USA [2]. Approximately 85% of all lung cancers are NSCLC, and EGFR is often over-expressed in NSCLC patients [131]. The EGFR is a protein involved in cell signalling pathways that control cell division and survival; this protein is encoded by the EGFR gene located in chromosome 7. The mutations in the EGFR gene cause the EGFR protein to be over-expressed and could result in uncontrolled cell proliferation, migration and resistance from apoptosis, all of which are linked with cancer development [317]. Recalling that protein synthesis initiates at transcription (DNA to RNA) and moves on with translation (RNA to protein) [318], it is useful to detect the mutation of the EGFR gene before the erroneous expression of EGFR protein is present.

A study showed that EGFR mutation was found in 31.6% of all NSCLC patients [143]. Three categories of mutant-DNA have been discovered: exon-19 deletions within the tyrosine kinase domain of EGFR account for about 60% of all mutations; single point replacement (L858R) in exon-21 make-up 25% of all cases; whereas duplications/insertions in exon-20 together with the nucleotide alterations in exons-21, 20 and 18 accounts for the remaining 15% [144], [145]. The most common mutation, exon-19 deletion, was shown to be reactive to erlotinib and gefitinib, tyrosine kinase inhibitors (TKIs) that were introduced more than a decade ago. TKIs have been extensively employed as the prioritised treatment for chemotherapy-free patients, or as the secondary treatment for post-chemotherapy patients [319], with enhanced clinical outcomes as

compared to those treated with the standard cytotoxic chemotherapy [149]. Given the fact that TKI is more effective for patients with exon-19 mutations, the subtype of EGFR mutation should be determined to enable the precise screening of prospective responders. Direct sequencing is the most general approach to identifying DNA mutation; nonetheless, its application is limited by the high cost and the need for trained personnel to perform the procedure [144]. These impediments are motivating the requisite for faster, simpler, and more economical assay, wherein electrochemical genosensor emerges as a promising platform. DNA genomes extracted from tumour tissue of lung cancer patients who underwent biopsy can be PCR-amplified using primers that correspond to the EGFR sequence. The PCR-amplified products could then be detected as wild-type or mutated type using a genosensor [146].

Genosensors exploit the explicit binding between oligonucleotides and have been widely employed to detect various infectious and genetic diseases [116]–[118] using different analytical strategies including optical, fluorescence and electrochemical techniques [320]–[322]. The electrochemical technique is possibly one of the most widespread among all the analytical strategies thanks to its cost-effective fabrication, good stability, high sensitivity, and viability for real sample analysis [117], [323], [324]. One of the fundamental concerns for genosensors is the immobilisation of the capture-DNA (the biorecognition element); nonetheless, this concern is addressed with the use of linker-functionalised nanomaterials to achieve specific DNA immobilisation. Amongst numerous nanomaterials, graphene has been greatly explored thanks to its extraordinary properties. Graphene holds a very high prospective in DNA sensing because of its ability to allow easy and reliable immobilisation of DNA. Biolinker PY attaches to graphene through a π-π hydrophobic interaction [325]; allowing amino-modified DNA to be immobilised on the graphene via a stable amide covalent bond. Encouraged by the decent performance of the ZG-modified sensor presented in chapters 3 and 4, it is anticipated that a biosensor enhanced with the PY-functionalised-ZG (PY-ZG) nanocomposite could present itself as a promising genosensor.

In this chapter, an impedance-based genosensor enhanced with PY-ZG nanocomposite has been fabricated to distinguish between wild-type and mutated exon-19 sequences. Stable and controllable DNA-immobilisation achieved via PY-ZG nanocomposite, to our best knowledge, has not been reported elsewhere. Rct that varies following DNA-hybridisation was used to quantify the detection. The response of the sensor was amplified by optimising the ratio of PY, the concentration and the immobilisation time of the capture-DNA, as well as the hybridisation time and temperature of the capture-target DNA. Devoid of complicated fabrication procedures, the genosensor presented here is simple and cost-effective.

5.2 EXPERIMENTAL DETAILS

5.2.1 APPARATUS AND MATERIAL

On top of the chemical mentioned in chapter 3 and chapter 4, additional chemicals for the synthesis of the genosensor include 1-pyrenebutyric-acid-N-hydroxysuccinimide-ester (PY), Tris-EDTA (TE) buffer and desalted oligonucleotides that were acquired from Merck (USA). TE buffer was used as the buffer for all oligonucleotides. The electrochemical measurements of all electrodes were performed using Autolab PGSTAT302N potentiostat (Metrohm, Netherlands) interfaced with analysis software NOVA 1.11.

5.2.2 PREPARATION OF PY-FUNCTIONALISED-ZG

ZG nanocomposite was synthesised according to the protocol described in chapter 3. Subsequently, the as-synthesised ZG nanocomposite was functionalised with PY to enable oligonucleotides binding: different masses of PY was mixed with 5 mg of the ZG nanocomposite and the mixture was sonicated for 30 minutes in ethanol/DI water, followed by centrifugation and repeated wash to remove unbound PY. The cleaned sediment was collected and denoted as PY-ZG nanocomposite. The nanocomposite with different PY: ZG ratios, namely 2:1, 4:1, 6:1, 8:1 were denoted as 2PY-ZG, 4PY-ZG, 6PY-ZG, and 8PY-ZG, respectively.

5.2.3 DNA SEQUENCE DESIGN

The key objective of this work is to differentiate the wild-type exon-19 sequence from the mutated exon-19 sequences. Several types of exon-19 mutations have been reported [326]; nonetheless, in-frame deletions L747-P753 and E746-A750 are two of the most frequently observed exon-19 mutations that are sensitive to TKIs which inhibit abnormal cell proliferation by disabling the activity of the tyrosine kinases [146], [327]. The deletion sequences were designed to correspond to the L747-P753 and the E746-A750 mutation, as shown in Table 5.1. Within the tyrosine kinase domain of EGFR, the L747-P753 mutation is an 18-base deletion at c. 2240 -2257, whereas the E746-A750 mutation is a 15-base deletion that occurred at c. 2236-2250 [326], [328]. The wild-type sequence (c. 2227-2259), which is sufficient to reflect both of the mutations, was designed based on the non-mutated sequence observed in healthy patients [329]. The capture-DNA was designed to be fully complementary to the wild-type target-DNA. A non-target sequence was designed to be fully non-complementary to the capture-DNA for the specificity test.

Table 5.1. Exon-19 DNA Sequences

Mutation Type	**Sequences**
	2227 2236 2240 2250 2257 2274 2277
Wild-type	5’-GCTATCAAGGAATTAAGAGAAGCAACATCTCCG-3'
L747-P753	5’-GCTATCAAGGAAT ----- 18-base deletion - - - - - CGAAAGCCAACAAGGAAATC -3’
E746-A750	5’-GCTATCAAG - - - 15- base deletion- - - ACATCTCCGAAAGCCAACAAGGAA -3’
Amino-modified capture-DNA	5-NH_2-CGGAGATGTTGCTTCTCTTAATTCCTTGATAGC-3′
Non-target DNA	5’-AATGCCTCGAAGAAGCGCAGCCATGCCATCGTG -3′

5.2.4 FABRICATION OF THE GENOSENSOR AND ELECTROCHEMICAL MEASUREMENTS

The working electrode of the SPCE was rinsed with PBS before the fabrication. The re-dispersed PY-ZG nanocomposite was drop-casted onto the working electrode to produce PY-ZG/SPCE. Subsequently, 5 μL of the capture-DNA (0.1 μM in TE buffer) was incubated on the working electrode of the PY-ZG/SPCE for an hour to produce cDna/PY-ZG/SPCE. Non-specifically adsorbed DNA was removed by washing the SPCE repeatedly with PBS buffer, and the SPCE was dried at room temperature. The hybridisation of DNA was accomplished by incubating 5 μL of the target-DNA (the wild-type sequence, the mutated sequences or the non-target sequence) onto the working electrode of the cDna/PY-ZG/SPCE for an hour. Subsequently, the non-hybridised oligonucleotide was removed by washing the SPCE repeatedly with PBS buffer. After hybridisation, the double-helix DNA SPCE were abbreviated accordingly in bracket: exon-19 wild-type DNA (tDna/cDna/PY-ZG/SPCE), L747-P753 mutation DNA (mDna1/cDna/PY-ZG/SPCE), E746-A750 mutation DNA (mDna2/cDna/PY-ZG/SPCE) and non-target DNA (ntDna/cDna/PY-ZG/SPCE). The fabrication of the biosensor is illustrated in Scheme 5.1. Anti-fouling step was not required since the exon-19 genosensor was not intended to work with serum-based biomarkers that may coexist with biofoulants such as lipids, polysaccharides and proteins. Real samples for a genosensor were usually extracted DNA (from tumour tissue of patients) that have been PCR-amplified and purified, thus containing no biofoulant [146], [329].

Electrochemical studies were performed on the fabricated SPCEs in PBS buffer containing 10 mM of redox probe $[Fe(CN)_6]^{3-/4-}$. EIS was performed in the frequency range of 1MHz to 10 mHz. CV was recorded at a scan rate of 100 mV/s from -0.4 V to 0.8 V. 10 cycles were run for each CV scan. The electron transfer rate is different for the double-helix DNA (capture-target DNA) SPCE and the single-stranded DNA (capture-DNA) SPCE. Hence, hybridisation events were characterised by the change in the Rct obtained from EIS. In order to correct SPCE-to-SPCE deviations, the normalised Rct difference ($\Delta R/R$) was adopted as the indicator for hybridisation efficiency, as shown in equation 5.1.

$$\Delta R/R=(R_{ct2}-R_{ct1})/R_{ct1} \qquad \text{(Eq 5.1)}$$

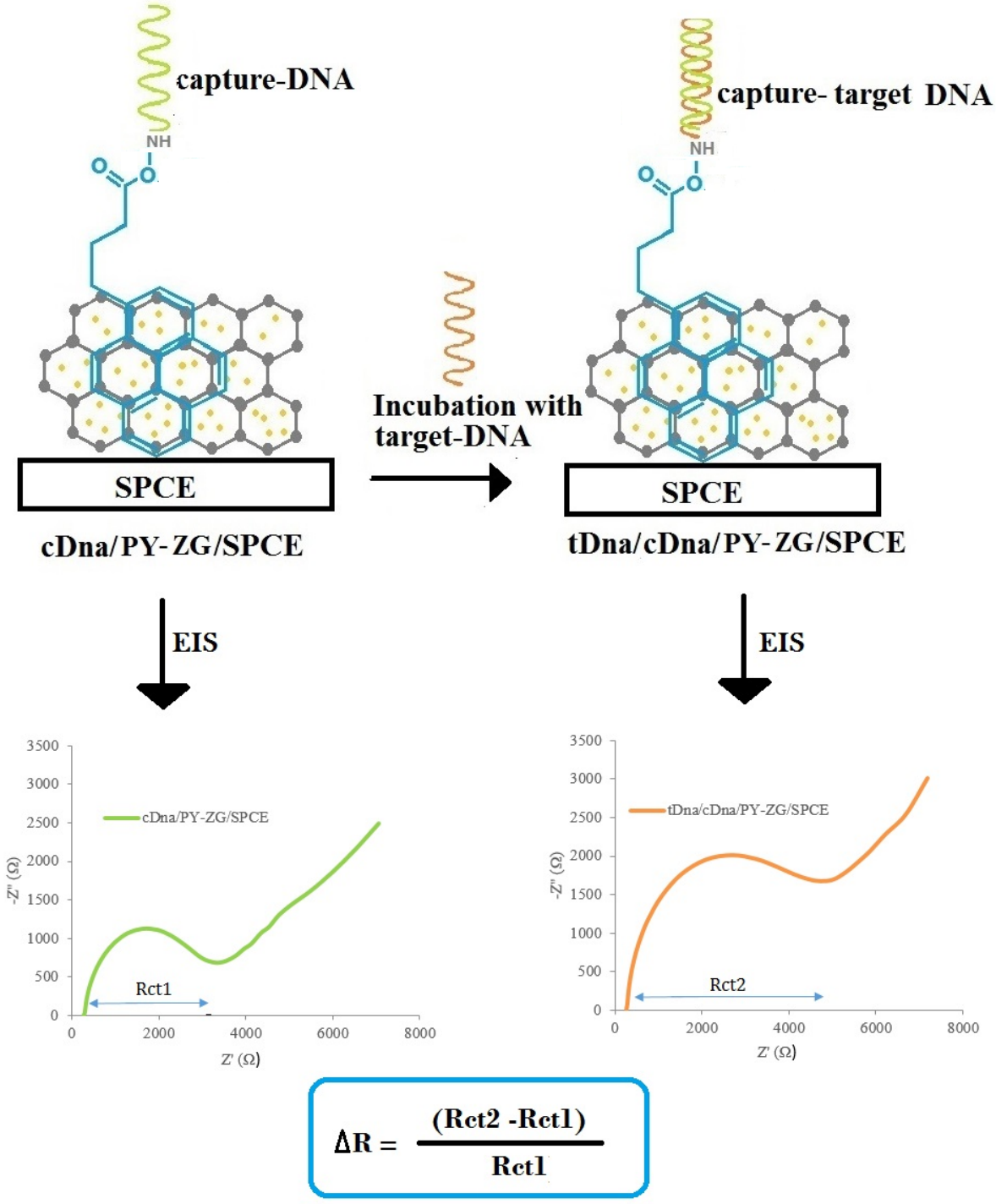
where R_{ct2} and R_{ct1} represent the Rct of the tDna/cDna/PY-ZG/SPCE and the cDna/PY-ZG/SPCE, respectively.

Rct obtained from EIS was as well employed to determine the electron transfer rate (Ket). Ket can be calculated based on equation 5.2.

$$Ket = RT/ n^2F^2 ARctC_r \qquad \text{(Eq 5.2)}$$

Where R is the gas constant, T is absolute temperature, n is the number of electrons involved in the redox, F is the Faraday constant, A is the area of the working electrode, and C_r is the concentration of the redox probe.

IBM SPSS Statistic was used to analyse the statistical significance of the data collected.



Scheme 5.1: Fabrication of the DNA sensor. The analytical signal is given by the impedance difference before and after the hybridisation of DNA strands.

5.2.5 DETECTION MECHANISM OF THE GENOSENSOR

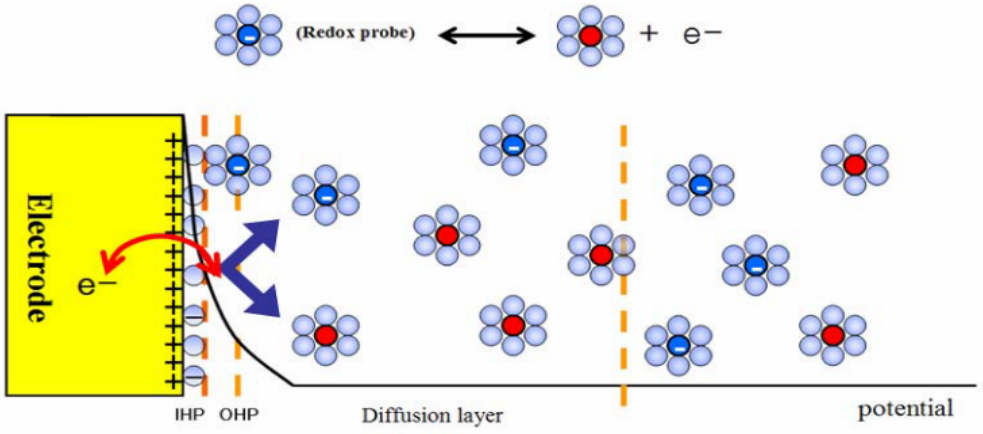


Figure 5.1: Diffusion of redox probe at an electrode/electrolyte interface. The diffusion of the redox ions is greatly affected by the presence of substrate on the electrode surface [330].

A simplified electrode/electrolyte interface is illustrated in Figure 5.1 [330]. A redox pair such as ferri/ferrocyanide $[Fe(CN)6]^{3-/4-}$ is commonly used as a redox indicator for the electron transfer kinetics at the interface. When a potential is applied to the electrode, the redox probes start to diffuse through the bulk solution towards the electrode where the redox reaction occurs. In EIS, the electron transfer to/from the redox probe is evaluated through Rct observed in the Nyquist plot. Electron transfer kinetics at the interface is affected by a substrate layer on the electrode surface [331], in the case of a genosensor, the layer of immobilised DNAs on the electrode surface affects the electron transfer. It has been suggested that the hybridised sensor (target DNA + probe DNA) would demonstrate a higher Rct than that of the non-hybridised sensor. The increase of Rct can be explained by the presence of more negative charges from the DNA backbone (charged phosphate) after hybridisation. This negative layer at the electrode surface caused more repulsion for the negatively charged $[Fe(CN)6]^{3-/4-}$ to diffuse towards the electrode and thus reduce the redox (electron transfer) at the electrode, leading to higher Rct. [332].

The increase of Rct after DNA hybridization has been widely observed and reported in reputed journals such as that in, to name a few, Biosensors and Bioelectronics [90], [333]–[335], Nanoscale

[124], Analytica Chimica Acta [336], Microchemical Journal [337], [338] and electroanalysis [339]

5.2.6 ESTIMATION OF CAPTURE-DNA DENSITY

Estimation of the capture-DNA density was performed through the Methylene Blue (MB) analysis. The accumulation of MB was performed on the cDna/PY-ZG/SPCE and the tDna/cDna/PY-ZG/SPCE where 50 μM of MB (in PBS buffer) was incubated on the working electrode of the SPCEs for 30 minutes, and the SPCES were subsequently rinsed with PBS buffer to remove unbound MB. Based on the assumption that each guanine base will bind to one MB molecule, the density of the capture-DNA layer can be estimated using the DPV measurement. DPV was performed within -0.6 V to -0.1 V under step voltage of 5 mV, pulse amplitude of 100 mV, and pulse width: period ratio of 50 ms: 500 ms. The quantity of MB (MB_{mol}) was estimated based on the equation shown in equation 5.3

$$MB_{mol}=Q/ (neN_A) \qquad \text{(Eq 5.3)}$$

Where Q is the quantity of electric charge during the MB reduction process, n (2) is the number of electrons involved in the MB reduction, e (1.6×10^{-19} C) is the charge on an electron, and N_A (6.02×10^{23} $mol^{-1)}$ is the Avogadro's number.

5.2.7 STABILITY AND SPECIFICITY STUDY

In order to assess the stability of the fabricated genosensor, a series of cDna/PY-ZG/SPCE was fabricated and stored at 4 °C. EIS analysis was performed on the preserved SPCEs once every two days and the ΔR/R from the preserved SPCEs was compared to that from the freshly prepared SPCEs. The specificity of the developed platform was investigated by incubating the cDna/PY-ZG/SPCE with 1 μM of different DNA sequences, including the exon-19 wild-type sequence, the exon-19 mutated sequences, and the non-target sequence. The ΔR/R for each type of incubation was measured.

5.3 RESULTS AND DISCUSSION

5.3.1 CHARACTERISATION OF THE FABRICATION STEPS

The step-wise fabrication of the sensor is characterised by EIS. The classic impedance spectrum, also known as the Nyquist plot, analyses the performance of the modified SPCE in both the high and low-frequency domains. As mentioned in chapter 3, the critical information in the high-frequency domain is the diameter of the semi-circle, which represents the Rct at the interface of the SPCE. Figure 5.2 (a) shows the impedance spectrum that revealed the fabrication process of the genosensor. The ZG/SPCE exhibited a low Rct of 1.7 kΩ owing to the good conductivity of the ZG nanocomposite; nevertheless, following the successful functionalisation of the nanocomposite with biolinker PY, the PY-ZG/SPCE showed an increased Rct of 3.2 kΩ. The biolinker PY formed a physical barrier at the sensor surface and caused sluggish electron transfer due to its hydrophobic nature [125]. After immobilisation with the capture-DNA, the cDna/PY-ZG/SPCE was negatively charged due to the skeleton of the immobilised capture-DNA, and the layer reduced the approach of the redox probe to the sensor interface as a result of electrostatic repulsion. Consequently, the Rct of cDna/PY-ZG/SPCE was further increased to 3.7 kΩ. The fabricated cDna/PY-ZG/SPCE was applied to recognise its targeted wild-type exon-19 sequence. As expected, after hybridisation, the Rct of the tDna/cDna/PY-ZG/SPCE was amplified to 4.7 kΩ. The double-stranded DNA formed after the hybridisation presented more phosphate skeletons that were negatively charged on the SPCE. The double-helix DNA layer amplified the repulsion towards the redox probe and acted as a stronger obstruction for the electron transfer at the electrode/electrolyte interface. The Rct of each modification step can be translated into the charge transfer rate, Ket based on equation 5.2 presented in the experimental section 5.2.4 [340]–[342].

The Ket decreased in the order of ZG/SPCE (1.25×10^{-4} cm s^{-1})> PY-ZG/SPCE (6.65×10^{-5} cm s^{-1}) > cDna/PY-ZG/SPCE (5.75×10^{-5} cm s^{-1}) > tDna/cDna/PY-ZG/SPCE (4.53×10^{-5} cm s^{-1}). The persistently decreased Ket agreed with the continually increased Rct owing to the formation of a more repulsive surface layer after each modification step.

The electrochemical properties of all the SPCEs were further analysed using the CV, as shown in Figure 5.2 (b). Whilst EIS characterised the electrochemical performance of an SPCE by its Rct; CV characterised the performance of an SPCE through its redox peak current and ΔEp. The CV analysis showed that the peak current decreased in the order of ZG/SPCE (116 μA) > PY-ZG/SPCE (73μA) > cDna/PY-ZG/SPCE (64 μA) > tDna/cDna/PY-ZG/SPCE (56 μA). The continually decreased peak current complemented the continually increased Rct as a result of the reduced rate of charge transfer after each modification step. In addition, an increase of ΔEp was observed following each modification step. The anodic peak drifted to further positive potential, and the cathodic peak shifted to further negative potential. The ΔEp increased in the order of ZG/SPCE (0.37 V) < PY-ZG/SPCE (0.50 V) < cDna/PY-ZG/SPCE (0.65 V) < tDna/cDna/PY-ZG (0.74 V). The increasing peak separation reflected the shift of over-potential induced by the poorer redox reversibility following each successful modification step. Electrochemical reversibility represented the electron transfer kinetics between the modified SPCE and the redox probe $[Fe(CN)_6]^{3-/4-}$, in which each modification step instigated the SPCE to appear as a higher barrier for electron transfer. The Nernstian equilibrium was established with more delay upon changes in the applied potential. A more negative (positive) potential was required to reduce (oxidise) the redox probe $[Fe(CN)_6]^{3-/4-}$, and consequently led to a larger ΔEp [343].

PY is an organic molecule containing a pyrene moiety and a succinimide ester. The pyrene group, being highly aromatic, is known to interact actively with the basal plane of graphene through π–π stacking. Despite being a non-covalent functionalisation, the pyrene-graphene interaction is strong and stable, as evidenced in the work of other groups [125], [325], [344].

Meanwhile, the succinimide ester groups are responsive to the amines-nucleophilic substitution that would form the amide bonds. Amines are plentiful on the exterior of most proteins and amino-modified oligonucleotide sequences. In this work, the amino-modified capture-DNA was immobilised onto the SPCE by forming an amide bond with the N-hydroxysuccinimide esters

available on the PY [334]. In simpler terms, PY binds to the graphene at one end and helps to immobilise protein or amino-modified DNA at the other end, giving rise to its role as a biolinker.

In order to verify that biolinker PY has undeniably contributed to the DNA-immobilisation, the ZG/SPCE electrode without the biolinker was incubated with 5 μL of the capture-DNA and subsequently tested with EIS. The Rct difference before and after the incubation was negligible (< 1%), indicating that DNA was not immobilised. The immobilisation of DNA was not feasible without the functionalisation of the SPCE with PY which provides amide bonding. In comparison, SPCE functionalised with the PY biolinker exhibited an Rct difference of 16% after incubation with 5 μL of the capture-DNA, indicating the immobilisation of capture-DNA and ascertaining the presence of amide bond.

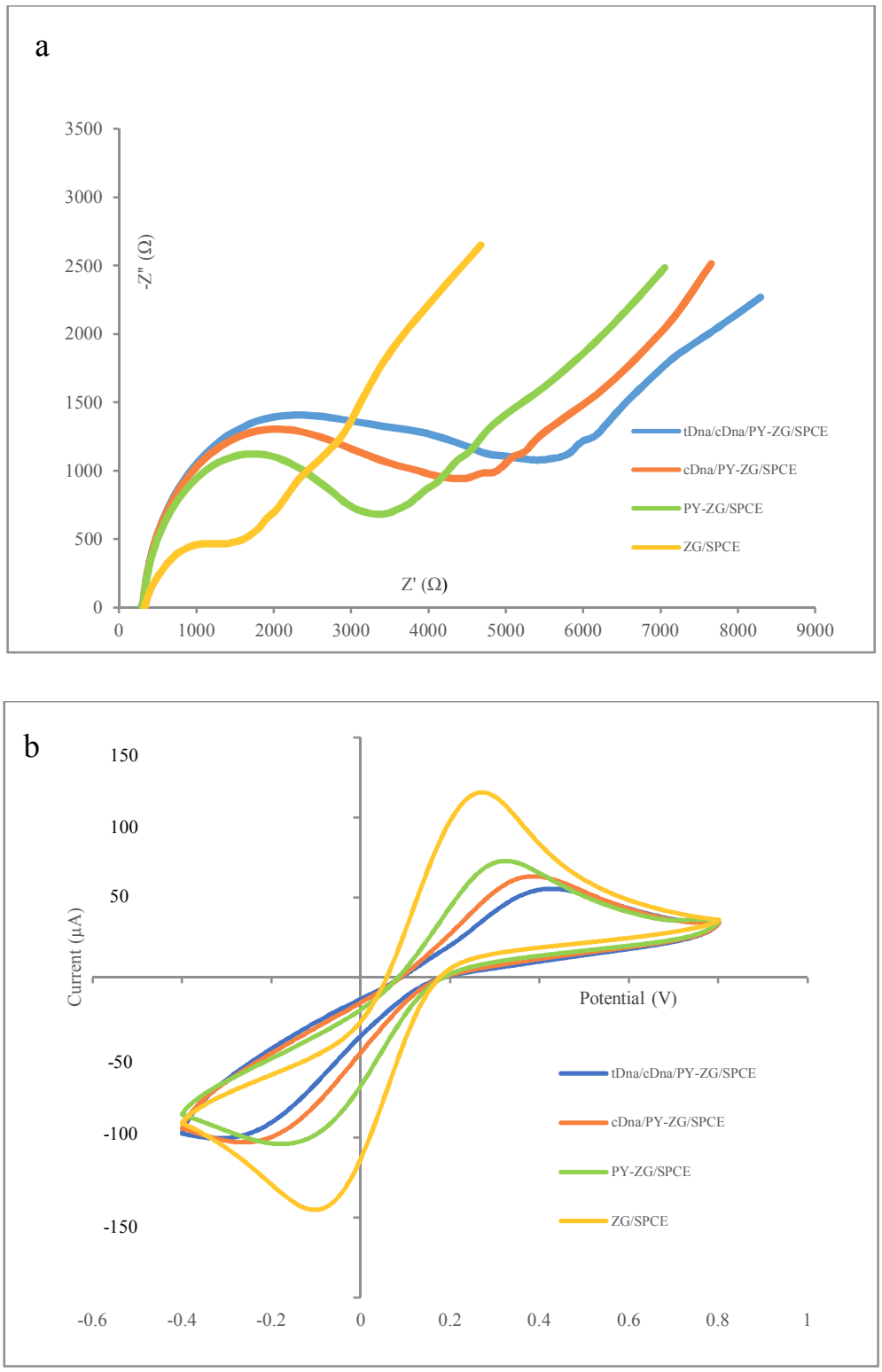


Figure 5.2. (a) Impedance spectrum and (b) CVs of the ZG/SPCE, PY-ZG/SPCE, cDna/PY-ZG/SPCE, and tDna/cDna/PY-ZG/SPCE in PBS with 10 mM of $[Fe(CN)_6]^{3-/4-}$*. The results from CV and EIS confirmed the success of each fabrication step.*

5.3.2 OPTIMISATION OF THE FABRICATION AND SENSING PARAMETERS

Upon establishing the effectiveness of the developed platform as a genosensor, a few fabrication parameters including the ratio of the PY, the concentration and the immobilisation time of the capture-DNA were manipulated to amplify the response of the sensor. The response of a DNA-sensor is likewise dependent on the hybridisation conditions, thus, the impact of the hybridisation temperature and hybridisation time was also studied to improve the performance of the biosensor.

At the outset, the influence of the different PY: ZG ratios (2:1, 4:1, 6:1, and 8:1) was investigated. SPCEs modified with different PY: ZG ratios were immobilised with 10 μM of the capture-DNA for 60 minutes. All the SPCEs were subsequently incubated with 1 μM of the target-DNA for 60 minutes at room temperature. An increased ΔR/R was observed when the PY: ZG ratio was increased from 2:1 to 4:1, as shown in Figure 5.3 (a), reflecting that a higher ratio of PY resulted in the availability of more amine-binding sites, and the hybridisation efficiency was enhanced following a greater amount of immobilised DNA. However, as the ratio of PY: ZG was further increased to 6:1 and 8:1, the ΔR/R decreased rapidly, signifying a reduction in the hybridisation due to an overly-packed capture-DNA layer. The intermolecular interaction between the target-DNA and the capture-DNA was limited on an overly-dense surface [345]. Furthermore, it is worth noting that at the 8:1 ratio, a decrease in the Rct was observed following the hybridisation event. The overly-high PY ratio introduced an abundance of amide linkages on the electrode surface. This may have resulted in a high density of randomly oriented capture-DNA, which formed an extremely negative barrier on the electrode surface. Following the hybridisation event, a more rigid and better oriented double-helix DNA layer was formed, resulting in a less repulsive sensor surface, and the subsequent reduction of the Rct. Such finding is consistent with other works reported elsewhere [346], [347]. ANOVA test showed that the PY: ZG ratio was a statistically significant parameter that can affect the sensor response ($p < 0.05$). Since the ratio of 4:1 had demonstrated the highest ΔR/R, it was used in all the subsequent analyses, generally denoted as PY-ZG.

To further optimise the capture-DNA layer, the SPCEs were modified with different concentrations of the capture-DNA ranging from 0.001 μM to 10 μM; and were subsequently incubated with 1 μM of the target-DNA for 60 minutes at room temperature. The observed ΔR/R increased accordingly when a higher concentration of the capture-DNA was used, reached a plateau at 0.1 μM, and reduced thereafter, as depicted in Figure 5.3 (b). These findings suggested that hybridisation has a pronounced dependence on the concentration of the capture-DNA [345]: at low concentrations, the immobilised DNA strands were sparsely spread across the sensor surface, and the formation of an adequately regimented monolayer was prohibited [348], when the concentration was increased, the formation of a more closely-packed DNA layer induced a stronger repulsive force towards the redox probe and subsequently improved the detection. Nevertheless, an overly-dense capture-DNA layer was formed when the concentration of the capture-DNA was too high. Hybridisation decreased due to the hindered inter-molecule interactions between the DNA strands. ANOVA test showed that the concentration of the capture-DNA was a statistically significant parameter that can affect the sensor response ($p < 0.05$). The most optimum concentration was determined to be 0.1 μM; thus SPCEs modified with 0.1 μM of the capture-DNA were adopted for all the subsequent analyses.

Subsequently, the influence of the immobilisation time was assessed. The SPCEs were incubated with 0.1 μM of the capture-DNA for different durations of 30, 60, 90, and 120 minutes; and were subsequently incubated with 1 μM of the target-DNA for 60 minutes at room temperature. The ΔR/R increased significantly when the incubation time was increased from 30 minutes to 60 minutes. However, a further increase in the incubation time resulted in a decreased ΔR/R response, implying a less effective detection (Figure 5.3 (c)). In good accordance with the aforementioned observations, a densely packed surface caused by the long immobilisation time offered low accessibility for the incoming target-DNA strands due to the steric crowding of the bases and resulted in a lower sensor response [349]. Accompanying, the ANOVA test endorsed that

immobilisation time has a significant influence on ΔR/R ($p < 0.05$). Therefore, the immobilisation time of 60 minutes was established as the protocol for all the subsequent analyses.

The impact of the hybridisation temperature and hybridisation time was studied to improve the performance of the biosensor. The optimised cDna/PY-ZG/SPCE were incubated with 1 μM of the target-DNA for a different duration ranging from 30 minutes to 120 minutes at room temperature. The effect of increasing the hybridisation time is presented in Figure 5.3 (d). The result showed that the ΔR/R increased notably with an extended hybridisation time from 30 minutes to 60 minutes and reached a plateau after 60 minutes, manifesting the complete hybridisation of the target-DNA with all the immobilised capture-DNA [121]. The paired-sample test showed that the ΔR/R difference from 30 minutes to 60 minutes was statistically significant ($p < 0.05$) while further increment of the hybridisation time was statistically insignificant ($p > 0.05$) in affecting ΔR/R. Therefore, 60 minutes was selected as the optimum hybridisation time. The influence of the hybridisation temperature was subsequently evaluated. The optimised cDna/PY-ZG/SPCE was incubated with 1 μM of the target-DNA at varying temperatures from 21 °C to 41 °C for 60 minutes, as shown in Figure 5.3 (e). As the temperature was increased from 21 °C to 26 °C, the hybridisation efficiency was fairly enhanced. It was evident that surface hybridisation experienced kinetic freezing at low temperatures and reached facile equilibration at an optimum hybridisation temperature [350]. Interestingly, the integrity of the capture-DNA layer also has a pronounced dependence on temperature [351], where desorption of the monolayer may have contributed to the statistically significant reduction ($p < 0.05$) of the hybridisation efficiency following the warmer hybridisation environment from 26 °C to 41 °C. Since the highest sensor response was observed at 26 °C, it was selected as the hybridisation temperature for subsequent analysis.

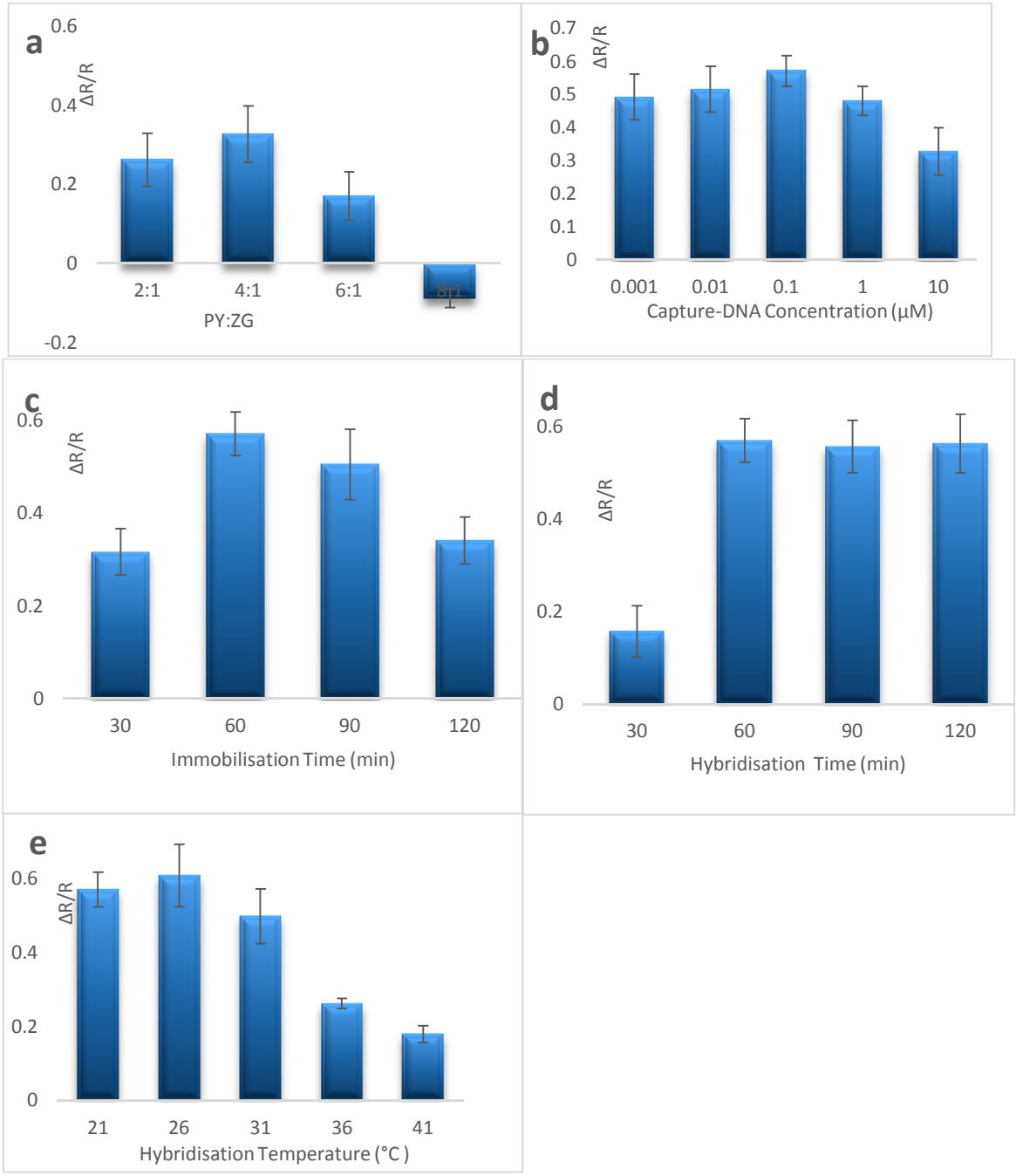


Figure 5.3. Effects of (a) PY ratio, (b) capture-DNA concentration, (c) capture-DNA immobilisation time, (d) hybridisation time, and (e) hybridisation temperature on the sensor response ΔR/R. The most optimum ratio of PY: ZG was found to be 4:1, whereas SPCE immobilised with 0.1 μM of the capture-DNA for 60 minutes was observed to present the highest hybridisation efficiency when incubated with the target-DNA for 60 minutes at 26 ℃. Hence, these parameters were adopted as the sensing protocol.

5.3.3 ANALYTICAL PERFORMANCES, SPECIFICITY, REPRODUCIBILITY AND STABILITY

Since there are numerous types of exon-19 mutation, it is not practical for a genosensor to detect all the mutation types as different capture-DNA probes will have to be immobilised to correspond to the various mutation types. Therefore, to determine if a patient is having mutated or non-mutated exon-19, it is more practical to detect the wild-type (exon-19 DNA without mutation). When the genosensor detects wild-type DNA, it indicates that the exon-19 is non-mutated; likewise, if the sensor provides a no/low response, it indicates that the wild-type DNA is absent. The absence of wild-type DNA, in turn, suggests that the exon-19 is mutated. The developed genosensor was employed to detect the target-DNA (wild-type sequence) of various concentrations. The normalised Rct difference between the cDna/PY-ZG/SPCE and the tDna/cDna/PY-ZG/SPCE was presented as the calibration curve in Figure 5.4 (a). An increase in the target-DNA concentration led to the amplification of the Rct, evincing the greater extent of hybridisation. The analytical signal ($\Delta R/R$) was linearly correlated to the logarithmic value of the target-DNA ranging from 5 nM to 1 μM, with a regression equation of $\Delta R/R = 0.23 \log C\ (M) + 1.99$, and a correlation coefficient of $R^2 = 0.99$. The LOD was estimated to be 1.7 nM (S/N =3). The performance of the developed sensor is comparable to other reported electrochemical genosensors listed in Table 5.2.

Table 5.2. Comparison of The Analytical Performance of the ZG Genosensor Against Other Platforms

Electrodes	*Detection Technique*	*Linear Range*	*LOD*	*Reference*
Graphene oxide/GCE	DPV	55 nM – 2.2 μM	7.6 nM	[352]
Carbon nanotube/ choline/GCE	DPV	60 nM – 125 μM	18 nM	[353]
Peptide nucleic acid/gold electrode	CV	1 nM – 100 μM	1 nM	[354]
Peptide nucleic acid/nanoporous gold electrode	EIS	10 nM–10 μM	1 nM	[355]
PY-ZG/SPCE	EIS	5 nM – 1 μM	1.7 nM	This work

It is imperative to develop a biosensor that is specific to its intended targets. The specificity of the developed platform was investigated by incubating the cDna/PY-ZG/SPCE with 1 μM of different DNA sequences, including the exon-19 wild-type sequence, the exon-19 mutated sequences, and the non-target sequence. As shown in Figure 5.4 (b), the hybridisation of the capture-DNA with the 18-base deletion DNA and the 15-base deletion DNA generated a ΔR/R of 0.19 and 0.16 respectively. Meanwhile, a negligible Rct change was recorded following the incubation of the SPCE with the non-target DNA. It was established that the developed sensor was specific to the exon-19 wild-type DNA and inert toward non-target DNAs.

Subsequently, to characterise the reproducibility of the biosensor, a series of cDna/PY-ZG/SPCE were simultaneously fabricated and hybridised with the target-DNA. EIS was performed on all the SPCEs, and the ΔR/R was recorded. An RSD of 8.3% was obtained, manifested a comparable reproducibility with works reported elsewhere [124], [340], [356]. In order to assess the stability of the fabricated genosensor, a series of cDna/PY-ZG/SPCE was fabricated and stored at 4 °C. EIS analysis was performed on the preserved SPCEs once every two days and the ΔR/R from the preserved SPCEs was compared to that from the freshly prepared SPCEs. Suggestive of good stability, the deviation of the ΔR/R after 2, 4, and 6 days of storage was negligible, whereas the decrease in the response after 8 days of storage was less than 10%, as presented in Figure 5.4 (c).

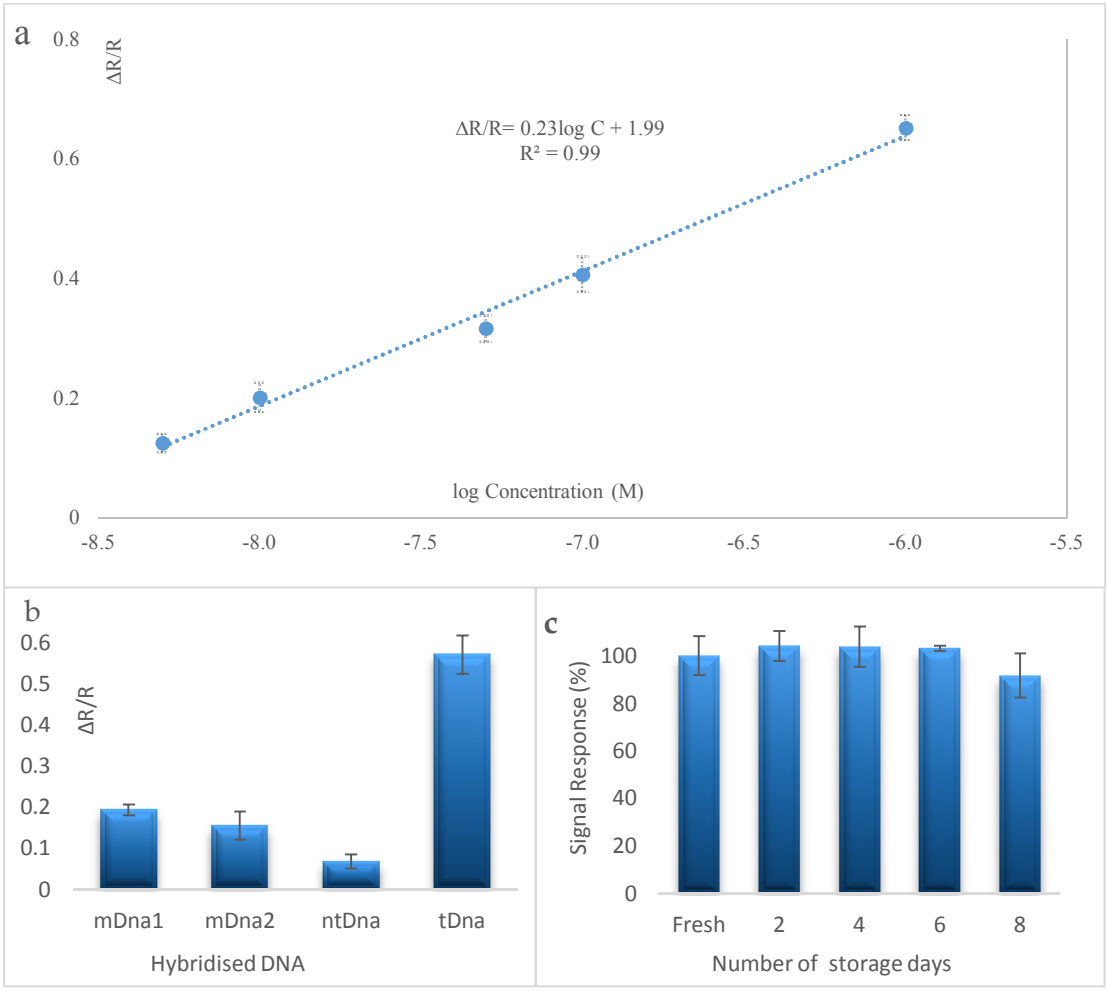


Figure 5.4. (a) The relationship between the ΔR/R and the logarithm of target-DNA concentration, (b) specificity test, and (c) stability test. The sensor exhibited a correlation of $R^2 = 0.99$ for the detection of exon-19 wild-type DNA.

5.3.4 ESTIMATION OF CAPTURE-DNA DENSITY

MB is a common electrochemical probe for the investigation of hybridisation events due to its distinct affinity towards the double-stranded and single-stranded oligonucleotides. In a one-proton and two-electrons reduction process, MB reduces to leucomethylene blue and gives rise to a measurable electrical signal [357]. Figure. 5.5 shows the DPV peak measured at the cDna/PY-ZG/SPCE and the tDna/cDna/PY-ZG/SPCE after 30 minutes of MB accumulation. The peak observed at -0.38 V for the cDna/PY-ZG/SPCE arose due to the redox of MB bonded to the guanine bases of the capture-DNA [358]. Following the hybridisation event, a remarkable higher peak current was observed, ascribed to the higher intercalative affinity of MB to the double-stranded oligonucleotide as compared to the single-stranded oligonucleotide [117]. The density of the capture-DNA layer can be estimated using the DPV measurement, based on the assumption that each guanine base will bind to one MB molecule. According to equation 5.3 outlined in the experimental details section 5.2.6, MB_{mol} was estimated to be 6.75 pmol for the cDna/PY-ZG/SPCE (Q = 1.3 µC). Given that there were 7 guanine bases in the capture-DNA sequence, and the apparent area of the SPCE (diameter = 4 mm) was 0.1256 cm^2, the density of the capture-DNA layer was approximated to be 7.7 pmol cm^{-2}, which is comparable to other reported sensors [359].

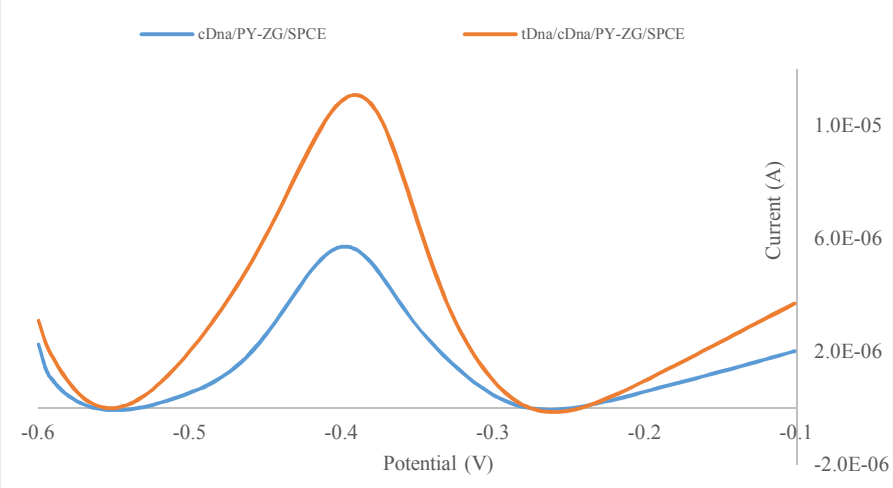


Figure 5.5. DPV curves of the cDna/PY-ZG/SPCE (single-stranded DNA) and the tDna/cDna/PY-ZG/SPCE (double-stranded DNA). Hybridised SPCE exhibited higher current due to the greater intercalative affinity of MB towards double-stranded hybridised DNAs.

5.3.5 ADVANTAGES OF THE GENOSENSOR

The performance of the ZG-modified genosensor is comparable to other similar works reported. On top of the comparative analytical performance, an added advantage of our sensor lies in the use of disposable SPCE. The small-size electrodes required minimal preparation work and were also free of contamination caused by repeated usage.

Besides, the DNA-immobilisation technique presented in this work was stable, controllable, and straightforward; It was a substantial enhancement in comparison to the common physical absorption method that suffers from random DNA orientation, relatively weak binding, and the risk of DNA desorption [360]. It was also more cost-effective and simpler to perform as compared to chemical-assisted or affinity-assisted immobilisation methods, such as the streptavidin-biotin immobilisation method which is limited by its multi-step preparation and the high cost of streptavidin-biotin chemical.

In addition, a vast number of genosensors use labels such as organic fluorescent dye molecules, magnetic microbeads, and secondary reporters [146], [324], [361] to realise the detection and quantification of DNA, while the genosensor presented in this work was able to quantify wild-type DNA using a label-free approach that was more economical and simpler to accomplish. Label-free detection eliminates experimental errors induced by labels such as the blocking of active binding epitopes and the inaccessibility of labelling sites that could lead to failed detection [362].

5.4 SUMMARY

The EGFR is involved in cell signalling pathways that control cell division and survival, thus mutations in the EGFR could result in the rapid division of cancer cells. Out of the several types of EGFR mutations, mutation of the exon-19 is the most common. Detection of exon-19 mutation enables the precise screening of prospective respondents to TKIs since this mutation was shown to be reactive to TKIs that gave favourable clinical outcomes for lung cancer patients. Therefore, this work presented a label-free genosensor to distinguish between wild-type and mutated exon-19 sequences based on a platform enhanced by PY-functionalised-ZG nanocomposite. The results from CV and EIS endorsed the effective immobilisation of the capture-DNA onto the SPCEs, and a significant change in Rct acknowledged the successful hybridisation of capture-DNA with target-DNA. Real samples for a genosensor are usually extracted DNA from tumour tissue. The DNA extracted can be amplified to the concentration workable to the genosensor. Under optimised fabrication and hybridisation conditions, the sensor was able to quantify the exon-19 wild-type DNA in the range of 5 nM to 1 μM (which is within the possible concentration from PCR-amplification), with a linearity coefficient of R^2= 0.99 and a LOD of 1.7 nM. The genosensor was capable of differentiating mutated exon-19 DNA from the wild-type DNA by generating distinctive signals for wild-type and mutated type sequences, giving it the ability to identify potential lung malignancies.

The proposed assay transduced DNA mutation via impedance change on the electrode surface, obviating the complicated fabrication protocols and the use of labels in the detection scheme. As such, this work not only demonstrated a reliable technique for the detection of lung cancer-associated DNA mutation but also offered a promising platform for the detection of other genetic mutational diseases in general.

6 AN IMMUNOSENSOR FOR THE RAPID DETECTION OF TUMOUR MARKER CARCINOEMBRYONIC ANTIGEN BASED ON GRAPHENE/ZIRCONIA-ENHANCED PLATFORM

6.1 INTRODUCTION

A disheartening 1.8 million new cancer cases and 600,00 deaths were estimated for the year 2020 in the US [1]. The actual mortality is expected to be higher due to the barrier to getting cancer diagnosis amid the current COVID-19 pandemic. Diagnostic evaluations were either postponed or had prolonged waiting times because hospital resources and laboratory facilities were relocated to alleviate the burden on health care caused by COVID-19. A feasible solution to address the issue of laboratory shortage is the development of biosensors for rapid cancer diagnosis via tumour markers. Rapid screening offers the opportunity for early detection, which is known to increase the survival rate for cancers of the lung [131]. Correspondingly, a glycoprotein involved in cell adhesion, the CEA is known to be overexpressed in lung cancer [186], [191], [363]. The CEA level of a healthy individual is ideally below 5.0 ng/ml (7.0 ng/ml for smokers) [140], therefore serum CEA levels higher than that of healthy persons led to its diagnostic role as a tumour marker. Although conventional methods such as the ELISA and PCR are well developed in CEA diagnosis [210], [211], they still suffer from some drawbacks such as the need for trained personnel to perform the test [212], lengthy assay duration [213], background noise [214] and potential false readings associated with the complex coloured sample [215]. These drawbacks are more pronounced during a pandemic where laboratory resources are scarce. In contrast, electrochemical immunoassay, due to its rapidness, specificity and feasibility for miniaturisation, has received more attention in recent years [364], [365].

Immunosensors typically consist of a biological element (antibody) immobilised on the sensor to detect its targeted protein (antigen) via specific affinity. Immunosensor exploits the specific

affinity between antibody and antigen to quantify detection, in which electrochemical change induced by the binding of antigen-antibody is translated into a measurable signal. Immunosensor has established itself as a promising testing method for tumour markers, and the recent trend shows that various graphene-based nanocomposites have been incorporated to amplify signal response and consequently enhance the sensitivity of tumour marker detection [8]–[10]. As mentioned in earlier chapters, graphene-nanocomposite combines the physiochemical attributes of graphene and its hybridised components to deliver a novel material that has enhanced properties including effective surface area, biocompatibility and electrical conductivity that out-perform graphene and its hybridised component individually [15].

In this study, a disposable and label-free electrochemical immunosensor based on ZG nanocomposite for the detection of CEA was proposed. Rct that increased in response to CEA antigen-antibody binding was used as the analytical signal to quantify CEA concentration. Fabrication steps and sensing conditions were optimised to amplify the signal before the sensor was tested against CEA of various concentrations. The analytical performances of the as-fabricated CEA immunosensor, together with its specificity, stability and reproducibility were evaluated. Upon establishing that the immunosensor is capable of CEA detection, it was tested against human serum samples containing various CEA concentrations to demonstrate real-sample applications. The result of this work provides an insight into the promising potential of a ZG-based immunosensor to substitute conventional lab-based assays and provide rapid detection of tumour marker CEA.

6.2 EXPERIMENTAL DETAILS

6.2.1 APPARATUS AND MATERIAL

On top of chemicals mentioned in chapters 3, 4 and 5, additional chemicals for the development of the immunosensor include CEA and antibody for CEA (Ab) that were purchased from Cloud-Clone Corp (USA), bovine serum albumin (BSA), skim milk powder and human serum that were acquired from Sigma-Aldrich (USA) as well as Immunoglobulin G (IgG) that was purchased from Thermos Scientific (USA). The CEA antibody was a monoclonal antibody that has specificity for a single antigenic epitope. The electrochemical measurements of all electrodes were performed using Autolab PGSTAT302N potentiostat (Metrohm, Netherlands) interfaced with analysis software NOVA 1.11

6.2.2 FABRICATION OF THE IMMUNOSENSOR AND ELECTROCHEMICAL MEASUREMENTS

ZG nanocomposite was synthesised according to the protocols established in chapter 3 while PY-ZG was synthesised as described in chapter 5. For optimisation of the PY ratio, ZG: PY proportion of 1:2, 1:4, 1:8 and 1:16 was achieved by including 10 mg, 20 mg, 40 mg and 80 mg of PY respectively into the mixture of PY-ZG. Re-dispersed PY-ZG was drop-casted on the working electrode of SPCE that has been rinsed with PBS to yield PY-ZG/SPCE. The PY-ZG/SPCE electrode was washed and left to dry in ambient conditions. Successively, 5 µL of the CEA Ab (10 µg/ml) was incubated on the working electrode for 50 minutes before the incubation was halted by rinsing and soaking the electrode in PBS for 5 minutes. The Ab-immobilised electrode was denoted as Ab/PY-ZG/SPCE. Next, active-site blocking was achieved by incubating the working electrode with 1% skim milk for 20 minutes, followed by rinsing and soaking of the electrode with PBS to halt incubation. The electrode that has been treated with blocking buffer was denoted as SM/Ab/ PY-ZG/SPCE, and it was ready for the detection of CEA. Detection of CEA was achieved by incubating 5 µL of the CEA solution on the working electrode of SM/Ab/PY-ZG/SPCE for 75

minutes to allow the formation of Ab-CEA immuno-complex. The electrode after Ab-CEA binding is denoted as CEA/SM/Ab/PY-ZG/SPCE. The fabrication step of the immunosensor is illustrated in Scheme 6.1.

The electrochemical measurements of all electrodes were performed in 30 ml of PBS containing 10 mM of redox species $[Fe(CN)_6]^{3-/4-}$. CV was recorded at a scan rate of 100 mV/s and swept from – 0.4 V to 0.8 V. Rct was acquired from EIS performed within the frequency range of 100 kHz to 50 mHz under open circuit potential. Every electrochemical measurement was collected in triplicates to provide an averaged value. IBM SPSS Statistic was used to analyse the statistical significance of the collected data.

The sensor response is denoted by relative Rct (rRct), which is the relative Rct difference between SM/Ab/PY-ZG/SPCE and CEA/SM/Ab/PY-ZG/SPCE Equation 6.1 represents the mathematical expression of rRct.

$$rRct = \frac{(Rct_1) - (Rct_0)}{(Rct_0)} \qquad \text{(Eq 6.1)}$$

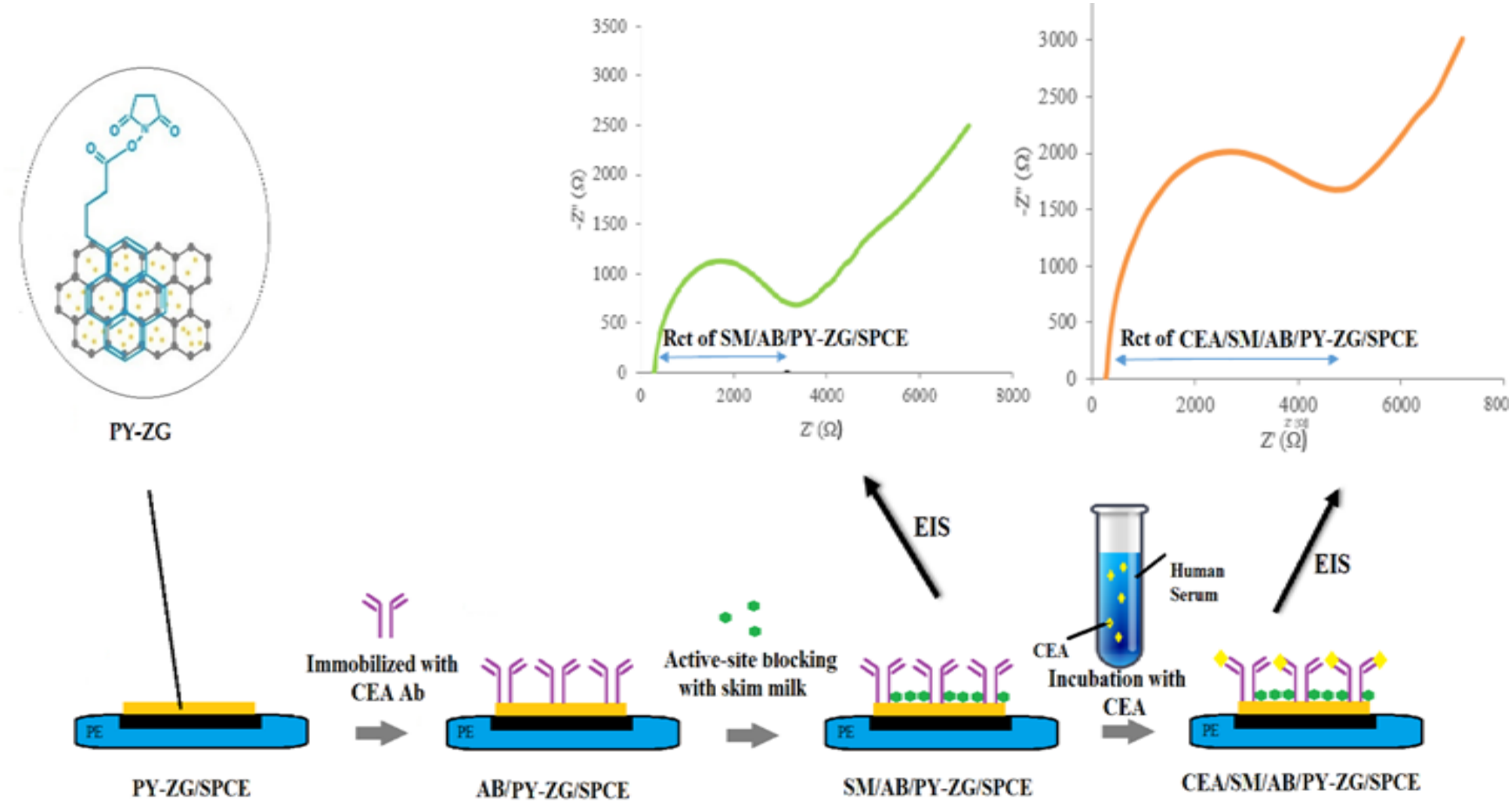
where Rct_0 and Rct_1 represent the Rct of SM/Ab/PY-ZG/SPCE and CEA/SM/Ab/PY-ZG/SPCE respectively.

6.2.3 STABILITY, INTERFERENCE AND CEA RECOVERY TEST IN SERUM

For stability study, a series of functionalised SPCE was stored under 4 °C. The stored SPCEs were retrieved and tested with 1 ng/ml of CEA at an interval of 5 days, 10 days, 15 days and 20 days. The electrochemical signal response of the stored SPCE was comparable to that of freshly prepared SPCE. Stability is given by the percentage of signal retained by the stored electrode as compared to the fresh SPCE. The interference study was evaluated by measuring the rRct in the presence of other interfering species namely glucose (Glc), acetaminophen (Ap), Immunoglobulin G (IgG) and bovine serum albumin (BSA). The immunosensor was initially tested against samples containing only the interfering species (1 mg/ml) in which the rRct was measured in interference-only samples. Subsequently, CEA (1 ng/ml) was mixed with these interfering species individually (1

mg/ml) and the rRct of the mixtures were measured by the immunosensor. The rRct from samples with interfering species was compared to the rRct from the sample containing only the CEA (1 ng/ml). The deviation in rRct was observed.

The real sample analysis (recovery test) was performed by spiking human serum with CEA to prepare samples of various CEA concentrations (0.01 ng/ml, 0.1 ng/ml, 1 ng/ml and 10 ng/ml). EIS was performed on all samples using the as-fabricated immunosensor. Matrix effect provoked by serum components may affect the signal response; therefore, a standard approach to neutralise matrix effect was through dilution [366], [367]. A 100x dilution factor to achieve complete elimination of matrix effect was employed as the protocol for the analysis of CEA in human serum. This dilution factor was consistent with practices reported elsewhere [214], [366], [368]. The rRct measured from spiked samples and the calibration equation were applied to determine the CEA concentration in each sample



Scheme 6.1. Fabrication of the CEA immunosensor. The detection was governed by the amount of Ab-CEA immuno-complex formed on the electrode surface.

6.3 RESULTS AND DISCUSSION

6.3.1 ELECTROCHEMICAL CHARACTERISATION OF THE SENSING PLATFORM

The fabrication of the immunosensor involved layer-by-layer functionalisation of the SPCE. The electrode was first functionalised with PY-ZG nanocomposite to enable protein binding, followed by the immobilisation of the Ab probe, and the incubation with skim milk to prevent non-specific binding. The immobilised Ab probe would in turn enable the binding with CEA due to antibody-antigen affinity and gave rise to the analytical signal. The layer-by-layer functionalisation of the immunosensor was characterised by CV and EIS.

CV considers the redox peak current and the ΔEp as the core characteristic of a sensor. Figure 6.1 (a) represents the CV of each functionalisation step. Two distinct redox peaks were found in the CV measurement of ZG/SPCE, occurring at about 0.25 V and -0.05 V. The peak current of ZG/SPCE was the highest among all electrodes, attributed to the large surface area and good conductivity of the nanocomposite. Upon integration of the molecular bi-linker PY into the nanocomposite, the peak current of PY-ZG/SPCE showed a decreased response. As discussed in chapter 5, it was stipulated that the PY, being a hydrophobic element, formed an insulating layer at the sensor-electrolyte interface and contributed to the reduced charge transfer kinetics [125]. Further decrease in the peak current was observed following the immobilisation of the Ab probe (Ab/PY-ZG/SPCE) and the subsequent blocking of active sites with skim milk (SM/Ab/PY-ZG/SPCE). The decrease in current for both steps can be ascribed to the reduction of redox species diffusions due to the obstruction from the insulating layer of protein molecules (the Ab and the blocking milk) on the electrode surface [369]. The functionalised sensor SM/Ab/PY-ZG/SPCE was ready for the detection of CEA. The platform was able to bind with CEA and instigated a further decrease of the peak current. The decrease advocated the formation of Ab-CEA immuno-complexes that impeded the electron transfer at the sensor-electrolyte interface [370]. Besides, an increasing trend of ΔEp was observed alongside the decreasing pattern of peak current. The ΔEp

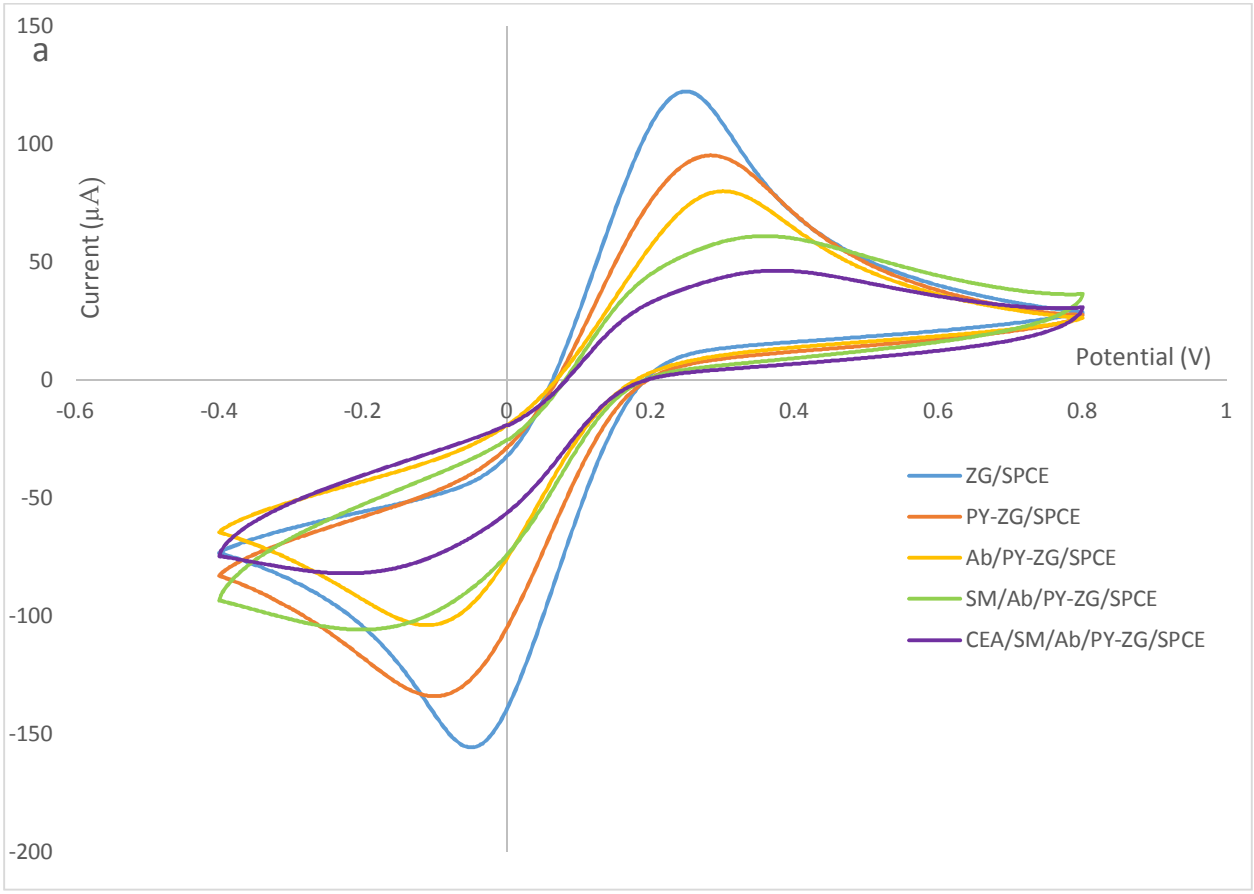
was observed to be the smallest for ZG/SPCE (0.31 V) and the largest for CEA/SM/Ab/PY-ZG/SPCE (0.62 V). The ΔEp represented the degree of redox reversibility, which was the reduction and re-oxidation of redox species. A widening ΔEp, where the anodic (cathodic) peak drifted to a further positive (negative) voltage, signified poorer redox reversibility. Each modification step created a more insulative charge transfer barrier so much so that a higher positive (negative) voltage was required to oxidise (reduce) the redox ions and to achieve Nernstian equilibrium [343]. It was obvious that charge-transfer kinetic was becoming more sluggish subsequent to each modification step, with CEA/SM/Ab/PY-ZG/SPCE being the most sluggish of all given the antibody-antigen complex on its surface. In summary, the increasing trend of ΔEp together with the decreasing trend of peak current supported the fact that each functionalisation step was successful and the sensing platform was competent to form Ab-CEA immuno-complex for analytical application.

Meanwhile, EIS is a sensitive electrochemical assay that can be employed to monitor affinity-driven events involving proteins, DNA, nucleic acids or even whole cells at the electrode-electrolyte interface. Recent literature presented ultrasensitive biosensors based on EIS that allowed detection down to attomolar (aM) concentrations [371]–[373], opening up a new avenue to detect proteins and genetic elements that can exist at tremendously low concentrations at the initial stages of a particular disease. The binding of CEA to the Ab on the electrode leads to conformational change which in turn induces impedance change and provides a label-free technique that permits straightforward measurement of antibody-antigen binding. The semi-circle in the high-frequency region of a Nyquist plot represents the Rct caused by the proteins on the electrode. Figure 6.1 (b) shows the impedance spectrum of each functionalisation layer. The ZG/SPCE exhibited a low Rct of 1.7 kΩ owing to the good conductivity of the nanocomposite; nonetheless, after the sequential modifications: PY-functionalisation, Ab immobilisation and active-site blocking, the PY-ZG/SPCE, Ab/PY-ZG/SPCE and SM/Ab/PY-ZG/SPCE electrodes exhibited increased Rct of 2.4 kΩ, 3.2 kΩ and 4.7 kΩ, respectively. This observation was

consistent with that obtained from CV measurements in which each functionalisation step deposited more molecules on the electrode surface and augmented the barrier for charge transfer at the sensor interface. The SM/Ab/PY-ZG/SPCE electrode once incubated with the targeted CEA yielded electrode CEA/SM/Ab/PY-ZG/SPCE that demonstrated Rct of 6.1 kΩ, in accordance with the aforementioned fact that specific Ab-CEA immuno-complex was formed on the electrode surface and increased charge transfer resistance [128].

Besides, the charge transfer rate, Ket can be calculated based on the observed Rct using equation 5.2 of chapter 5 [340]–[342]. The Ket, calculated for each electrode according to the functionalisation sequence, exhibited a decreasing trend, with CEA/SM/Ab/PY-ZG/SPCE demonstrating the lowest Ket among all the electrodes (3.48×10^{-5} cm s^{-1}), endorsing that its faradaic process was the slowest among all the electrodes owing to the bulky Ab-CEA immuno-complex on the electrode surface [341]. In brief, Ket decreased in the order of ZG/SPCE (12.6×10^{-5} cm s^{-1}) > PY-ZG/SPCE (8.82×10^{-5} cm s^{-1}) > Ab/PY-ZG/SPCE (6.68×10^{-5} cm s^{-1}) > SM/Ab/PY-ZG/SPCE (4.53×10^{-5} cm s^{-1}) > CEA/SM/Ab/PY-ZG/SPCE (3.48×10^{-5} cm s^{-1}). The consistently decreased Ket was coherent with the continually decreased peak current in CV since the charge transfer kinetic governed the magnitude of the current. In a nutshell, a strong agreement between EIS analysis and CV analysis was observed, and this coherency distinctly signified the effective fabrication of an immunosensor for CEA detection.

To demonstrate that the increment of Rct was specifically caused by the binding of antibody-antigen binding, ZG/SPCE, the biolinker-free electrodes (which made the immobilisation of CEA-Ab infeasible) were tested against 0.1 ng/ml of CEA. It was observed that the Rct difference before and after the CEA exposure was negligible (< 2 %), On the other hand, the electrode with immobilised Ab (SM/Ab/PY-ZG/SPCE) showed approximately 68% of Rct increase when exposed to 0.1 ng/ml of CEA. Intrinsically, the results supported the fact that the increment of Rct was indeed a response to the binding of CEA antibody-antigen.



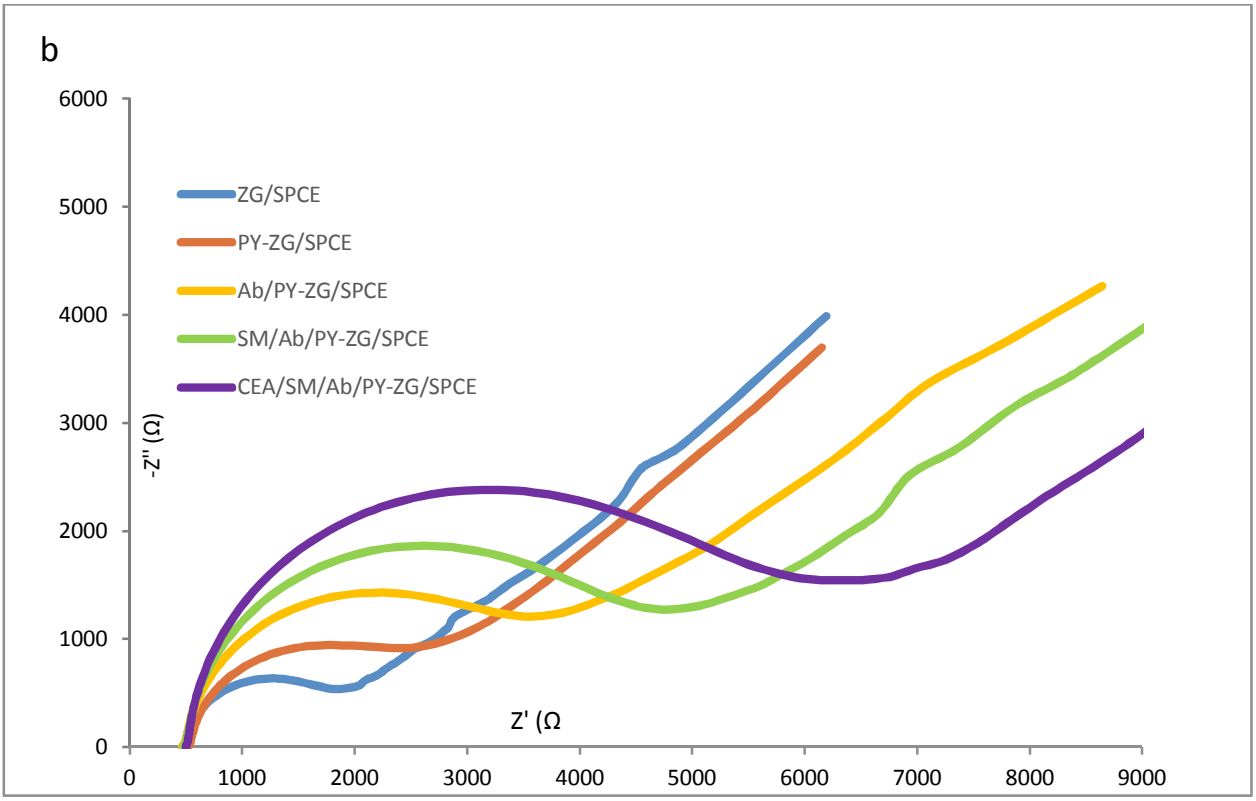


Figure 6.1. (a) CVs and (b) EIS of ZG/SPCE, PY-ZG/SPCE, Ab/PY-ZG/SPCE, SM/Ab/PY-ZG/SPCE and CEA/SM/Ab/PY-ZG/SPCE. Each functionalisation step introduced a higher physical barrier at the electrode surface and increased the charge transfer resistance.

6.3.2 OPTIMISATION OF FABRICATION AND SENSING PARAMETERS

The sensor response can be amplified through optimisation of the fabrication parameters, viz., the ZG: PY ratio, the Ab concentration, the Ab immobilisation time and the active-site blocking time. The sensing condition, namely the Ab-CEA binding time or in other words, the sensor reaction time was also investigated to intensify the sensor signal. In addition to signal amplification, the optimisation steps aimed as well to reduce wastage and prevent an unproductive state caused by overly-dense electrode surfaces that hindered antigen-antibody binding.

To determine the optimum ZG: PY ratio, SPCEs functionalised with different ratios (1:2, 1:4, 1:8, and 1:16) were immobilised with 15 μg/ml of Ab for 75 minutes, followed by active-site blocking with 1% skim milk for 20 minutes. The functionalised electrodes were subsequently incubated with 5 ng/ml of CEA for 50 minutes. As shown in Figure 6.2 (a), rRct increased gradually following the adjustment of the ZG: PY ratio from 1:2 to 1:4, and reduced thereafter. The inferior sensor response at a low PY ratio was suggestive of inadequate PY on the electrode surface that resulted in an insufficient amount of immobilised Ab for effective binding [374]. On the contrary, a high PY ratio introduced abundant amide linkages on the electrode surface and resulted in a thick layer of immobilised Ab that consequently hindered the binding of Ab-CEA due to steric limitations [375]. ANOVA test showed that the ZG: PY ratio was a significant parameter affecting the sensor response ($p < 0.05$). Since ZG: PY of 1:4 was the most optimum ratio, it was adopted in subsequent analyses.

Likewise, the optimum concentration of Ab was investigated by immobilizing Ab of different concentrations (1 μg/ml, 5 μg/ml, 10 μg/ml, and 15 μg/ml) onto the electrode for 75 minutes, followed by active-site blocking with 1% skim milk for 20 minutes and CEA-incubation for 50 minutes. As shown in Figure 6.2 (b), rRct increased significantly following higher Ab concentration, reached a maximum at 10 μg/ml and levelled off thereafter. This result is consistent with the finding from the optimisation of ZG: PY ratio discussed earlier: low concentration of Ab was indicative of overly sparse immobilised Ab for effective CEA detection, whereas high

concentration of immobilised Ab induced steric hindrances which would, in turn, limit the Ab-CEA immuno-complex that can be formed [376], [377]. Similarly, the ANOVA test endorsed that Ab concentration has a significant influence on rRct ($p < 0.05$). Since maximum rRct was observed for electrodes immobilised with 10 µg/ml of Ab, this concentration was adopted in subsequent analyses.

Subsequently, the influence of Ab immobilisation time on rRct was considered. Electrodes were immobilised with 10 µg/ml of Ab for varying durations (25 minutes, 50 minutes, 75 minutes and 100 minutes) followed by active-site blocking for 20 minutes and CEA-incubation for 50 minutes. As shown in Figure 6.2 (c), the rRct for 25 minutes of immobilisation time was the lowest among all electrodes. It was stipulated that a certain threshold of time was required for the proteins to form specific binding during incubation [378] and 25 minutes of immobilisation time was below the threshold. Afterwards, rRct was observed to increase when the immobilisation time was adjusted to 50 minutes; nonetheless, the subsequent increase to 75 minutes and 100 minutes led to a lower rRct, implying less efficient Ab-CEA binding. Although extended incubation time furnished ample time for Ab to be immobilised well on the sensor, prolonged immobilisation time caused steric limitation and competitive binding of CEA [379]. As supported by the ANOVA test, adjustment of the Ab immobilisation time was statistically significant on rRct ($p < 0.05$). Since 50 minutes of immobilisation generated the most amplified sensor response, it was selected for subsequent analyses.

The active-site blocking step was optimised by varying the blocking time. Functionalised electrodes were immobilised with 10 µg/ml of Ab for 50 minutes followed by active-site blocking with 1% skim milk for various blocking times (no blocking, 10 minutes, 20 minutes and 30 minutes). All the electrodes were later subjected to incubation with CEA for 50 minutes. As shown in Figure 6.2 (d), the electrode without the blocking step presented high rRct due to the presence of non-specific binding [380]. The incubated CEA was attached not only to the Ab but also to the PY bi-linker due to the presence of amides on the exterior of CEA, causing an inaccurately high

sensor response. When the blocking time was increased, rRct reduced and reached a plateau after 20 minutes, manifesting that the protein binding sites were saturated with blocking buffer. This observation was supported by the result from the paired-sample test which showed that the rRct difference from 20 minutes to 30 minutes was statistically insignificant ($p > 0.05$). The further increase of blocking time beyond 20 minutes imposed no effect on rRct. Hence, 20 minutes of blocking time were selected to suppress non-specific bindings on the electrode surface.

The Ab-CEA binding time was investigated by varying the incubation time with the CEA solution. Electrodes were immobilised with 10 µg/ml of Ab for 50 minutes followed by active-site blocking with 1% skim milk for 20 minutes. The electrodes were then incubated with CEA for varying durations (25 minutes, 50 minutes, 75 minutes and 100 minutes). Amplified rRct was observed as the binding time was increased from 25 minutes to 75 minutes (Figure 6.2 (e)), depicting the greater Ab-CEA immuno-complex formation. However, prolonged binding time (100 minutes) did not result in further change, which implied that the equilibrium of immuno-reaction and the formation of Ab-CEA immuno-complex was saturated [9]. This observation was validated with aid of the paired-sample test which showed a statistically significant rRct difference from 25 minutes to 75 minutes ($p < 0.05$) but a statistically insignificant rRct change from 75 minutes to 100 minutes ($p > 0.05$). As such, 75 minutes of binding time was considered the plateau and was adopted for subsequent analyses.

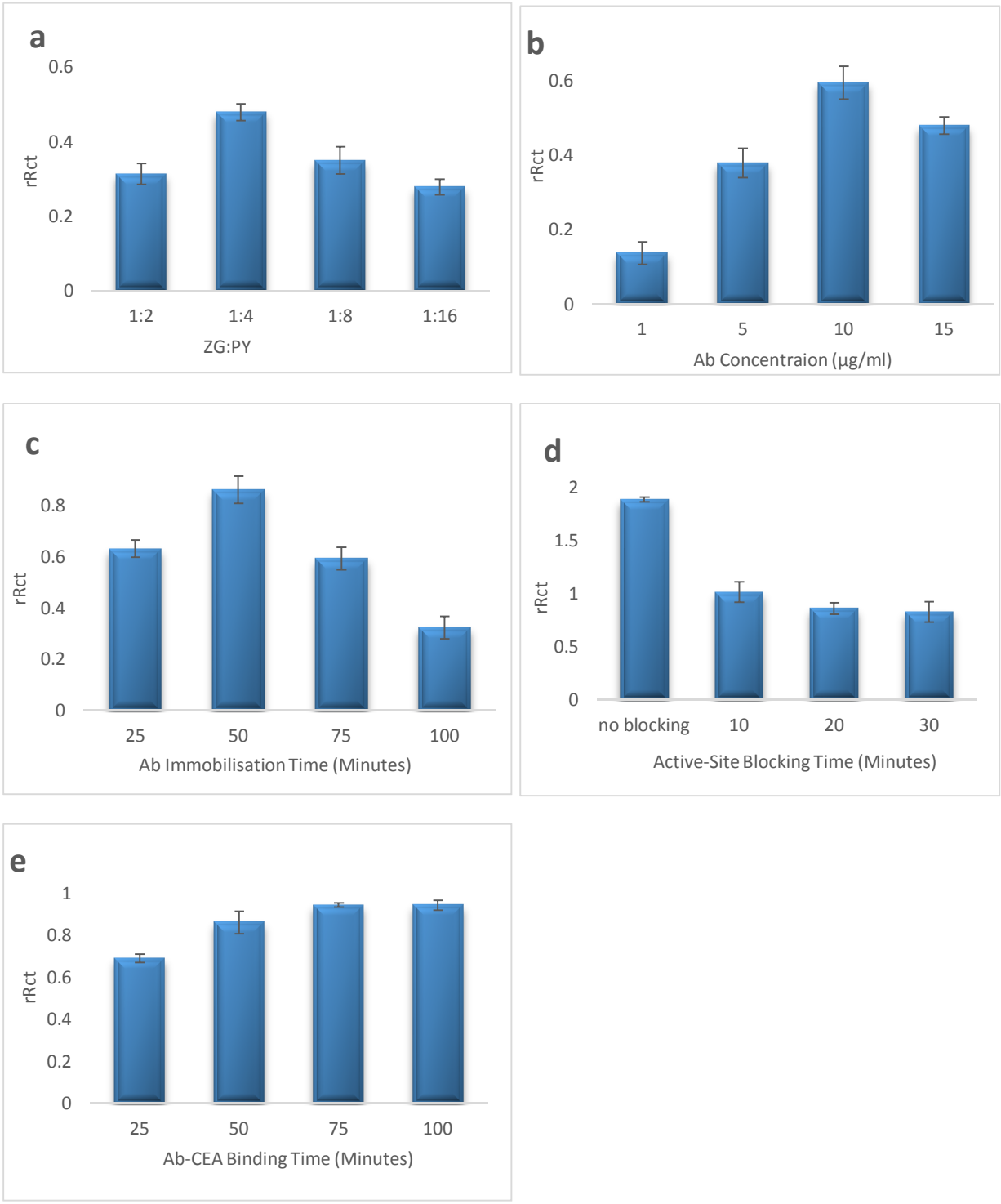


Figure 6.2. Influence of (a) ZG: PY ratio, (b) Ab concentration, (c) Ab immobilisation time, (d) active-site blocking time and (e) Ab-CEA binding time on signal response rRct. The adopted value for ZG: PY ratio, Ab concentration, Ab immobilisation time, active-site blocking time and Ab-CEA binding time was 1:4, 10 µg/ml, 50 minutes, 20 minutes and 75 minutes respectively, for enhanced sensor performance.

6.3.3 ANALYTICAL PERFORMANCE, SPECIFICITY, STABILITY AND REPRODUCIBILITY

Under optimised sensing conditions, the immunosensor was employed to react with different concentrations of CEA, ranging from 0.01 ng/ml to 10 ng/ml. Along with the increase in CEA concentration, the magnitude of rRct increased due to the greater formation of Ab-CEA immuno-complexes, which serve as the obstructive structure that impeded the diffusion of redox species. The sensor response was found to be linearly associated with the logarithmic value of the CEA concentration (Figure 6.3 (a)), with a correlation coefficient of R^2 = 0.9944 and a calibration equation of rRct= 0.46 log C + 5.24. The LOD of the sensor was estimated to be 4.25 pg/ml (S/N=3). The concentration of CEA in a healthy individual is within the range of 2.5 ng/ml to 5.0 ng/ml wherein a majority of research works took CEA > 5 ng/ml as the cutoff level for possible malignant conditions [363]. The working range of the sensor fitted well into the physiological range of CEA concentration, useful for early detection of CEA over-expression. The performance of the fabricated immunosensor is comparable to other CEA sensing platforms listed in Table 6.1.

Sensor specificity is of utmost importance as it outlines the ability of the developed immunosensor to distinguish CEA from other interfering species specifically. As such, the specificity of the immunosensor was evaluated by measuring the rRct in the presence of other interfering species such as glucose (Glc), acetaminophen (Ap), Immunoglobulin G (IgG) and bovine serum albumin (BSA). The immunosensor was initially tested against samples containing only the interfering species, in which the rRct measured in interference-only samples were insignificant as shown in Figure 6.3 (b), demonstrating inertness towards non-CEA species. Subsequently, CEA was mixed with these interfering species individually and the mixtures were measured by the immunosensor. It was observed that interfering species that co-exist with CEA did not present substantial influence on the rRct value, where the deviation of rRct as compared to that measured from the CEA-only sample ranged merely from 1% to 8%. The inertness towards non-CEA species and the selectivity towards CEA that co-existed with interfering species evidenced the good specificity of the as-

developed immunosensor. Then, the stability of the immunosensor was evaluated. Since this work aims to develop an economical and disposable sensing platform for the rapid testing of CEA, the fabricated immunosensor should be stable under proper storage to provide a reasonable shelf life. For stability study, a series of functionalised SPCE was stored under 4 °C and tested with 1 ng/ml of CEA at an interval of 5 days, 10 days, 15 days and 20 days as shown in Figure 6.3 (c). The signal response of the stored electrodes was comparable to that of freshly prepared electrodes. Even with prolonged storage of 20 days, the immunosensor retained more than 90% of the signal response. The result implied that the bioactivity of Ab was well preserved and the immunosensor has demonstrated decent stability. Reproducibility is a crucial concern pertaining to the practical application of immunosensor. In order to illustrate the reproducibility of the immunosensor, a series of electrodes were concurrently fabricated and incubated with 1 ng/ml of CEA, followed by the EIS test. The rRct values measured by the different electrodes were in close agreement. An RSD of 4.27 % was obtained, demonstrating a comparable if not better reproducibility with works reported in the literature [8], [128], [381]

Table 6.1: Analytical Performance of the Fabricated CEA Immunosensor Against Other Reported CEA Sensors

Platform	Technique	Working Range (ng/ml)	Detection Limit (ng/ml)	Ref
Anti-CEA/nano-gold/carbon nanotubes-chitosan/GCE	DPV	0.30 - 20	0.01	[380]
Streptavidin-functionalised nitrogen-doped graphene/GCE	DPV	0.02 -12	0.01	[365]
Ferrocene derivatives /gold nanoparticles/gold electrode	SWV	0.05 - 20	0.01	[214]
Quantum dot coated silica /lead/sandwiched CEA/gold substrate	SWV	0.05 - 25	0.005	[382]
poly(3,4ethylenedioxythiophene):poly(4-styrene sulfonate)/conducting whatman paper strip	EIS	6 - 20	2.68	[383]
CEA/SM/Ab/PY-ZG/SPCE	EIS	0.01 - 10	0.004	This work

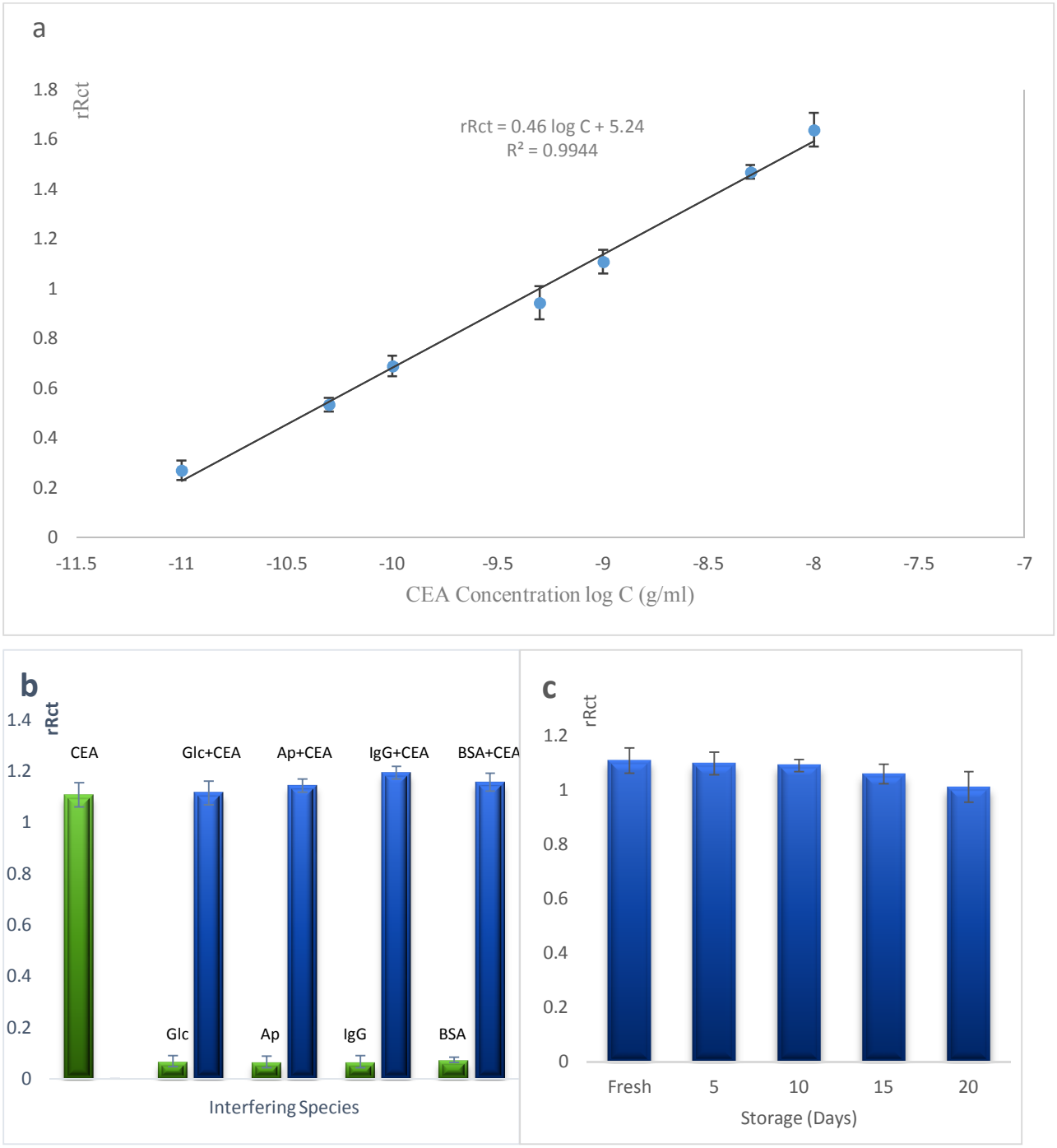


Figure 6.3. (a) Linear correlation between rRct and logarithmic value of CEA concentration, (b) specificity study of the immunosensor and (c) stability study of the immunosensor. The fabricated immunosensor was highly selective to CEA and was able to quantity CEA ranging from 0.01 ng/ml to 10 ng/ml.

6.3.4 DETECTION OF CEA IN HUMAN SERUM

The competence of the immunosensor to detect CEA present in human serum was evaluated to study its feasibility to function within complex biological matrices. Human serum is recognised to be a complex biological medium containing several components such as organic molecules (insulin, bilirubin, glucose, uric acid, urea, fibrinogen, globulins, albumin), lipids (triglycerides, phospholipids, cholesterol) and ions (Mg^{2+}, Ca^{2+}, K^{+}, Na^{+}) [313]. Therefore, it was worthy to challenge an immunosensor against detection in human serum. As shown in Table 6.2, good recoveries were found ranging from 103% to 106%, manifesting a close agreement with the actual CEA concentration. The finding suggested that the proposed immunosensor possesses a high affinity to CEA even in a complex biological matrix, rendering it a promising sensing platform for real sample analysis.

Table 6.2: Recovery Test of Spiked Human Sample

Sample	Spiked CEA Concentration (ng/ml)	Detected CEA Concentration (ng/ml)	Recovery (%)
1	0.01	0.01035	103.5
2	0.10	0.10521	105.2
3	1.00	1.00475	100.5
4	10.0	10.6044	106.0

6.3.5 ADVANTAGES OF THE IMMUNOSENSOR

A vast number of CEA sensors engaged labels or tags such as secondary protein labels, fluorescent chemical compounds and magnetic nanomaterial to detect the presence and quantify the concentration of CEA [222], [384], [385]. In contrast with labelled methods, label-free sensing platforms measured the physical or chemical changes directly and transduced the changes into quantifiable analytical data. Immunosensor proposed in this study, a label-free platform, measured the formation of Ab-CEA immuno-complex and transduced it to the change in Rct, a quantitative parameter. Label-free detection eliminated experimental errors induced by the labelling tags such

as sample degradation during the labelling process, inconsistent labelling due to steric hindrance and the failure to identify versatile tags that function reliably [362], [386]. The immunosensor proposed was as proficient as the other sensors in CEA detection, yet it was more economical and simpler to fabricate. Without the intervention of label molecules, label-free CEA immunosensor significantly shortens the required time and effort for assay development, thus enhancing its potential for rapid CEA detection.

Equally beneficial is the Ab-immobilisation strategy employed in this study. Immobilisation of CEA Ab onto the ZG via PY has not been reported in the literature. Immobilisation proposed here exploited π-π interaction, the dominating supramolecular force to firmly stack PY on graphene sheets [387]; PY, in turn, utilised amines-nucleophilic substitution to form amide bonds with the Ab. The Ab-PY-ZG linkage in this work was reliable and direct; It was a significantly more robust immobilisation technique in comparison to the physical absorption method that bound proteins hydrophobically or electrostatically resulting in uncontrollable orientation and desorption [388]. The Ab-PY-ZG immobilisation method was also cheaper and simpler to perform than affinity methods such as immobilisation using thiols group and streptavidin-biotin which required costly reagents and alteration of the Ab conformation before immobilisation [377].

Another supplementary benefit of the CEA immunosensor lies in its disposable nature. Keeping in view the aim to develop a point-of-care sensing platform, the CEA sensor proposed in this work was realised with disposable SPCE that required no surface polishing. The preparation work was minimal. On top of that, its single-use practice also eliminated the risk of cross-contaminations. Thus said, our disposable SPCE platform could be more promising.

6.4 SUMMARY

This work presented an immunosensor for CEA detection based on the ZG nanocomposite. CEA is a glycoprotein involved in cell adhesion and it is known to be over-expressed in lung cancer. The CEA level of a healthy individual is ideally below 5.0 ng/ml, therefore serum CEA levels higher than that of healthy persons led to its diagnostic role as a cancer indicator. ZG nanocomposite was functionalised with biolinker PY to immobilise CEA antibody probes. Results from CV and EIS validated the accomplishment of each fabrication step and endorsed the specific formation of CEA-Ab immuno-complex upon detection. After the optimisation of fabrication steps and sensing conditions, the proposed immunosensor exhibited good responses toward CEA detection, with a 4.25 pg/ml LOD and correlation coefficient of R^2= 0.99 within a linear working range from 0.01 ng/ml to 10 ng/ml. Furthermore, the immunosensor exhibited high specificity for CEA against interfering species, decent stability for up to 20 days with minor response deviation, and reasonable reproducibility of 4.27% RSD. The performance of the immunosensor to detect CEA present in human serum was also evaluated. Good recovery of CEA was found, suggesting that the proposed immunosensor possesses a high affinity to CEA even in a complex biological matrix, rendering it a promising sensing platform for real sample analysis.

7 CONCLUSION, LIMITATIONS AND FUTURE WORKS

7.1 CONCLUSION

This study has detailed the synthesis and characterisation of graphene and ZG nanocomposite that were produced via a simple and efficient synthesis route. The performances of the as-synthesised ZG nanocomposite as electrochemical sensors for the detection of lung carcinoma DNA mutation/biomarkers were demonstrated and evaluated. The cytotoxicity of the ZG nanocomposite on human lung and skin cells was also assessed. The conclusions drawn from these studies are summarised as follows:

(1) A facile and green approach for the synthesis of graphene and ZG nanocomposite without any harsh chemicals has been reported. Solvent-exfoliation and one-pot hydrothermal methods were used to produce pristine graphene and the well-hybridised ZG nanocomposite. The synthesis route was efficient and scalable. Material characterisation using Raman spectrography, XRD, TEM, SEM and EDX collectively showed that pristine graphene sheets were synthesised via exfoliation and ZrO_2 nanoparticles were homogeneously distributed on the surface of graphene sheets. Both graphene and ZrO_2 retained their crystalline structures without any disruption caused by the synthesis process. Only the presence of carbon and ZrO_2 was detected in the composition analysis indicating the absence of harsh chemical residual and the void of impurities. The ZG nanocomposite was employed to modify SPCEs and tested accordingly using CV and EIS. As a result of the synergistic effect between graphene and ZrO_2, the ZG/SPCE exhibited improved electrochemical activity towards potassium ferricyanide, an active redox probe, as compared to that from bare electrodes, the graphene/SPCE and the ZrO_2/SPCE. It is anticipated that the ZG/SPCE platform could be explored for a greater variety of electrochemical sensing. Thanks to the scalable and green synthesis method, the synthesised ZG nanocomposite was free from residual chemicals resulting in low cytotoxicity. The microscopic study revealed that ZG-treated cells appeared to have

retained comparable morphology and proliferation rate as the untreated cells. Meanwhile, the MTT assay showed that exposure to ZG was non-cytotoxic for HaCat cells up to 72 hours of incubation, and also for MRC5 cells incubated with less than 250 μg/ml of the nanocomposite. The high cell viability and the superior IC50 (> 500 μg/ml) indicated that the ZG nanocomposite was safe on the lung and skin, the two organs most susceptible to nanocomposite toxicity through inhalation and physical contact. This finding strongly endorsed the application of the as-synthesised ZG for the functionalisation of the immunosensor demonstrated in this work.

(2) An electrochemical sensor based on the ZG/SPCE was fabricated for the detection of acetaminophen via DPV to demonstrate the feasibility of the ZG-based sensing platform for analyte detection. The electrochemical sensor exhibited favourable performances for acetaminophen detection within the concentration of 10 μM to 100 μM, with a LOD of 75.5 nM. Repeatability of < 3% RSD, reproducibility of 5 % RSD, stability of 95% after 5 days of storage and decent selectivity to acetaminophen in the presence of interfering species were observed. Besides, the proposed sensor was also tested against the detection of acetaminophen in commercial tablets where an acceptable recovery in the range of 80% to 85% for three different types of pharmaceutical samples was observed, supporting the practical applicability of the electrochemical sensor. The findings in this chapter suggested that the ZG-based platform has promising potential for fast, low cost and accurate electrochemical sensings.

(3) Owing to the good electrochemical performance of the sensing platform in detecting acetaminophen, the potential of the ZG-based platform to serve as a biosensor was further explored where a genosensor (DNA sensor) for the differentiation of exon-19 wild-type and mutated sequence in the EGFR was fabricated. The mutation of exon-19 is often observed in patients with lung cancer and this mutation type is sensitive to TKIs with

favourable clinical outcomes. The ZG nanocomposite platform was functionalised with biolinker PY that took advantage of the supramolecular force, π-π interaction to firmly stack on graphene sheets and in turn utilise the strong amines-nucleophilic substitution to form amide bonds with the amine-modified capture-DNA. The results from CV and EIS endorsed the effective immobilisation of the capture-DNA onto the SPCEs. Under optimised fabrication and sensing conditions, the genosensor was able to quantify the wild-type DNA in the range of 5 nM to 1 μM, with a linearity coefficient of R^2= 0.99 and a LOD of 1.7 nM. The genosensor was also capable of differentiating mutated exon-19 DNA from the wild-type DNA by generating distinctive signals for wild-type and mutated sequences, giving it the ability to identify potential lung malignancies. The proposed assay transduced DNA mutation via impedance change on the electrode surface, obviating the complicated fabrication protocols and the use of labels in the detection scheme. As such, this work not only demonstrated a reliable technique for the detection of lung cancer-associated DNA mutation but also offered a promising platform for the detection of other genetic mutational diseases in general.

(4) This work has proposed an immunosensor for the detection of CEA tumour markers. CEA is a glycoprotein involved in cell adhesion and it is known to be over-expressed in lung cancer. The serum CEA level of a healthy individual is ideally below 5.0 ng/ml, therefore serum CEA level higher than that of healthy persons led to its diagnostic role as a lung cancer indicator. ZG nanocomposite was functionalised with PY to immobilise CEA antibody probes which would, in turn, recognise and bind to CEA. Results from CV and EIS validated the accomplishment of each fabrication step and endorsed the specific formation of CEA antigen-antibody upon detection. After the optimisation of fabrication steps and sensing conditions, the proposed immunosensor exhibited good responses towards CEA detection, with a 4.25 pg/ml LOD and correlation coefficient of R^2= 0.99

within a linear working range from 0.01 ng/ml to 10 ng/ml, which fits the physiological concentration of CEA in serum. Furthermore, the immunosensor exhibited high specificity for CEA against interfering species, decent stability for up to 20 days with minor response deviation, and reasonable reproducibility of 4.27% RSD. The performance of the immunosensor to detect CEA present in human serum was also evaluated. Good recovery of CEA was found, suggesting that the proposed immunosensor possesses a high affinity to CEA even in a complex biological matrix, rendering it a promising sensing platform for real sample analysis.

The key characteristics of the acetaminophen sensor, genosensor and immunosensor reported in this work offered appealing merits on their own: the handiness of disposable design, the stable and straightforward PY biolinker immobilisation technique, the highly biocompatible ZG electrode material, the scalability of label-free detection and the potential for rapid testing; hence, hybridizing all these merits produced a promising electrochemical testing platform and subsequently opened up a new way for early detection of malignant conditions.

7.2 LIMITATIONS AND FUTURE WORKS

The work achieved in this report has built a foundation for future work to be based upon. This study has demonstrated that the as-synthesised ZG nanocomposite has very favourable electrochemical sensing potentials and could open up new opportunities for the exploration of various applications. Nonetheless, there were limitations to the current study due to the unavailability of resources. Some limitations and feasible future works are discussed in this section.

Firstly, the SPCEs reported in this study were modified with ZG nanocomposite via the drop-casting method in which a few micro-litre of the ZG-dispersion was pipetted to the working electrode and dried at ambient conditions. The method is simple and direct but various factors such as the presence of bubbles and the location of the first drop could affect the uniformity of the deposited layers and thus introduce inconsistency into the electrochemical performances of the sensor [389]. Future work could be geared towards the printing of electrodes using ZG-based inks to eliminate the modification step for faster and more consistent sensor fabrication.

This study has fabricated an electrochemical genosensor and immunosensor for the detection of EGFR mutation and CEA. Nonetheless, the measurements of the sensor were performed using a bench-top potentiostat and thus limiting its actual point-of-care applications due to the bulkiness of the potentiostat. Further work can focus on the miniaturisation of the biosensors to practically serve as a point-of-care sensor that could provide diagnosis rapidly without the use of sophisticated equipment. The design of a handheld potentiostat integrated with smartphone-based analysis software would allow more convenient point-of-care testing, even for inexperienced personnel.

Elevated CEA level was observed occasionally in patients without lung malignancies; one of the reasons being the effect of a medication like lithium [390]. In other words, benign etiologies of elevated CEA may lead to false-positive lung cancer. Therefore, the exploration to turn the ZG platform into a sensor capable of multianalyte detection is research-worthy. Simultaneous detection of multianalyte associated with lung cancer is beneficial for more accurate and sensitive

detection. For instance, a study has investigated the diagnostic value of two proteins, the CEA and CYFRA-21 in lung cancer patients [191]. Both tumour markers have their own diagnostic and prognostic value, however greater specificity and positive predictive value were obtained for patients with over-expression of both CEA and CYFRA-21 protein. Therefore, efforts can be geared towards the development of sensing strategies that permit simultaneous electrochemical detection of dual tumour markers, such as CEA and CYFRA-21 in a single run, without interfering with each other. This in itself presents an advancement towards highly accurate point-of-care lung cancer detection.

Besides, the genosensor developed in this study was evaluated using synthetic oligonucleotides that were designed to correspond to exon-19 mutation. There was a lack of study on the performance of the genosensor with real samples, that is, exon-19 DNA extracted from the tumour tissue of cancer patients. The current work has no access to hospitals/institutions that could provide tumour tissue from cancer patients. Extracted DNA from patients could consist of different mutation types that may interfere with the sensor readings. Future works could be geared towards the acquisition of DNA genomes from tumour tissues of lung cancer patients, followed by PCR amplification of the desired sequence (the wild-type or the mutated type) using the appropriate primers. An effective protocol that degrades phosphorylated duplex DNA into single-stranded DNA suitable for the electrochemical sensor should also be established. It is anticipated that the genosensor once tested against clinical samples could present itself as a more promising tool for mutation discrimination.

REFERENCES

[1] American Cancer Society, "Cancer facts & figures 2020," *Atlanta Am. Cancer Soc.*, pp. 1–71, 2020.

[2] R. L. Siegel, K. D. Miller, H. E. Fuchs, and A. Jemal, "Cancer Statistics , 2021," *CA A Cancer J. Clin.*, vol. 71, no. 1, pp. 7–33, 2021.

[3] M. Coleman *et al.*, "Trends and socioeconomic inequalities in cancer survival in England and Wales up to 2001," *Br. J. Cancer*, vol. 90, pp. 1367–1373, 2004.

[4] J. D. Mathews *et al.*, "Cancer risk in 680 000 people exposed to computed tomography scans in childhood or adolescence : data linkage study of 11 million Australians," *Br. Med. J.*, vol. 346, no. 7910, pp. 1–18, 2013.

[5] E. Gershman, R. Guthrie, K. Swiatek, and S. Shojaee, "Management of hemoptysis in patients with lung cancer," *Ann. Transl. Med.*, vol. 7, no. 15, pp. 1–12, 2019.

[6] R. Ghosal, P. Kloer, K. E. Lewis, R. Unit, and P. Philip, "A review of novel biological tools used in screening for the early detection of lung cancer," *Postgrad. Med. J.*, vol. 85, no. 1005, pp. 358–363, 2009.

[7] B. Eftekhari-Sis, M. A. Aliabad, and F. Karimi, "Graphene oxide based nano-biosensor for the detection of deletion mutation in exon 19 of EGFR gene, leading to lung cancer," *Mater. Lett.*, vol. 183, pp. 441–443, 2016.

[8] L. Zhu *et al.*, "Electrochemical immunoassay for carcinoembryonic antigen using gold nanoparticle-graphene composite modified glassy carbon electrode," *Talanta*, vol. 116, pp. 809–815, 2013.

[9] Y. Yang, K. Cao, M. Wu, C. Zhao, H. Li, and C. Hong, "3D graphene / MWNTs nano-frameworks embedded Ag-Au bimetallic NPs for carcinoembryonic antigen detection," *Microchem. J.*, vol. 148, pp. 548–554, 2019.

[10] P. Butmee, G. Tumcharern, G. Thouand, K. Kalcher, and A. Samphao, "An ultrasensitive immunosensor based on manganese dioxide-graphene nanoplatelets and core shell Fe3O4@Au nanoparticles for label-free detection of carcinoembryonic antigen," *Bioelectrochemistry*, vol. 132, p. 107452, 2020.

[11] K. S. Novaselov *et al.*, "Electric field effect in atomically thin carbon films," *Science*, vol. 306, pp. 666–669, 2004.

[12] A. Kaplan *et al.*, "Current and future directions in electron transfer chemistry of graphene,"

Chem. Soc. Rev., vol. 46, no. 15, pp. 4530–4571, 2017.

[13] S. Suzuki, M. E. Schmidt, and M. Muruganathan, "Recent progress of graphene-based nanoelectronic devices and NEMS for challenging applications," in *2016 13th IEEE International Conference on Solid-State and Integrated Circuit Technology (ICSICT)*, 2016, pp. 474–477.

[14] E. R. Ezeigwe, C. J. Sin, P. S. Khiew, C. W. Siong, and M. T. T. Tan, "Cobalt oxide nanoparticles grown on exfoliated graphene for enhanced electrochemical performance," *Mater. Chem. Phys.*, vol. 183, pp. 56–64, 2016.

[15] I. Khalil, N. M. Julkapli, W. A. Yehye, W. J. Basirun, and S. K. Bhargava, "Graphene-gold nanoparticles hybrid-synthesis, functionalization, and application in a electrochemical and surface-enhanced Raman scattering biosensor," *Materials (Basel).*, vol. 9, no. 6, p. 406, 2016.

[16] S. S. Low, M. T. T. Tan, H. S. Loh, P. S. Khiew, and W. S. Chiu, "Facile hydrothermal growth graphene/ZnO nanocomposite for development of enhanced biosensor," *Anal. Chim. Acta*, vol. 903, pp. 131–141, 2016.

[17] S. Cao, L. Zhang, Y. Chai, and R. Yuan, "Electrochemistry of cholesterol biosensor based on a novel Pt-Pd bimetallic nanoparticle decorated graphene catalyst," *Talanta*, vol. 109, pp. 167–172, 2013.

[18] H. Teymourian, A. Salimi, and S. Khezrian, "Fe3O4 magnetic nanoparticles/reduced graphene oxide nanosheets as a novel electrochemical and bioelectrochemical sensing platform," *Biosens. Bioelectron.*, vol. 49, pp. 1–8, 2013.

[19] Z. Fan *et al.*, "A flexible and disposable hybrid electrode based on Cu nanowires modified graphene transparent electrode for non-enzymatic glucose sensor," *Electrochim. Acta*, vol. 109, pp. 602–608, 2013.

[20] F. Gao *et al.*, "Application of graphene-pyrenebutyric acid nanocomposite as probe oligonucleotide immobilization platform in a DNA biosensor," *Mater. Sci. Eng. C*, vol. 33, no. 7, pp. 3851–3857, 2013.

[21] P. F. Manicone, P. Rossi Iommetti, and L. Raffaelli, "An overview of zirconia ceramics: Basic properties and clinical applications," *J. Dent.*, vol. 35, no. 11, pp. 819–826, 2007.

[22] Y. Zhao *et al.*, "Low temperature degradation of alumina-toughened zirconia in artificial saliva," *J. Wuhan Univ. Technol. Mater. Sci. Ed.*, vol. 28, no. 4, pp. 844–848, 2013.

[23] Y. S. Ko and Y. U. Kwon, "Mesoporous zirconia thin films with three-dimensional pore

structures and their application to electrochemical glucose detection," *ACS Appl. Mater. Interfaces*, vol. 5, no. 9, pp. 3599–3606, 2013.

[24] G. Sumana, M. Das, S. Srivastava, and B. D. Malhotra, "A novel urea biosensor based on zirconia," *Thin Solid Films*, vol. 519, no. 3, pp. 1187–1191, 2010.

[25] R. Sandoval, A. M. Cooper, K. Aymar, A. Jain, and K. Hristovski, "Removal of arsenic and methylene blue from water by granular activated carbon media impregnated with zirconium dioxide nanoparticles," *J. Hazard. Mater.*, vol. 193, pp. 296–303, 2011.

[26] S. Kumar, J. G. Sharma, S. Maji, and B. D. Malhotra, "Nanostructured zirconia decorated reduced graphene oxide based efficient biosensing platform for non-invasive oral cancer detection," *Biosens. Bioelectron.*, vol. 78, pp. 497–504, 2016.

[27] H. Teymourian, A. Salimi, S. Firoozi, A. Korani, and S. Soltanian, "One-pot hydrothermal synthesis of zirconium dioxide nanoparticles decorated reduced graphene oxide composite as high performance electrochemical sensing and biosensing platform," *Electrochim. Acta*, vol. 143, pp. 196–206, 2014.

[28] S. Abbas, F. Shahzad, and S. Batool, "Progress in cancer biomarkers monitoring strategies using graphene modified support materials," *Talanta*, vol. 210, p. 120669, 2020.

[29] G. Yang, Z. Xiao, C. Tang, and Y. Deng, "Recent advances in biosensor for detection of lung cancer biomarkers," *Biosens. Bioelectron.*, vol. 141, p. 111416, 2019.

[30] K. J. Huang, L. Wang, J. Li, and Y. M. Liu, "Electrochemical sensing based on layered MoS2-graphene composites," *Sensors Actuators, B Chem.*, vol. 178, pp. 671–677, 2013.

[31] D. Grieshaber, R. Mackenzie, J. Vörös, and E. Reimhult, "Electrochemical biosensors - sensor principles and architectures," *Sensors*, vol. 8, pp. 1400–1458, 2008.

[32] F. Patolsky, G. Zheng, and C. M. Lieber, "Nanowire-based biosensor," *Anal. Chem.*, vol. 78, no. 13, pp. 4260–4269, 2006.

[33] A. T. E. Vilian, S. Chen, L. Huang, M. A. Ali, and F. M. A. Al-Hemaid, "Simultaneous determination of catechol and hydroquinone using a Pt/ZrO2-RGO/GCE composite modified glassy carbon electrode," *Electrochim. Acta*, vol. 125, pp. 503–509, 2014.

[34] J. Gong, X. Miao, H. Wan, and D. Song, "Facile synthesis of zirconia nanoparticles-decorated graphene hybrid nanosheets for an enzymeless methyl parathion sensor," *Sensors Actuators, B Chem.*, vol. 162, pp. 341–347, 2012.

[35] M. Kaur and K. Pal, "An investigation for hydrogen storage capability of zirconia-reduced graphene oxide nanocomposite," *Int. J. Hydrogen Energy*, vol. 41, no. 47, pp. 21861–

21869, 2016.

[36] H. Zou, Y. Zhang, L. Liu, L. Shi, and W. Li, "The toughening mechanism and mechanical properties of graphene-reinforced zirconia ceramics by microwave sintering," *Adv. Appl. Ceram.*, vol. 117, no. 7, pp. 420–426, 2018.

[37] E. A. Trusova *et al.*, "Nanoscale Advances The phase composition, morphology and nanostructured powder," *nanoscale Adv.*, vol. 2, pp. 182–189, 2020.

[38] Y. Kristianto, A. Taufik, and R. Saleh, "Preparation and catalytic performance of ZrO2 - nanographene platelets composites," *J. Phys. Conf. Ser.*, vol. 776, pp. 1–7, 2016.

[39] A. T. Ezhil Vilian, M. Rajkumar, and S.-M. Chen, "In situ electrochemical synthesis of highly loaded zirconium nanoparticles decorated reduced graphene oxide for the selective determination of dopamine and paracetamol in presence of ascorbic acid," *Colloids Surfaces B Biointerfaces*, vol. 115, pp. 295–301, 2014.

[40] B. H. Cho and W. B. Ko, "Preparation of Graphene-ZrO2 Nanocomposites by Heat Treatment and Photocatalytic Degradation of Organic Dyes," *J. Nanosci. Nanotechnol.*, vol. 13, no. 11, pp. 7625–7630, 2013.

[41] S. S. Low, M. T. T. Tan, P. S. Khiew, H.-S. Loh, and W. S. Chiu, "One Step Green Preparation of Graphene/ZnO Nanocomposite for Electrochemical Sensing," *J. Nanosci. Nanotechnol.*, vol. 16, no. 7, pp. 7420–7426, 2016.

[42] M. Gorguner and M. Akgun, "Acute Inhalation Injury," *Eurasian J. Med.*, vol. 42, pp. 28–35, 2010.

[43] S. N. Kales and D. C. Christiani, "Acute Chemical Emergencies," *N. Engl. J. Med.*, vol. 350, pp. 800–808, 2004.

[44] O. Parkash and R. H. Shueb, "Diagnosis of dengue infection using conventional and biosensor based techniques," *Viruses*, vol. 7, no. 10, pp. 5410–5427, 2015.

[45] A. G. Dinmohamed *et al.*, "Fewer cancer diagnoses during the COVID-19 epidemic in the Netherlands," *Lancet Oncol.*, vol. 2019, pp. 750–751, 2020.

[46] E. Raymond, C. Thieblemont, S. Alran, and S. Faivre, "Impact of the COVID-19 Outbreak on the Management of Patients with Cancer," *Target. Oncol.*, vol. 15, no. 3, pp. 249–259, 2020.

[47] M. J. Allen, V. C. Tung, and R. B. Kaner, "Honeycomb carbon : A review of graphene," *Chem. Rev.*, vol. 110, pp. 132–145, 2010.

[48] S. Han *et al.*, "Highly sensitive biosensor based on synergistic effect of Fe3O4-Co3O4 bimetallic oxides and graphene," *RSC Adv.*, vol. 6, pp. 82033–82039, 2016.

[49] J. A. V. Albelda, A. Uzunoglu, G. N. C. Santos, and L. A. Stanciu, "Graphene-titanium dioxide nanocomposite based hypoxanthine sensor for assessment of meat freshness," *Biosens. Bioelectron.*, vol. 89, pp. 518–524, 2017.

[50] H. Devnani, S. Ansari, S. Piara, and R. Jain, "ZrO2-graphene-chitosan nanocomposite modified carbon paste sensor for sensitive and selective determination of dopamine," *Mater. Today Chem.*, vol. 4, pp. 17–25, 2017.

[51] K. S. Kim *et al.*, "Large-scale pattern growth of graphene films for stretchable transparent electrodes," *Nature*, vol. 457, no. 7230, pp. 706–710, 2008.

[52] S. Pei and H. Cheng, "The reduction of graphene oxide," *Carbon N. Y.*, vol. 50, no. 9, pp. 3210–3228, 2011.

[53] X. Zhang, H. Li, X. Cui, and Y. Lin, "Graphene / TiO2 nanocomposites : synthesis, characterization and application in hydrogen evolution from water photocatalytic splitting," *J. Mater. Chem.*, vol. 20, pp. 2801–2806, 2010.

[54] Z. Yin, S. Wu, X. Zhou, X. Huang, Q. Zhang, and F. Boey, "Electrochemical deposition of ZnO nanorods on transparent reduced graphene oxide electrodes for hybrid solar cells," *Small*, vol. 6, no. 2, pp. 307–312, 2010.

[55] P. Villalobos and I. I. Wistuba, "Lung Cancer Biomarkers Lung cancer Genotyping Biomarkers Molecular targets," *Hematol. Clin. NA*, vol. 31, no. 1, pp. 13–29, 2017.

[56] C. R. Sears and P. J. Mazzone, "Biomarkers in Lung Cancer," *Clin. Chest Med.*, vol. 41, no. 1, pp. 115–127, 2019.

[57] B. C *et al.*, "Electronic confinement and coherence in patterned epitaxial graphene," *Science*, vol. 312, pp. 1191–1197, 2006.

[58] C. Berger *et al.*, "Ultrathin Epitaxial Graphite : 2D Electron Gas Properties and a Route toward graphene-based nanoelectronics," *J. Phys. Chem. B*, vol. 108, pp. 19912–19916, 2004.

[59] J. Hass *et al.*, "Highly ordered graphene for two dimensional electronics," *Appl. Phys. Lett.*, vol. 89, p. 143106, 2006.

[60] H. Hibino, H. Kageshima, F. Maeda, M. Nagase, Y. Kobayashi, and H. Yamaguchi, "Microscopic thickness determination of thin graphite films formed on SiC from quantized oscillation in reflectivity of low-energy electrons," *Phys. Rev. B*, vol. 77, pp. 0754131–

0754137, 2008.

[61] K. V Emtsev *et al.*, "Towards wafer-size graphene layers by atmospheric pressure graphitization of silicon carbide," *Nat. Mater.*, vol. 8, no. 3, pp. 203–207, 2009.

[62] X. Li, "Large-Area Synthesis of High-Quality and Uniform Graphene Films on Copper Foils," *Science*, vol. 324, pp. 1312–1314, 2009.

[63] X. Dong *et al.*, "One-step growth of graphene -carbon nanotube hybrid materials by chemical vapor deposition," *Carbon N. Y.*, vol. 49, no. 9, pp. 2944–2949, 2011.

[64] C. Hu, T. Lu, F. Chen, and R. Zhang, "A brief review of graphene–metal oxide composites synthesis and applications in photocatalysis," *J. Chinese Adv. Mater. Soc.*, vol. 1, no. 1, pp. 21–39, 2013.

[65] W.S. Hummers Jr and R. E. Offeman, "Preparation of Graphitic Oxide," *J. Am. Chem. Soc.*, vol. 80, no. 6, pp. 1339–1339, 1958.

[66] J. Yang and S. Gunasekaran, "Electrochemically reduced graphene oxide sheets for use in high performance supercapacitors," *Carbon N. Y.*, vol. 51, pp. 36–44, 2012.

[67] S. Stankovich *et al.*, "Synthesis of graphene-based nanosheets via chemical reduction of exfoliated graphite oxide," *Carbon N. Y.*, vol. 45, pp. 1558–1565, 2007.

[68] H. Bai, C. Li, and G. Shi, "Functional composite materials based on chemically converted graphene," *Adv. Mater.*, vol. 23, pp. 1089–1115, 2011.

[69] D. C. Marcano *et al.*, "Improved Synthesis of Graphene Oxide," *ACS Nano*, vol. 4, no. 8, pp. 4806–4814, 2010.

[70] S. Gilje, R. B. Kaner, G. G. Wallace, D. A. N. Li, and M. B. Mu, "Processable aqueous dispersions of graphene nanosheets," *Nat. Nanotechnol.*, vol. 3, pp. 101–105, 2008.

[71] S. Dubin *et al.*, "One-Step , Solvothermal Reduction Method for Producing Reduced Graphene Oxide Dispersions in Organic Solvents," *ACS Nano*, vol. 4, no. 7, pp. 3845–3852, 2010.

[72] M. J. Mcallister *et al.*, "Single Sheet Functionalized Graphene by Oxidation and Thermal Expansion of Graphite," *Chem. Mater.*, vol. 19, no. 4, pp. 4396–4404, 2007.

[73] H. C. Schniepp *et al.*, "Functionalized Single Graphene Sheets Derived from Splitting Graphite Oxide," *J. Phys. Chem. B*, vol. 110, pp. 8535–8539, 2006.

[74] W. Lv, D. Tang, Y. He, C. You, Z. Shi, and X. Chen, "Low-Temperature Exfoliated Graphenes: Vacuum-Promoted Exfoliation and Electrochemical Energy Storage," *Am.*

Chem. Soc., vol. 3, no. 11, pp. 3730–3736, 2009.

[75] A. Kaniyoor, T. T. Baby, and S. Ramaprabhu, "Graphene synthesis via hydrogen induced low temperature exfoliation of graphite oxide," *J. Mater. Chem.*, vol. 20, pp. 8467–8469, 2010.

[76] E. H. L. Falcao *et al.*, "Microwave exfoliation of a graphite intercalation compound," *Carbon N. Y.*, vol. 45, pp. 1364–1369, 2007.

[77] T. Wei, Z. Fan, G. Luo, C. Zheng, and D. Xie, "A rapid and efficient method to prepare exfoliated graphite by microwave irradiation," *Carbon N. Y.*, vol. 47, no. 1, pp. 337–339, 2008.

[78] U. Khan, A. O. Neill, M. Lotya, S. De, and J. N. Coleman, "High-concentration solvent exfoliation of graphene," *Small*, vol. 6, no. 7, pp. 864–871, 2010.

[79] R. Hao, W. Qian, L. Zhang, and Y. Hou, "Aqueous dispersions of TCNQ-anion-stabilized graphene sheets," *Chem. Commun.*, vol. 48, pp. 6576–6578, 2008.

[80] R. J. Smith, M. Lotya, and J. N. Coleman, "The importance of repulsive potential barriers for the dispersion of graphene using surfactants," *New J. Phys.*, vol. 12, pp. 1–11, 2010.

[81] A. Jana, E. Scheer, and S. Polarz, "Synthesis of graphene-transition metal oxide hybrid nanoparticles and their application in various fields," *Beilstein J. Nanotechnol.*, vol. 8, no. 1, pp. 688–714, 2017.

[82] R. Asmatulu, "Nanocoatings for corrosion protection of aerospace alloys," in *Corrosion protection and control using nanomaterials*, Woodhead Publishing Limited, 2012, pp. 357–374.

[83] Q. Liu *et al.*, "Graphene-modified nanostructured vanadium pentoxide hybrids with extraordinary electrochemical performance for Li-ion batteries," *Nat. Commun.*, vol. 6, no. 6127, pp. 1–10, 2015.

[84] R. Hu, J. Zhao, and J. Zheng, "Synthesis of SnO2/rGO hybrid materials by sol-gel/thermal reduction method and its application inelectrochemical capacitors," *Mater. Lett.*, vol. 197, pp. 59–62, 2017.

[85] J. Du *et al.*, "Hierarchically ordered macro-mesoporous TiO_2-graphene composite films: improved mass transfer, reduced charge recombination, and their enhanced photocatalytic activities.," *ACS Nano*, vol. 5, no. 1, pp. 590–596, 2011.

[86] E. Yilmaz and M. Soylak, "Functionalized nanomaterials for sample preparation methods," in *Handbook of Nanomaterials in Analytical Chemistry*, Elsevier Inc., 2020, pp. 373–414.

[87] L. Baraket and A. Ghorbel, “Control preparation of aluminium chromium mixed oxides by sol-gel process,” in *Preparation of Catalysts VII*, vol. 118, Elsevier Masson SAS, 1998, pp. 657–667.

[88] J. Shen, B. Yan, M. Shi, H. Ma, N. Li, and M. Ye, “One step hydrothermal synthesis of TiO2-reduced graphene oxide sheets,” *J. Mater. Chem.*, vol. 21, no. 10, p. 3415, 2011.

[89] J. Song *et al.*, “Synthesis of graphene oxide based cuo nanoparticles composite electrode for highly enhanced nonenzymatic glucose detection,” *ACS Appl. Mater. Interfaces*, vol. 5, no. 24, pp. 12928–12934, 2013.

[90] S. S. Low, H. S. Loh, J. S. Boey, P. S. Khiew, W. S. Chiu, and M. T. T. Tan, “Sensitivity enhancement of graphene/zinc oxide nanocomposite-based electrochemical impedance genosensor for single stranded RNA detection,” *Biosens. Bioelectron.*, vol. 94, pp. 365–373, 2017.

[91] E. R. Ezeigwe, M. T. T. Tan, P. S. Khiew, and C. W. Siong, “Solvothermal synthesis of graphene–MnO2 nanocomposites and their electrochemical behavior,” *Ceram. Int.*, vol. 41, no. 9, pp. 11418–11427, 2015.

[92] K. Zhang *et al.*, “Synthesis of Nitrogen-Doped MnO/Graphene Nanosheets Hybrid Material for Lithium Ion Batteries,” *Appl. Mater. Interfaces*, vol. 4, pp. 658–664, 2012.

[93] Z. He *et al.*, “Nanostructure control of graphene-composited TiO2 by a one-step solvothermal approach for high performance dye-sensitized solar cells,” *Nanoscale*, vol. 3, pp. 4613–4616, 2011.

[94] K. Hareesh, J. F. Williams, N. A. Dhole, K. M. Kodam, V. N. Bhoraskar, and S. D. Dhole, “Bio-green synthesis of Ag–GO, Au–GO and Ag–Au–GO nanocomposites using Azadirachta indica : its application in SERS and cell viability,” *Mater. Res. Express*, vol. 3, no. 7, p. 075010, 2016.

[95] X. Huang, X. Zhou, L. Zhou, K. Qian, Y. Wang, and Z. Liu, “A facile one-step solvothermal synthesis of SnO2/ graphene nanocomposite and its application as an anode material for lithium-ion batteries,” *Chemphyschem*, vol. 12, pp. 278–281, 2011.

[96] V. Munusami, K. Arutselvan, S. Vadivel, and S. Govindasamy, “High sensitivity LPG and H2 gas sensing behavior of MoS2/graphene hybrid sensors prepared by facile hydrothermal method,” *Ceram. Int.*, no. in press, pp. 1–10, 2022.

[97] Q. Yan, E. Leen, H. Loh, and M. T. T. Tan, “Highly sensitive and specific graphene / TiO2 impedimetric immunosensor based on plant-derived tetravalent envelope glycoprotein

domain III (EDIII) probe antigen for dengue diagnosis," *Biosens. Bioelectron.*, vol. 176, p. 112895, 2021.

[98] W. J. Li, E. W. Shi, W. Z. Zhong, and Z. W. Yin, "Growth mechanism and growth habit of oxide crystals," *J. Cryst. Growth*, vol. 203, no. 1, pp. 186–196, 1999.

[99] J. Yan and Z. Fan, "Fast and reversible surface redox reaction of graphene-MnO 2 composites as supercapacitor electrodes," *Carbon N. Y.*, vol. 8, pp. 3825–3833, 2010.

[100] J. Yan *et al.*, "Rapid microwave-assisted synthesis of graphene nanosheet / CO3O4 composite for supercapacitors," *Electrochim. Acta*, vol. 55, no. 23, pp. 6973–6978, 2010.

[101] Z. Yufei, L. Laiquan, S. Haiquan, H. Wei, and D. Xiaoxhen, "Binary metal oxide: advanced energy storage materials in supercapacitors," *J. Mater. Chem. A*, vol. 3, pp. 43–59, 2015.

[102] S. Wu, Z. Yin, Q. He, X. Huang, X. Zhou, and H. Zhang, "Electrochemical deposition of semiconductor oxides on reduced graphene oxide-based flexible, transparent, and conductive electrodes," *J. Phys. Chem. C*, vol. 114, no. 27, pp. 11816–11821, 2010.

[103] S. Fanny Chiat Orou *et al.*, "Antibacterial activity by ZnO nanorods and ZnO nanodisks: A model used to illustrate 'Nanotoxicity Threshold,'" *J. Ind. Eng. Chem.*, vol. 62, pp. 333–340, 2018.

[104] J. S. Y. Chia, M. T. T. Tan, P. S. Khiew, J. K. Chin, and C. W. Siong, "A bio-electrochemical sensing platform for glucose based on irreversible, non-covalent pi-pi functionalization of graphene produced via a novel, green synthesis method," *Sensors Actuators, B Chem.*, vol. 210, pp. 558–565, 2015.

[105] S. Yang, Z. Lu, and S. Luo, "Direct electrodeposition of a biocomposite consisting of reduced graphene oxide , chitosan and glucose oxidase on a glassy carbon electrode for direct sensing of glucose," *Microchim. Acta*, vol. 180, no. 1–2, 2012.

[106] P. Wu *et al.*, "Direct electrochemistry of glucose oxidase assembled on graphene and application to glucose detection," *Electrochim. Acta*, vol. 55, no. 28, pp. 8606–8614, 2010.

[107] C. Fu, W. Yang, X. Chen, and D. G. Evans, "Direct electrochemistry of glucose oxidase on a graphite nanosheet-Nafion composite film modified electrode," *Electrochem. commun.*, vol. 11, no. 5, pp. 997–1000, 2009.

[108] A. T. E. Vilian, S.-M. Chen, M. A. Ali, and F. M. A. Al-Hemaid, "Direct electrochemistry of glucose oxidase immobilized on ZrO2 nanoparticles-decorated reduced graphene oxide sheets for a glucose biosensor," *RSC Adv.*, vol. 4, no. 57, p. 30358, 2014.

[109] C. Shan, H. Yang, D. Han, Q. Zhang, A. Ivaska, and L. Niu, "Graphene/AuNPs/chitosan

nanocomposites film for glucose biosensing," *Biosens. Bioelectron.*, vol. 25, no. 5, pp. 1070–1074, 2010.

[110] C. V Krishnan, M. Garnett, and B. Chu, "Spatiotemporal Oscillations in Biological Molecules : Hydrogen Peroxide and Parkinson's Disease," *Int. J. Electrochem. Sci.*, vol. 3, pp. 1364–1385, 2008.

[111] H. Chang *et al.*, "Layer-by-layer assembly of graphene, Au and poly (toluidine blue O) films sensor for evaluation of oxidative stress of tumor cells elicited by hydrogen peroxide," *Biosens. Bioelectron.*, vol. 41, pp. 789–794, 2013.

[112] J. Bai and X. Jiang, "A facile one-pot synthesis of copper sulfide-decorated reduced graphene oxide composites for enhanced detecting of H2O2 in biological environments," *Anal. Chem.*, vol. 85, pp. 8095–8101, 2013.

[113] S. R. Ali, R. R. Parajuli, Y. Ma, Y. Balogun, and H. He, "Interference of ascorbic acid in the sensitive detection of dopamine by a nonoxidative sensing approach," *J. Phys. Chem. B*, vol. 111, no. 42, pp. 12275–12281, 2007.

[114] J. Chang, K. Chang, C. Hu, W. Cheng, and J. Zen, "Improved voltammetric peak separation and sensitivity of uric acid and ascorbic acid at nanoplatelets of graphitic oxide," *Electrochem. commun.*, vol. 12, no. 4, pp. 596–599, 2010.

[115] Y. Fan, J. Liu, H. Lu, and Q. Zhang, "Electrochemical behavior and voltammetric determination of paracetamol on Nafion/TiO2–graphene modified glassy carbon electrode," *Colloids Surfaces B Biointerfaces*, vol. 85, no. 2, pp. 289–292, 2011.

[116] A. A. Ensafi, M. Taei, H. R. Rahmani, and T. Khayamian, "Sensitive DNA impedance biosensor for detection of cancer, chronic lymphocytic leukemia, based on gold nanoparticles/gold modified electrode," *Electrochim. Acta*, vol. 56, no. 24, pp. 8176–8183, 2011.

[117] S. Z. Mousavisani, J. B. Raoof, A. P. F. Turner, R. Ojani, and W. C. Mak, "Label-free DNA sensor based on diazonium immobilisation for detection of DNA damage in breast cancer 1 gene," *Sensors Actuators, B Chem.*, vol. 264, pp. 59–66, 2018.

[118] A. Azadbakht, M. Roushani, A. R. Abbasi, and Z. Derikvand, "Design and characterization of electrochemical dopamine-aptamer as convenient and integrated sensing platform," *Anal. Biochem.*, vol. 507, pp. 47–57, 2016.

[119] C. X. Lim, H. Y. Hoh, P. K. Ang, and K. P. Loh, "Direct voltammetric detection of DNA and pH sensing on epitaxial graphene : an insight into the role of oxygenated defects," *Anal.*

Chem., vol. 82, no. 17, pp. 7387–7393, 2010.

[120] Q. Wang, M. Zheng, J. Shi, and F. Gao, "Electrochemical Oxidation of Native Double-Stranded DNA on a Graphene-Modified Glassy Carbon Electrode," *Electroanalysis*, vol. 23, no. 4, pp. 915–920, 2011.

[121] H. P. Peng *et al.*, "Label-free electrochemical DNA biosensor for rapid detection of mutidrug resistance gene based on Au nanoparticles/toluidine blue-graphene oxide nanocomposites," *Sensors Actuators, B Chem.*, vol. 207, pp. 269–276, 2015.

[122] A. Singh *et al.*, "Graphene oxide-chitosan nanocomposite based electrochemical DNA biosensor for detection of typhoid," *Sensors Actuators, B Chem.*, vol. 185, pp. 675–684, 2013.

[123] S. S. Low *et al.*, "A Proof of Concept: Detection of Avian Influenza H5 Gene by a Graphene-Enhanced Electrochemical Genosensor," *J. Nanosci. Nanotechnol.*, vol. 16, no. 3, pp. 2438–2446, 2016.

[124] L. Q. Luo, Z. Zhang, Y. P. Ding, D. M. Deng, X. L. Zhu, and Z. X. Wang, "Label-free electrochemical impedance genosensor based on 1-aminopyrene/graphene hybrids," *Nanoscale*, vol. 5, no. 13, pp. 5833–5840, 2013.

[125] S. Singal, A. K. Srivastava, S. Dhakate, and A. M. Biradar, "Electroactive graphene-multi-walled carbon nanotube hybrid supported impedimetric immunosensor for the detection of human cardiac troponin-I," *RSC Adv.*, vol. 5, pp. 74994–75003, 2015.

[126] F. S. Felix and L. Angnes, "Electrochemical immunosensors- a powerful tool for analytical applications," *Biosens. Bioelectron.*, vol. 102, pp. 470–478, 2018.

[127] L. Liu, Y. Zhang, R. Du, J. Li, and X. Yu, "An ultrasensitive electrochemical immunosensor based on the synergistic effect of quaternary Cu2SnZnS4 NCs and cyclodextrin functionalized-graphene," *Analyst*, vol. 142, pp. 780–786, 2017.

[128] R. Wang, J. J. Feng, Y. Xue, L. Wu, and A. J. Wang, "A label-free electrochemical immunosensor based on AgPt nanorings supported on reduced graphene oxide for ultrasensitive analysis of tumor marker," *Sensors Actuators, B Chem.*, vol. 254, pp. 1174–1181, 2018.

[129] Q. Zhang, X. Li, C. Qian, L. Dou, F. Cui, and X. Chen, "Label-free electrochemical immunoassay for neuron specific enolase based on 3D macroporous reduced graphene oxide/polyaniline film," *Anal. Biochem.*, vol. 540–541, pp. 1–8, 2018.

[130] Y. Zeng *et al.*, "A sandwich-type electrochemical immunoassay for ultrasensitive detection

of non-small cell lung cancer biomarker CYFRA21-1," *Bioelectrochemistry*, vol. 120, pp. 183–189, 2017.

[131] American Cancer Society, "Cancer facts & figures 2018," *Atlanta Am. Cancer Soc.*, pp. 1–71, 2018.

[132] K. Pantel and M. R. Speicher, "The biology of circulating tumor cells," *Oncogene*, vol. 35, no. 10, pp. 1216–1224, 2015.

[133] H. Sasaki *et al.*, "Elevated serum epidermal growth factor receptor level is correlated with lymph node metastasis in lung cancer," *Int J Clin Oncol*, vol. 8, pp. 79–82, 2003.

[134] L. Wang, "Screening and Biosensor-Based Approaches for Lung Cancer Detection," *Sensors*, vol. 17, no. 2420, pp. 1–22, 2017.

[135] J. Brabender, R. Metzger, D. Salonga, K. D. Danenberg, P. V Danenberg, and P. M. Schneider, "Comprehensive expression analysis of retinoic acid receptors and retinoid X receptors in non-small cell lung cancer : implications for tumor development and prognosis," *Carcinogenesis*, vol. 26, no. 3, pp. 525–530, 2005.

[136] S. A. Belinsky, "Gene-promoter hypermethylation as a biomarker in lung cancer," *Nat. Rev. Cancer*, vol. 4, pp. 1–11, 2004.

[137] A. K. Greenberg, H. Yee, and W. N. Rom, "Preneoplastic lesions of the lung," *Respir Res*, vol. 3, no. 20, pp. 1–10, 2002.

[138] B. Wang, Y. He, Y. Tian, R. Yang, Y. Zhu, and H. Qiu, "Clinical utility of haptoglobin in combination with CEA , NSE and CYFRA21-1 for diagnosis of lung cancer," *Asian Pacific J. Cancer Prev.*, vol. 15, pp. 9611–9614, 2014.

[139] P. Indovina, E. Marcelli, P. Maranta, and G. Tarro, "Lung cancer proteomics : recent advances in biomarker discovery," *Int. J. Proteomics*, vol. 2011, pp. 1–7, 2011.

[140] M. R. Younesi, S. L. Aligoudarzi, M. Lashgari, M. J. Tari, R. Bigdeli, and V. Asgary, "A prospective study of serum carcinoembryonic antigen in patients with newly diagnosed colorectal cancer and healthy individuals," *Ann. Clin. Lab. Res.*, vol. 4, no. 2, pp. 1–5, 2016.

[141] F. Xue, L. Zhu, L. Wang, and Q. Wang, "Serum neuron specific enolase levels correlate with patient prognosis for advanced lung cancer," *Int J Clin Exp Med*, vol. 8, no. 6, pp. 9498–9504, 2015.

[142] T. Kosaka, Y. Yatabe, H. Endoh, H. Kuwano, T. Takahashi, and T. Mitsudomi, "Mutations of the epidermal growth factor receptor gene in lung cancer : biological and clinical implications," *Cancer Res.*, vol. 64, pp. 8919–8923, 2004.

[143] N. Kumari, S. Singh, D. Haloi, and S. Kumar, "Epidermal Growth Factor Receptor Mutation Frequency in Squamous Cell Carcinoma and Its Diagnostic Performance in Cytological Samples : A Molecular and Immunohistochemical Study," *world J. Oncol.*, vol. 10, no. 3, pp. 142–150, 2019.

[144] P. A. Jänne and B. E. Johnson, "Effect of epidermal growth factor receptor tyrosine kinase domain mutations on the outcome of patients with non-small cell lung cancer treated with epidermal growth factor receptor tyrosine kinase inhibitors," *Clin. Cancer Res.*, vol. 12, no. 14, p. 4416s–4420s, 2006.

[145] D. M. Jackman *et al.*, "Exon 19 deletion mutations of epidermal growth factor receptor are associated with prolonged survival in non-small cell lung cancer patients treated with gefitinib or erlotinib," *Clin. Cancer Res.*, vol. 12, no. 13, pp. 3908–3914, 2006.

[146] X. H. Weng *et al.*, "Genotyping of common EGFR mutations in lung cancer patients by electrochemical biosensor," *J. Pharm. Biomed. Anal.*, vol. 150, pp. 176–182, 2018.

[147] T. Kozuki *et al.*, "Mutation of the epidermal growth factor receptor gene in the development of adenocarcinoma of the lung," *Lung Cancer*, vol. 58, no. 1, pp. 30–35, 2007.

[148] H. Yasuda, S. Kobayashi, D. B. Costa, and B. Israel, "EGFR exon 20 insertion mutations in non-small-cell lung cancer : preclinical data and clinical implications," *Lancet Oncol.*, vol. 13, no. 1, pp. e23–e31, 2012.

[149] Y. W. Choi *et al.*, "EGFR exon 19 deletion is associated with favorable overall survival after first-line gefitinib therapy in advanced non-small cell lung cancer patients," *Am. J. Clin. Oncol.*, vol. 41, no. 4, pp. 385–390, 2016.

[150] Q. Liu, S. Yin Lim, R. A. Soo, M. Kyoung Park, and Y. Shin, "A rapid MZI-IDA sensor system for EGFR mutation testing in non-small cell lung cancer (NSCLC)," *Biosens. Bioelectron.*, vol. 74, pp. 865–871, 2015.

[151] P. Wang, P. Joshi, A. Alazemi, and P. Zhang, "Upconversion nanoparticle-based ligase-assisted method for specific and sensitive detection of T790M mutation in epidermal growth factor receptor," *Biosens. Bioelectron.*, vol. 62, pp. 120–126, 2014.

[152] E. Burcu, M. Ayd, and M. Kemal, "Electrochemical immunosensor based on chitosan/conductive carbon black composite modified disposable ITO electrode : An analytical platform for p53 detection," *Biosens. Bioelectron.*, vol. 121, pp. 80–89, 2018.

[153] A. Mogi and H. Kuwano, "TP53 Mutations in Nonsmall Cell Lung Cancer," *J. Biomed. Biotechnol.*, vol. 2011, pp. 1–9, 2010.

[154] S. A. Ahrendt *et al.*, "p53 Mutations and Survival in Stage I Non-Small-Cell Lung Cancer : Results of a Prospective Study," *J. Natl. Cancer Inst.*, vol. 95, no. 13, pp. 961–970, 2003.

[155] M. Olivier, M. Hollstein, and P. Hainaut, "TP53 mutations in human cancers: origins, consequences, and clinical use," *Cold Spring Harb Perspect Biol*, vol. 2, no. 1, pp. 1–17, 2010.

[156] Y. Matsumura, Y. Owada-ozaki, and H. Suzuki, "Significance of testing for TP53 gene mutations in lung adenocarcinoma using targeted gene sequencing," *J. Thorac. Dis.*, vol. 10, no. 33, pp. 4147–4150, 2018.

[157] A. M. Attallah and M. M. Abdel-aziz, "Detection of serum p53 protein in patients with different gastrointestinal cancers," *Cancer Detect. Prev.*, vol. 27, pp. 127–131, 2003.

[158] D. Segerba *et al.*, "PRIMA-1 reactivates mutant p53 by covalent binding to the core domain," *Cancer Cell*, vol. 15, pp. 376–388, 2009.

[159] V. J. N. Bykov *et al.*, "Reactivation of mutant p53 and induction of apoptosis in human tumor cells by maleimide Analogs," *J. Biol. Chem.*, vol. 280, no. 34, pp. 30384–30391, 2005.

[160] R. Elshafey, M. Siaj, and A. C. Tavares, "Au nanoparticle decorated graphene nanosheets for electrochemical immunosensing of p53 antibodies for cancer prognosis," *Analyst*, vol. 141, pp. 2733–2740, 2016.

[161] Z. Liu, G. Zhang, and Z. Chen, "Prussian blue-doped nanogold microspheres for enzyme-free electrocatalytic immunoassay of p53 protein," *Microchim. Acta*, vol. 181, pp. 581–588, 2014.

[162] H. Afsharan, B. Khalilzadeh, H. Tajalli, and M. Mollabashi, "A sandwich type immunosensor for ultrasensitive electrochemical quantification of p53 protein based on gold nanoparticles/graphene oxide," *Electrochim. Acta*, vol. 188, pp. 153–164, 2016.

[163] N. Ras and S. Pathways, "Significance of Ras Signaling in Cancer and Strategies for its Control," *Oncol. Hematol. Rev.*, vol. 11, no. 2, pp. 147–152, 2015.

[164] N. Mitin and K. L. Rossman, "Signaling Interplay in Ras Superfamily Function," *Curr. Biol.*, vol. 15, pp. 563–574, 2005.

[165] N. Vasan, J. L. Boyer, and R. S. Herbst, "A RAS renaissance : emerging targeted therapies for KRAS-mutated non–small cell lung cancer," *Oncol. Hematol. Rev.*, vol. 20, no. 15, pp. 3921–3930, 2014.

[166] J. Downward, "Targeting RAS signalling pathways in cancer therapy," *Nat. Rev. Cancer*,

vol. 3, pp. 11–22, 2003.

[167] S. Lin, C. Hsu, J. Tsai, J. Wang, T. Hsieh, and C. Wu, "Decreased GTPase activity of K-ras mutants deriving from human functional adrenocortical tumours," *Br. J. Cancer*, vol. 82, pp. 1035–1040, 2000.

[168] R. et al J.C., "K-Ras oncogene activation as a prognostic marker in adenocarcinoma of the lung," *N. Engl. J. Med.*, vol. 323, no. 9, pp. 561–564, 1990.

[169] Y. Su, Y. Liang, H. Wu, J. Jiang, W. Lai, and C. Zhang, "A three-dimensional cloth-based micro fluidic label-free proximity hybridization-electrochemiluminescence biosensor for ultrasensitive detection of K-ras gene," *Sensors Actuators B. Chem.*, vol. 296, p. 126654, 2019.

[170] R. D. Agata *et al.*, "Direct plasmonic detection of circulating RAS mutated DNA in colorectal cancer patients," *Biosens. Bioelectron.*, vol. 170, p. 112648, 2020.

[171] L. Lin *et al.*, "A chronocoulometric LNA sensor for amplified detection of K-ras mutation based on site-specific DNA cleavage of restriction endonuclease," *Biosens. Bioelectron.*, vol. 42, pp. 409–414, 2013.

[172] X. Zhou, X. Liu, X. Xia, X. Yang, and H. Xiang, "Sensitive, enzyme-free and label-free electrochemical sensor for K-ras G12D point mutation detection based on double cascade amplification reaction," *J. Electroanal. Chem.*, vol. 870, p. 114270, 2020.

[173] X. Lin, Z. Xiao, T. Chen, S. H. Liang, and H. Guo, "Glucose metabolism on Tumor Plasticity, Diagnosis and Treatment," *Front. Oncol.*, vol. 10, pp. 1–10, 2020.

[174] H. Mirzaei and M. R. Hamblin, "Regulation of glycolysis by non-coding RNAs in cancer : Switching on the Warburg Effect," *Mol. Ther. Oncolytics*, vol. 19, pp. 218–239, 2020.

[175] D. Ferrigno, G. Buccheri, and C. Giordano, "Neuron-specific enolase is an effective tumour marker in non-small cell lung cancer (NSCLC)," *Lung Cancer*, vol. 41, pp. 311–320, 2003.

[176] N. Cells and J. M. Paul, "Neuron specific enolase, a clinically useful marker for neurons and neuroendocrine cells," *Ann Rev Neurosci*, vol. 10, pp. 269–95, 1987.

[177] L. G. M. Jorgensen *et al.*, "Serum neuron-specific enolase (S-NSE) and the prognosis in small-cell lung cancer (SCLC): a combined multivariable analysis on data from nine centres," *Br. J. Cancer*, vol. 74, pp. 463–467, 1996.

[178] S. Jang, J. Kim, C. Kim, D. Kim, S. Rhee, and K. Choi, "P19 ras represses proliferation of non-small cell lung cancer possibly through interaction with neuron-specific enolase (NSE)," *Cancer Lett.*, vol. 289, no. 1, pp. 91–98, 2010.

[179] S. Wu, L. Liu, G. Li, F. Jing, H. Mao, and Q. Jin, "Multiplexed detection of lung cancer biomarkers based on quantum dots and microbeads," *Talanta*, vol. 156–157, pp. 48–54, 2016.

[180] Z. Wei, J. Zhang, A. Zhang, Y. Wang, and X. Cai, "Electrochemical detecting lung cancer-associated antigen based on graphene-gold nanocomposite," *Molecules*, vol. 22, no. 392, pp. 1–9, 2017.

[181] H. Li, Q. Xiao, J. Lv, Q. Lei, and Y. Huang, "Dopamine modified hyperbranched TiO2 arrays based ultrasensitive photoelectrochemical immunosensor for detecting neuron specific enolase," *Anal. Biochem.*, vol. 531, pp. 48–55, 2017.

[182] H. Herrmann, H. Bär, L. Kreplak, S. V Strelkov, and U. Aebi, "Intermediate filaments : from cell architecture to nanomechanics," *Nat Rev Mol Cell Biol*, vol. 8, pp. 562–573, 2007.

[183] P. A. Coulombe and M. B. Omary, "'Hard' and 'soft ' principles defining the structure, function and regulation of keratin intermediate filaments," *Curr. Opin. Cell Biol.*, vol. 14, pp. 110–122, 2002.

[184] V. Barak, H. Goike, K. W. Panaretakis, and R. Einarsson, "Clinical utility of cytokeratins as tumor markers," *Clin. Biochem.*, vol. 37, pp. 529–540, 2004.

[185] G. Buccheri and D. Ferrigno, "Lung tumor markers of cytokeratin origin: an overview," *Lung Cancer*, vol. 34, pp. 65–69, 2001.

[186] T. Hanagiri *et al.*, "Preoperative CYFRA 21-1 and CEA as prognostic factors in patients with stage I non-small cell lung cancer," *Lung Cancer*, vol. 74, no. 1, pp. 112–117, 2011.

[187] M. Muraki, Y. Tohda, T. Iwanaga, H. Uejima, Y. Nagasaka, and S. Nakajima, "Assessment of serum CYFRA 21-1 in lung cancer," *Am. Cancer Soc.*, vol. 77, pp. 1274–1277, 1996.

[188] J. Pujol, J. Grenier, J. Daurã, A. Daver, H. Pujol, and F. Michel, "Serum fragment of cytokeratin subunit 19 measured by CYFRA 21-1 immunoradiometric assay as a marker of lung cancer," *Cancer Res.*, vol. 53, pp. 61–66, 1993.

[189] J. Pujol, J. Boher, J. Grenier, and X. Quantin, "Cyfra 21-1, neuron specific enolase and prognosis of non-small cell lung cancer: prospective study in 621 patients," *Lung Cancer*, vol. 31, pp. 221–231, 2001.

[190] S. Linder, "Cytokeratin Markers Come of Age," *Tumor Biol.*, vol. 28, no. 4, pp. 189–195, 2007.

[191] K. Okamura, K. Takayama, M. Izumi, T. Harada, K. Furuyama, and Y. Nakanishi, "Diagnostic value of CEA and CYFRA 21-1 tumor markers in primary lung cancer," *Lung*

Cancer, vol. 80, no. 1, pp. 45–49, 2013.

[192] M. J. Edelman, L. Hodgson, P. Y. Rosenblatt, and R. H. Christenson, "CYFRA 21-1 as a prognostic and predictive marker in a non–small-cell lung cancer in a prospective trial: CALGB 150304," *J. Thorac. Oncol.*, vol. 7, no. 4, pp. 649–654, 2012.

[193] W. Lan, Y. Lin, Z. Men, and L. Yan, "Surface-decorated S. cerevisiae for flow cytometric array immunoassay," *Anal Bioanal Chem*, vol. 409, pp. 5259–5267, 2017.

[194] M. H. Chapman *et al.*, "Circulating CYFRA 21-1 is a specific diagnostic and prognostic biomarker in biliary tract cancer," *J. Clin. Exp. Hepatol.*, vol. 1, no. 1, pp. 6–12, 2011.

[195] Y. Zeng *et al.*, "A sensitive label-free electrochemical immunosensor for detection of cytokeratin 19 fragment antigen 21-1 based on 3D graphene with gold nanoparticle modified electrode," *Talanta*, vol. 178, pp. 122–128, 2018.

[196] N. Lu *et al.*, "Ultrasensitive detection of dual cancer biomarkers with integrated CMOS-compatible nanowire arrays," *Anal. Chem.*, vol. 87, no. 22, pp. 11203–11208, 2015.

[197] X. Li *et al.*, "Ultrasensitive label-free detection for lung cancer CYFRA 21-1 DNA based on ring-opening polymerization," *Talanta*, vol. 223, p. 121730, 2020.

[198] N. Sabrina, A. Delmira, T. Gabriel, M. Alvaro, and M. Adalberto, "Cytokeratins 14 and 19 in odontogenic cysts and tumors: a review," *Odontoestomatologia*, vol. 16, no. 24, 2014.

[199] H. Gold and S. O. Freedman, "Demonstration of tumor-specific antigens in human colonic carcinomata by immunological tolerance and absorption techniques," *J Exp Med*, vol. 121, no. 3, pp. 439–462, 1964.

[200] J. H. T. Luong and S. K. Vashist, "Immunosensing procedures for carcinoembryonic antigen using graphene and nanocomposites," *Biosens. Bioelectron.*, vol. 89, pp. 293–304, 2017.

[201] D. Ahnen, P. Nakane, and W. Brown, "Ultrastructural localization of carcinoembryonic antigen," *Cancer*, vol. 49, pp. 2077–2090, 1982.

[202] M. R. Dallas *et al.*, "Divergent roles of CD44 and carcinoembryonic antigen in colon cancer metastasis," *FASEB J*, vol. 26, no. 6, pp. 2648–2656, 2012.

[203] H. U. Dai *et al.*, "Increased lung cancer risk in patients with interstitial lung disease and elevated CEA and CA125 serum tumour markers," *Respirology*, vol. 19, pp. 707–713, 2014.

[204] G. M. Oremek, H. Sauer-Eppel, and T. H. Bruzdziak, "Value of tumour and inflammatory markers in lung cancer," *Anticancer Res*, vol. 27, no. 4A, pp. 1911–1915, 2007.

[205] J. J. Kim, K. Hyun, J. K. Park, and S. W. Moon, "The significance of serum carcinoembryonic antigen in lung adenocarcinoma," *Korean J Thorac Cardiovasc*, vol. 48, pp. 335–344, 2015.

[206] Y. Sakao, S. Tomimitsu, Y. Takeda, M. Natsuaki, and T. Itoh, "Carcinoembryonic antigen as a predictive factor for postoperative tumor relapse in early-stage lung adenocarcinoma," *Cardio-Thoracic Surg.*, vol. 25, pp. 520–522, 2004.

[207] C. Doddoli, J. Mancini, and L. Greillier, "Prognostic value of combination of Cyfra 21-1, CEA and NSE in patients with advanced non-small cell lung cancer," *Respir. Med.*, vol. 98, pp. 357–362, 2004.

[208] S. Analysis *et al.*, "Increased CYFRA 21-1, CEA and NSE are prognostic of poor outcome for locally advanced squamous cell carcinoma in lung: A nomogram and recursive partitioning risk," *Transl. Oncol.*, vol. 11, no. 4, pp. 999–1006, 2018.

[209] Z. Feng, W. Mengmeng, Y. Lin, C. Zhenping, W. Zhaoqiang, and C. Hong, "Sensitive sandwich ELISA based on a gold nanoparticle layer for cancer detection," *Analyst*, vol. 137, pp. 1779–1784, 2012.

[210] R. M. Lequin, "Enzyme Immunoassay (EIA)/ Enzyme-Linked Immunosorbent Assay (ELISA)," *Clin. Chem.*, vol. 51, no. 12, pp. 2415–2418, 2005.

[211] X. U. Dong, L. I. Xu-fen, Z. Shu, and J. Wen-zhi, "Quantitative real-time RT-PCR detection for CEA, CK20 and CK19 mRNA in peripheral blood of colorectal cancer patients," *J. ZheJiang Univ. Sci. B*, vol. 7, no. 6, pp. 445–451, 2006.

[212] K. Terato, C. Do, J. Chang, and T. Waritani, "Preventing further misuse of the ELISA technique and misinterpretation of serological antibody assay data," *Vaccine*, vol. 34, no. 39, pp. 4643–4644, 2016.

[213] J. Pan and Q. Yang, "Antibody-functionalized magnetic nanoparticles for the detection of carcinoembryonic antigen using a flow-injection electrochemical device," *Anal. Bioanal. Chem.*, vol. 388, pp. 279–286, 2007.

[214] X. Gu, Z. She, and T. Ma, "Electrochemical detection of carcinoembryonic antigen," *Biosens. Bioelectron.*, vol. 102, pp. 610–616, 2018.

[215] F. Ricci, G. Adornetto, and G. Palleschi, "A review of experimental aspects of electrochemical immunosensors," *Electrochim. Acta*, vol. 84, pp. 74–83, 2012.

[216] H. Li, L. Shi, D. Sun, P. Li, and Z. Liu, "Fluorescence Resonance Energy Transfer Biosensor Between Upconverting Nanoparticles and Palladium Nanoparticles for

Ultrasensitive CEA Detection," *Biosens. Bioelectron.*, vol. 86, pp. 791–798, 2016.

[217] R. Han, Y. Sun, Y. Dai, D. Gao, X. Wang, and C. Luo, "A chemiluminescence aptasensor for sensitive detection of carcinoembryonic antigen based on dual aptamer-conjugates biorecognition," *Sensors Actuators B. Chem.*, vol. 326, p. 128833, 2021.

[218] Z. Altintas, Y. Uludag, Y. Gurbuz, and I. E. Tothill, "Surface plasmon resonance based immunosensor for the detection of the cancer biomarker carcinoembryonic antigen," *Talanta*, vol. 86, pp. 377–383, 2011.

[219] F. Arduini *et al.*, "Electrochemical biosensors based on nanomodified screen-printed electrodes : Recent applications in clinical analysis," *Trends Anal. Chem.*, vol. 79, pp. 114–126, 2016.

[220] L. Zhang, W. Yang, Y. Yang, H. Liu, and Z. Gu, "Smartphone-based point-of-care testing of salivary α-amylase for personal psychological measurement," *Analyst*, vol. 140, pp. 7399–7406, 2015.

[221] Z. Hong, G. Chen, S. Yu, R. Huang, and C. Fan, "A potentiometric aptasensor for carcinoembryonic antigen (CEA) on graphene oxide nanosheets using catalytic recycling of DNase I with signal amplification," *Anal. Methods*, vol. 10, pp. 5364–5371, 2018.

[222] F. Pei *et al.*, "A sandwich-type amperometric immunosensor fabricated by Au@Pd NDs/ Fe2+-CS/PPy NTs and Au NPs/NH2-GS to detect CEA sensitively via two detection methods," *Biosens. Bioelectron.*, vol. 122, pp. 231–238, 2018.

[223] C. Yeh, K. Su, and Y. Lin, "Development of an impedimetric immunobiosensor for measurement of carcinoembryonic antigen," *Sensors Actuators A. Phys.*, vol. 241, pp. 203–211, 2016.

[224] P. Skládal, "Piezoelectric biosensors," *Trends Anal. Chem.*, vol. 79, pp. 127–133, 2016.

[225] S. G. Patching, "Surface plasmon resonance spectroscopy for characterisation of membrane protein–ligand interactions and its potential for drug discovery," *Biochim. Biophys. Acta J.*, vol. 1838, no. 1, pp. 43–55, 2014.

[226] Š. Barbora, W. Piotr, M. Bocková, and J. Homola, "Optical biosensors based on plasmonic nanostructures : A review," *Proc. IEEE*, vol. 104, no. 12, pp. 2380–2408, 2016.

[227] N. Chiu, T. Lin, and C. Kuo, "Highly sensitive carboxyl-graphene oxide-based surface plasmon resonance immunosensor for the detection of lung cancer for cytokeratin 19 biomarker in human plasma," *Sensors Actuators B. Chem.*, vol. 265, pp. 264–272, 2018.

[228] Y. Yu, Z. Huang, Y. Zhou, A. Liu, W. Chen, and J. Lin, "Facile and highly sensitive

photoelectrochemical biosensing platform based on hierarchical architectured polydopamine/tungsten oxide nanocomposite film," *Biosens. Bioelectron.*, vol. 126, pp. 1–6, 2019.

[229] X. Wang, Y. Wang, M. Jiang, Y. Shan, X. Jin, and M. Gong, "Functional electrospun nanofibers-based electrochemiluminescence immunosensor for detection of the TSP53 using RuAg/SiO2 NPs as signal enhancers," *Anal. Biochem.*, vol. 548, pp. 15–22, 2018.

[230] D. Wang *et al.*, "Highly selective detection of single-nucleotide polymorphisms using a quartz crystal microbalance biosensor based on the toehold-mediated strand displacement reaction," *Anal. Chem.*, vol. 84, pp. 7008–7014, 2012.

[231] Z. Altintas and I. E. Tothill, "Chemical DNA-based biosensor platforms for the detection of TP53 mutation," *Sensors Actuators B. Chem.*, vol. 169, pp. 188–194, 2012.

[232] Y. Chen, X. Huang, H. Shi, and B. Mu, "A novel and cost-effective method for early lung cancer detection in immunized serum," *Asian Pacific J. Cancer Prev.*, vol. 12, no. 11, pp. 3009–3012, 2011.

[233] K. Zhang *et al.*, "A microfluidic system with surface modified piezoelectric sensor for trapping and detection of cancer cells," *Biosens. Bioelectron.*, vol. 26, no. 2, pp. 935–939, 2010.

[234] J. Chen, S. Sadhasivam, and F. Lin, "Label free gravimetric detection of epidermal growth factor receptor by antibody immobilization on quartz crystal microbalance," *Process Biochem.*, vol. 46, no. 2, pp. 543–550, 2011.

[235] G. Shen, H. Wang, T. Deng, G. Shen, and R. Yu, "A novel piezoelectric immunosensor for detection of carcinoembryonic antigen," *Talanta*, vol. 67, pp. 217–220, 2005.

[236] A. Khanmohammadi *et al.*, "Electrochemical biosensors for the detection of lung cancer biomarkers : A review," *Talanta*, vol. 206, p. 120251, 2020.

[237] Y. Shoja and A. Kermanpur, "Diagnosis of EGFR exon21 L858R point mutation as lung cancer biomarker by electrochemical nanoparticles modified pencil graphite electrode," *Biosens. Bioelectron.*, vol. 113, pp. 108–115, 2018.

[238] N. Taheri, H. Khoshsafar, M. Ghanei, A. Ghazvini, and H. Bagheri, "Dual-template rectangular nanotube molecularly imprinted polypyrrole for label-free impedimetric sensing of AFP and CEA as lung cancer biomarkers," *Talanta*, vol. 239, p. 123146, 2022.

[239] C. M. Silveira, T. Monteiro, and M. G. Almeida, "Biosensing with paper-based miniaturized printed electrodes – A modern trend," *Biosensors*, vol. 6, no. 51, pp. 1–17, 2016.

[240] J. Lu, L. Hao, F. Yang, Y. Liu, H. Yang, and S. Yan, "Ultrasensitive electrochemical detection of CYFRA 21-1 via in-situ initiated ROP signal amplification strategy," *Anal. Chim. Acta*, vol. 1180, p. 338889, 2021.

[241] W. Li, X. Qiao, C. Hong, and Y. Song, "A sandwich-type electrochemical immunosensor for detecting CEA based on CeO2-MoS2 absorbed Pb2+," *Anal. Biochem.*, vol. 592, pp. 1–8, 2020.

[242] Y. Fang, Y. Li, M. Zhang, B. Cui, Q. Hu, and L. Wang, "A novel electrochemical strategy based on porous 3D graphene-starch architecture and silver deposition for ultrasensitive detection of neuron-specific enolase," *Analyst*, vol. 144, pp. 2186–2194, 2019.

[243] H. Yang, Y. Xu, Q. Hou, Q. Xu, and C. Ding, "Magnetic antifouling material based ratiometric electrochemical biosensor for the accurate detection of CEA in clinical serum," *Biosens. Bioelectron.*, vol. 208, p. 114216, 2022.

[244] J. Wang, "Electrochemical biosensors: Towards point-of-care cancer diagnostics," *Biosens. Bioelectron.*, vol. 21, no. 10, pp. 1887–1892, 2006.

[245] Y. Xiang, T. Lan, and Y. Lu, "Using the widely available blood glucose meter to monitor insulin and HbA1c," *J. Diabetes Sci. Technol.*, vol. 8, no. 4, pp. 855–858, 2014.

[246] Y. Fan, J. Liu, Y. Wang, J. Luo, H. Xu, and S. Xu, "A wireless point-of-care testing system for the detection of neuron-specific enolase with microfluidic paper-based analytical devices," *Biosens. Bioelectron.*, vol. 95, pp. 60–66, 2017.

[247] S. Shin *et al.*, "Chemical Smartphone-based portable electrochemical biosensing system for detection of circulating microRNA-21 in saliva as a proof-of-concept," *Sensors Actuators B. Chem.*, vol. 308, p. 127718, 2020.

[248] J. S. Y. Chia *et al.*, "A novel one step synthesis of graphene via sonochemical-assisted solvent exfoliation approach for electrochemical sensing application," *Chem. Eng. J.*, vol. 249, pp. 270–278, 2014.

[249] B. Jin, P. Wang, H. Mao, B. Hu, H. Zhang, and Z. Cheng, "Multi-nanomaterial electrochemical biosensor based on label-free graphene for detecting cancer biomarkers," *Biosens. Bioelectron.*, vol. 55, pp. 464–469, 2014.

[250] M. Choudhary *et al.*, "Graphene oxide based label free ultrasensitive immunosensor for lung cancer biomarker,hTERT," *Biosens. Bioelectron.*, vol. 4, no. 4, p. 1000143, 2013.

[251] B. G. Sozzi *et al.*, "Quantification of free circulating DNA as a diagnostic marker in lung cancer," *J. Clin. Oncol.*, vol. 21, no. 21, pp. 3902–3908, 2003.

[252] B. Nohwal and C. S. Pundir, “An electrochemical CD59 targeted noninvasive immunosensor based on graphene oxide nanoparticles embodied pencil graphite for detection of lung cancer,” *Microchem. J.*, vol. 156, p. 104957, 2020.

[253] G. Li and F. Tian, “Guanine-decorated graphene nanostructures for sensitive monitoring of neuron-specific enolase based on an enzyme-free electrocatalytic reaction,” *Anal. Sci.*, vol. 29, no. November, pp. 1195–1201, 2013.

[254] V. K. Singh *et al.*, “Fabrication of sensitive bioelectrode based on atomically thin CVD grown graphene for cancer biomarker detection,” *Biosens. Bioelectron.*, vol. 105, pp. 173–181, 2018.

[255] H. Gronbeck, A. Curioni, and W. Andreoni, “Thiols and Disulfides on the Au (111) Surface : The Headgroup - Gold Interaction,” *J. Am. Chem. Soc.*, vol. 122, pp. 3839–3842, 2000.

[256] Z. Zhong, S. Patskovskyy, P. Bouvrette, J. H. T. Luong, and A. Gedanken, “The surface chemistry of Au colloids and their interactions with functional amino acids,” *Jounrnal Phys. Chem. B*, vol. 108, no. 13, pp. 4046–4052, 2004.

[257] M. Chen *et al.*, “Three-dimensional electrochemical DNA biosensor based on 3D graphene-Ag nanoparticles for sensitive detection of CYFRA21-1 in non-small cell lung cancer,” *Sensors Actuators B Chem.*, vol. 255, pp. 2910–2918, 2018.

[258] B. Su, D. Tang, J. Tang, Y. Cui, and G. Chen, “Multiarmed star-like platinum nanowires with multienzyme assembly for direct electronic determination of carcinoembryoninc antigen in serum,” *Biosens. Bioelectron.*, vol. 30, no. 1, pp. 229–234, 2011.

[259] R. Elshafey, A. C. Tavares, M. Siaj, and M. Zourob, “Electrochemical impedance immunosensor based on gold nanoparticles-protein G for the detection of cancer marker epidermal growth factor receptor in human plasma and brain tissue,” *Biosens. Bioelectron.*, vol. 50, pp. 143–149, 2013.

[260] M. B. Pomfret, C. Stoltz, B. Varughese, and R. A. Walker, “Structural and compositional characterization of yttria-stabilized zirconia: evidence of surface-stabilized, low-valence metal species,” *Anal. Chem.*, vol. 77, no. 6, pp. 4884–4888, 2005.

[261] Z. Cao, S. An, and X. Song, “Effect of thermal treatment at high temperature on phase stability and transformation of Yb2O3 and Y2O3 co-doped ZrO2 ceramics,” *Sci. Rep.*, no. 12, p. 9955, 2022.

[262] T. Yamaguchi, “Application of Zr02 as a catalyst and a catalyst support,” *Catal. today*, vol.

20, no. 94, pp. 199–218, 1994.

[263] T. Jin, T. Okuhara, and J. M. White, "Ultra-high vacuum preparation and characterization of ultra-thin layers of Si02 on Zr02 and Ti02 some by Chemical Vapour Deposition of Si(OEt)," *J. Chem. Soc. Chem. Commun.*, no. 16, pp. 1248–1249, 1987.

[264] L. P. Lin, S. Y. Tham, H. S. Loh, and M. T. T. Tan, "Biocompatible graphene-zirconia nanocomposite as a cyto-safe immunosensor for the rapid detection of carcinoembryonic antigen," *Sci. Rep.*, no. 0123456789, pp. 1–17, 2021.

[265] A. Ali *et al.*, "Graphene oxide-metal nanocomposites for cancer biomarker detection," *RSC Adv.*, vol. 7, pp. 35982–35991, 2017.

[266] H. Zhou *et al.*, "Highly specific enrichment of phosphopeptides by zirconium dioxide nanoparticles for phosphoproteome analysis," *Electrophoresis*, vol. 28, pp. 2201–2215, 2007.

[267] H. Wang, J. Wang, D. Choi, Z. Tang, H. Wu, and Y. Lin, "EQCM immunoassay for phosphorylated acetylcholinesterase as a biomarker for organophosphate exposures based on selective zirconia adsorption and enzyme-catalytic precipitation," *Biosens. Bioelectron. J.*, vol. 24, pp. 2377–2383, 2009.

[268] D. Du, J. Liu, X. Zhang, and Y. Lin, "One-step electrochemical deposition of a graphene-ZrO2 nanocomposite: Preparation, characterization and application for detection of organophosphorus agents," *Chem, J Mater*, vol. 21, pp. 8032–8037, 2011.

[269] G. Liu *et al.*, "Nanoparticle-Based Electrochemical Immunosensor for the Detection of Phosphorylated Acetylcholinesterase : An Exposure Biomarker of Organophosphate Pesticides and Nerve Agents," *Chem. Eur. J*, vol. 14, pp. 9951–9959, 2008.

[270] N. Zhu, A. Zhang, Q. Wang, P. He, and Y. Fang, "Electrochemical detection of DNA hybridization using methylene blue and electro-deposited zirconia thin films on gold electrodes," *Anal. Chim. Acta*, vol. 510, pp. 163–168, 2004.

[271] S. Liu, J. Xu, and H. Chen, "ZrO2 gel-derived DNA-modified electrode and the effect of lanthanide on its electron transfer behavior," *Bioelectrochemistry*, vol. 57, pp. 149–154, 2002.

[272] E. Murugan and A. Poongan, "A new sensitive electrochemical sensor based on BiVO4/ZrO2@ graphene modified GCE for concurrent sensing of acetaminophen, phenylephrine hydrochloride and cytosine in medications and human serum samples," *Diam. Relat. Mater.*, vol. 126, p. 109117, 2022.

[273] P. P. Ricci and O. J. Gregory, “Sensors for the detection of ammonia as a potential biomarker for health screening,” *Sci. Rep.*, vol. 11, p. 7185, 2021.

[274] K. Zhang, L. Zhang, N. Zhang, H. Wang, H. Shi, and Q. Liu, “Label-free impedimetric sensing platform for microRNA-21 based on ZrO2-reduced graphene oxide nanohybrids coupled with catalytic hairpin assembly amplification,” *RSC Adv.*, vol. 8, pp. 16146–16151, 2018.

[275] M. Zavridou, “miRNA-21 as a novel therapeutic target in lung cancer,” *Lung Cancer Targets Ther.*, vol. 7, pp. 19–27, 2016.

[276] X. Li *et al.*, “Highly conducting graphene sheets and Langmuir -Blodgett films,” *Nat. Nanotechnol.*, vol. 3, pp. 538–542, 2008.

[277] S. Alarifi, D. Ali, A. Verma, S. Alakhtani, and B. A. Ali, “Cytotoxicity and genotoxicity of copper oxide nanoparticles in human skin keratinocytes cells,” *Int. J. Toxicol.*, vol. 32, no. 4, pp. 296–307, 2013.

[278] Y. Jia, B. Ma, X. Wei, and Z. Qian, “The in vitro and in vivo toxicity of gold nanoparticles,” *Chinese Chem. Lett.*, vol. 28, no. 4, pp. 691–702, 2017.

[279] S. Sruthi, J. Ashtami, and P. V Mohanan, “Biomedical application and hidden toxicity of Zinc oxide nanoparticles,” *Mater. Today Chem.*, vol. 10, pp. 175–186, 2018.

[280] M. Pelin *et al.*, “Differential cytotoxic effects of graphene and graphene oxide on skin keratinocytes,” *Sci. Rep.*, vol. 7, p. 40572, 2017.

[281] J. Lu, J. B. Zang, S. X. Shan, H. Huang, and Y. H. Wang, “Synthesis and characterization of core-shell structural MWNT-zirconia nanocomposites,” *Nano Lett.*, vol. 8, no. 11, pp. 4070–4074, 2008.

[282] E. R. Ezeigwe, M. T. T. Tan, P. S. Khiew, and C. W. Siong, “One-step green synthesis of graphene/ZnO nanocomposites for electrochemical capacitors,” *Ceram. Int.*, vol. 41, no. 1, pp. 715–724, 2014.

[283] A. C. Ferrari *et al.*, “Raman spectrum of graphene and graphene layers,” *Phys. Rev. Lett.*, vol. 97, no. 187401, pp. 1–4, 2006.

[284] K. Nam, J. Cho, and H. Yeo, “Thermomechanical behavior of polymer composites based on edge-selectively functionalized,” *Polymers (Basel).*, vol. 10, no. 29, pp. 1–11, 2018.

[285] F. Mori, M. Kubouchi, and Y. Arao, “Effect of graphite structures on the productivity and quality of few-layer graphene in liquid-phase exfoliation,” *J. Mater. Sci.*, vol. 53, no. 18, pp. 12807–12815, 2018.

[286] Kurniasari *et al.*, "Defect and Magnetic Properties of Reduced Graphene Oxide Prepared from Old Coconut Shell," in *IOP Conf. Series: Materials Science and Engineering*, 2017, p. 012021.

[287] H. Toraya, M. Yoshimura, and S. Somiya, "Calibration curve for quantitative analysis of the monoclinic-tetragonal ZrO2 system by x-ray diffraction.," *Commun. Am. Ceram. Soc.*, vol. 67, pp. C119–C121, 1984.

[288] W. Khaodee, B. Jongsomjit, P. Praserthdam, S. Goto, and S. Assabumrungrat, "Impact of temperature ramping rate during calcination on characteristics of nano-ZrO2 and its catalytic activity for isosynthesis," *J. Mol. Catal. A Chem.*, vol. 280, pp. 35–42, 2008.

[289] P. K. Lee, P. M. Nia, and P. M. Woi, "Facile self-assembled Prussian blue-polypyrrole nanocomposites on glassy carbon: Comparative synthesis methods and its electrocatalytic reduction towards H2O2," *Electrochim. Acta*, vol. 246, pp. 841–852, 2017.

[290] N. M. Ahmad, J. Abdullah, N. A. Yusof, A. H. Ab Rashid, S. A. Rahman, and M. R. Hasan, "Amperometric biosensor based on zirconium oxide/polyethylene glycol/tyrosinase composite film for the detection of phenolic compounds," *Biosensors*, vol. 6, no. 31, pp. 1–14, 2016.

[291] E. R. Lee, Y. J. Kang, J. H. Kim, H. T. Lee, and S. G. Cho, "Modulation of apoptosis in HaCaT keratinocytes via differential regulation of ERK signaling pathway by flavonoids," *J. Biol. Chem.*, vol. 280, no. 36, pp. 31498–31507, 2005.

[292] L. Horvath, A. Magrez, M. Burghard, K. Kern, L. Forro, and B. Schwaller, "Evaluation of the toxicity of graphene derivatives on cells of the lung luminal surface," *Carbon N. Y.*, vol. 64, pp. 45–60, 2013.

[293] International Organization for Standardization, "ISO 10993-5 Biological Evaluation of Medical Devices. Part 5: Tests for In Vitro Cytotoxicity," Geneva, Switzerland, 2009.

[294] K. Bachmann, "Drug-Drug interactions with an emphasis on drug metabolism and transport," in *Pharmacology*, 1st ed., Elsevier Inc., 2009, pp. 303–325.

[295] S. Lanone *et al.*, "Comparative toxicity of 24 manufactured nanoparticles in human alveolar epithelial and macrophage cell lines," *Part. Fibre Toxicol.*, vol. 6, no. 14, pp. 1–12, 2009.

[296] E. Asadpour, H. R. Sadeghnia, A. Ghorbani, M. Sedaghat, and M. T. Boroushaki, "Oxidative stress-mediated cytotoxicity of zirconia nanoparticles on PC12 and N2a cells," *J. Nanoparticle Res.*, vol. 18, no. 1, pp. 1–13, 2016.

[297] H. Zhang *et al.*, "Use of metal oxide nanoparticle band gap To develop a predictive

paradigm for oxidative stress and acute pulmonary inflammation," *ACS Nano*, vol. 6, no. 5, pp. 4349–4368, 2012.

[298] A. Ivask *et al.*, "Toxicity of 11 metal oxide nanoparticles to three mammalian cell types in vitro," *Curr. Top. Med. Chem.*, vol. 15, no. 18, pp. 1914–1929, 2015.

[299] W. Hu *et al.*, "Protein corona-mediated mitigation of cytotoxicity of graphene oxide," *ACS Nano*, vol. 5, no. 5, pp. 3693–3700, 2011.

[300] Q. Y. Siew, S. Y. Tham, H. S. Loh, P. S. Khiew, W. S. Chiu, and M. T. T. Tan, "One-step green hydrothermal synthesis of biocompatible graphene/TiO2 nanocomposites for non-enzymatic H2O2 detection and their cytotoxicity effects on human keratinocyte and lung fibroblast cells," *J. Mater. Chem. B*, vol. 6, no. 8, pp. 1195–1206, 2018.

[301] I. Mohar, B. D. Stamper, P. M. Rademacher, C. C. White, S. D. Nelson, and T. J. Kavanagh, "Acetaminophen-induced liver damage in mice is associated with gender-specific adduction of peroxiredoxin-6," *Redox Biol.*, vol. 2, pp. 377–387, 2014.

[302] G. L. Gupte, "Management of paracetamol overdose," *Paediatr. Child Health (Oxford).*, vol. 26, no. 10, pp. 459–463, 2016.

[303] S. Kesavan and S. Abraham John, "Stable determination of paracetamol in the presence of uric acid in human urine sample using melamine grafted graphene modified electrode," *J. Electroanal. Chem.*, vol. 760, pp. 6–14, 2016.

[304] Y. Teng, L. Fan, Y. Dai, M. Zhong, X. Lu, and X. Kan, "Electrochemical sensor for paracetamol recognition and detection based on catalytic and imprinted composite film," *Biosens. Bioelectron.*, vol. 71, pp. 137–142, 2015.

[305] A. Babaei, D. J. Garrett, and A. J. Downard, "Selective simultaneous determination of paracetamol and uric acid using a glassy carbon electrode modified with multiwalled carbon nanotube/chitosan composite," *Electroanalysis*, vol. 23, no. 2, pp. 417–423, 2011.

[306] X. Kang, J. Wang, H. Wu, J. Liu, I. A. Aksay, and Y. Lin, "A graphene-based electrochemical sensor for sensitive detection of paracetamol," *Talanta*, vol. 81, no. 3, pp. 754–759, 2010.

[307] B. J. Venton and D. J. Discenza, "Chapter 3 voltammetry," in *Electrochemistry for Bioanalysis*, Elsevier, 2021, pp. 27–50.

[308] J. Li *et al.*, "High-sensitivity paracetamol sensor based on Pd/graphene oxide nanocomposite as an enhanced electrochemical sensing platform," *Biosens. Bioelectron.*, vol. 54, pp. 468–475, 2014.

[309] Y. Zhang, X. Liu, L. Li, Z. Guo, Z. Xue, and X. Lu, "An electrochemical paracetamol sensor based on layer-by-layer covalent attachment of MWCNTs and a G4.0 PAMAM modified GCE," *Anal. Methods*, vol. 8, no. 10, pp. 2218–2225, 2016.

[310] A. Rochefort and J. D. Wuest, "Interaction of substituted aromatic compounds with graphene," *Langmuir*, vol. 25, no. 1, pp. 210–215, 2009.

[311] M. Baccarin, F. A. Santos, F. C. Vicentini, V. Zucolotto, B. C. Janegitz, and O. Fatibello-Filho, "Electrochemical sensor based on reduced graphene oxide/carbon black/chitosan composite for the simultaneous determination of dopamine and paracetamol concentrations in urine samples," *J. Electroanal. Chem.*, vol. 799, pp. 436–443, 2017.

[312] B. Habibi, M. Jahanbakhshi, and M. H. Pournaghi-Azar, "Simultaneous determination of acetaminophen and dopamine using SWCNT modified carbon-ceramic electrode by differential pulse voltammetry," *Electrochim. Acta*, vol. 56, no. 7, pp. 2888–2894, 2011.

[313] P. Panuwet *et al.*, "Biological matrix effects in quantitative tandem mass spectrometry-based analytical methods : Advancing biomonitoring," *Anal. Chem.*, vol. 46, no. 2, pp. 93–105, 2016.

[314] A. O. Riordan *et al.*, "Acute kidney injury in patients admitted to a liver intensive therapy unit with paracetamol-induced hepatotoxicity," *Nephrol Dial Transpl.*, vol. 26, pp. 3501–3508, 2011.

[315] M. Lipcsey *et al.*, "Urine hydrogen peroxide levels and their relation to outcome in patients with sepsis, septic shock, and major burn injury," *Biomedicines*, vol. 10, no. 4, p. 848, 2022.

[316] S. O. Eraga, M. I. Arhewoh, M. U. Uhumwangho, and M. A. Iwuagwu, "Characterisation of a novel, multifunctional, co-processed excipient and its effect on release profile of paracetamol from tablets prepared by direct compression," *Asian Pac. J. Trop. Biomed.*, vol. 5, no. 9, pp. 768–772, 2015.

[317] T. Mitsudomi and Y. Yatabe, "Epidermal growth factor receptor in relation to tumor development: EGFR gene and cancer," *FEBS J.*, vol. 277, pp. 301–308, 2010.

[318] D. Bregon and P. W. Doetsch, "Transcriptional mutagenesis: causes and involvement in tumor development," *Nat. Rev. Cancer*, vol. 11, no. 3, pp. 218–227, 2013.

[319] Z. Yang, A. Hackshaw, Q. Feng, X. Fu, and Y. Zhang, "Comparison of gefitinib, erlotinib and afatinib in non-small cell lung cancer : a meta-analysis," *Int. J. Cancer*, vol. 140, no. 12, pp. 2805–2819, 2017.

[320] M. Barozzi *et al.*, "Optical fiber sensors for label-free DNA detection," *J. Light. Technol.*,

vol. 35, no. 16, pp. 3461–3472, 2017.

[321] L. Miotke, A. Maity, H. Ji, J. Brewer, and K. Astakhova, "Enzyme-free detection of mutations in cancer DNA Using synthetic oligonucleotide probes and fluorescence microscopy," *PLoS One*, vol. 10, no. 8, pp. 1–11, 2015.

[322] H. Imran, P. N. Manikandan, and V. Dharuman, "Graphene oxide supported liposomes for efficient label free electrochemical DNA biosensing," *Sensors Actuators, B Chem.*, vol. 260, pp. 841–851, 2018.

[323] C. L. Sun, W. L. Cheng, T. K. Hsu, C. W. Chang, J. L. Chang, and J. M. Zen, "Ultrasensitive and highly stable nonenzymatic glucose sensor by a CuO/graphene-modified screen-printed carbon electrode integrated with flow-injection analysis," *Electrochem. commun.*, vol. 30, pp. 91–94, 2013.

[324] T. Tian *et al.*, "Paper-based biosensor for noninvasive detection of epidermal growth factor receptor mutations in non-small cell lung cancer patients," *Sensors Actuators, B Chem.*, vol. 251, pp. 440–445, 2017.

[325] V. A. Karachevtsev *et al.*, "Noncovalent interaction of single-walled carbon nanotubes with 1-pyrenebutanoic acid succinimide ester and glucoseoxidase," *J. Phys. Chem. C*, vol. 115, no. 43, pp. 21072–21082, 2011.

[326] J. H. Bae, S. M. Jo, and H. S. Kim, "Comprehensive detection of diverse exon 19 deletion mutations of EGFR in lung cancer by a single probe set," *Biosens. Bioelectron.*, vol. 74, pp. 849–855, 2015.

[327] N. Karachaliou, M. A. Molina-vila, R. Rosell, N. Karachaliou, M. Angel, and R. Rosell, "The impact of rare EGFR mutations on the treatment response of patients with non-small cell lung cancer," *Expert Rev. Respir. Med.*, vol. 9, no. 3, pp. 241–244, 2015.

[328] T. Lynch *et al.*, "Activating mutations in the epidermal growth factor receptor underlying responsiveness of non–small-cell lung cancer to gefitinib," *N. Engl. J. Med.*, vol. 350, no. 21, pp. 2129–2139, 2004.

[329] X. W. Xu *et al.*, "Detection EGFR exon 19 status of lung cancer patients by DNA electrochemical biosensor," *Biosens. Bioelectron.*, vol. 80, pp. 411–417, 2016.

[330] S. Park and J. Yoo, "Electrochemical impedance spectroscopy for better electrochemical measurements," *Anal. Chem.*, pp. 455–461, 2003.

[331] J. Y. Park and S. M. Park, "DNA hybridization sensors based on electrochemical impedance spectroscopy as a detection tool," *Sensors*, vol. 9, no. 12, pp. 9513–9532, 2009.

[332] J. Kafka, O. Pänke, B. Abendroth, and F. Lisdat, “A label-free DNA sensor based on impedance spectroscopy,” *Electrochim. Acta*, vol. 53, no. 25, pp. 7467–7474, 2008.

[333] W. Zhang, T. Yang, X. Li, D. Wang, and K. Jiao, “Conductive architecture of Fe2O3 microspheres / self-doped polyaniline nanofibers on carbon ionic liquid electrode for impedance sensing of DNA hybridization,” *Biosens. Bioelectron.*, vol. 25, pp. 428–434, 2009.

[334] H. A. Rafiee-Pour, M. Behpour, and M. Keshavarz, “A novel label-free electrochemical miRNA biosensor using methylene blue as redox indicator: Application to breast cancer biomarker miRNA-21,” *Biosens. Bioelectron.*, vol. 77, pp. 202–207, 2016.

[335] W. Wang, X. Fan, S. Xu, J. J. Davis, and X. Luo, “Low fouling label-free DNA sensor based on polyethylene glycols decorated with gold nanoparticles for the detection of breast cancer biomarkers,” *Biosens. Bioelectron.*, vol. 71, pp. 51–56, 2015.

[336] P. Teengam, W. Siangproh, A. Tuantranont, T. Vilaivan, O. Chailapakul, and C. S. Henry, “Electrochemical impedance-based DNA sensor using pyrrolidinyl peptide nucleic acids for tuberculosis detection,” *Anal. Chim. Acta*, vol. 1044, pp. 102–109, 2018.

[337] L. Ribovski, V. Zucolotto, and B. C. Janegitz, “A label-free electrochemical DNA sensor to identify breast cancer susceptibility,” *Microchem. J.*, vol. 133, pp. 37–42, 2017.

[338] M. Shamsipur, L. Samandari, L. Farzin, and A. Besharati-seidani, “Development of an ultrasensitive electrochemical genosensor for detection of HIV-1 pol gene using a gold nanoparticles coated carbon paste electrode impregnated with lead ion-imprinted polymer nanomaterials as a novel electrochemical probe,” *Microchem. J.*, vol. 160, no. PB, p. 105714, 2021.

[339] K. Zhang, H. Ma, L. Zhang, and Y. Zhang, “Fabrication of a sensitive impedance biosensor of DNA hybridization based on gold nanoparticles modified gold electrode,” *Electroanalysis*, vol. 20, no. 19, pp. 2127–2133, 2008.

[340] S. Kumar *et al.*, “Reduced graphene oxide modified smart conducting paper for cancer biosensor,” *Biosens. Bioelectron.*, vol. 73, pp. 114–122, 2015.

[341] E. P. Randviir, “A cross examination of electron transfer rate constants for carbon screen-printed electrodes using Electrochemical Impedance Spectroscopy and cyclic voltammetry,” *Electrochim. Acta*, vol. 286, pp. 179–186, 2018.

[342] A. Bardea, E. Katz, and I. Willner, “Probing antigen-antibody interactions on electrode supports by the biocatalyzed precipitation of an insoluble product,” *Electroanalysis*, vol.

12, no. 14, pp. 1097–1106, 2000.

[343] N. Elgrishi, K. J. Rountree, B. D. McCarthy, E. S. Rountree, T. T. Eisenhart, and J. L. Dempsey, "A practical beginner's guide to cyclic voltammetry," *J. Chem. Educ.*, vol. 95, no. 2, pp. 197–206, 2018.

[344] R. J. Chen, Y. Zhang, D. Wang, and H. Dai, "Noncovalent sidewall functionalization of carbon nanotubes for protein immobilization," *J. Am. Chem. Soc.*, vol. 123, no. 16, pp. 3838–3839, 2001.

[345] A. W. Peterson, "The effect of surface probe density on DNA hybridization," *Nucleic Acids Res.*, vol. 29, no. 24, pp. 5163–5168, 2001.

[346] J. J. Gooding, A. Chou, F. J. Mearns, E. Wong, and K. L. Jericho, "The ion gating effect: using a change in flexibility to allow label free electrochemical detection of DNA hybridisation.," *Chem. Commun.*, vol. 9, no. 15, pp. 1938–1939, 2003.

[347] T. Ito, K. Hosokawa, and M. Maeda, "Detection of single-base mismatch at distal end of DNA duplex by electrochemical impedance spectroscopy," *Biosens. Bioelectron.*, vol. 22, no. 8, pp. 1816–1819, 2007.

[348] V. Biagiotti, A. Porchetta, S. Desiderati, K. W. Plaxco, G. Palleschi, and F. Ricci, "Probe accessibility effects on the performance of electrochemical biosensors employing DNA monolayers," *Anal. Bioanal. Chem.*, vol. 402, no. 1, pp. 413–421, 2012.

[349] L. M. Demers *et al.*, "A fluorescence-based method for determining the surface coverage and hybridization efficiency of thiol-capped oligonucleotides bound to gold thin films and nanoparticles," *Anal. Chem.*, vol. 72, no. 22, pp. 5535–5541, 2000.

[350] D. Ge, X. Wang, K. Williams, and R. Levicky, "Thermostable DNA immobilization and temperature effects on surface hybridization," *Langmuir*, vol. 28, no. 22, pp. 8446–8455, 2012.

[351] J. I. A. Rashid and N. A. Yusof, "The strategies of DNA immobilization and hybridization detection mechanism in the construction of electrochemical DNA sensor: A review," *Sens. Bio-Sensing Res.*, vol. 16, pp. 19–31, 2017.

[352] J. Chen, B. Fu, T. Liu, Z. Yan, and K. Li, "A graphene oxide-DNA electrochemical sensor based on glassy carbon electrode for sensitive determination of methotrexate," *Electroanalysis*, vol. 30, no. 2, pp. 288–295, 2018.

[353] P. Wang, X. Li, Z. Dai, X. Zou, and X. Han, "An efficient electrochemical method for direct screening of the mutation status of DNA base in oligonucleotides," *Sensors Actuators, B*

Chem., vol. 201, pp. 222–227, 2014.

[354] B. Y. Won, H. C. Yoon, and H. G. Park, "Enzyme-catalyzed signal amplification for electrochemical DNA detection with a PNA-modified electrode," *Analyst*, vol. 133, pp. 100–104, 2008.

[355] W. Tao, P. Lin, H. Liu, S. Ke, and X. Zeng, "A rapid, label-free and impedimetric DNA sensor based on PNA-modified nanoporous gold electrode," *Int. J. Electrochem. Sci.*, vol. 12, pp. 10511–10523, 2017.

[356] P. Kara, Y. Erzurumlu, P. B. Kirmizibayrak, and M. Ozsoz, "Electrochemical aptasensor design for label free cytosensing of human non-small cell lung cancer," *J. Electroanal. Chem.*, vol. 775, pp. 337–341, 2016.

[357] E. Farjami, L. Clima, K. V. Gothelf, and E. E. Ferapontova, "DNA interactions with a methylene blue redox indicator depend on the DNA length and are sequence specific," *Analyst*, vol. 135, no. 6, pp. 1443–1448, 2010.

[358] C. Lin, Y. Wu, F. Luo, D. Chen, and X. Chen, "A label-free electrochemical DNA sensor using methylene blue as redox indicator based on an exonuclease III-aided target recycling strategy," *Biosens. Bioelectron.*, vol. 59, pp. 365–369, 2014.

[359] Y. Hu, K. Wang, Q. Zhang, F. Li, T. Wu, and L. Niu, "Decorated graphene sheets for label-free DNA impedance biosensing," *Biomaterials*, vol. 33, no. 4, pp. 1097–1106, 2012.

[360] S. B. Nimse, K. Song, M. D. Sonawane, D. R. Sayyed, and T. Kim, "Immobilization techniques for microarray: challenges and applications," *Sensors*, vol. 14, pp. 22208–22229, 2014.

[361] P. Du, H. Li, and W. Cao, "Construction of DNA sandwich electrochemical biosensor with nanoPbS and nanoAu tags on magnetic microbeads," *Biosens. Bioelectron.*, vol. 24, pp. 3223–3228, 2009.

[362] P. Taylor, B. T. Cunningham, and L. G. Laing, "Advantages and application of label-free detection assays in drug screening," *Expert Opin. Drug Discov.*, vol. 3, no. 8, pp. 891–901, 2008.

[363] M. Grunnet and J. B. Sorensen, "Lung Cancer Carcinoembryonic antigen (CEA) as tumor marker in lung cancer," *Lung Cancer*, vol. 76, pp. 138–143, 2012.

[364] X. Li, M. Yu, Z. Chen, X. Lin, and Q. Wu, "A sensor for detection of carcinoembryonic antigen based on the polyaniline-Au nanoparticles and gap-based interdigitated electrode," *Sensors Actuators B. Chem.*, vol. 239, pp. 874–882, 2017.

[365] Z. Yang, Q. Lan, J. Li, J. Wu, Y. Tang, and X. Hu, "Efficient streptavidin-functionalized nitrogen-doped graphene for the development of highly sensitive electrochemical immunosensor," *Biosens. Bioelectron.*, vol. 89, pp. 312–318, 2016.

[366] E. Sánchez-Tirado, A. González-Cortés, P. Yáñez-Sedeño, and J. M. Pingarrón, "Carbon nanotubes functionalized by click chemistry as scaffolds for the preparation of electrochemical immunosensors. Application to the determination of TGF-beta 1 cytokine," *Analyst*, vol. 141, pp. 5730–5737, 2016.

[367] S. Samanman, A. Numnuam, and W. Limbut, "Highly-sensitive label-free electrochemical carcinoembryonic antigen immunosensor based on a novel Au nanoparticles- graphene-chitosan nanocomposite cryogel electrode," *Anal. Chim. Acta*, vol. 853, pp. 521–532, 2015.

[368] M. Rizwan, S. Elma, S. A. Lim, and M. U. Ahmed, "AuNPs/CNOs /SWCNTs /chitosan-nanocomposite modified electrochemical sensor for the label-free detection of carcinoembryonic antigen," *Biosens. Bioelectron.*, vol. 107, pp. 211–217, 2018.

[369] S. Kumar, S. Kumar, S. Tiwari, and S. Srivastava, "Biofunctionalized nanostructured zirconia for biomedical application: A smart approach for oral cancer detection," *Adv. Sci.*, vol. 2, no. 5, pp. 1–9, 2015.

[370] A. Vasudev, A. Kaushik, and S. Bhansali, "Electrochemical immunosensor for label free epidermal growth factor receptor (EGFR) detection," *Biosens. Bioelectron.*, vol. 39, no. 1, pp. 300–305, 2013.

[371] T. Bertok *et al.*, "Label-free detection of glycoproteins by the lectin biosensor down to attomolar level using gold nanoparticles," *Talanta*, vol. 108, pp. 11–18, 2013.

[372] P. A. Rasheed and N. Sandhyarani, "Attomolar detection of BRCA1 gene based on gold nanoparticle assisted signal amplification," *Biosens. Bioelectron.*, vol. 65, pp. 333–340, 2015.

[373] A. R. Cardoso, F. T. C. Moreira, R. Fernandes, and M. G. F. Sales, "Novel and simple electrochemical biosensor monitoring attomolar levels of miRNA-155 in breast cancer," *Biosens. Bioelectron.*, vol. 80, pp. 621–630, 2016.

[374] P. Khashayar, G. Amoabediny, B. Larijani, and H. Morteza, "Fabrication and verification of conjugated AuNP-antibody nanoprobe for sensitivity improvement in electrochemical biosensors," *Sci. Rep.*, vol. 7, no. 1, p. 16070, 2017.

[375] A. Makaraviciute, A. Ramanavicius, and A. Ramanaviciene, "Development of a reusable protein G based SPR immunosensor for direct human growth hormone detection in real

samples," *Anal. Methods*, vol. 7, pp. 9875–9884, 2015.

[376] K. Omidfar, M. Darzianiazizi, A. Ahmadi, M. Daneshpour, and H. Shirazi, "A high sensitive electrochemical nanoimmunosensor based on Fe3O4/TMC/Au nanocomposite and PT-modified electrode for the detection of cancer biomarker epidermal growth factor receptor," *Sensors Actuators, B Chem.*, vol. 220, pp. 1311–1319, 2015.

[377] N. G. Welch, J. A. Scoble, B. W. Muir, P. J. Pigram, and N. G. Welch, "Orientation and characterization of immobilized antibodies for improved immunoassays (Review)," *Biointerphases*, vol. 12, no. 2, p. 02D301-1-02D301-13, 2017.

[378] J. Han *et al.*, "Ultrasensitive non-enzymatic immunosensor for carcino-embryonic antigen based on palladium hybrid vanadium pentoxide / multiwalled carbon nanotubes," *Biosens. Bioelectron.*, vol. 77, pp. 1104–1111, 2016.

[379] X. Gu, Z. She, and T. Ma, "Electrochemical detection of carcinoembryonic antigen," *Biosens. Bioelectron.*, vol. 102, pp. 610–616, 2018.

[380] K. Huang, D. Niu, W. Xie, and W. Wang, "A disposable electrochemical immunosensor for carcinoembryonic antigen based on nano-Au / multi-walled carbon nanotubes – chitosans nanocomposite film modified glassy carbon electrode," *Anal. Chim. Acta*, vol. 659, pp. 102–108, 2010.

[381] M. M. Ardakani and Z. T. Ardakani, "Fabrication of an ultrasensitive and selective electrochemical aptasensor to detect carcinoembryonic antigen by using a new nanocomposite," *Biosens. Bioelectron.*, vol. 129, pp. 1–6, 2019.

[382] J. Qian, H. Dai, X. Pan, and S. Liu, "Simultaneous detection of dual proteins using quantum dots coated silica nanoparticles as labels," *Biosens. Bioelectron.*, vol. 28, pp. 314–319, 2011.

[383] S. F. Z. Bakri and A. Hariri, "Conducting paper based sensor for cancer biomarker detection," *J. Phys. Conf. Ser.*, vol. 704, p. 012010, 2016.

[384] Q. Hao, L. Wang, S. Niu, C. Ding, and X. Luo, "Ratiometric electrogenerated chemiluminescence sensor based on a designed anti-fouling peptide for the detection of carcinoembryonic antigen," *Anal. Chim. Acta*, vol. 1136, pp. 134–140, 2020.

[385] N. Gan, L. Jia, Q. Mary, and L. Zheng, "A sandwich electrochemical immunosensor using magnetic DNA nanoprobes for carcinoembryonic antigen," *Int. J. Mol. Sci.*, vol. 12, pp. 7410–7423, 2011.

[386] S. Sang, Y. Wang, Q. Feng, Y. Wei, J. Ji, and W. Zhang, "Progress of new label-free

techniques for biosensors: a review," *Crit. Rev. Biotechnol.*, vol. 36, no. 3, pp. 465–481, 2015.

[387] E. M. Perez and N. Martin, "p–p interactions in carbon nanostructures," *Chem. Soc. Rev.*, vol. 44, pp. 6425–6433, 2015.

[388] W. Kusnezow and J. D. Hoheisel, "Solid supports for microarray immunoassays," *J. Mol. Recognit.*, vol. 16, pp. 165–176, 2003.

[389] J. Richter, M. Nnaji, and H. Park, "Solvent effect to the uniformity of surfactant-free salmon-DNA thin films," *Polymers (Basel).*, vol. 13, p. 1606, 2021.

[390] F. Rahman and M. W. Saif, "Elevated level of serum carcinoembryonic antigen (CEA) and search for a malignancy : A case report," *Cureus*, vol. 8, no. 6, pp. 8–11, 2016.